5-2003

The Role of Surface States in Electron-Phonon Coupling on the Open Surfaces of Simple Metals

Shu-Jung Tang
University of Tennessee - Knoxville

To the Graduate Council:

I am submitting herewith a dissertation written by Shu-Jung Tang entitled "The Role of Surface States in Electron-Phonon Coupling on the Open Surfaces of Simple Metals." I have examined the final electronic copy of this dissertation for form and content and recommend that it be accepted in partial fulfillment of the requirements for the degree of Doctor of Philosophy, with a major in Physics.

Ward Plummer, Major Professor

We have read this dissertation and recommend its acceptance:

Tom A. Callcott, David G. Madrus, Charles S. Feigerle

Accepted for the Council:
Dixie L. Thompson

Vice Provost and Dean of the Graduate School

(Original signatures are on file with official student records.)

To the Graduate Council:

I am submitting herewith a dissertation written by Shu-Jung Tang entitled " The role of surface states in electron-phonon coupling on the open surfaces of simple metals." I have examined the final electronic copy of this dissertation for form and content and recommend that it be accepted in partial fulfillment of the requirements for the degree of Doctor of Philosophy, with a major in Physics.

Ward Plummer

Major Professor

We have read this dissertation
and recommend its acceptance:

Tom A. Callcott

David G. Madrus

Charles S. Feigerle

Accepted for the Council:

Anne Mayhew

Vice Provost and Dean of
Graduate studies

(Original signatures are on files with official student records.)

THE ROLE OF SURFACE STATES IN ELECTRON-PHONON COUPLING ON THE OPEN SURFACES OF SIMPLE METALS

A Dissertation

Presented for the

Doctor of Philosophy

Degree

The University of Tennessee, Knoxville

Shu-Jung Tang

December 2002

DEDICATION

This thesis is dedicated to my father, Lin-Chuan Tang
whose love and spirit always stay in my heart
and my persevering mother, Pi-Chuen Yeh
for her endless support and love

ACKNOLEDGEMENTS

My graduation school years can be divided into three stages. In the first two years, I only took courses and worked as a half-time TA. I would like to thank professor Geoffrey Canright and professor Adolfo Eguiluz for the wonderful classes they taught, classics mechanics and quantum mechanics. I benefited a lot from them no matter in the physics knowledge or the way to think physics. I also want to thank professor Chia C. Shih for his generous help and advice when I met all kinds of problems in the life. I also want to thank those people who were my classmates then and had given me a lot of help no matter in the class or life.

The second stage started from the third year when I joined Dr.Plummer's group and moved to the Baton Rouge for doing experiments through Photoemission technique in a synchrotron center called CAMD. Start doing research in a place far from my school made my graduate student life in a completely different scenario from the first stage. While I was taking courses, I met setbacks in exams sometimes but I could still overcome them and achieve good results eventually. However, doing research is not that simple, especially in a place where you are the only one motivated for your experiment and result. I would like to thank Hisao Ishii, Eizi Morikawa, and Phil Sprunger for their conduct in the knowledge and technique of beam line and Photoemission. I would like to thank Yaroslav Losovyi, Weichang Zhao, Orhan Kizilkaya, and Dustin Hite for any help they have given to me. I would like to thank Xingyu Gao for instructing me how to write integral function program for the curve fitting. I would like to thank this person, Kevin Koch, for helping each other grow up no matter in the research or life. I would like to

thank Juraj Topolancik for assisting me to build the Scienta energy analyzer system and taking me to the world of beer. I would specially thank this nice lady, Chantal Khan Malek for her good heart and caring about me. I would like to thank the owner, Susan, of the Yangtze cafe Chinese restaurant for always giving me discount for the meal and her caring of my life.

After 5 years of research in CAMD, I came back to my school in Tennessee to concentrate writing my thesis. I would like to thank Mrs. Mary Jo, the secretary in the group, for helping me solve all the troubles (I-20 problem, class and registration problems…) I met. I also want to thank the post doctor, Ismail, and the graduate student, Dane Gillaspie, in the group for all the help and helpful suggestions from them. Most importantly, I'm very grateful to my adviser, Ward Plummer, for his support and his insight in me. An old Chinese saying," There is no good horse until an expert see it and develop it." Thank you, Dr. Plummer.

At last, I want to thank my parents again for their endless love and support. My father died of cancer when I was in the military service. All he hoped in his life was to see his children make good achievement and be useful. He himself is a very tough person who had ever almost lost his two legs in the serious injury form the war. However, through his unbelievable perseveration, he overcame all the difficulties and made so many miracles in his life. He always has strong confidence in himself and in his children. Even though I cannot talk to him and hear him any more while I 'm in US, his spirit and strong confidence always stay in my heart and push me going forward. "Dad, I hope I didn't let you down and I can see your smile again in the dream"

ABSTRACT

Symmetry is the beauty of nature. It is the mirror of the way nature minimizes the energy of the system, and achieves the stable state. In the bulk crystal, 3D symmetry has ensured the minimum of free energy contributed by electrostatic energy, vibrational energy and many body self-energy. When the crystal is broken to form two surfaces, the 3D symmetry is destroyed, leading to high free energy on the surface. In order to minimize the free energy, the electronic charge on or near the surface rearranges to form an electronic and lattice structure quite distinct from the bulk. My research is to investigate the interplay between surface electronic structure and lattice structure through electron-phonon coupling of surface states on the open surface of simple metals, such as $\mathrm{Be}(10\bar{1}0)$ and $\mathrm{Mg}(10\bar{1}0)$

Through the technique of angle-resolved photoemission, I investigated the band structures, line shapes, widths of surface states and their temperature dependence. At T = 0, electron structures are in the ground state, but as the temperature was increased, electron-phonon coupling became more important as more electron-hole pairs were excited within $k_B T$ energy which corresponded to the phonon energies. On the $(10\bar{1}0)$ surface Brillouin zone at the zone boundary $\bar{A}$, there are two surface states (S1 and S2) coexisting in a gap in the bulk projection. These appear on both $\mathrm{Be}(10\bar{1}0)$ and $\mathrm{Mg}(10\bar{1}0)$. Through fitting the temperature-dependent surface state width contributed to by the imaginary part of self-energy from electron-phonon coupling, the electron-phonon coupling strength parameter, λ, was determined for both surface states on both surfaces.

The λ value of S1 and S2 (λ_{S1} = 0.647 and λ_{S2} = 0.491, respectively) on Be$(10\bar{1}0)$ is more than two times larger than the bulk value (λ_{bulk} = 0.24). However, for Mg$(10\bar{1}0)$, the determined electron-phonon coupling parameters of S1 and S2 surface states are not larger (λ_{S1} = 0.20, λ_{S2} = 0.31) than the bulk value (λ_{bulk} = 0.31). According to many previous studies, Be surfaces have very special electronic and lattice behaviors. Therefore, a larger electron -phonon interaction on the Be surface would be expected. Furthermore, according to the comparison of fitting goodness between Einstein and Debye models for the temperature dependence of surface state widths, I found the most localized S1 surface state had dominant coupling with localized high-energy optical phonon at about 64 meV. This large coupling even causes the large distortion of the S1 surface state band on crossing the optical phonon energy as observed in high-resolution photoemission spectrum. Based on these results, I have attempted to construct a picture of the interplay between the electronic structure and dynamic lattice structure for the large negative thermal expansion of the Be$(10\bar{1}0)$ surface. The behavior of surface states on Mg$(10\bar{1}0)$ shows a big contrast with that on Be$(10\bar{1}0)$, which I attribute to the close relationship between the surface state and bulk state on Mg$(10\bar{1}0)$.

TABLE OF CONTENTS

LIST OF TABLES

LIST OF FIGURES

Chapter 1 Theory of Electronic Structure of Simple Metals

1.1 Nearly Free Electron Metals

Nearly free electron (NFE) metals, simple metals, provide a good environment to study the electrons-electron and electrons-phonon interactions. Their electronic structures are simple, in the sense that there are only *s* and *p* electrons outside of a closed-shell noble gas configuration. Therefore, it is easy to identify the many body effects in the nearly free electron metals, which only consist of two basic elements, ions and conduction electrons. The conduction electrons move in what amounts to an almost constant potential (pseudopotentials). The Pauli exclusion principle coupled with efficient electron-electron screening further ensures the high mobility of the conduction electrons in the nearly free electron metal system. Therefore, it is reasonable to consider such a system as a free electron gas modified by the presence of a weak periodic potential. As a result, correlation effects become relevant and visible experimentally to the microscope properties of the system.

For example, the correlation between the ions and conduction electrons would have strong effects to modify the motions of conduction electrons and vibrations of the ions. Many interesting phenomenon, i.e., superconductivity, have been attributed to the electron-phonon interaction.

1.2 Electrons in a Weak Periodic Potential

To further look into the electronic system in NFE metals, we should start from the Schrödinger equation in a weak periodic potential [1]. The general form of the Schrödinger equation can be expressed as

$$H\psi = (-\frac{\hbar^2}{2m}\nabla^2 + U(\vec{r}))\psi = \varepsilon\psi \tag{1.1}$$

From Bloch's theory, the wave function in a periodic potential U($\vec{r}$) can be put in the form $\psi_k(\vec{r}) = e^{i\vec{k}*\vec{r}}u_k(\vec{r})$ where the periodic function $u_k(\vec{r})$ as well as U($\vec{r}$) can be expressed as a Fourier series. Namely, $u_k(\vec{r}) = \sum_{\vec{g}} c_{\vec{k}-\vec{g}}\, e^{-i\vec{g}\bullet\vec{r}}$, $U(\vec{r}) = \sum_{\vec{g}} U_{\vec{g}}\, e^{i\vec{g}\bullet\vec{r}}$. $\vec{k}$ is the momentum of the wave function, and $\vec{g}$ is a reciprocal lattice vector. C's and U's are Fourier coefficients. With those expressions for $u_k(\vec{r})$ and U($\vec{r}$), the Schrödinger equation (1.1) in a periodic potential can be expressed as a set of

$$[\frac{\hbar^2}{2m}(\vec{k}-\vec{g})^2 - \varepsilon]c_{\vec{k}-\vec{g}} + \sum_{\vec{g}'} U_{\vec{g}'-\vec{g}}c_{\vec{k}-\vec{g}'} = 0 \tag{1.2}$$

In the free electron case, U($\vec{r}$) =0, all the Fourier components $U_{\vec{g}}$ are precisely zero. Then equation (1.2) becomes

$$(\varepsilon^0_{\vec{k}-\vec{g}} - \varepsilon)c_{\vec{k}-\vec{g}} = 0\,, \text{ where } \varepsilon^0_{\vec{k}-\vec{g}} = \frac{\hbar^2}{2m}(\vec{k}-\vec{g}\,)^2 \tag{1.3}$$

Equation (1.3) requires either $c_{\vec{k}-\vec{g}} = 0$ or $\varepsilon^0_{\vec{k}-\vec{g}} - \varepsilon = 0$ for each $\vec{g}$. There are two cases for the condition $\varepsilon^0_{\vec{k}-\vec{g}} - \varepsilon = 0$. One has no degeneracy where the only solution is a

free electron wave function, with $\varepsilon^0_{\vec{k}-\vec{g}} = \varepsilon$ for a certain single reciprocal wave vector $\vec{g}$. Another is degeneracy where a group of reciprocal lattice vectors $\vec{g}_1 \ldots \vec{g}_n$, satisfying $\varepsilon^0_{\vec{k}-\vec{g}_1} = \cdots = \varepsilon^0_{\vec{k}-\vec{g}_n}$. When ε is equal to the common value of these free electron energies, there are *n* independent degenerate plane wave solutions. Since any linear combination of degenerate solutions is also a solution, one has complete freedom in choosing the coefficients $c_{\vec{k}-\vec{g}}$ for $\vec{g} = \vec{g}_1, \ldots, \vec{g}_n$. When moving on to NFE systems where there is a very weak electronic potential U, the distinct criteria for two different cases are whether different free electron energy levels are equal aside from terms of order U. In other words, the interesting thing to see is how the perturbation from the weak potential affects (1) the single free electron wave function and (2) the degeneracy of a group of wave functions with different wave vector .

Case (1) : $\left| \varepsilon^0_{\vec{k}-\vec{g}_1} - \varepsilon^0_{\vec{k}-\vec{g}} \right| >> U$ for fixed $\vec{k}$ and all $\vec{g} \neq \vec{g}_1$. We wish to investigate the effect of the potential on the free electron level given by:

$$\varepsilon = \varepsilon^0_{\vec{k}-\vec{g}_1}, \quad c_{\vec{k}-\vec{g}} = 0 \text{ for } \vec{g} \neq \vec{g}_1 \tag{1.4}$$

Setting $\vec{g} = \vec{g}_1$ in Equation (1.2), we get

$$\left(\varepsilon - \varepsilon^0_{\vec{k}-\vec{g}_1}\right) c_{\vec{k}-\vec{g}_1} = \sum_{\vec{g}} U_{\vec{g}-\vec{g}_1} c_{\vec{k}-\vec{g}} \tag{1.5}$$

The additive constant in the potential energy has been picked up to make $U_{\vec{g}} = 0$ when $\vec{g}_1 = 0$. Therefore only terms with $\vec{g} \neq \vec{g}_1$ appear on the right hand side. We are examining the solution for which $c_{\vec{k}-\vec{g}} = 0$ when $\vec{g} \neq \vec{g}_1$ in the limit of vanishing U so

the right-hand side of Equation (1.5) can be seen as a second order in U. This can be confirmed by rewriting Equation (1.2) as

$$c_{\vec{k}-\vec{g}} = \frac{U_{\vec{g}_1-\vec{g}} c_{\vec{k}-\vec{g}_1}}{\varepsilon - \varepsilon^0_{\vec{k}-\vec{g}}} + \sum_{\vec{g}'\neq\vec{g}_1} \frac{U_{\vec{g}'-\vec{g}} c_{\vec{k}-\vec{g}'}}{\varepsilon - \varepsilon^0_{\vec{k}-\vec{g}}} = \frac{U_{\vec{g}_1-\vec{g}} c_{\vec{k}-\vec{g}_1}}{\varepsilon - \varepsilon^0_{\vec{k}-\vec{g}}} + O(U^2) \text{ for } \vec{g} \neq \vec{g}_1 \tag{1.6}$$

Putting this back to (1.5), we find

$$\left(\varepsilon - \varepsilon^0_{\vec{k}-\vec{g}_1}\right) c_{\vec{k}-\vec{g}_1} = \sum_{\vec{g}} \frac{U_{\vec{g}-\vec{g}_1} c_{\vec{g}_1-\vec{g}}}{\varepsilon - \varepsilon^0_{\vec{k}-\vec{g}}} c_{\vec{k}-\vec{g}_1} + O(U^3) \tag{1.7}$$

Replacing the ε in the denominator on the right-hand side by $\varepsilon^0_{\vec{k}-\vec{g}_1}$.

$$\varepsilon = \varepsilon^0_{\vec{k}-\vec{g}_1} + \sum_{\vec{g}} \frac{\left|U_{\vec{g}-\vec{g}_1}\right|^2}{\varepsilon^0_{\vec{k}-\vec{g}_1} - \varepsilon^0_{\vec{k}-\vec{g}}} c_{\vec{k}-\vec{g}_1} + O(U^3) \tag{1.8}$$

The contribution from the second term in the right-hand side of Equation (1.8) is almost zero since the parts of $\varepsilon^0_{\vec{k}-\vec{g}_1} - \varepsilon^0_{\vec{k}-\vec{g}} > 0$ cancel out the parts of $\varepsilon^0_{\vec{k}-\vec{g}_1} - \varepsilon^0_{\vec{k}-\vec{g}} < 0$. Therefore, in this case of no near degeneracy, the shift in energy from free energy value due to the weak potential is almost negligible, second order in U.

Case (2): For several states $\vec{g}_1, \ldots, \vec{g}_n$ such that their energies are all within the order U of each other but $\left| \varepsilon^0_{\vec{k}-\vec{g}} - \varepsilon^0_{\vec{k}-\vec{g}_i} \right| >> U$, i =1,….,n for $\vec{g} \neq \vec{g}_1, \ldots, \vec{g}_n$.

For simplicity, consider the case of two almost degenerate states, *n* = 2. Following the same procedure used in **Case(1)** except that two equations of (1.2) are treated separately,

$$(\varepsilon - \varepsilon^0_{\vec{k}-\vec{g}_1})\, c_{\vec{k}-\vec{g}_1} = \sum_{j=1}^{m=2} U_{\vec{g}_j-\vec{g}_1}\, c_{\vec{k}-\vec{g}_j} + \sum_{j=1}^{m=2} \left(\sum_{\vec{g}\neq\vec{g}_1,\ldots\vec{g}_m} \frac{U_{\vec{g}-\vec{g}_1} U_{\vec{g}_j-\vec{g}}}{\varepsilon - \varepsilon^0_{\vec{k}-\vec{g}}} \right) c_{\vec{k}-\vec{g}_j} + O(U^3) \tag{1.9}$$

$$(\varepsilon-\varepsilon^0_{\vec{k}-\vec{g}_2})\,c_{\vec{k}-\vec{g}_2}=\sum_{j=1}^{m=2}U_{\vec{g}_j-\vec{g}_2}\;c_{\vec{k}-\vec{g}_j}\;+\;\sum_{j=1}^{m=2}\left(\sum_{\vec{g}\neq\vec{g}_1,\cdots\vec{g}_m}\frac{U_{\vec{g}-\vec{g}_2}U_{\vec{g}_j-\vec{g}}}{\varepsilon-\varepsilon^0_{\vec{k}-\vec{g}}}\right)c_{\vec{k}-\vec{g}_j}+O(U^3)\qquad(1.10)$$

From the equations above, we find that to an accuracy of order U^2 the determination of the shifts in the two nearly degenerate levels reduces to the solutions of two coupled equations. The second terms on the right-hand sides of the two equations above are of higher order than the first terms. Consequently, we can just consider the first linear terms for the shifts of energy levels. Namely,

$$(\varepsilon-\varepsilon^0_{\vec{k}-\vec{g}_1})\,c_{\vec{k}-\vec{g}_1}=U_{\vec{g}_2-\vec{g}_1}\,c_{\vec{k}-\vec{g}_2}$$

$$(\varepsilon-\varepsilon^0_{\vec{k}-\vec{g}_2})\,c_{\vec{k}-\vec{g}_2}=U_{\vec{g}_1-\vec{g}_2}\,c_{\vec{k}-\vec{g}_1}\qquad(1.11)$$

Here, we introduce variables particularly convenient for the two-level problem .

$$\vec{q}=\vec{k}-\vec{g}_1\;\text{ and }\;\vec{K}=\vec{g}_2-\vec{g}_1\qquad(1.12)$$

Then $(\varepsilon-\varepsilon^0_{\vec{q}})\,c_{\vec{q}}=U_{\vec{K}}\,c_{\vec{q}-\vec{K}}$

$$(\varepsilon-\varepsilon^0_{\vec{q}-\vec{K}})\,c_{\vec{q}-\vec{K}}=U_{-\vec{K}}\,c_{\vec{q}}=U^*_{\vec{K}}\,c_{\vec{q}}\qquad(1.13)$$

The condition for two nearly degenerate states is then

$$\varepsilon^0_{\vec{q}}\approx\varepsilon^0_{\vec{q}-\vec{k}},\left|\varepsilon^0_{\vec{q}}-\varepsilon^0_{\vec{q}-\vec{K}'}\right|>>U,\text{ for }\vec{K}'\neq\vec{K},0\qquad(1.14)$$

If we assume $|\vec{q}|=|\vec{q}-\vec{K}|$, this means that $\vec{q}$ must lie on the Bragg plane bisecting the line joining the origin of $\vec{k}$ space to the reciprocal lattice point $\vec{K}$. Since $\vec{g}_1$ and $\vec{g}_1$ are all reciprocal lattice vectors, the position at the middle point between the origin and $\vec{K}$, namely $\frac{1}{2}\vec{K}$, is the **Brillouin zone boundary**. This geometric importance indicates that

two nearly degenerate levels apply to an electron whose wave vector very nearly satisfies the condition for a single Bragg scattering. Correspondingly, the general case of many nearly degenerate levels applies to the treatment of a free electron level whose wave vectors are close to the zone boundaries where many simultaneous Bragg reflections can occur. In other words, the weak potential forms a "forbidden zone" at the zone boundary, which all the wave functions of the wave vectors on the Bragg plane cannot penetrate.

Equation (1.11) can have a solution when:

$$(\varepsilon - \varepsilon_{\vec{q}}^{0})(\varepsilon - \varepsilon_{\vec{q}-\vec{K}}^{0}) = \left|U_{\vec{K}}\right|^{2} \tag{1.15}$$

The two roots: $$\varepsilon = \frac{1}{2}\left(\varepsilon_{\vec{q}}^{0} + \varepsilon_{\vec{q}-\vec{K}}^{0}\right) \pm \left[\left(\frac{\varepsilon_{\vec{q}}^{0} - \varepsilon_{\vec{q}-\vec{K}}^{0}}{2}\right)^{2} + \left|U_{\vec{K}}\right|^{2}\right]^{\frac{1}{2}} \tag{1.16}$$

give the dominant effect of the periodic potential on the energies of the two free electron levels $\varepsilon_{\vec{q}}^{0}$ and $\varepsilon_{\vec{q}-\vec{K}}^{0}$ when $\vec{q}$ is close to the Bragg plane determined by $\vec{K}$. If $\vec{q}$ is on the Bragg plane, then

$$\varepsilon_{\vec{q}}^{0} = \varepsilon_{\vec{q}-\vec{K}}^{0}, \varepsilon = \varepsilon_{\vec{q}}^{0} \pm \left|U_{\vec{K}}\right| \tag{1.17}$$

One level is uniformly raised by $\left|U_{\vec{K}}\right|$, and the other is lowered by the same amount. The forbidden zone in between is the so-called forbidden energy band gap, FEG. Figure 1.1 illustrates the formation of the energy band gap through this two free electron band model.

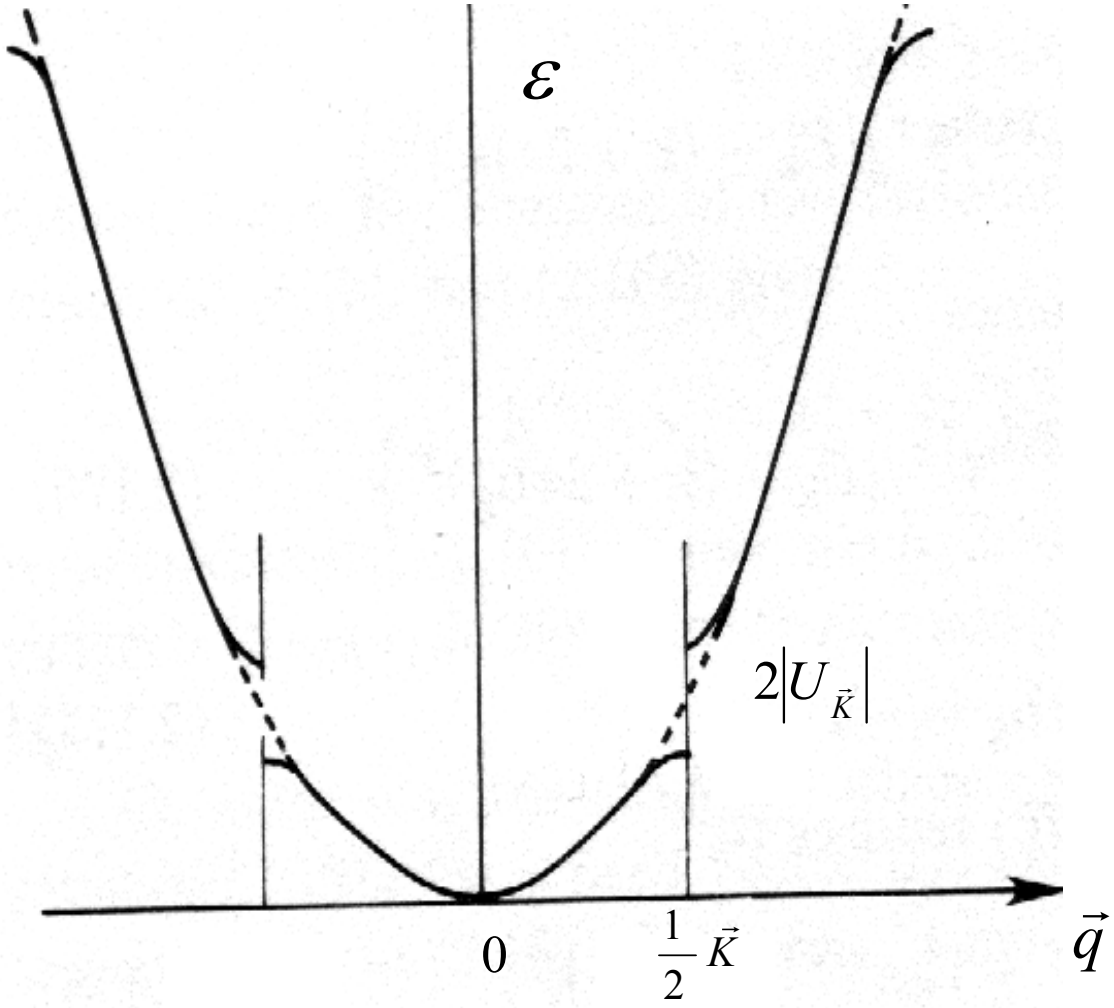

Figure 1.1 Formation of the band gap at the zone boundary

The form of wave functions corresponding to the two solutions $\varepsilon = \varepsilon_{\vec{q}}^{0} \pm \left|U_{\vec{K}}\right|$ can be obtained when applying (1.17) back to (1.13). The two coefficients $c_{\vec{q}}$ and $c_{\vec{q}-\vec{K}}$ satisfy

$$c_{\vec{q}} = \pm \mathrm{sgn}(U_{\vec{K}}) c_{\vec{q}-\vec{K}} \tag{1.18}$$

Since these two coefficients are the dominant ones in the plane wave expansion, it follows that if $U_{\vec{K}} > 0,$ then

$$\left|\psi^{+}(\vec{r})^2\right| \propto (\cos \vec{K} \bullet \vec{r})^2 \qquad \text{top edge} \qquad s \text{ type}$$

$$\left|\psi^{-}(\vec{r})^2\right| \propto (\sin \vec{K} \bullet \vec{r})^2 \qquad \text{bottom edge} \quad p \text{ type} \tag{1.19}$$

If $U_{\vec{K}} < 0,$ then

$$\left|\psi^{+}(\vec{r})^2\right| \propto (\sin \vec{K} \bullet \vec{r})^2 \qquad \text{top edge} \qquad \text{p type}$$

$$\left|\psi^{-}(\vec{r})^2\right| \propto (\cos \vec{K} \bullet \vec{r})^2 \qquad \text{bottom edge} \quad \text{s type} \tag{1.20}$$

The *s*-type wave function has most amplitudes at the ions but the p type wave function has most amplitudes between the ions. From (1.19) and (1.20), it is easily seen that when the crystal potential is repulsive, the energy will be lower for the electronic charges to distribute between the ions. (*p* type at the bottom, *s* type at the top). The gap is called inverted gap. When the crystal potential is attractive, the energy will be lower for electron charges to distribute at the ions. (*s* type the at bottom, *p* type at the top). The gap is called directed gap.

1.3 Theory of Surface States in Nearly Free Electron Systems

In the gap region, the wave vector $\vec{k}$ assumes complex values which give rise to decaying wave functions that lie in the gaps between the k-real bands of the infinite crystal. Thus, the energy *E* vs k diagram has a *k* real band alternating with a *k* complex gap [2], i.e.,

$$k = \varsigma + i\mu,\ \mu \geq 0 \tag{1.21}$$

To further investigate the relation mathematically, we consider the one-dimensional case. With further simplification $K_1 = 0,\quad q = k,$ and $K = K_2 = 2\pi b_n$, the two roots in (1.17) change to be

$$\varepsilon = \frac{1}{2}\left(k^2 + (k - 2\pi b_n)^2\right) \pm \left[\left(\frac{k^2 - (k - 2\pi b_n)^2}{2}\right)^2 + |U_n|^2\right]^{\frac{1}{2}}, \tag{1.22}$$

,where $\vec{b}_n$ is a reciprocal lattice vector and $\hbar^2/2m$ is set to be 1. In order for ε to be real, the discriminant in (1.22) must be zero or positive. Therefore, $(k - \pi b_n)^2 \geq -U_n{}^2 / 4\pi^2 b_n{}^2$, and the limit maximum value for *k* should be,

$$k_m = \pi b_n \pm i\,|U_n|/2\pi b_n,\ \ \varsigma_m = \pi b_n = \pm\pi n / a \text{ , and } \mu_m = \pm|U_n|\,a/2\pi n, \tag{1.23}$$

where *a* is the lattice constant. The corresponding energy is

$$\varepsilon_k^m = \frac{1}{2}(k_m^2 + (k_m - 2\pi b_n)^2) = (\pi n / a)^2 - \left|U_n a / 2\pi n\right|^2. \tag{1.24}$$

However, the energies of the upper and lower edges of forbidden energy band gap, FEG, are $\varepsilon^{\pm} = (\pi n/a)^2 \pm |U_n|$. Consider the FEG at first Brillouin zone boundary, n = 1. The wave functions of two edges are of the forms $\cos(\pi z/a) = \mathrm{Re}(e^{\pm i\pi z/a})$ and $\sin(\pi z/a) = \mathrm{Re}(e^{\pm i(\pi z/a - \pi/2)})$, according to (1.19) and (1.20). Thus, in crossing the entire band gap from one band edge to the other, a phase factor of $-\pi/2$ is introduced into the wave function. Therefore, for any energy in the FEG, a phase factor $\delta, -\frac{\pi}{2} < \delta < \frac{\pi}{2}$ is in the wave function expression. Now, we consider the reciprocal vector $\vec{b}_n$ along the direction normal to the surface. The position of the crystal surface is at $z = 0$. Then the wave vector for the state in the first FEG is $k = i\mu \pm \pi/a$, and the wave function is

$$\psi(z) = e^{uz} \cos(\pi z/a + \delta), z \le 0 \tag{1.25}$$

The wave function of the state can analytically cross the FEG from one band edge to another with changing phase shift. On the other hand, the wave function (1.25) is a mixture of the wave functions associated with the upper and lower FEG edges. Namely,

$$\cos(\pi z/a + \delta) = \frac{1}{2} e^{i\delta} (e^{i\pi z/a} + e^{-2i\delta} e^{-i\pi z/a}) \tag{1.26}$$

with

$$\sin 2\delta = 2\pi\mu/U_1 a \tag{1.27}$$

$$\cos 2\delta = -(\varepsilon - \pi^2/a^2 + \mu^2)/U_1 \tag{1.28}$$

The imaginary part of the wave vector μ will go to zero at both FEG edges. Since $\mu \geq 0,$ (1.27) gives the following relations between the potential energy and phase shift

$$U_1 < 0, \qquad -\pi/2 \leq \delta \leq 0$$

$$U_1 > 0, \qquad 0 \leq \delta \leq \pi/2 \tag{1.29}$$

Therefore, if a surface state exists in the FEG, then the wave function must have the form $\psi_c(z) = \beta e^{\mu z} \cos(\pi z/a + \delta), z \leq 0$. The imaginary part of wave vectors $\mu \geq 0,$ so it represents an oscillatory wave damping into the bulk. However, for the vacuum part above the surface, $z > 0,$ we have to use a different wave function, $\psi_v(z)$, to represent the surface state. The actual potential shape in the vacuum from the crystal surface is long- range barrier like .The corresponding, $\psi_v(z)$, should be in the form [3]

$$\psi_v(z) = \alpha e^{-k_0 z} + r_c e^{i\phi_c} e^{+ik_0 z} \tag{1.30}$$

according to multiple-reflection theory [4]. This barrier potential outside the crystal surface causes the surface state wave function to reflect back and forth between the crystal bulk and surface barrier with the condition

$$\phi \equiv \phi_c + \phi_B = 2\pi n, \qquad \text{where n is an integer} \tag{1.31}$$

Figure 1.2 illustrates the formation of the surface states through the multiple-reflection theory. $r_c e^{i\phi_c}$ and $r_B e^{i\phi_B}$ are the respective electron reflectivities defined by Echenique and Pendry [4]. There are two types of surface states derived from this theory; the image surface state and crystal-induced surface state. The image surface states (n > 0) are generated by the long-range part of the surface barrier potential. Therefore they are

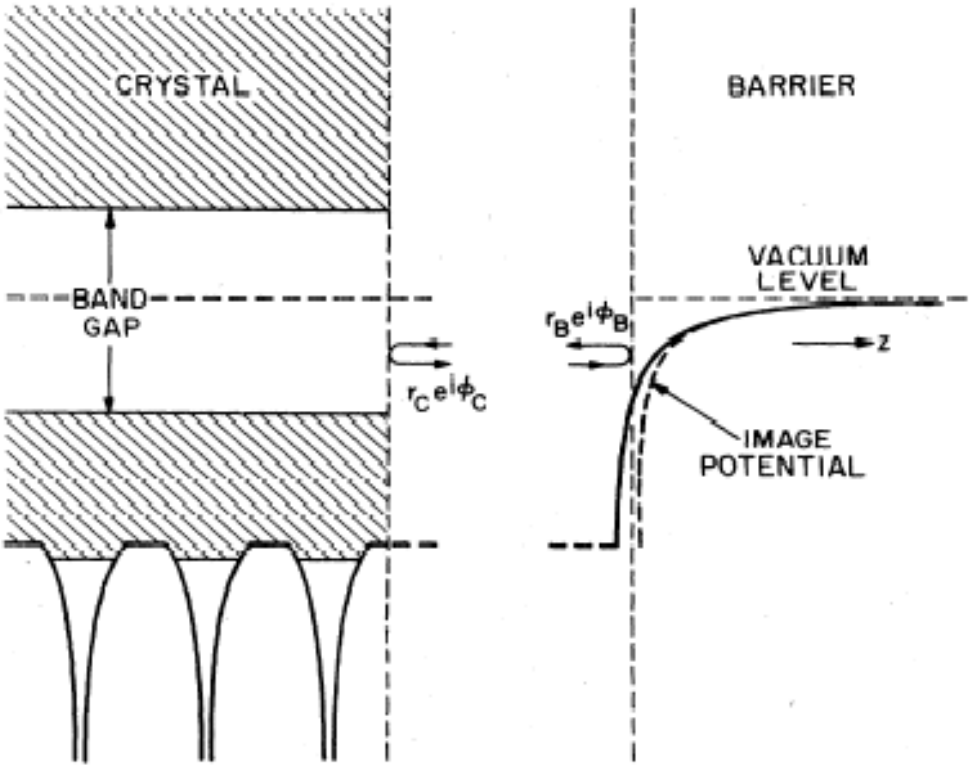

Figure 1.2 Schematic potential in the vicinity of a crystal surface [3].

bound weakly to the surface implying that their amplitude is concentrated relatively far away from it. Their energy lies above the Fermi leveling and very close to the vacuum levels in the FEG.

Since the 1980's, the existence of image surface states has been confirmed from surfaces of Cu, Au, and Ag by the inverse photoemission and two-photon photoemission spectroscopy [5-7]. In my research, the main attention was focused on the behavior of crystal-induced surface states investigated by the angle-resolved photoemission technique. Therefore, I just considered the case, $n \le 0$, which corresponds to short-range step potential V_0 outside the crystal surface. Hence, for the crystal-induced surface states,

$$\psi_v(z) = \alpha e^{-k_0 z} \text{ and } k_0 = (V_0 - E)^{1/2}, \quad E < V_0 \text{ when } z > 0. \tag{1.32}$$

Matching the boundary condition at $z = z_0$ for $(\psi_c(z)\ ,\ \psi_v(z))$ and their first derivatives lead to

$$(\pi/a)\tan(\pi z_0/a + \delta) = (\mu + k_0) \tag{1.33}$$

which is the equation of surface state energy since $\delta, \mu,$ and k_0 are all energy dependent. The match point $z = z_0$ is not necessarily at the crystal surface. Two special cases are of interest,

$$z_0 = 0 \qquad \Rightarrow (\pi/a)\tan\ \delta = (\mu + k_0) \tag{1.34}$$

$$z_0 = -a/2 \qquad \Rightarrow (\pi/a)\cot\ \delta = -(\mu + k_0) \tag{1.35}$$

Since μ and k_0 are always positive, (1.34) and (1.35) can be satisfied only for $0 \le \delta \le \pi/2$ or $\pi/2 \le \delta \le 0$, respectively. Consequently, the necessary condition for a surface state to appear in the FEG is

$$U_1 < 0 \quad for \quad z_0 = -a/2 \tag{1.36}$$

$$U_1 > 0 \quad for \quad z_0 = 0. \tag{1.37}$$

This important result was noted first by Maue [8] and discussed subsequently by Goodwin [9], Forstmann[10], and Pendry and Gurman [11]. Condition (1.36) is usually the case for the Tamm surface state, which forms in the directed gap with *s*-band at the bottom. The Tamm state originated from the idea of a monatomic chain whose end atoms are subject to large perturbations [12]. It usually represented the surface state existing in nonhybridizational energy band gaps,(directed gap). However, with more surface states observed from transition metals which cannot be explained in terms of the Shockley model [13], its definition has been generalized to the d-like surface state split off from the *d* bulk band [14]. Condition (1.37) is the case for the Shockley surface state, which forms in the inverted gap with the *p*-band at the bottom. The Shockley state comes from the concept of hybridization of crossed energy bands, which hence causes an inverted gap. After studying the potential with the termination midway between two atoms, Shockley [13] proposed the idea as follows. When atoms are far apart, their wave functions do not overlap. Their energy levels are discrete and labeled in ascending orders, *p, d*, etc., levels. As the atoms coalesce, their wave functions overlap and bonding occurs between the atoms to form the crystal. The interaction between the atoms leads to a broadening of the discrete atomic levels into bands. A further reduction of the lattice spacing results in a crossing of *s*-and *p*-bands, after which a FEG is formed with upper and lower edges of inverted symmetry, so the p-band become the lower one. This picture is illustrated in Figure 1.3. There is no doubt that Shockely states are more likely to occur in the nearly free electron metals where the atoms are close together and interact

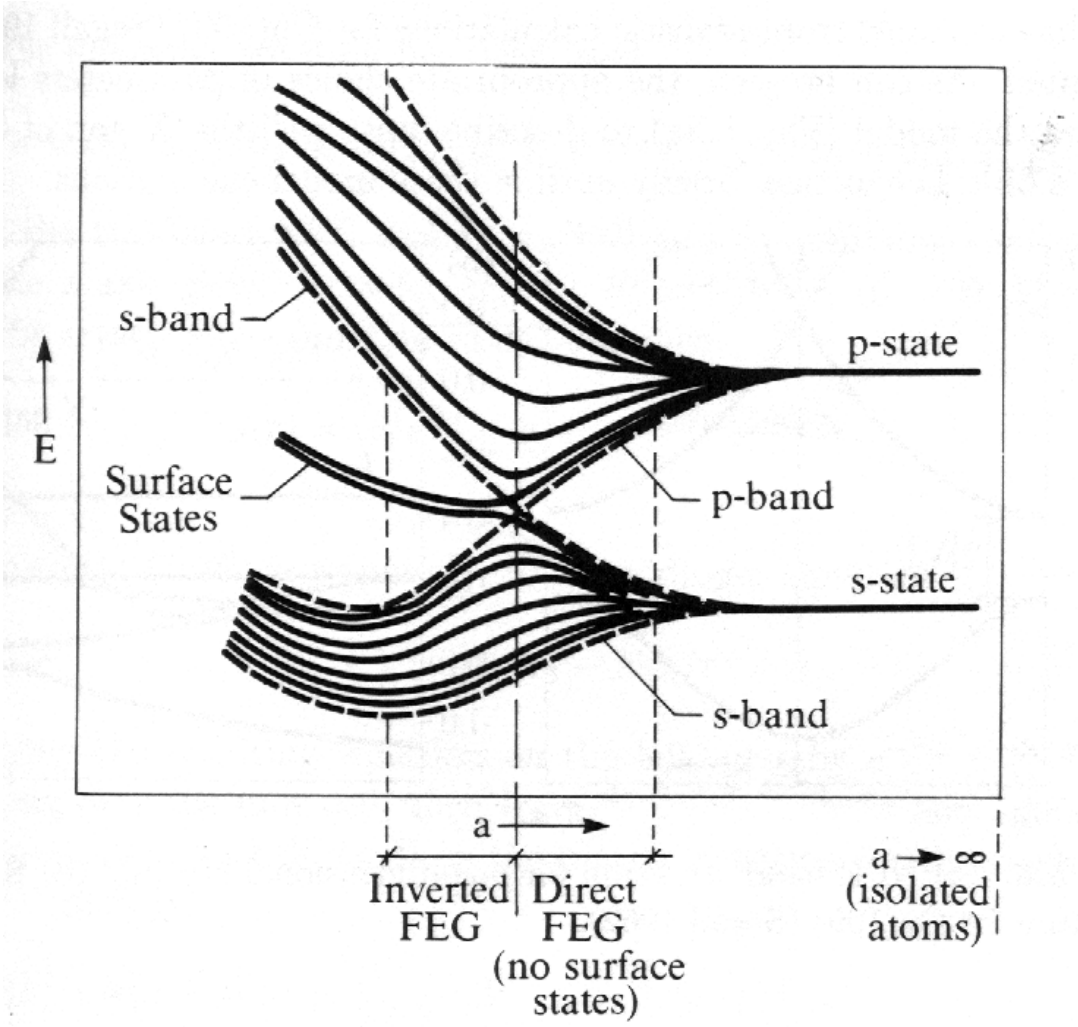

Figure 1.3 Creation of *s*- and *p*-band from isolated *s*- and *p*-atomic level

strongly through their electrons in *s* and *p* bands. The behavior of the Shockely states in different nearly free electron metals has been extensively investigated by E.W. Plummer and his group [15].

1.4 The Properties of the Surface State at the Zone Boundary

So far, I have discussed the existence of the surface state in the FEG at the zone boundary. However, the EFG can also be formed inside the Brillouin zone resulting from the crossing of two bands of the same symmetry. The surface state existing in the energy band gap formed by *s*-*d* band hybridization inside the Brillouin zone has been predicted and investigated through theory [16] and experiment [17], respectively. As my focus is on the two Shockley surface states coexisting in the same energy band gap at the same surface zone boundary, I will concentrate on the special properties of the surface state derived from EFG at the zone boundary. Here, I need to clarify the terms "zone boundary" and "surface zone boundary." Zone boundary is referred to as the symmetry points at the edges of a 3-dimensional reciprocal Brillouin zone (3DBZ). The surface zone boundary is one of the symmetry points at the edges of the surface Brillouin zone (SBZ), which is the projection from the 3DBZ in a certain direction. Figure 1.4 gives a clear illustration by using the Mg bulk and (0001), $(10\bar{1}0)$ electronic structure. In the direction from Γ to A in the bulk band, a gap forms at the zone boundary at Γ in the second brillouin zone. This gap is projected to the partial band gap around the surface zone center $\bar{\Gamma}$ on (0001) SBZ. On the other hand, the bulk band dispersion from A to L

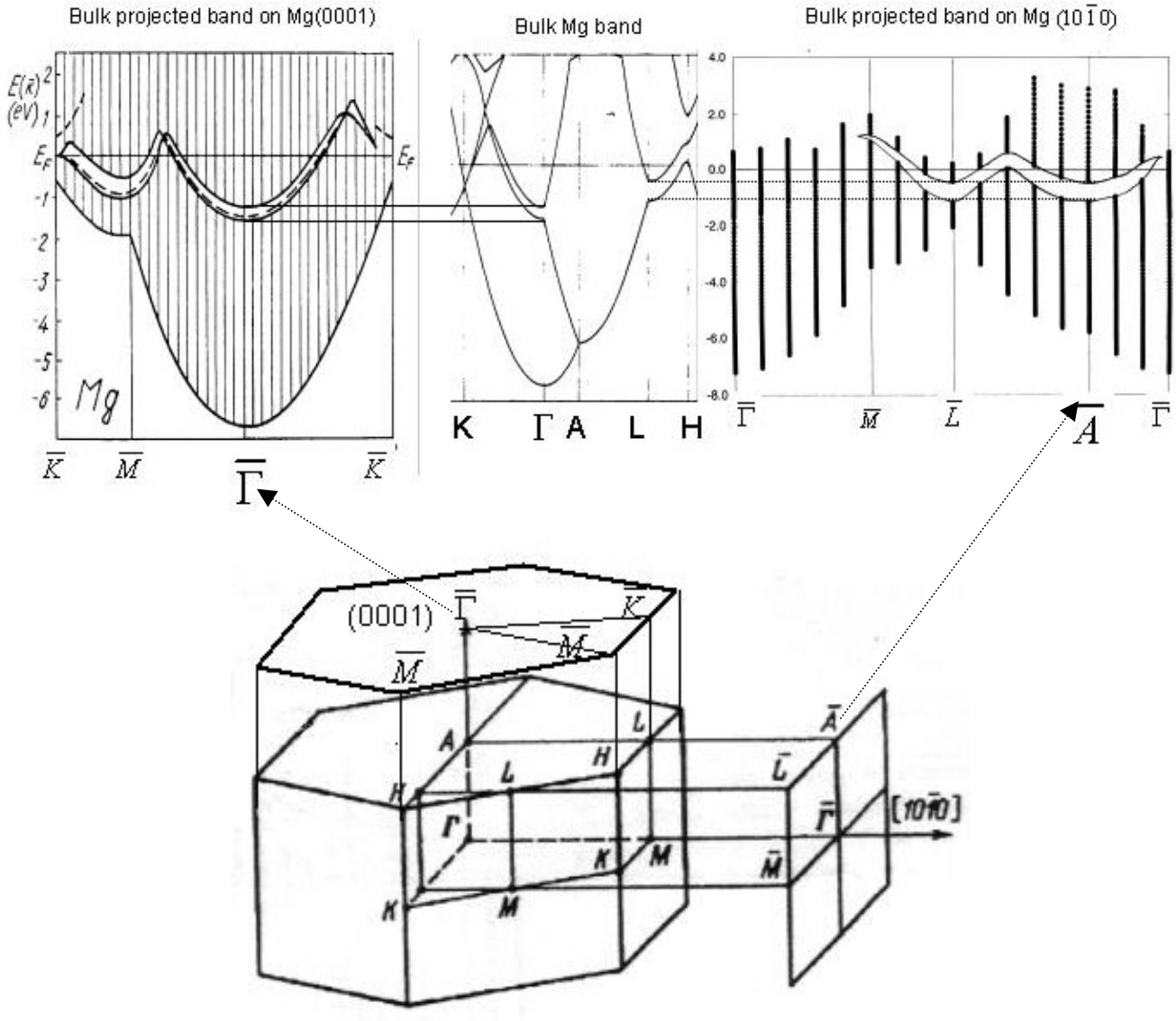

Figure 1.4 Projection of the reciprocal hcp structure to the $(10\bar{1}0)$ surface and (0001) surface Brillouin zone. Projection of the Mg bulk band gap at the zone boundary to the partial band gap at the surface zone center on Mg(0001) and the surface zone boundary on Mg $(10\bar{1}0)$ are also shown.

also opens a gap at the zone boundary at L. The gap is projected to the partial band gap at surface zone boundary at $\overline{A}$ on $(10\overline{1}0)$ SBZ. The partial band gap only exists in some region of SBZ in nearly free electron metals as opposed to the total band gap, which exists all the way through the SBZ on semiconductor surface. The electronic surface states were studied and detected on the semiconductor surfaces much earlier than on nearly free electron metal surfaces. Their existence was derived in an indirect manner by analyzing the physics underlying the rectifying action of metal-semiconductor junctions by Allen and Gbeli in 1962 [18]. An important breakthrough on the experimental front was due to optical experiments [19] and to the application of photoconductivity and surface photovoltage spectroscopy [20]. Chiarotti et al. [19] presented direct measurements of the optical absorption due to the presence of a band of surface states below the bottom of the conduction band on cleaved Ge(111) and Si(111) surfaces in 1971 . The results obtained were explained by the hypothesis that optical transitions take place between two bands of surface states, localized in FEG, one band below and one above E_F at the surface. Photoemission spectroscopy and, in particular, angle-resolved UV photoemission (ARUPS) were later successfully applied to the semiconductor surface and were used to determine many features of the surface electronic structure. The experimental results obtained for Si(100) and Si(111) surfaces were summarized by Eastman in 1980 [21].

In considering the surface states in NFE metals, Forstmann and Pendry [16] predicted its existence in partial gaps in 1970. However it is more difficult to substantially prove the existence of surface states because angular resolution is needed in the spectroscopy to observe a surface state existing in the partial band gap. Otherwise, it

can hardly be seen in the high background of the integrated bulk state density. In 1970, E. W. Plummer et al.[17] found two peaks (one at E = -0.37 eV and another at E =-1.5 eV) sensitive to surface contaminants in the energy distribution of field-emitted electrons from the single-crystal W(100) surface. These two states were considered as derived from the two gaps created by the splitting of the three Δ_7 bands in the center of 3DBZ. The possibility for the peak at E = –1.5 eV to be a surface state was ruled out in a later experiment [22]. However, the peak at –0.37 eV was confirmed again to be the surface state through the photoemission by B. J. Waclawski and E. W. Plummer in 1972 [23]. This is also the first observation of a metallic surface state in a photoemission experiment. However, the first observation of Shockley-like surface state split off sp bands at the Brillouin zone boundary is from L gap in copper by P. O. Gartland in 1973 [24] through photoemission investigations on the Cu(111) surface.

1.4.1 The Penetration Depth of the Surface State at Zone Boundary

The imaginary part of a surface state's wave vector actually represents the penetration (decay) length into the bulk. In other words, the degree of localization of a surface state can be seen from the value of imaginary part μ. We can go back to the original picture for the formation of the surface state in EFG. At the bottom and top of the bulk band edge, the imaginary part of the wave vector is 0. Therefore, we can imagine there is a real energy curve connecting two bulk band edges through EFG with a complex wave vector in the E vs k (ζ, μ) space as shown in the Figure 1.5.

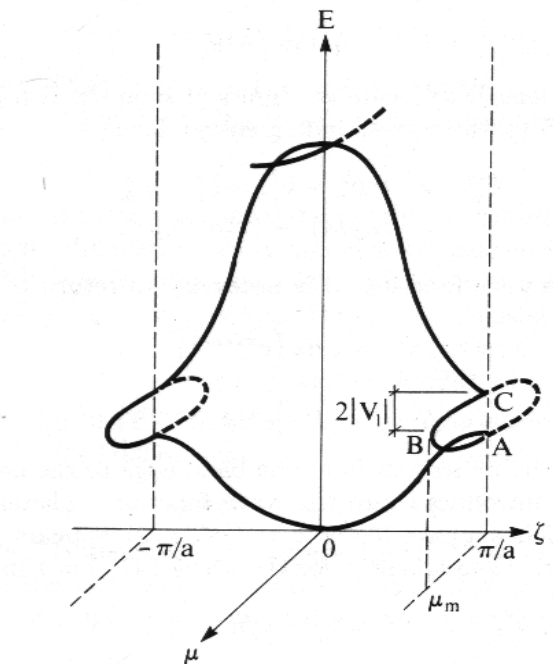

Figure 1.5 Variation of energy E in complex plane (ζ, μ), $k = \zeta + i\mu$

Starting at the bulk band edge at A with $\mu = 0$, we go along the real curve with increasing μ reaching maximum limit value μ_m at the saddle point B. After the B point, μ decreases along the real line and goes to zero again at the top bulk band edge C. From this picture, even without explicit mathematical expression, we can intuitively realize the energy separation between the surface state and the corresponding bulk band edge it split off from is inversed to the penetration length of the surface state into the bulk. From the equation (1.27), we see the size of the band gap $2|U_1|$ is also inversed to $1/\mu$. Therefore, we come to two conclusions. (1) The surface state with larger energy separation from the bulk band energy is more localized. (2) The localization of a surface state in the larger band gap is more than that of a surface state in a smaller band gap. Figure 1.6a,b illustrate these two points through the surface state wave functions at different energy positions in the gap and the surface state wave function in the middle of the band gap with different gap size. These two points will also be further confirmed from the samples that were investigated and discussed in the chapter 4,5: two surface states located at the same band gap at $\bar{A}$ in Mg$(10\bar{1}0)$ and Be$(10\bar{1}0)$, respectively. G. Louie et al [25] have shown that the intensity of the surface state at $\bar{\Gamma}$ on Cu(111) in the photoemission spectra is periodic with $K_\perp$ and has a maximum when the photon energy corresponds to the direct transition from the bulk band edge. According to this finding, the surface state penetration length can actually be measured through the width of pure surface state intensity vs the real part of the wave vector perpendicular to the surface. As has been concluded through the study of different surface states on different samples [26-28], the maximum of the surface state intensity is at the $K_\perp$ of the bulk band edge,

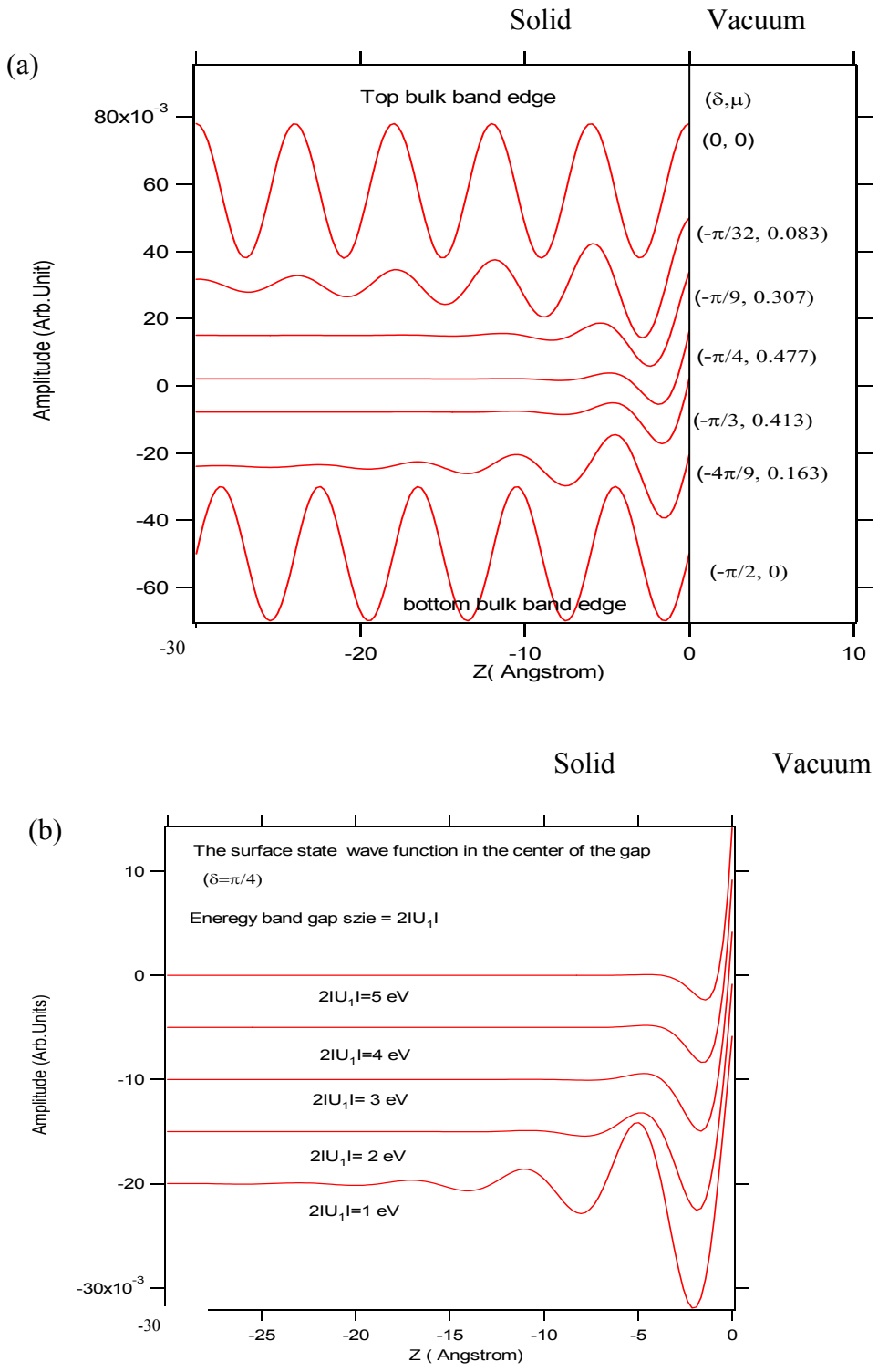

Figure 1.6 Relation between the surface state wave function and (a) the energy position and (b) the size of the gap

and the width of the I vs $K_{\perp}$ spectra distribution is inversed to the penetration length.

Now, we will transfer from the concept of the surface state at the zone boundary to the surface state at the surface zone boundary. In the surface Brillouin zone, we examine the 2D dispersions (E vs $k_{\parallel}$) of the surface state band. Here, a question arise " In spite of the size of energy band gap, would the penetration length of the surface state at the surface zone boundary be generally larger than that of the surface state at the surface zone center?" One thing to note is that a typical free electron surface state should disperse parabolically from the bottom of the band at the surface zone center toward the surface zone boundary. The zone boundary is the place, as emphasized in section 1.2, where the crystal potential has the most effects on the nearly degenerate electronic states. For the surface state dispersing from the surface zone boundary, even though its dispersion shape is parabolic, the electrons of the surface state are still subject to the periodic potential of the crystal and have substantially different dynamic behavior from the motion of free particles. C.T Chen et al [29] explain the flat dispersion of the image state (n=1) from the surface zone boundary at $\bar{Y}$ to the surface zone center at $\bar{\Gamma}$ on Cu(110) by giving the picture of a battle between the crystal and vacuum. The crystal is trying to pull the surface state dispersion curve into a form which disperses upward away from $\bar{Y}$ at a rate imposed by the projected bulk band gap, but the vacuum, on the other hand, is pulling toward free-electron-like behavior with upward dispersion centered on $\bar{\Gamma}$. Actually, the best elucidation is from the previous observations of the behavior of Friedel charge density oscillations on the surfaces. The screening of a charged point impurity in a simple metal results in long-range modulations in the charge density caused by an abrupt change in the density of states at the Fermi energy E_F. The wave vector of these

modulations is $2k_F$, two times that for the electrons at the Fermi level. Figure 1.7 shows the 2D charge density oscillations from Cu(111), Cu(110), Be(0001) and Be$(10\bar{1}0)$ surfaces [30–33]. On Cu(111) and Be(0001), the charge oscillation waves are mainly produced by the surface states dispersing from $\bar{\Gamma}$, and it shows isotropic circular pattern with corresponding circular Fermi contour around the surface zone center. However, for Cu(110) and B$(10\bar{1}0)$, the charge oscillation waves are produced from the surface states dispersing from surface zone boundaries at $\bar{Y}$ and $\bar{A}$, respectively, showing anisotropic scattering from the step edges. The corresponding Fermi contours are the semi-elliptic lines between the surface zone boundary and surface zone center. Only the Bloch wave functions representing the surface states from the surface zone boundary can explain anisotropic behavior of the charge oscillation waves. It is thus confirmed that the surface states at the surface zone boundary experience much more crystal potential than those at the surface zone center, but it does not indicate any information about the surface state penetration length into the bulk. Compared with Cu(110) [33], the two-dimensional electronic gas is even much more non-free-electron-like on Be$(10\bar{1}0)$, and the surface state responsible for screening is actually very localized on the surface. It has to do with the unique property of the Be$(10\bar{1}0)$ surface which will be discussed in detail in Chapter 4 and Chapter 6.

Be(0001)

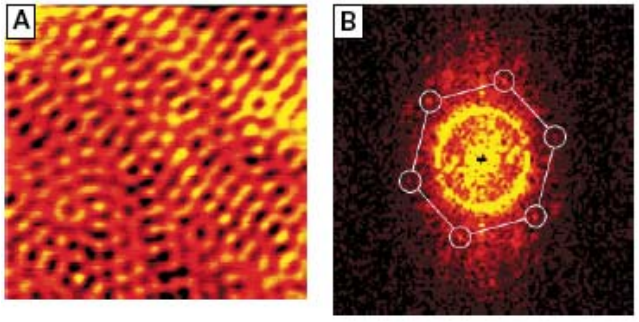

Cu(111)

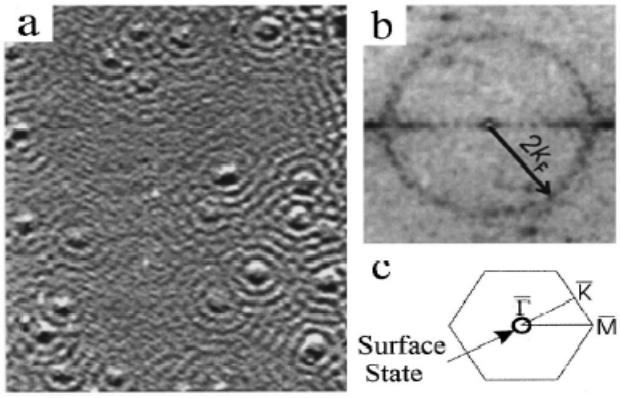

Be(10$\bar{1}$0)

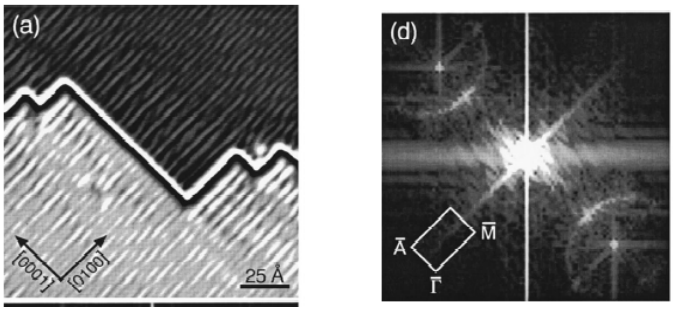

Cu(110)

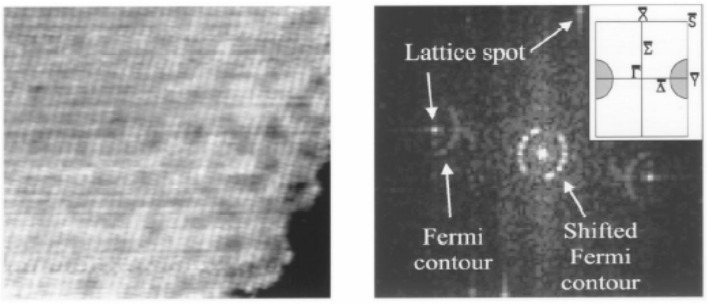

Figure 1.7 Charge density oscillations and corresponding Fermi contours for Be(0001) [30], Cu(111) [31], Be(1010)[32],and Cu(110)[33]

1.4.2 Accommodation of Two Surface States at the Same Band Gap at the Surface Zone Boundary

The question of how many surface states can exist at the same energy band gap has been discussed by Forstmann [10] and Pendry [11] since 1970. However, the first experimental finding of two Shockley crystal-induced surface states coexisting at the energy band gap at the same surface zone boundary was from $\overline{Y}$ on Cu(110) by Bartynski et al. [34]. They observed that in addition to the previous found surface state at 0.44 eV below the Fermi level, there is an unoccupied state located at 2.5 eV above the Fermi level. By considering two symmetry points L and L' at the zone boundaries along the direction projected to $\overline{Y}$ at the (110) surface Brillouin zone, we can picture two FEGs at the zone boundaries L ($\vec{k}_\perp = \vec{k}_0$) and L' ($\vec{k}_\perp = -\vec{k}_0$), respectively, as shown in Figure 1.8a. Each FEG (L or L') can accommodate a surface state with different parity (even or odd). To prove this, Bartynski et al. constructed the even and odd solutions with the symmetry operation $\vec{k}_{II} = -\vec{k}_{II}$ appropriate to the $\overline{Y}$ point. Namely,

$$\psi_e = \exp(\kappa r_\perp)\cos(\vec{k}_{II}\cdot\vec{r}_{II})[(a_1 + i|a_2|)\exp(ik_0 r_\perp) - (a_1 - i|a_2|)\exp(-ik_0 r_\perp)] \quad (1.38)$$

$$\psi_o = \exp(\kappa r_\perp)\sin(\vec{k}_{II}\cdot\vec{r}_{II})[(a_1 + i|a_2|)\exp(ik_0 r_\perp) + (a_1 - i|a_2|)\exp(-ik_0 r_\perp)] \quad (1.39)$$

where a_1 and a_1 are the amplitudes of the upper (*s*-like) and lower (*p*-like) Bloch wave functions at the band edges. Only the solutions for crystal-induced surface states are concerned so potential jumping discontinuous to the vacuum level are assumed, and thus the exterior wave function is either $\cos(\vec{k}_{II}\cdot\vec{r}_{II})$ for the even solutions or $\sin(\vec{k}_{II}\cdot\vec{r}_{II})$ for

the odd solutions times $e^{-\sqrt{|E|}z}$, where E is the perpendicular energy with respect to vacuum level. For a surface state to exist, the wave function and its derivative must be continuous at the interface. To satisfy this condition, the logarithmic derivative $\gamma = (1/\psi)(\delta\psi/\delta z)$ of the internal and external wave functions must be equal at the solid-vacuum interface. Figure1.8b gives the best illustration showing the curves of γ_e γ_o and γ_{ext} versus energies within the gap. From this figure, it's shown that the γ_{ext} will pass through both the γ_o and γ_e curves. This, in turns, corresponds to the existence of two surface states of two different symmetries in the energy gap. Since the origin is put on the atom, (1.38) corresponds to the *s*-like surface state with most amplitudes placed on the atoms and (1.39) corresponds to the *p*-like surface state with most amplitudes placed between atoms. Figure 1.8b also shows the initial energy of the even (*s*-like) surface state is higher than the odd (*p*-like) surface state. This is consistent with the fact that for a Shockley inverted band gap, the top bulk edge is s-like and the bottom edge is *p*-like. N.V. Smith [3] generalizes this idea to the rule that a band gap associated with a reciprocal-lattice vector $\vec{g}$ can support at least one crystal-induced surface state on surfaces whose normal is not necessarily parallel to $\vec{g}$. He further emphasizes that due to the parallel component of $\vec{g}$ to the surface, there is a contribution $2U_{\vec{g}}\cos(\vec{k}_{\text{II}} \cdot \vec{r}_{\text{II}})$ to the surface corrugation potential which creates a gap at the boundary of the surface Brillouin zone between the wave functions of even and odd symmetry. In case where two such surface states are actually observed, their energy separation is a measure of the surface-corrugation potential, which is proportional to the covalent-like property of the

(a)

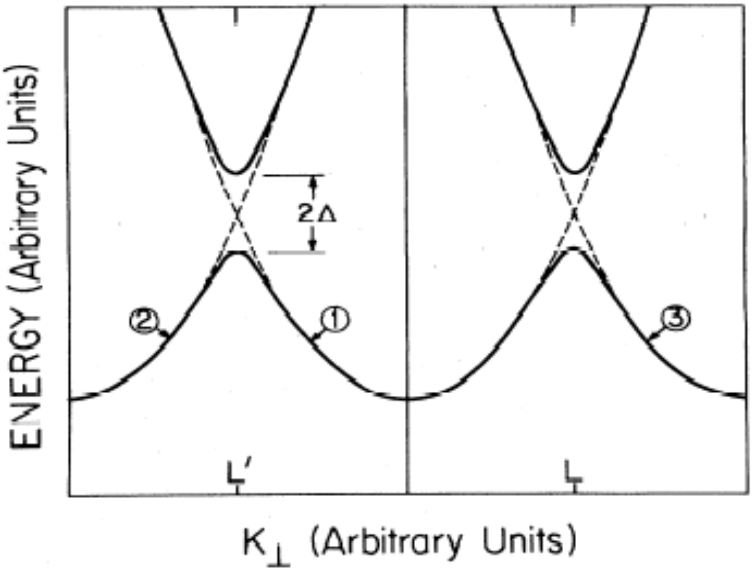

(b)

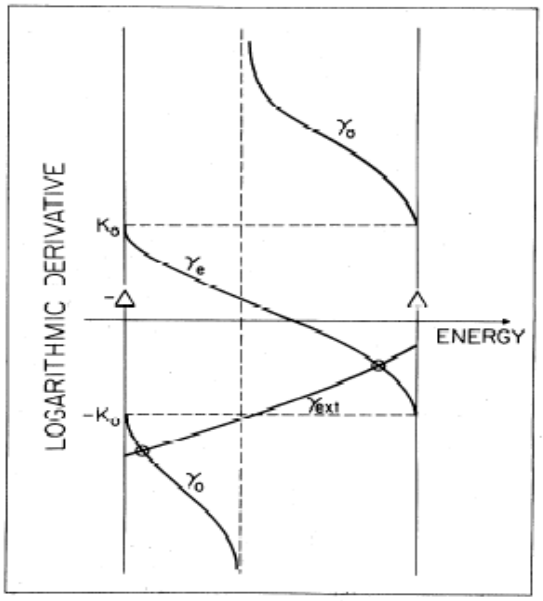

Figure 1.8 Existence of two surface states at $\bar{Y}$ at the band gap L on Cu (110)[34]

surface. In investigations of the surface states on simple metals, Bartynski further found two surface states at $\overline{M}$ on Be(0001) [35], but only one surface state at the same $\overline{M}$ on Mg(0001) [36]. Recent studies of the open surface for both metals [37–40] show that there are two surface states coexisting with even (s-like) and odd (p-like) parities at $\overline{A}$ for both $\mathrm{Be}(10\overline{1}0)$ and $\mathrm{Mg}(10\overline{1}0)$. From these measurements and calculations [30–33], the band gap size and the energy separation between two surface states for $\mathrm{Be}(10\overline{1}0)$ are at least four times larger than those for $\mathrm{Mg}(10\overline{1}0)$. The central work of my research was to investigate the difference in the electron-phonon interaction between the two surface states at the same energy band gap at $\overline{A}$ for $\mathrm{Be}(10\overline{1}0)$ and $\mathrm{Mg}(10\overline{1}0)$, respectively.

1.5 Thesis Syllabus

Surface states are the main objects I study in my research. In Chapter 1, I have introduced the formation and important properties of the surface states in a band gap at the zone boundary. The underlying picture of this thesis is to show that many special properties on a surface can be explored through the study of the surface states. I studied one of the most important many-body interactions, electron-phonon interactions, on the open surfaces of the simple metals, $\mathrm{Mg}(10\overline{1}0)$ and $\mathrm{Be}(10\overline{1}0)$, through the surface states at the surface zone boundary at $\overline{A}$. In Chapter 2, I discuss previous studies of many-body interactions from the simple metal surfaces. Then, I will show how those previous studies lead to my motivation to study the electron-phonon interactions on the $\mathrm{Be}(10\overline{1}0)$ and $\mathrm{Mg}(10\overline{1}0)$ surfaces through the surface states. The photoemission technique and instruments I used for studying the surface states is introduced in Chapter

3. In Chapter 4 and 5, I present my experimental results of the electronic structures and electron-phonon interactions on $Be(10\bar{1}0)$ and $Mg(10\bar{1}0)$. In Chapter 6, I discuss in detail how the interesting results, which I obtained from the band structures and electron-phonon coupling of the localized surface state on $Be(10\bar{1}0)$ can be correlated to the special lattice behavior and possible superconductivity on this surface. The corresponding results from $Mg(10\bar{1}0)$ are also discussed in comparison with $Be(10\bar{1}0)$.

Chapter 2 Central Theory and Motivation of the Experiment

2.1. Photoemission and Many-Body Interactions

Many-body physics is the study of interactions among particles. Needless to say, the more varieties and amounts of the particles in the system, the more complicated the many-body physics. The solid which comprises at least 10^{23} particles in the system is certainly the best stage for many-body interaction which leads to a rich variety of phenomena including magnetism, superconductivity, superfluidity, phase transition, etc. Two central categories of many-body interactions for a solid crystal are electron-electron and electron-phonon interactions. These interactions would cause excitation in the system. Excited states of the system are best specified with reference to the ground state. A given excited state is obtained by exciting a certain number of particles across the Fermi surface S_F. Such a procedure is equivalent to creating an equal number of particles outside S_F and of holes inside S_F. Particles and holes thus appear as elementary excitations whose configurations give rise to all excited states [1]. Quasiparticle and quasihole are referred to as excited states induced by the many-body interactions. The procedure of photoemission is removing the electron at the ground state and exciting it into the vacuum level, through interaction with the photons. Therefore, the remaining hole state below the Fermi level is a very good object from which we can learn the many-body interaction. The corresponding Schrodinger equation for the quasihole is [2]

$$-\frac{1}{2}\nabla^2\phi + V(r)\phi + \int dr' \Sigma(r,r';E)\phi(r') = E\phi \tag{2.1}$$

which is also called the Dyson function. Σ is a complex quantity which denotes the self-energy of the interacting system. The real part of self-energy Σ describes the screening of the quasiparticles (holes), but the imaginary part indicates the decay of them. The spectra function

$$A(k,\omega) = \frac{\left|\mathrm{Im}\,\Sigma(k,\omega)\right|}{\left[\omega - \varepsilon^0(k) - \mathrm{Re}\,\Sigma(k,\omega)\right]^2 + \left[\mathrm{Im}\,\Sigma(k,\omega)\right]^2} \tag{2.2}$$

in the Lorentzian shape has always been used to represent the position and shape for the peak of the hole state in the photoemission spectra [2]. From Eq(2.2), we can easily see that the imaginary part of the self-energy represents the peak width, but the real part of self-energy indicates ashift of the hole state energy ω from the ground state energy $\varepsilon^0(k)$ by the many-body interaction. Effects of the electron-electron interaction on the electron band structure in the nearly free electron metals have been investigated by E. W. Plummer's group in the last 20 years [3]. The difference between the measured and calculated bandwidth on different nearly free electron metals has been attributed to the real part of self-energy as described by the following equation.

$$-\mathrm{Re}[\Sigma(0) - \Sigma(k_F)] = [E(k_F) - E(0)] - [\varepsilon(k_F) - \varepsilon(0)] \tag{2.3}$$

where E(k) is measured and $\varepsilon(k)$ is calculated. Most calculations are performed with a theoretical scheme based on density functional theory [4] with an added assumption that the nonlocal exchange-correlation energy can be written as a function of the local density , LDA [5]. The chemical characters in Figure 2.1a.b show data associated with measured bandwidth of the NFE metals. In Figure 2.1a, the energy difference ΔE between

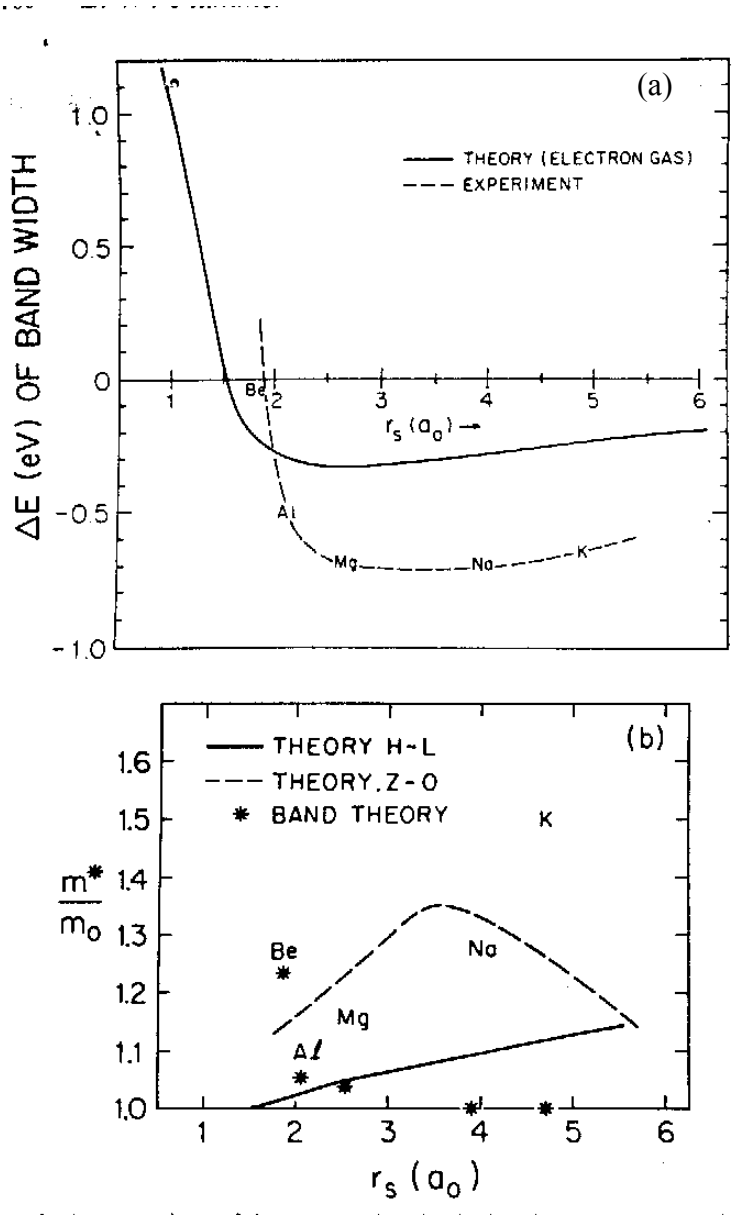

Figure 2.1 Comparison of the measured and calculated bandwidths and effective mass for different free electron metals [3]. (a) Characters and the dash line: the deviation of the measured bandwidth from LDA calculated bandwidth. Solid line: the real part of the self-energy from the interacting electron gas. (b) The measured and calculated effective mass of several simple metals. Characters are the measured results. Solid, dash lines and * are the calculated results form different ways.

the measured bandwidth and the best LDA calculation is plotted as a function of $\mathbf{r_s}$ (inverse of metal density) which is defined as the ratio of the average potential energy between electrons to the kinetic energy for the electrons in the metal. The theoretical calculation shown by the solid line is $\mathrm{Re}[\Sigma(k_F) - \Sigma(0)]$, obtained from the self-energy of interacting electron gas through the Dyson equation by Hedin [6,7]. Both theory and experiment agree on the sign of the real part of the self-energy, and the trend with $\mathbf{r_s}$ is similar. In Figure 2.1b, the data and theory have been plotted in a manner that displays each contribution separately. The effective masses m^*/m of the calculated and measured bands are plotted, where the effective mass is defined to give the proper bandwidth. The solid line is the Hendin-Lundqvist's calculation [6] through the self-energy of the interacting electron gas. The dashed line is still the self-energy calculation with consideration of spin fluctuations by Zhu and Overhauser [7]. The * mark represents the LDA band theory calculation. It is obvious that there are still some things left out of the theory calculations. Nevertheless, from both figures, the uniqueness of Be from other simple metals is clearly shown in the sense that it has the smallest deviation between the measured and LDA calculated results, and the effective mass by the LDA calculation is largest. This may not mean that the weaker electron-electron interaction in Be but the larger crystal potential in Be is indicated. Actually, the covalent bonding nature in the Be bulk was expected and has been confirmed by M.Y. Chou et al. [8]. As for Mg, its nearly free electron property is strong and similar to those of other simple metals like Na and K.

Now, I would like to illustrate the case where the large imaginary part of self-energy due to e-e interaction causes the oscillation of the real part of self-energy, and ,

hence, leads to the distorted bulk unoccupied bands. Jensen et al. [9], in an extensive photoemission study of the electronic structure of Be, found the distortion of the unoccupied band in the energy range 10–22 eV above E_F. This energy range is not only within the final energies to which there is strong direct transition along Δ from the initial occupied band, but also is around the threshold of plasmon excitation, 19 eV. The interesting unoccupied band structure (10–20 eV) as shown by the dots in Figure 2.2a is thus attributed to the many-body distortion caused by the electron-plasmon interaction. A plasmon is a quantum of a plasma oscillation, which represents a collective longitudinal excitation of the conduction electron gas. Figure 2.2b clearly shows the structure of the distorted band through the deviation between theory and experiment versus the reduced momentum (k / k_F). The size of the distortion is shown by the arrows. Arrow B indicates the wave vector of an electron in Be propagating in the Δ direction at an energy equal to E_F plus Be plasmon energy, and arrow A shows the corresponding wave vector for a free electron gas. At this energy, $\mathrm{Im}\,\Sigma$ increases dramatically due to the interaction with plasmon, and as a consequence of Kramers-Kronig relation [6.7], there is an oscillation in $\mathrm{Re}\,\Sigma$ which leads to the distortion of the bands [10]. The solid curve in figure 2.2b is the theoretical prediction of real part of self-energy for an electron gas of the density of Be [10]. The curves in Figures 2.2c [6] are the imaginary parts of self-energy which start to turn large at the k position corresponding to the A point in figure 2.2b. The curve of $\mathbf{r_s} = 2$ is for Be. Comparison between theory and experiment shows that the structure is similar in magnitude, position, and width, but there seems to

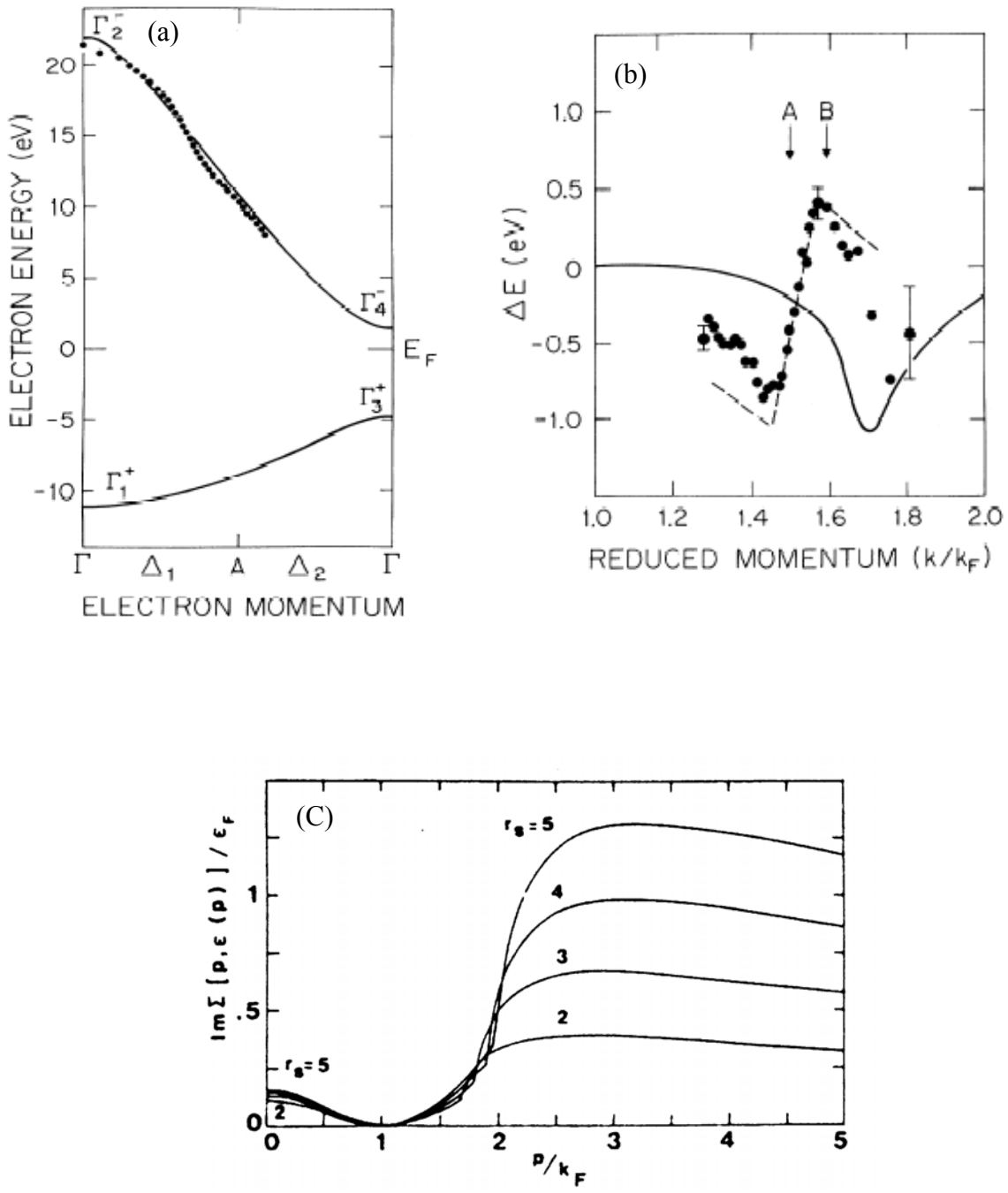

Figure 2.2 Distortion of the unoccupied bulk band in Be due to electron-plasmon interaction [9]. (a) Measured unoccupied band (dots) and self consistent band calculations (solid curve); (b) Comparison between the measured unoccupied band distortion and theory calculations of the real part of self-energy for electron-electron interactions; (c) Imaginary part of self-energy for electron-electron interactions [6]

be a phase problem. The disagreement between theory and experiment in this case is most likely a result of the interaction of the plasmons with interband transitions. This example shows the coupling of an excited state with band structure above E_F due to the many−body effects.

Now, we turn more attention to the imaginary part of self-energy, $\mathrm{Im}\Sigma$. As I indicated in the beginning, $\mathrm{Im}\Sigma$ is directly related to the peak width of the photoemission spectra. However, in addition to the contribution from many−body effects, the surface disorder [11] and the instrument resolution both affected the peak width observed. Even if we just consider the contribution from the electron-electron interaction, the complexity is revealed through the equation [9,12]

$$W = [(2\Gamma_{hole})^2 + (2R\Gamma_{el})^2]^{1/2} \tag{2.4}$$

Here, W is the peak width; $\hbar/2\Gamma_{hole}$ and $\hbar/2\Gamma_{el}$ are the hole (initial state) and electron (final state) lifetimes, respectively; and R is the ratio of the slopes ($\partial E/\partial k$) of the initial and final bands. Figure 2.3a and 2.3b shows the peak width of bulk states versus the reduced momentum (k/k_F) for normal emission on Be(0001) [9] and Mg(0001) [12], respectively. The dots are the measured data and the solid curve is the prediction for hole width in the jellium [13]. For Be(0001), the match between data and theory is quite good near the Fermi energy. As for Mg(0001), over all the momenta, the peak width measured is much larger than the one predicted by the electron-gas calculation for the hole lifetime. It is obvious that the discrepancy between data and theory comes from final electron state lifetime at the k momentum position where the ratio of the slopes between the initial-and final-state bands, R, is large. It is difficult to measure the final

state lifetime because, in reality, there is no transition observed from E_F where the hole contribution vanishes. Some attempts such as measuring the heights of peaks [9] or the intensity of Fermi level [12] as a function of photon energy have been used to approximate the contribution from final electron state lifetime. The sum of contributions from the hole lifetime (the electron gas calculation) and from the electron lifetime (attempts by Bartynski et al, [12]) are shown by the dashed line in Figure 2.3a for Mg(0001). Both the dots and dashed line show similar trends of the variation of peak widths versus reduced momentum but there is still quite a quantitative difference.

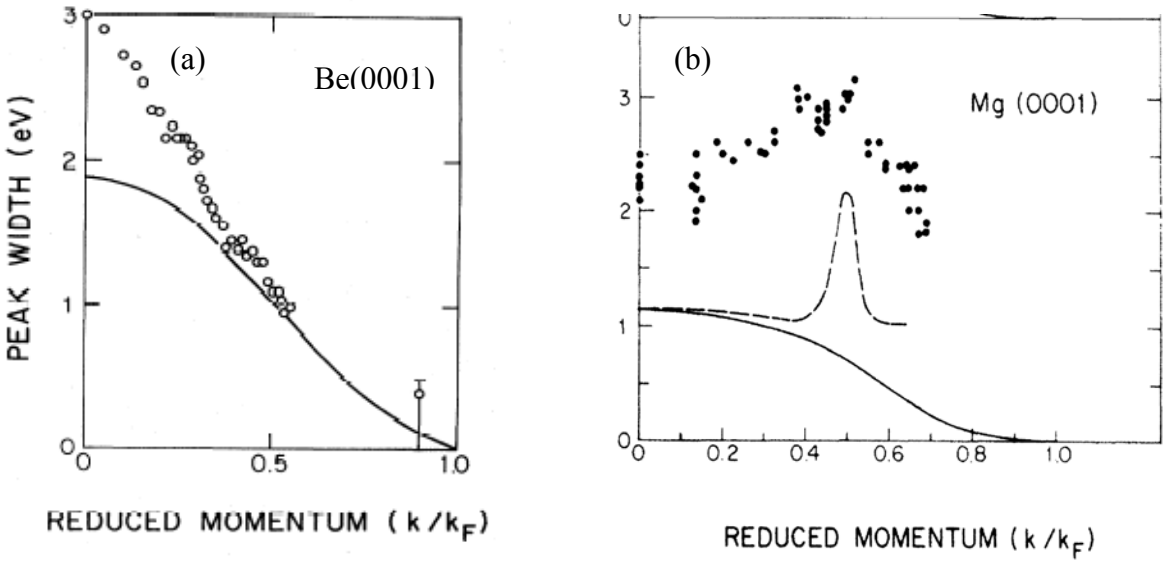

Figure 2.3 Measured and calculated bulk state peak width versus reduced momentum for Be(0001) [9] and Mg(0001)[12].

Up to now, I have briefly stated the previous work of studying the electron-electron interaction on the 3D bulk state in nearly free electron metals through photoemission. At this point a question arose, "By standing on the shoulders of former people's work in the last 20 years, what is the most relevant direction for me in continuing the study of many-body effects on the electronic structure of simple metals?" The relation between the localization of the electronic structure and the resulting many body effects has been an extremely interesting issue recently. To study this relation, the crystal surfaces, which accommodate surface states, are certainly the center of interest. Generally, surface states have a penetration into the bulk for a few layers on most metal surfaces. However, for Be, the electronic structure is nearly covalent-like in the bulk. Formation of the Be surface breaks the "bonds" formed by relatively localized orbitals. These broken bonds form bands that would often be fairly narrow, thereby leading to a large local density of states at the surface. This makes me wonder if the many-body effect would be more on the surface than in the bulk for Be. Actually, according to all the previous studies on the Be surface, this is very possible. For both Be(0001) and Be$(10\bar{1}0)$ surfaces, their unique properties distinct from the bulk such as high density of states around the Fermi level [14,15], the large Friedel charge density oscillations [16,17], large surface core level shift [18,19], large outward or inward surface relaxation and thermal expansions [20–23] have drawn much attention in the past 10 years. Are these unique behaviors of the Be surface related to "anomaly large many body effects" on the surface? One direct way to explore the answer to this question is to look at the behavior of the surface state using photoemission, which is the central idea of my research. Consider the real part of self-energy from the *e-e* interaction first.

Immediately, we think of examining the bandwidths of the surface state. Table 2.1 shows the measured and calculated electron bandwidths of surface states on Be(0001), $\mathrm{Be}(10\bar{1}0)$, Mg(0001), and $\mathrm{Mg}(10\bar{1}0)$, respectively. It appears that there are no obvious differences between the two. How about the imaginary part of self-energy for the surface state? Due to the fact that surface states do not exhibit any dispersion with $k_{\perp}$, we can completely rule out any contribution to the surface state peak width from the final electron state, which is difficult to measure and calculate. Therefore, only the surface initial hole state lifetime is considered. This actually opens a big door for us to access the many-body effects on surface state through the imaginary part of self-energy. In fact, with a more advanced and higher resolution energy analyzer, in recent years, many photoemission experiments have been carried out to measure the line shape and linewidth of surface state of metals [30-33] in order to study many-body effects on the surface.

2.2. Line Shape and Linewidth of the Surface States

The intrinsic linewidth of the surface state is always referred to as its decay lifetime because of many-body effects. However, the measured peak width in the photoemission spectra has contributions from other effects. Before discussing many-body effects on the surface state line shape and linewidth, I would like to introduce some other contributions.

Table 2.1 The measured and calculated surface state bandwidths on Be and Mg surfaces

Surface state Bandwidths	$Be(10\bar{1}0)$,S1 $\bar{A}$	Be(0001) $\bar{\Gamma}$	$Mg(10\bar{1}0)$,S1 $\bar{A}$	Mg(0001) $\bar{\Gamma}$
Measurements	0.33eV Ref [25] 0.46eV Ref [24] 0.37eV Ref [47]	2.8eV Ref [26] 2.73eV Ref [27]	0.61eV Ref [45]	1.6eV Ref [12] 1.7eV Ref [29]
Calculations	0.4eV Ref [25]	2.6eV Ref [14]	0.55 eV Ref [28]	1.56eV Ref [14]

2.2.1 Contribution from Instrument Resolution and Surface Disorder

I: Instrument Resolution

The first contribution is the instrument resolution. Figure 2.4 shows an example of the spectra of surface states at $\bar{A}$ on $\mathrm{Mg}(10\bar{1}0)$ taken by an old hemisphere energy analyzer with energy resolution of ~ 0.4 eV and by a 150-mm hemispherical analyzer (VSW HA150) with energy resolution of ~0.1 eV. The differences are clearly seen. The S1 surface state from the old analyzer has such a large width around 0.5 eV that the Fermi edge was not even resolved. However the peak width from the VSW HA 150 energy analyzer is reduced to 0.15 eV and the fermi edge is clearly shown. There is also angular resolution, Δk_{II}, which causes a broadening of the peak width [34]. The relation is similar to

$$\Delta E = \left| dE/dk_{\mathrm{II}} \right| \Delta k_{\mathrm{II}} \tag{2.5}$$

The slope $\left| dE/dk_{\mathrm{II}} \right|$ is totally determined by the band structure of the surface state.

II: Surface Disorder

The second contribution is the surface defect (disorder) scattering mechanism that was introduced by Tersoff and Kevan [35,36]. The surface defect endows the surface state electrons with a lateral mean free path L, which results in an uncertainty σ of the absolute value of k_{II}, given by

$$\sigma \approx 1/L \tag{2.6}$$

This linewidth contribution to measured photoemission peaks is quite similar to the effects from experimental angular resolution. In a first-order approximation, a resulting broadening on the energy scale can be calculated by the following relation

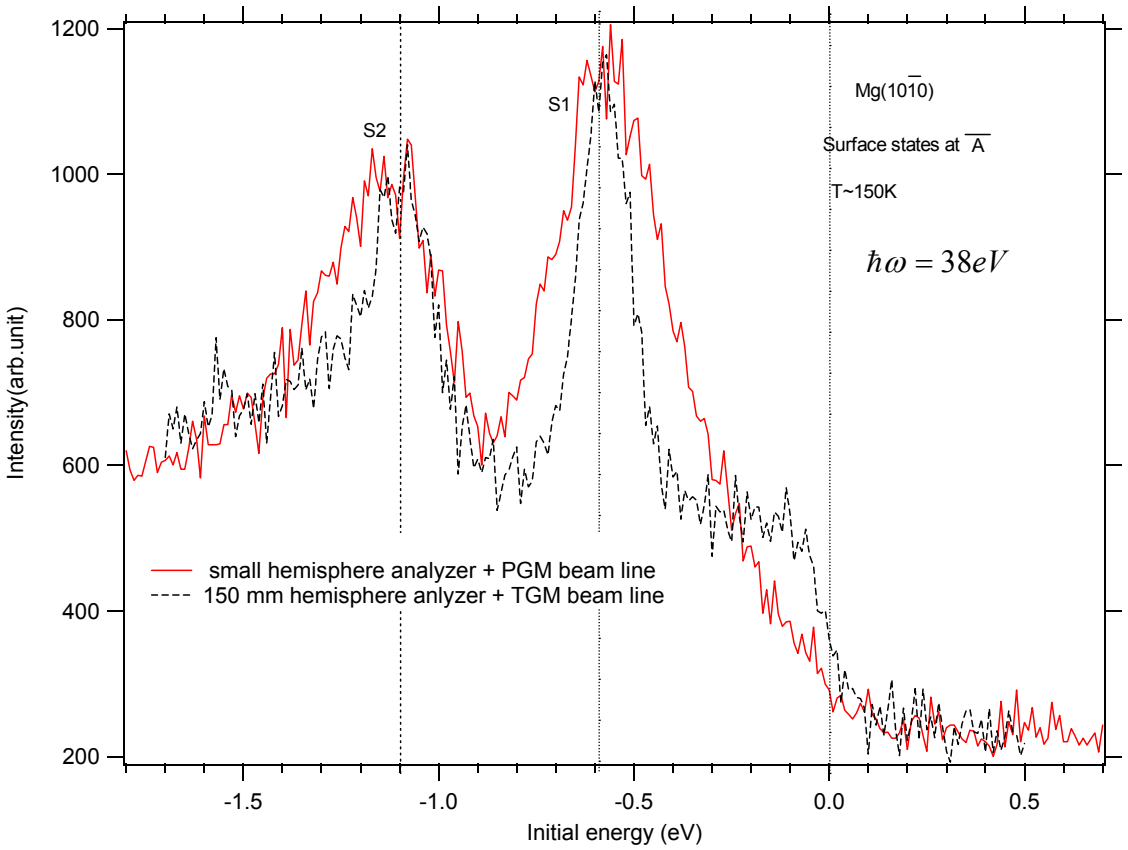

Figure 2.4 Effects of instrument resolution on the line shape and linewidth of surface states on $Mg(10\bar{1}0)$

$$\Delta E_{imp} = \frac{\partial E}{\partial |k_{\text{II}}|} \sigma_{imp} \tag{2.7}$$

The dispersion of a typical surface state band is parabolic according to the equation

$$E_i(k_{\text{II}}) = E_0 + (\hbar^2 / 2m^*)(k_{\text{II}} - k_0)^2 \tag{2.8}$$

where k_0 refers to the symmetry points in which the band dispersion is flat and at the bottom E_0. From relations (2.5) and (2.7), it is definitely true that the energy broadening from the instrument resolution and surface defect scattering is minimum at the bottom of the band where $|dE/dk_{\text{II}}| \approx 0$. However, it does not mean that this broadening effect should be negligible at the band bottom. Surface disorder tends to relax k_{II} conservation, leading to an effective integration of k vectors around the symmetry points at the bottom, and it has been shown that the surface state at $\bar{\Gamma}$ on Cu(111) has an asymmetry broadening line shape and a shift of initial energy to the Fermi level with increasing surface disorder [11,37]. Figure 2.5a and 2.5b show examples of the surface disorder effects on the surface states line shapes and linewidths at $\bar{A}$ on $\text{Be}(10\bar{1}0)$ and $\text{Mg}(10\bar{1}0)$, respectively. The broadening of the linewidth, more asymmetry line shape and the shift of the initial energy toward the Fermi level are all observed by the solid energy dispersion curves, EDCs, in Figures 2.5a, and 2.5b.

2.2.2 Contribution from Many-body Effects

The surface state intrinsic linewidth contributed by many-body effects is always associated with the inverse hole-decaying lifetime. As mentioned above, due to the lack of $k_\perp$ dependence for the surface state, the contribution from the photoelectron final state

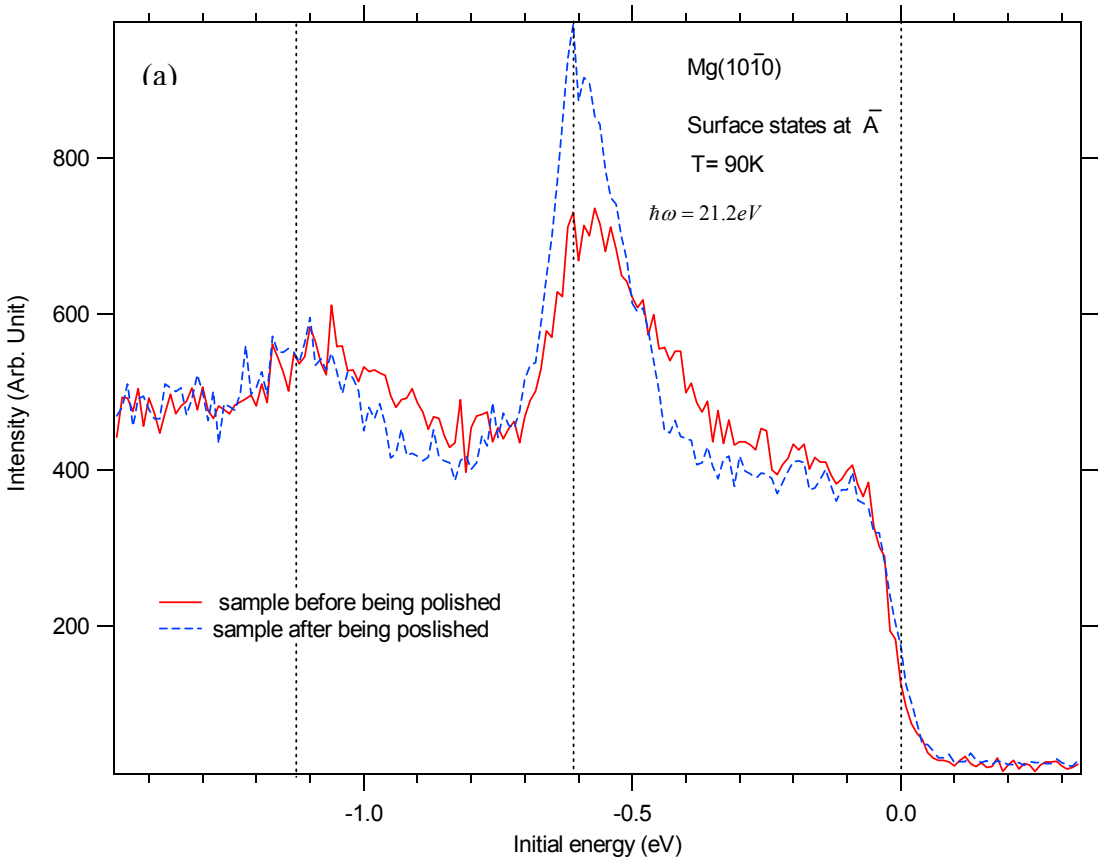

Figure 2.5 Effects of surface disorder on the line shapes and linewidths on the surface states of (a)Mg$(10\bar{1}0)$ and (b) Be$(10\bar{1}0)$

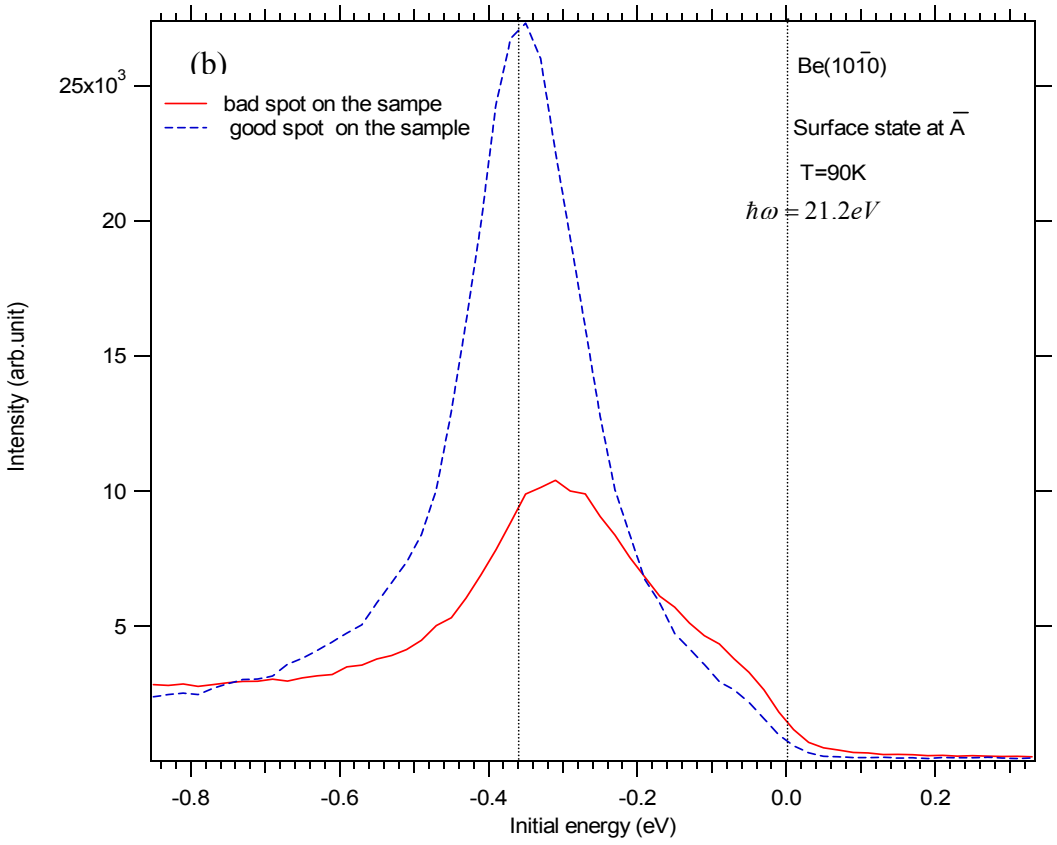

Figure 2.5 Continued

lifetime can be completely ruled out. The source for the hole-decaying lifetime is attributed to the electron-electron interaction and electron-phonon interaction, respectively. In the previous section for the many-body effects on the bulk state, only the electron-electron interaction was considered. Quinn [38,39] has calculated the energy dependence of inverse lifetime associated with *e-e* interaction in the 2D and 3D electron gas, respectively. The relations are the following

$$\text{2D} \quad 1/\tau_{e-e} \propto (E_F - E)^2 \tag{2.9}$$

$$\text{3D} \quad 1/\tau_{e-e} \propto (E_F - E)^2 \ln|E_F - E| \tag{2.10}$$

The result of the 3D is equivalent to that from the Landau Fermi liquid theory [1]. However, the reduced dimensionality makes the inverse lifetime for 2D have an additional logarithmic factor. The bandwidth of the surface state dispersion in nearly free election metals is mostly below 3 eV, as opposed to the bulk states whose bandwidths are mostly over 5 eV (11 eV for Be , 6.15 eV for Mg). Therefore, according to (2.9) and (2.10), the contribution to the inverse lifetime from e-e interactions for the bulk state is certainly much larger than the surface state for most measurable energy ranges. Correspondingly, contribution from the electron-phonon interaction to the peak width of the surface state would be more relevant. Since 1995, several groups [30–33] have investigated many-body effects, electron-electron and electron-phonon interactions, on the surface through the surface state linewidth and line shape. The difficulties are very much evident by the question of how to separate the different contributions to the line width and line shape among electron-electron interactions, electron-phonon interactions, and surface disorder scattering because none of them is exceptionally

dominant. However, B. A. McDougall et al. [30], by using the temperature dependence of the imaginary part of the self-energy due to electron-phonon interactions, successfully simulated the temperature dependent width of the surface state at $\overline{\Gamma}$ on Cu(111) and obtained an electron-phonon coupling strength constant $\lambda = 0.14$ which is consistent with the average result over the Fermi surface for the bulk, $\lambda = 0.15$, from cyclotron measurements. His result proves that, compared to e-e interactions and surface disorder scattering, electron-phonon interactions have the most dominant temperature dependence, and this special property can be used to extrapolate just the information of the electron-phonon coupling of the surface state. Inspired by that, T. Balasubramanian [31] further measured the temperature-dependent width of the surface state on Be(0001) and got an extraordinary electron-phonon coupling constant $\lambda = 1.15$, four times larger than the bulk value $\lambda = 0.24$. This result supports the idea that many body effects are much more dominant on the surface than in the bulk for Be. Furthermore, M. Hengsber et al. [32], motivated by the fact that most weight of the real part of self-energy from electron-phonon interaction are residing in the region between the maximum phonon energy and the Fermi level, investigated the line shape of the surface state dispersing through this region close to the Fermi level on Be(0001). As expected, they found a very sharp quasiparticle peak because of the strong electron-phonon coupling. These people's successful results have brought a lot of interests in the electron-phonon interactions of the surface state on the metal surface. Table 2.2 shows the electron-phonon coupling constant for the surface and bulk of several metals. What draws attention are the semimetals, Be and Ga, which have much larger λ values on the surface than in the bulk. Their density of states at the Fermi level is low in the bulk because of the covalent-like

Table 2.2 Electron-phonon coupling strength values of the bulk and surface for Cu [30,40,41] , Ag [42,43] , Mg [44,45] , Mo[46], Be [33,47],and Ga [48]. Two different values on the same surface come from different surface states.

E-P coupling strength , λ	Cu	Ag	Mg	Mo	Be	Ga
Bulk Value	0.15	0.13	0.3	0.42	0.26	0.98
Surface Value	(111) 0.14,0.85 (110) 0.23	(111) 0.12	$(10\bar{1}0)$ 0.21,0.31	(110) 0.35	(0001) 0.7 $(10\bar{1}0)$ 0.64,0.49	(010) 1.4

bonding, but their surfaces can support very localized surface states, which cross E_F and render the surface more metallic. The possibility of correlation between the electron-phonon coupling and surface superconductivity on Be(0001) has been implied [31].

I have studied the electronic structures and electron-phonon interactions on open surfaces, $(10\bar{1}0)$ of Be and Mg. The lattice structure and dynamic behavior of Be $(10\bar{1}0)$ and Mg $(10\bar{1}0)$ have already be found to be extremely interesting because oftheir oscillatory mutilayer relaxation and large negative first-layer thermal contraction [22,23,49,50]. Even though several different general models have been proposed to explain the lattice behavior on the surface, I believe electronic structure is a big factor, and furthermore, the relation between the electronic and lattice structure can be very intimate. My attempt in the study is to correlate the electron-phonon coupling with the lattice thermal expansion. Other than that, I will also try to show that Be $(10\bar{1}0)$ has more possibility to have surface superconductivity because of its more unique behavior of electron-phonon interaction than that on Be(0001). In words, the central goal of my research and thesis is to understand electron-phonon coupling and relationship to the physical properties on the surface through the study of surface state behavior on Be $(10\bar{1}0)$ and Mg $(10\bar{1}0)$.

2.3 Electron-Phonon Interaction

I would like to introduce some background about the electron-phonon interaction. Phonons are quantizations of the collective lattice vibrations in the solid. In the 1960 and

1970s, the main interest was to measure the frequency and temperature dependence of effective mass m^* and relaxation time τ of the electrons through the cyclotron-resonance technique [51,52]. The effects are supposed to be observable when the distance of the quasiparticles from the Fermi level $\hbar\omega$ or $k_B T$ is comparable to the Debye energy. Therefore, the cyclotron-resonance technique was only performable at low frequency and low temperature for different metals, e.g., ω ~35 GHz, $1.1K < T < 2.5\ K$ for Hg [51] and 70 GHz < ω <460 GHZ, $1.5\ K < T < 6\ K$ for Pd [52]. When the separation between the electron energy and Fermi level is within the Debye energy of the material, the strong electron-phonon interactions make the electron act as ifit is surrounded or dressed by the virtual phonon cloud, and the effective mass m^* (or electron velocity v^*) is modified. The electron-phonon interaction strength can be measured by the renormalization coefficient λ from the relation [52]

$$m^* = (1+\lambda)m, \qquad or \qquad v^* = \frac{1}{1+\lambda}v \tag{2.11}$$

The presence of electron-phonon interaction modifies the dispersion relation of the electron, and hence, the eigenvalues of the Hamiltonian do not correspond purely to electrons but, because of the interaction, to mixed electron-phonon states. The new total energy should be the initial ground state single-particle energy ε_k plus the complex self-energy Σ_{e-ph}:

$$E_k = \varepsilon_k + \mathrm{Re}\,\Sigma_{e-ph}(k, E_k) + i\,\mathrm{Im}\,\Sigma_{e-ph}(k, E_k) \tag{2.12}$$

Assuming the negligible k dependence of the self-energy, the electron-phonon strength at the Fermi level can be obtained by

$$\lambda(\omega=0,T)=-\frac{\partial \operatorname{Re}\Sigma_{e-ph}(\omega,T)}{\partial\omega}\Big|_{E_F} \tag{2.13}$$

and the real part and imaginary part of self-energy can be expressed as follows [53]

$$\operatorname{Re}\Sigma_{e-ph}(\omega;T)=\int_{-\infty}^{\infty}d\nu\int_{0}^{\omega_{\max}}d\omega'\alpha^2F(\omega')[\frac{1-f(\nu)}{\omega-\omega'-\nu}+\frac{f(\nu)}{\omega+\omega-\nu'}] \tag{2.14}$$

$$\operatorname{Im}\Sigma_{e-ph}(\omega,T)=\pi\hbar\int_{0}^{\omega_{\max}}\alpha^2F(\omega')[1-f(\omega-\omega')+2n(\omega')+f(\omega+\omega')]d\omega' \tag{2.15}$$

where n and *f* are the Bose-Einstein and Fermi distribution functions, respectively. Then

$$\lambda(\omega=0,T)=2\int_{0}^{\omega_{\max}}\frac{\alpha^2F(\omega')}{\omega'}G(\frac{\hbar\omega'}{k_BT})d\omega' \text{ , G(y)= } \int_{-\infty}^{\infty}\frac{\partial f(t)}{\partial t}\frac{y^2}{t^2-y^2}dt. \tag{2.16}$$

Figure 2.6 shows the curve of the function of G(y) which rises from its zero-temperature value of 1, reaching a peak value around 1.205 at $\frac{\hbar\omega}{k_BT}=0.26$ [54]. At high temperatures, G(y) approaches zero as an inverse square. Thus, we expect the renormalization λ to rise with temperature initially, reaching a peak value less than 20% higher than its zero-temperature value, at a temperature around $\frac{1}{4}$ the value of the most important group of phonons and decaying to zero at higher temperatures. The electron-phonon coupling strength constant λ is usually referred to as the value at $T=0,\omega=0$. That is,

$$\lambda(T=0,\omega=0)=2\int_{0}^{\omega_{\max}}\frac{\alpha^2F(\omega')}{\omega'}d\omega' \tag{2.17}$$

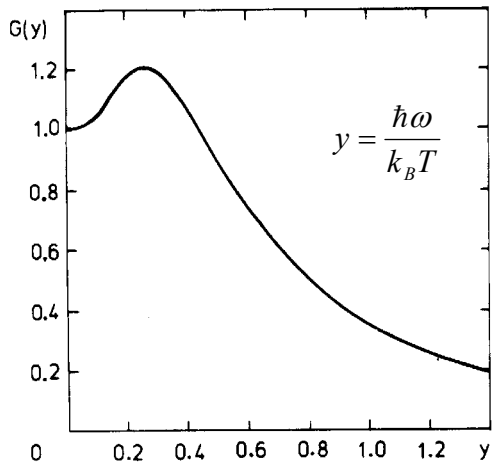

Figure 2.6 The temperature dependent function G(y) for electron-phonon coupling strength λ [54].

The Eliashberg coupling function $\alpha^2 F(\omega')$ in the above functions play the most important key role. This function represents the densities of phonon states, which mostly participate with the electron-phonon coupling. If the exact form of $\alpha^2 F(\omega')$ cannot be measured or calculated, the Debye model or Einstein model for the densities of phonon states has usually been used for approximation. And, this is actually the most fun part in my research results, as will be shown in the next chapter. Figure 2.7 shows the energy (frequency) dependence of $\alpha^2 F(\omega)$, $-\mathrm{Re}\,\Sigma_{e-ph}(\omega)$ and $\lambda(\omega)$, respectively, for Pd. As easily seen, the three quantities have very consistent relations WHEREthe two major

components of the phonons at 4.1 and 8.2 meV constitute two main peaks in $\alpha^2 F(\omega)$, $-\mathrm{Re}\Sigma_{e-ph}(\omega)$ and $\lambda(\omega)$ at the same energies. And from the temperature dependence of $-\mathrm{Re}\Sigma_{e-ph}(\omega)$, Figure 2.7b, we can see that when the temperature increases from 11 to 33 K, the real part of self-energy decreases. Therefore, from the temperature dependence of $-\mathrm{Re}\Sigma_{e-ph}(\omega)$ and $\lambda(\omega)$, we can see that the electron-phonon interaction decreases eventually with increasing temperature. This seems against common sense that there should be more phonos modes populated with the energies within the $k_B T$ distance from the Fermi level when the temperature increases. However, the densities of electron ground states below the Fermi level and unoccupied states above the Fermi level decrease with increasing temperature according to the Fermi Dirac distribution function. Hence, this reduces the probability of the excitations of the ground state electrons through electron-phonon interactions.

Now, we know $-\mathrm{Re}\Sigma_{e-ph}(\omega)$ and $\lambda(\omega)$ have a generally consistent relationship, which indicates the strength of electron-phonon interactions. What about $-\mathrm{Im}\Sigma_{e-ph}(\omega)$? Needless to say, it represents the scattering rate (inverse lifetime) of the qausiparticle because of electron-phonon interactions. According to (2.15), when the temperature is 0 or the energy of the electron is at the Fermi level, $-\mathrm{Im}\Sigma_{e-ph}(\omega)$ can be simplified to

$$\left|\mathrm{Im}\Sigma_{e-ph}(T=0,\omega)\right| = \pi\hbar\int_0^{\omega_{\max}} \alpha^2 F(\omega')d\omega' \tag{2.18}$$

$$\left|\mathrm{Im}\Sigma_{e-ph}(T,\omega=0)\right| = 2\pi\hbar\int_0^{\omega_{\max}} \alpha^2 F(\omega')[f(\omega')+n(\omega')]d\omega' \tag{2.19}$$

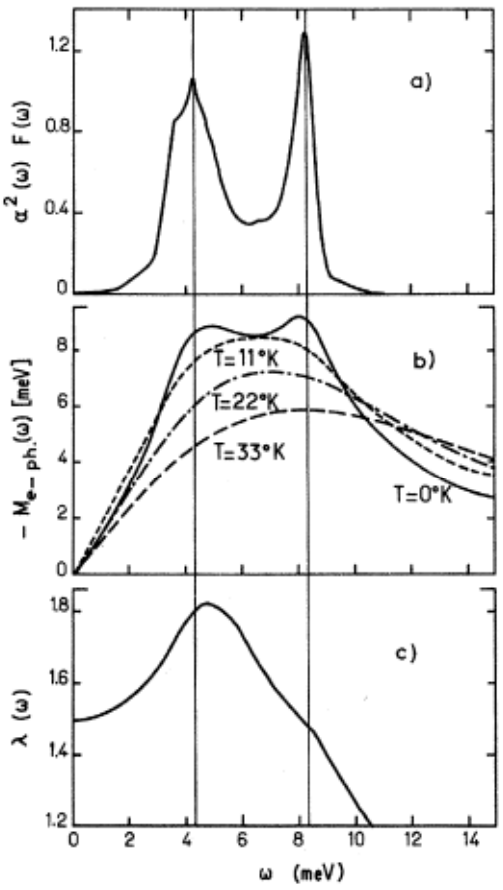

Figure 2.7 The energy (frequency) dependence of (a) $\alpha^2 F(\omega)$, (b) $-\mathrm{Re}\,\Sigma_{e-ph}(\omega)$, and (c) $\lambda(\omega)$ for Pd

If we assume the Debye model for the Eliashberg coupling function $\alpha^2 F(\omega')$, then

$$\alpha^2 F(\omega) = \lambda\left(\omega/\omega_D\right)^2 \; if\, \omega < \omega_D \tag{2.20}$$

and 0 elsewhere, where ω_D is the Debye frequency.

Then, for the energy dependence

$$\left|\mathrm{Im}\Sigma_{e-ph}(T=0,\omega)\right| = \hbar\lambda\pi\omega^3/(3\omega_D^2), \qquad \omega < \omega_D \tag{2.21}$$

$$\left|\mathrm{Im}\Sigma_{e-ph}(T=0,\omega)\right| = \hbar\lambda\pi\omega_D/3, \qquad \omega > \omega_D \ . \tag{2.22}$$

For the temperature dependence at very low temperatures, $k_B T << \hbar\omega_D$,

$$\left|\mathrm{Im}\Sigma_{e-ph}(T,\omega=0)\right| = \lambda\left(\frac{2\pi}{\omega^2{}_D}\right)\left(\frac{k_B}{\hbar}\right)^3 T^3 \int_0^\infty \frac{x^2}{\sinh(x)}dx, \tag{2.23}$$

At very high temperatures, $k_B T >> \hbar\omega_D$

$$\left|\mathrm{Im}\Sigma_{e-ph}(T,\omega=0)\right| = 2\pi k_B T \int_0^{\omega_{\max}} \frac{\alpha^2 F(\omega')}{\omega'}d\omega' = \pi k_B T\lambda = \tau^{-1}/2\hbar, \tag{2.24}$$

where τ is the lifetime of the electron due to electron-phonon interactions. Figure 2.8a shows the calculated result of the imaginary part of self-energy versus electron energy (ω) at several different temperatures for Pd. Compared with figure 2.7b, it seems intriguing that when the temperature or electron energy goes up, the electron scattering rate increases but the electron phonon coupling strength decreases dramatically; however, electron-phonon interaction indeed drives the scattering (decay) of the electrons to the lower energies. Actually, we can see it this way. Even though the electron-phonon interaction is the common driving force, the mechanism can be different. When the

distance of the electron energies from the Fermi level $\hbar\omega$ or $k_B T$ is comparable to the Debye energy, the electrons experience strong interactions with the phonons, dressed with phonon clouds, and favor the excitations of ground state electrons by absorbing phonons. The effective mass, velocity, and energy band dispersion isthus changed and distorted. When the electron energy is above the regime of Debye energy, the electron-phonon interactions still persist, but in a different way by increasing the scattering (decay) rate of the excited electrons. And this effect is proportional to the temperature and electron energy since higher values of both factors favor the production of phonons through the decaying of excited electrons. Figure 2.8b shows an example of electron scattering rate versus T^3 measured by cyclotron resonance for Pd [52]. Relation (2.23) is confirmed with the linear distribution of the data points. This cyclotron resonance experiments could not measure the electron scattering rate at high temperatures because the corresponding relaxation lifetime is too small. It is interesting that after 20 years, when E. Jensen's group [30,31] realized they could measure the scattering rate of the surface hole state through its temperature-dependent peak width in the photoemission spectra, their most interest was at higher temperature regime where the relation between the scattering rate and temperature was linear, as shown in (2.24).

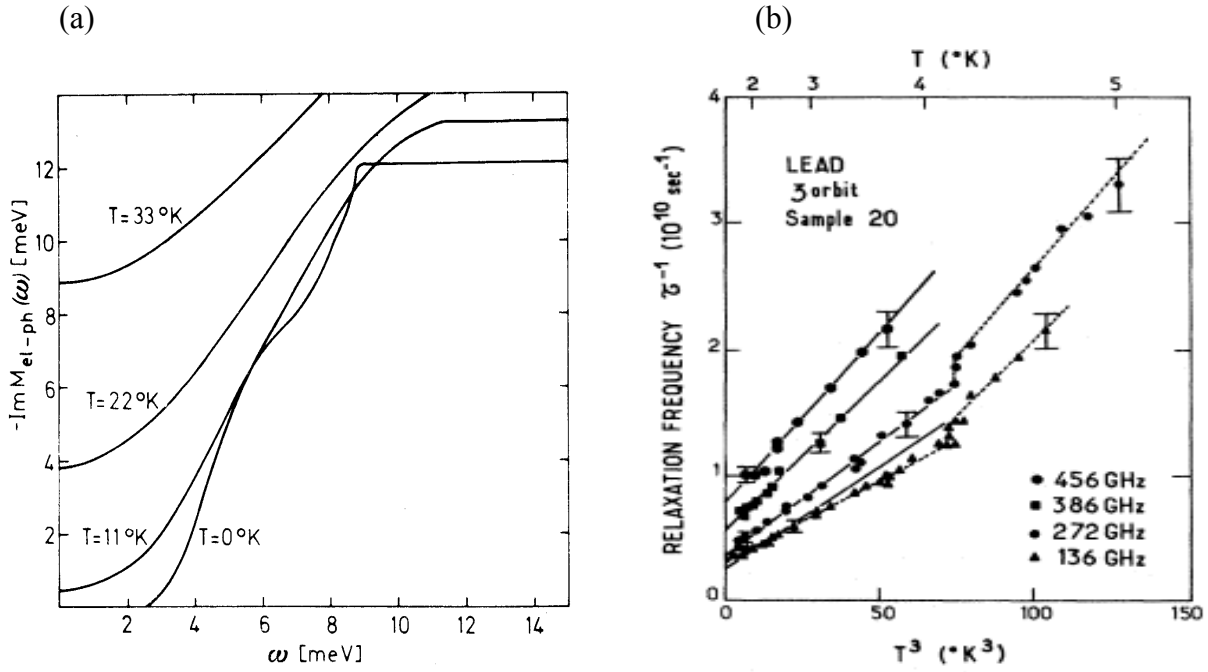

Figure 2.8 Energy (frequency) and temperature dependence of the imaginary part of self-energy for electron-phonon interaction in Pd [52,53]

Chapter 3 Experimental Techniques

3.1 Photoemission General Theory

The general theory of photoemission originates from the Fermi golden rule. If the perturbation Δ is small, then

$$w = \frac{2\pi}{\hbar}\left|\left\langle \psi_f^N \middle| \Delta \middle| \psi_i^N \right\rangle\right|^2 \delta\left(E_f^N - E_i^N - \hbar\omega\right) \tag{3.1}$$

is the transition rate between two *N*-electron final and initial states $|\psi_f^N\rangle$ and $|\psi_i^N\rangle$, which correspond to their energies E_f^N and E_i^N, respectively[1]. $\hbar\omega$ denotes the photon energy. The perturbation Δ to the system caused by the incident radiation is given by

$$\Delta = \frac{e}{2mc}\left(\vec{A}.\vec{p} + \vec{p}.\vec{A}\right) - e\Phi + \frac{e^2}{2mc^2}\vec{A}\cdot\vec{A} \tag{3.2}$$

where $\vec{A}$ and Φ are the vector and scalar potentials of the incident light field. With the further assumption that the vector potential of the system is fully determined by classical macroscopic dielectric theory, $\vec{\nabla}\cdot\vec{A} = 0$ and the scalar potential Φ can be set as zero. As the wavelength of the incident light of interest is large compared withtypical atomic distances, one can simply use the electronic dipole approximation by considering $\vec{A}$ as a constant vector $\vec{A}_0$, and then we get the final form for

$$\Delta = \frac{e}{mc}\vec{A}_0.\vec{p} \tag{3.3}$$

And the corresponding transition rate

$$w = \frac{2\pi e}{\hbar mc}\left|\left\langle \psi_f^N \left| \vec{p} \right| \psi_i^N \right\rangle \cdot \vec{A}_0\right|^2 \delta\left(E_f^N - E_i^N - \hbar\omega\right) \tag{3.4}$$

Even though I regard ψ_f^N and ψ_i^N as N electron states, this equation is actually still in the single-particle picture until there is further consideration about the explicit forms of the operator $\vec{p}$, $\vec{A}_0$ and N electron states wave functions. The relation between many body effects and Photoemission will be further considered in the next chapter. Now, I will just consider the single-particle picture to consider several basic and important properties of photoemission. Therefore,

$$w = \frac{2\pi e}{\hbar mc}\left|\left\langle \varphi_f \left| \vec{p} \right| \varphi_i \right\rangle \cdot \vec{A}_0\right|^2 \delta\left(\varepsilon_f - \varepsilon_i - \hbar\omega\right) \tag{3.5}$$

φ_f , φ_i , ε_f and ε_i represent the single-particle eigenfunctions and eigenenergies of the system. Needless to say, the transition rate w is proportional to the cross section of photoelectron excitation, and its maximum is right at the condition for the conservation of energies, namely,

$$\varepsilon_f - \varepsilon_i = \hbar\omega \tag{3.6}$$

among the final, initial and photon energy. When considering the 3D crystal system, this relation can be written as

$$\varepsilon_{kin} = \hbar\omega + \varepsilon_i - e\phi. \tag{3.7}$$

$e\phi$ is the work function of the crystal, and ε_{kin} is the kinetic energy of the excited photoelectron. To elucidate the photoemission procedure in the crystal, we can divide it into three stages [2]. The first stage is the optical excitation of an electron from an initial

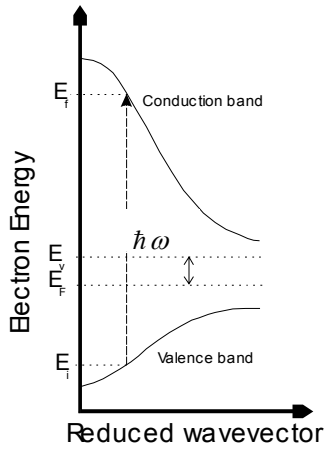

Figure 3.1 Optical excitation of the electron from initial state band to final state band

state into a final electron state within the crystal. This is simply described by the formula (3.6) and illustrated by Figure 3.1.

The second stage is the propagation of the electrons to the surface. A large number of electrons undergo an inelastic scattering process. They lose part of their final energies ε_f by electron-plasma or electron-phonon scattering. Such electrons contribute to the continuous background in the photoemission spectra, which is called the secondary background. They have lost information about their initial electronic level ε_i. The probability that an electron will reach the surface without inelastic scattering is given phenomenologically by the mean-free path λ. In general, λ mainly depends on the energy of the scattering electron, as shown in Figure 3.2 [3]. For photoemission, the electron kinetic energies range of interest is from 10 to 2000 eV, corresponding to mean-free path between 5 to 20Å. The small mean-free path of the photoelectrons makes the

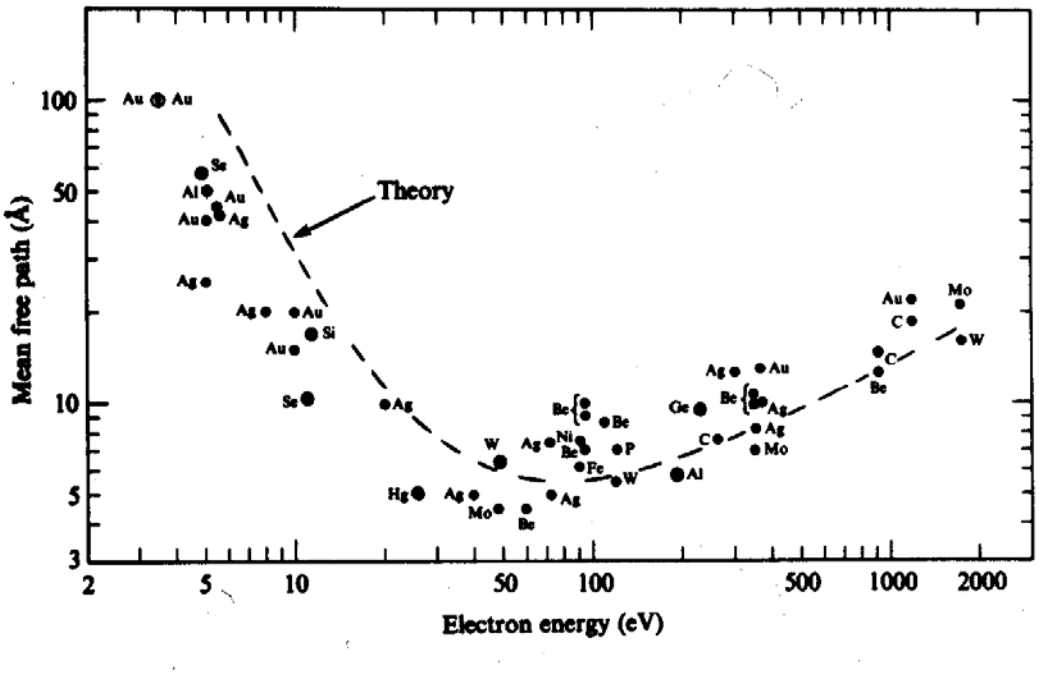

Figure 3.2 Electron escape depths versus kinetic energy

photoemission technique a good tool to detect the electronic structure on the crystal surface.

The third stage is the transmission of the photoelectron to the vacuum through the surface. One can consider this as the matching of a Bloch wave function in the crystal to the free-electron wave functions in the vacuum. Then, the key points would go to the conservation of the physical quantities of the photoelectrons through this vacuum-crystal interface. As for the momentum, the wave vector of the photoelectrons parallel to the surface must be conserved through the surface because of the 2D translational symmetry. That is ,

$$\vec{k}_{\text{Ш}}^{ex} = \vec{k}_{\text{Ш}}^{in} + \vec{G}_{\text{Ш}}. \tag{3.8}$$

However, the momentum perpendicular to the surface is not conserved because the surface breaks the translational symmetry in the direction perpendicular to the surface. There is a potential energy barrier at the surface, which decreases the component of the kinetic energy perpendicular to the surface as an electron emerges form the solid. Outside the crystal, the energy of the photoelectron is only the kinetic energy

$$\varepsilon_{kin} = \frac{\hbar^2 k^{ex^2}}{2m} = \frac{\hbar^2}{2m}(k_{\perp}^{ex^2} + k_{\text{Ш}}^{ex^2}) = \varepsilon_f - \varepsilon_{vac} \tag{3.9}$$

The work function $e\phi$ is defined as the difference between vacuum level and Fermi level.

$$e\phi = \varepsilon_{vac} - \varepsilon_F \tag{3.10}$$

Through (3.6)(3.9),and (3.10), the relation (3.7) is derived. The origin of the energy has always been considered at the Fermi level so the binding energy is the initial state energy with changed sign $\varepsilon_B = -\varepsilon_i$, and the relation between the energy and wave vector exterior to the crystal is

$$k_{\text{Ш}}^{ex} = \sqrt{\frac{2m}{\hbar^2}}\sqrt{\hbar\omega - \varepsilon_B - \phi}\sin\theta = \sqrt{\frac{2m}{\hbar^2}\varepsilon_{kin}}\sin\theta \tag{3.11}$$

$$k_{\perp}^{ex} = \sqrt{\frac{2m}{\hbar^2}\varepsilon_{kin} - (\vec{k}_{\text{Ш}} + \vec{G}_{\text{Ш}})^2} = \sqrt{\frac{2m}{\hbar^2}\varepsilon_{kin}}\cos\theta \tag{3.12}$$

Emission angle θ (between the sample surface normal and analyzer) and the kinetic energy of photon electron ε_{kin} are the quantities, which can be determined through a photoemission experiment setup, as illustrated in Figure 3.3. Inside the crystal, the wave vector of the photoelectron parallel to the surface $k_{\text{Ш}}^{in}$ can be obtained easily

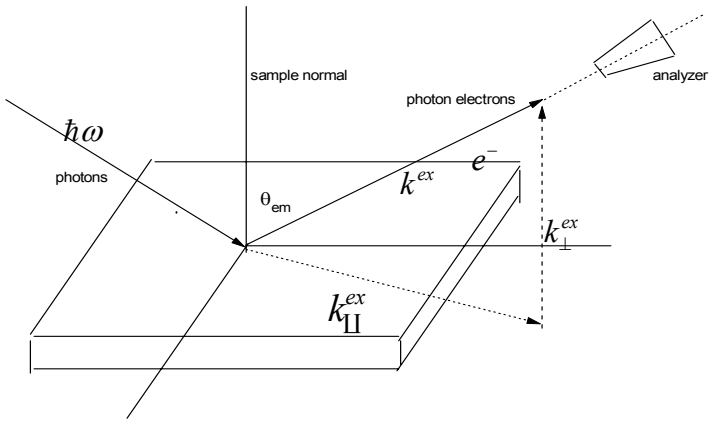

Figure 3.3 The geometry of incident beam, sample surface normal, and the emitted photoelectrons to the analyzer

through the relation (3.8),(3.11); however the wave vector perpendicular to the surface $k_{\perp}^{in}$ has no definite and exact ways to be obtained. A simple approximation is to assume free electron parabola for the final state. Namely,

$$\varepsilon_f \approx \hbar^2 \frac{k_f^{in\,2}}{2m^*} \tag{3.13}$$

Then, the kinetic energy of the electron in the vacuum can be

$$\varepsilon_{kin} = \hbar^2 \frac{k^{ex^2}}{2m} = \frac{\hbar^2 k_f^{in\,2}}{2m^*} + V_0 = \frac{\hbar^2((k_{\mathrm{II}}^{in} + G_{\mathrm{II}})^2 + (k_{\perp}^{in} + G_{\perp})^2)}{2m} + V_0 \tag{3.14}$$

m^* is the effective mass in the crystal, and V_0 is called inner potential. Therefore, the final wave vector perpendicular to the surface inside the crystal, $k_{f\perp}^{in}$, can be expressed as

$$k_{f\perp}^{in} = k_{\perp}^{in} + G_{\perp}^{in} = \sqrt{\frac{2m}{\hbar^2}(\varepsilon_{kin}\cos^2\theta + V_0)} \tag{3.15}$$

And, the final wave vector parallel to the surface can be expressed as

$$k_{\text{II}}^{ex} = k_{f\text{II}}^{in} = k_{\text{II}}^{in} + G_{\text{II}}^{in} = \sqrt{\frac{2m}{\hbar^2}}\sqrt{\hbar\omega - \varepsilon_B - e\phi}\sin\theta = \sqrt{\frac{2m}{\hbar^2}\varepsilon_{kin}}\sin\theta \tag{3.16}$$

With the relations, (3.15) and (3.16), we can map out whole band dispersions in the 3D reciprocal space. We can now make a straightforward comparison between the 2D surface state and 3D bulk state in terms of the photoemission. For the surface state, there is no perpendicular component of the wave vector, and therefore, no definite final state is required for the photoelectron to transit to because of the conservation of the parallel components of wave vectors through the crystal-vacuum interface. That is, from the relation $\varepsilon_f - \varepsilon_i = \hbar\omega$, if we fixed the initial energy of the surface state, then the final energy of the surface state would always go with the incident photon energy. In other words, as along as the surface state is at the same k_{II} point, its initial energy is completely independent of the photon energy. For the 3D bulk state, each initial state has only certain final states to transit to at each $k_{\perp}^{in}$ because of the assumed free electron final state energy. Therefore, when the photon energy changes, the corresponding $\varepsilon_f, \varepsilon_i$ and $k_{\perp}^{in}$ would also change for the $\varepsilon_f - \varepsilon_i = \hbar\omega$ transition to happen through wave vector conservation in the crystal bulk, $k_{\perp}^{in} + G_{\perp}^{in} = k_{\perp}^{f}$. Therefore, the initial energy of the bulk state is photon energy dependent, and this one-to-one transition between the initial state and final state at each $k_{\perp}^{in}$ for the photoemission is called "direct transition". In Chapter 5, these different behaviors of the surface state and bulk state will be illustrated through the photon energy dependence of the S1 surface at $\overline{A}$ and bulk state from A to L on $\text{Mg}(10\bar{1}0)$.

3.2 Photoemission — Experimental System

Through my entire research, I have used three different kinds of photoemission systems, including a small hemispherical deflecting-type analyzer[4], a 150-mm hemispherical Vacuum Scientific Workshop analyzer (VSW HA150) [5], and a 200-mm hemispherical Scienta 200 analyzer with PGM [6], and 6M TGM [7] beam lines and He light source, respectively, in a synchrotron center named CAMD (Center for Advanced Microscopic Structure and Device), [8,9,10] in Baton Rouge, Louisiana. A typical photoemission system is composed of three main components, the light source, high vacuum UHV system and Energy analyzer.

3.2.1 Light Source

I. Synchrotron Light

In photoemission, photons do the job of exciting electrons from inside the crystal. In order to get higher signals of photoelectrons (better statistics of spectra), the intensity of the incident beam has to be intense. Also, in order to get full, complete information on the electron structures in the sample, the variable range of the photon energies has to be large. The synchrotron center serves as a big light source to provide the light beams that fit the two requirements mentioned above for photoemission. Figure 3.4 shows the layout of the ring and the beam lines at CAMD. The synchrotron ring provides the circular orbit along which the electrons and ions are accelerated through the magnetic fields produced by those magnets, M's, in the figure.

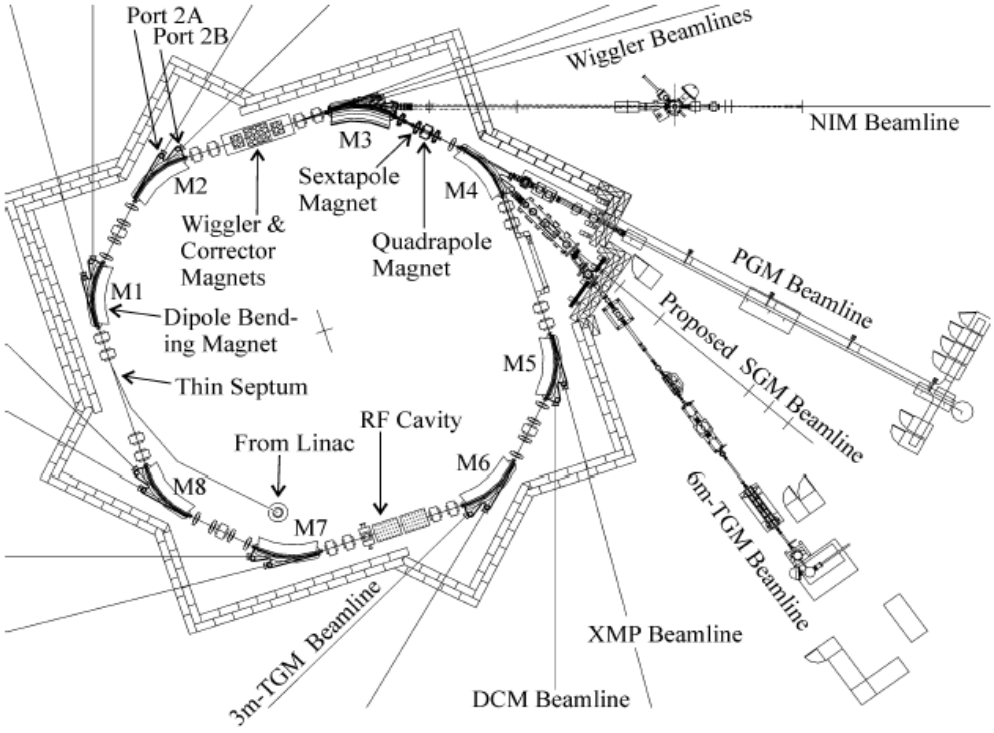

Figure 3.4 Layout of the synchrotron ring and beam lines at CAMD [8]

According to the elemental electromagnetism theory, radiation (electromagnetic waves) arises from the accelerated charges. Therefore, accelerated electron charges are continuously emitting lights through the circular orbit. Close to each magnet, as shown in Figure 3.4, there are outlets leading to each different beam line. Actually, for different purposes of different beam lines, magnets close to the outlets can also be designed in different ways. Like the Wiggler and corrector magnets, they can shift critical photon energies to much higher values for the beam lines requiring high fluxes of high photon

energy beams. As mentioned before, the photoemission technique is mainly for surface science study. Thus, the "useful" photon energy ranges will be the same as kinetic energy ranges which correspond to the mean free path between 5 and 20 Å. From Figure 3.2, this useful photon energy range is between 5 and 2000 eV. Usually, we regard the photoemission experiment using photon energy range between 5 and 200 eV as UPS and photon energy range between 200 and 2000 eV as XPS. UPS is the best to investigate the surface state, valence bulk state, and shallow core state as opposed to XPS, which is for the study of deep core level. Needless to say, UPS is what I used during my Ph.D. research career. Now, I will introduce the 6 M TGM beam line from which I obtained some of my data for $\mathrm{Be}(10\bar{1}0)$ and $\mathrm{Mg}(10\bar{1}0)$. All the information regarding the 6M TGM beam line are adopted from references [5,7].

Figure 3.5 shows the layout of the 6M TGM beam line. The distance between the entrance and exit slit is about 6 m, $r_a + r_b = 6m$. Mirrors (M's) serve to direct, align, and focus light from the Ring toward the target (end station). The slits control the fluxes (intensity) of the beam and change the resolution of the beam energy. Fluxes and resolution are, of course, against each other. The concave gating, the toroidal monochromator, plays the most crucial role for the beam line as it determines the photon energy to use. Table 3.1 shows the three gratings (low, medium, and high energy) used for the TGM beam line.

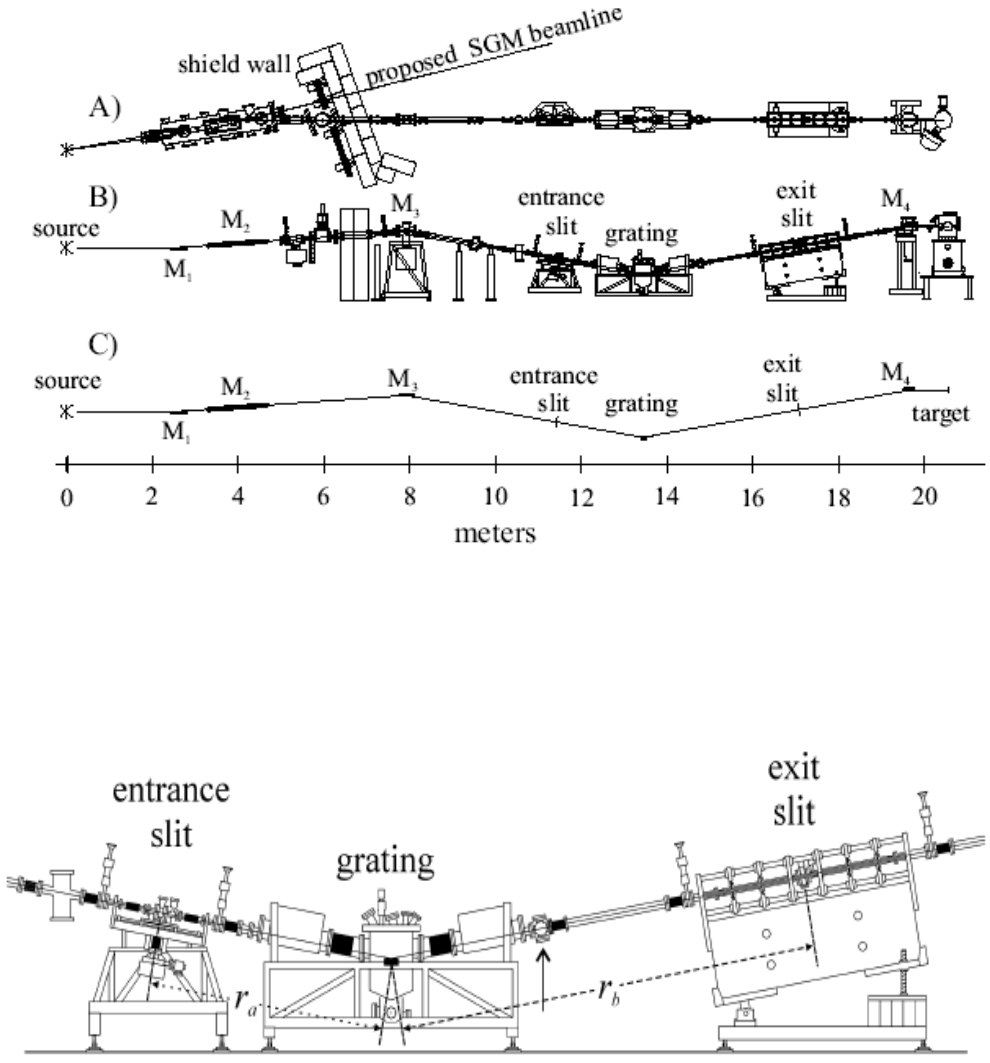

Figure 3.5 Layout of the 6M TGM beam line [5]

Table 3.1 Parameters for the three different gratings of the TGM beam line [5]

The 6m-TGM Gratings

Grating	Groove Density	Quoted High Energy Limit $\alpha = -82.773$ $\beta = 77.227$	Quoted Low Energy Limit $\alpha = -86.946$ $\beta = 73.054$
Low Energy Grating (LEG)	288 lines/mm	500 Å 24.8 eV	1415 Å 8.8 eV
Medium Energy Grating (MEG)	822 lines/mm	175 Å 70.8 eV	500 Å 24.8 eV
High Energy Grating (HEG)	2400 lines/mm	70 Å 177 eV	175 Å 70.8 eV

To change photon energy, the grating has to be rotated, and the relation can be expressed by

$$\sin\alpha + \sin\beta = Nk\lambda \tag{3.17}$$

where α and β are incident and diffracted angles, respectively, as shown in Figure 3.6. λ, N, and k are the radiation wavelength, grating line density, and diffraction order, respectively. A linear translation motor drives the rotation of the grating.

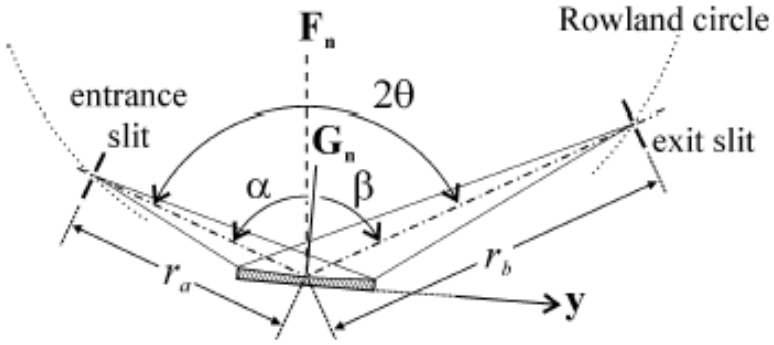

Figure 3.6 Geometry of the incident beam and diffracted beam with respect to the grating normal, entrance slit, and exit slit [7]

II. UV Discharge Lamp

Another substitute for the light source is the UV discharge lamp. When beam time is not available or there is a new analyzer to test, the UV discharge lamp is always the best choice for continuing the experiment. Most of my valuable data of Be$(10\bar{1}0)$ are measured using a new Scienta energy analyzer and UV discharge lamp with a helium source. Helium light provides photon energies of 21.2 (He I) and 40.8 eV (He II), respectively. The principle of the helium lamp is such that in a tube with two ends as anode and cathode, helium gases are filled inside with certain pressure. When a critical high voltage is applied between two ends, the discharge between them can be induced through excitation of the electrons from the ground-state He atoms filled in the tube. The radiation, helium light is thus produced through this massive excited and de-excited process of the electrons in He atoms and led to the targeted sample in the experimental chamber by a thin light capillary. Determination of the photon energies, either 21.2 or

40.8 eV is up to the pressure of helium gas in the tube and discharging current. Table 3.2 gives examples for the HIS UV lamp I used for the Scienta energy analyzer. Of course, a UV discharge lamp can be used with a different gas source to produce the lights of different photon energies. Examples are given in table 3.3.

3.2.2 UHV Experimental Chamber and Experiment Procedure:

I. UHV Chamber

An ultrahigh vacuum chamber is the main stage for all the necessary experimental procedures, and a good vacuum is very crucial for studying surface science. As for the samples I studies, $Be(10\bar{1}0)$ and $Mg(10\bar{1}0)$, they are extremely active to oxygen. Only ambient pressure lower than 1×10^{-10} Torr can make the lifetime of clean $Be(10\bar{1}0)$ and $Mg(10\bar{1}0)$ surfaces last for a couple of hours during measurements. In addition to the pumping through different kinds of pumps, baking the chamber at around 150° C for at least 48 hours is very essential to degas water, the main source of oxygen, out of the chamber. To be a experimental surface scientist, practical knowledge, skill, and patience to make a good vacuum for experimental chamber are deeply required.

II Sample Cleaning

Sputtering and annealing are the most essential and universal procedures to clean the sample surface in the experimental chamber. After filling the chamber with inert gas, i.e., Ne, the electrons injected from the sputter gun ionize the Ne atoms and force them

Table 3.2 Conditions for different Helium light energies

Line	ignition pressure (mbar) typ.	this system:	operational press. (mbar) typ:	this system	discharge current mA
He I	$5x10^{-2}$		$8x10^{-2}$		40 to 70
He II	$5x10^{-2}$		$1.5x10^{-2}$		maximum

Table 3.3 List of gases with the corresponding beam energies they produced

VUV source	Energy [eV]	rel. Intensity [%]	Wavelength [nm]	Satellite shift [eV]
H Lyman α	10.20	100	121.57	0
H Lyman β	12.09	10	102.57	2.67
He I α	21.22	100	58.43	0
He I β	23.09	1.2 ... 1.8	53.70	1.87
He I γ	23.74	0.5	52.22	2.52
He II α	40.81	100	30.38	0
He II β	48.37	<10	25.63	7.56
He II γ	51.02	n.a.	24.30	10.2
Ne I α	16.67	15	74.37	0
	16.85	100	73.62	0.18
Ne I β	19.69	<1	62.97	3.02
	19.78	<1	62.68	3.11
Ne II α	26.81	100	46.24	0
	26.91		46.07	
Ne II β	27.69	20	44.79	0.88
	27.76		44.66	0.95
	27.78		44.63	0.97
	27.86		44.51	1.05
Ne II γ	30.45		40.71	3.64
	30.55		40.58	3.74
Ar I	11.62	100	106.70	0
	11.83	50	104.80	0.21
Ar II	13.30	30	93.22	0
	13.48	15	91.84	0.18

to hit the sample surface. The contaminants residing on the sample surface are thus removed through this "hit and run" process. To make up for the holes the Ne ions cause, the following annealing process is needed to flatten the sample surface. The sputtering voltage, current, annealing temperatures, and time are different for different properties of the samples to clean. As for $Mg(10\bar{1}0)$ and $Be(10\bar{1}0)$, which always have thick oxide layers on the top of the surface in the beginning, the most efficient way to clean them is to reduce the sample-sputter gun distance and increase the sputtering voltage. Furthermore, sputtering and heating the sample have to be implemented at the same time to increase the mobility of the contaminants and ensure the flatness of the sample surface. There is still a 10-mins annealing after each sputtering. Table 3.4 shows the ways I used to clean the $Be(10\bar{1}0)$ and $Mg(10\bar{1}0)$, respectively. Notice that the sputtering voltage and annealing temperature for $Mg(10\bar{1}0)$ are lower than those for $Be(10\bar{1}0)$. That is because Mg is softer in light of its much lower melting point 650°C than that of $Be(10\bar{1}0)$, 1500°C. After averaging 12 cycles of sputter-annealing for about two days, I could observe sharp surface face states of these two samples.

Table 3.4 Special ways to clean the $Be(10\bar{1}0)$ and $Mg(10\bar{1}0)$ surfaces

	$V_{sputtering}$	$\Delta t_{sputtering}$	I_{sample}	$T_{sputtering}$	$T_{annealing}$
$Be(10\bar{1}0)$	1.5 keV	1 hr per cycle	16 ~ 22 μA	300 ~ 350 C	475 ~ 520 C
$Mg(10\bar{1}0)$	1.0 keV	1 hr per cycle	16 ~ 22 μA	125 ~150 C	175 ~ 200 C

III. Temperature Control of Sample

As shown in Figure 3.7, the $Be(10\bar{1}0)$ sample was mounted on a button heater, and a thermal couple wire was attached to Ta pieces which fixed the sample. A cryostat and liquid Helium (or liquid Nitrogen) flow were used to cool down the sample. It is very tricky to take the spectrum for the sample temperature above RT because the magnetic field produced by the button heater strongly influences the photoelectrons. The this difficulty was overcome by heating up $Be(10\bar{1}0)$ to 850K in the beginning; then, I turned off the button heater and immediately took the data with just 1 scan per spectrum. In order to ensure the correctness of the data in spite of possible temperature uncertainty, I continuously took the series of spectra until the sample temperature naturally decreased back to RT. The temperature control procedure for $Mg(10\bar{1}0)$ when measuring is similar except that only low-temperature data were taken due to the fact that surface thermal disorder on $Mg(10\bar{1}0)$ is likely to happen because of its low melting point.

3.2.3 Energy Analyzer—Scienta:

Even though I have used several different energy analyzers for my experiments, the most important and advanced one, which gave me the most convincing data, is the Scienta energy analyzer. The main elements for the Scienta Energy analyzer are shown in the Figure 3.8. The electronic lens set (L5-L9) has two main functions. The first function is to focus the photon electron beam to the entrance slit of the hemispherical orbit. A set of eight deflector plates arranged in an octagonal symmetry inside L7 was

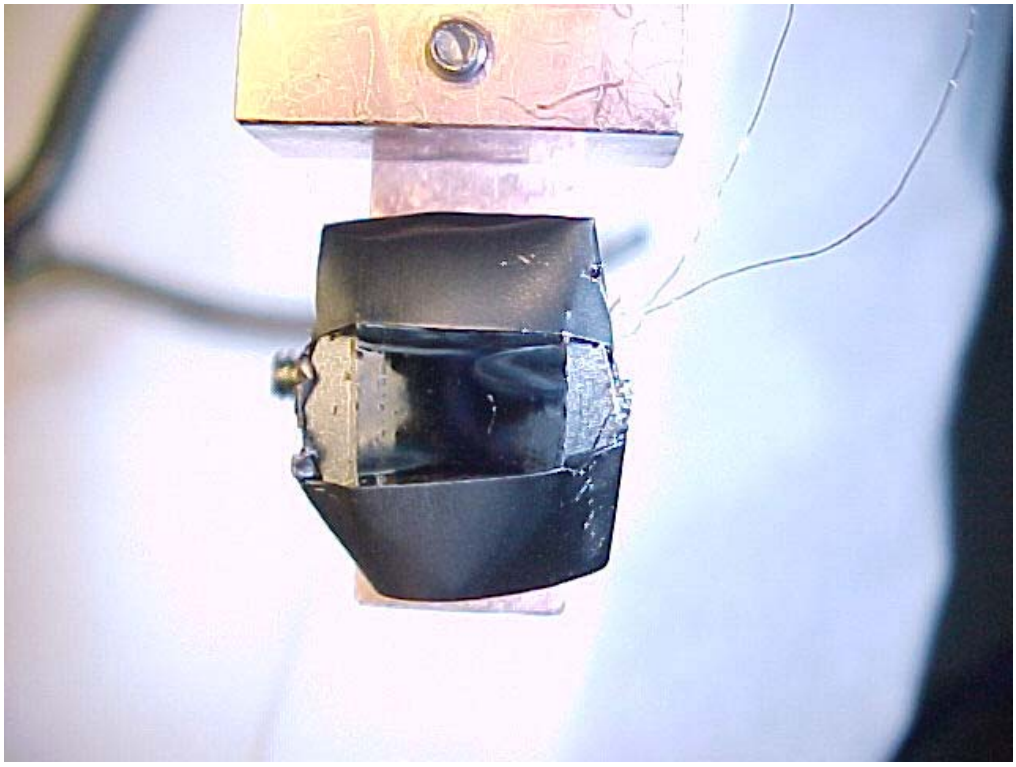

Figure 3.7. Be $(10\bar{1}0)$ sample mounted on a button heater

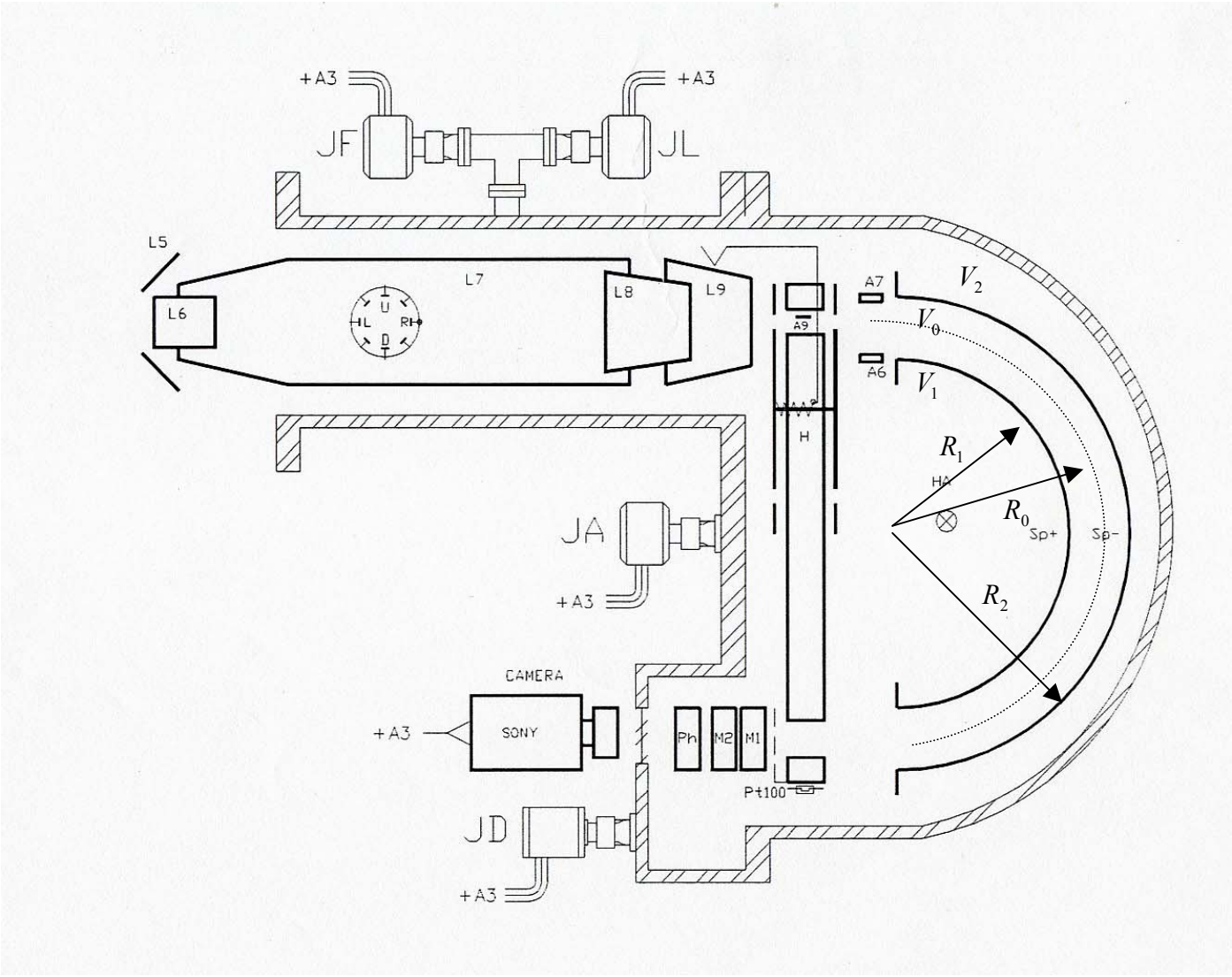

Figure 3.8 Layout of the main elements in the Scienta energy analyzer

used to correct misalignment of the excitation spot from the electron optical lens axis. Another function was to supply retarding voltage to slow down the photoelectrons and reduce their kinetic energies to the fixed passing energy.

$$E_{pass} = E_{kinetic} - V_{retarding} \tag{3.18}$$

Scanning of the kinetic energies for a spectrum is equivalent to the continuous change of the retarding voltages supported by the lens set. The hemisphere orbit lies between two hemispherical electrodes which energy disperses the photoelectron beam. With certain voltages (V_0 , V_1, and V_2) applied on the entrance slit (H) , inner sphere (sp+), and outer sphere (sp-), respectively, the passing energy E_{pass} is determined. After passing through the lens set, electrons with energies equal to E_{pass} within uncertainties ΔE will travel around the equipotential V_0 surface and reach the exit slit.

Relations among the applied voltages, the dimensions of hemispheres, and E_{pass} are as follows.

$$V_1 = \frac{2E_{Pass}}{e}(\frac{R_0}{R_1} - 1) + V_0 \,,\; V_2 = \frac{2E_{Pass}}{e}(\frac{R_0}{R_2} - 1) + V_0 \tag{3.19}$$

$$E_{pass} = e(V_1 - V_2)(\frac{R_1 R_2}{R_2^2 - R_1^2}) \tag{3.20}$$

R_0 , R_1, and R_2 are the radii of hemispherical orbit, inner hemisphere, and outer hemisphere , respectively

The energy resolution is determined by

$$\frac{\Delta E}{E_0} = \frac{w}{2R_0} + \beta^2 \tag{3.21}$$

where w is the slit width and β is the angle of the electrons entering the entrance slit of the hemispherical orbit.

From the relation (3.21), it is easy to see that the radii of the hemisphere and the slit width are relevant in determining the resolution of energy analyzer. The Scienta 200 energy analyzer has a large radius of the hemisphere (200mm), which makes this analyzer in a position to have high-resolution performance. The slit width is even more crucial because it is adjustable. One would think that as long as the slit width is chosen to be smallest, the highest resolution of the energy analyzer would be attained. However, it is not practical because the smaller slit would reduce more electron flux and the intensity of the spectrum would be noisier. The shape of the slit has a direct relationship with which lens mode to use. The curve (straight) slit is for non-imaging (imaging) mode. Table 3.5 is the list of the available combinations of slit width, shape, and aperture width for the Scienta 200. Figure 3.9a,b gives an example of the influence of the slit on the resolution of the analyzer through the Gaussian peak width extrapolated from the Fermi edge of the photoemission spectrum. The energy resolution obtained at slit No 8 is around 10 meV which is much smaller than the energy resolution, 61 meV, obtained without the slit. Therefore, to make the Scienta energy analyzer fully functional, the strong, intense, and high-resolution light source is indispensable.

In addition to the capability of high energy resolution performance, the most interesting feature of the Scineta energy analyzer is the 2D mapping of energy and k wave vector dispersion. The Scienta energy analyzer is designed where the size of the slit and aperture in the horizontal direction is fixed and as wide as an acceptance angle $\pm 7.5^\circ$ for electrons coming from the sample at different directions; however, the vertical

Table 3.5 The available set of slits and apertures for the Scienta 200 energy analyzer

No	Setting	Slit width [mm]	Slit length [mm]	Aperture width [mm]	Aperture length [mm]	Shape
1	100	0.3	30	1.3	30	Straight
2	200	0.5	30	1.9	30	Straight
3	300	1.5	30	3.2	30	Straight
4	400	2.5	30	5.0	30	Straight
5	500	4.0	30	6.0	30	Straight
6	600	0.2	25	1.0	30	Curved
7	700	0.3	25	1.3	30	Curved
8	800	0.5	25	1.9	30	Curved
9	900	0.8	25	2.2	30	Curved

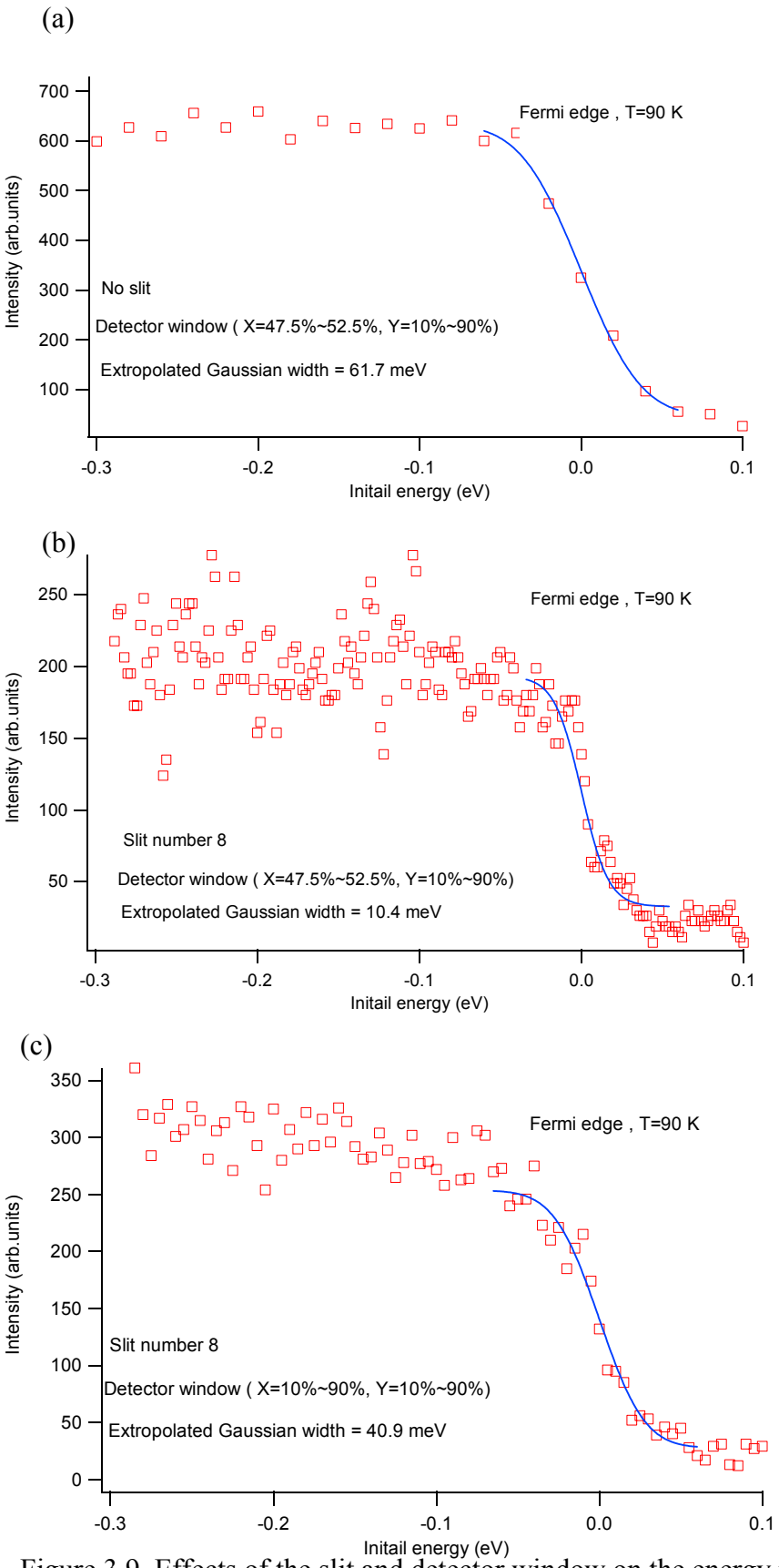

Figure 3.9 Effects of the slit and detector window on the energy resolution

direction of the slit is small and adjustable, where the energy of electrons only disperse. Therefore, a 2D image of energy (vertical direction) versus k wave vector (horizontal) direction can be transferred from the sample to the 2D detector at the exit of hemisphere. The detector assembly consists of two MCP plates and a phosphor screen as indicated by M1, M2, and Ph in Figure 3.8. The MCP pair multiplies each incoming electron 10^7 times, and this electron pulse is accelerated to the phosphor screen, where they produce a light flash. Under normal operating conditions, the voltage over the MCP pair is 1700–1850 V. The acceleration voltage between the last MCP and the phosphor screen is normally 3800 V. The CCD camera mounted behind the phosphor screen measures the signal in such a way that the camera lines are perpendicular to the energy axis. For a given set of spectrometer voltages, the number of the camera line where a light flash is detected is a unique function of the electron energy. The video signal from the camera is connected to the detector electronics. This contains a dedicated microprocessor, which is set up for a specific experiment from the PC and is then independently acquiring data. The microprocessor evaluates the flash positions perpendicular to the slit direction, which corresponds to the kinetic energy of the electrons. It also senses the number of pixies of which the video signal exceeds a given threshold for each line, which is proportional to the number of flashes on that line. The value is referred to as a physical channel and is stored in the counter. Because of nonlinearities in the analyzer, the camera position and the energy resolution required that the physical channels be mapped into logical channels. The logical channels correspond to the data points in a spectrum. The mapping is also performed in the microprocessor. The camera is connected to a real-time monitor, which shows the 2D distribution of the light flashes while making the measurements. Figure

3.10 shows an example of the light flash on a real-time monitor for transmission mode and angular mode, respectively, on taking the Au(111) *d*-band spectra.

During the measurements, there are several modes, which can be chosen to use for different purposes. Because of their importance, I organize them as follows.

1. Acquisition mode:

(1) Fixed mode: In fixed mode, the instrument is set up for a certain energy, fixed retardation voltage specified as the midpoint energy, and specified measuring time. The range of the spectrum is then determined by the passing energy through $E_{pass}/10$ and the physical size of the MCP. The detector accumulates counts during a specified time. The acquired data, in the logical channels, are transferred to the PC after completion. In my experience, this mode was usually used to calibrate the sample position with respect to the energy analyzer. Knowing the special peak originating from the feature of interest in the sample (i.e., surface state), the peak position is taken as the fixed energy. While doing the adjustment of x, y, z coordinates of the sample, I can get the best position of the sample where there is optimal signal from the surface state by attaining maximum intensity of this special peak in the fixed mode spectra.

Figure 3.10 Light flashes on real monitors for the transmission mode (left) and angular mode (right).

(2) Sweep mode: This is the most used mode for taking normal spectra. The scanning of kinetic energies in a spectra is equivalent to the continuous change of the retarding voltage provided by the lens set. Needless to say, a sweep mode measurement can be viewed as several fixed mode measurements.

2. Lens mode:

(1) Transmission mode: The voltage of the different lens elements can be set in different ways in order to optimize different properties. The transmission mode is basically the direct transferring of the real image from the sample to the detector. The vertical direction (normal to the slit) is for the energy disperses, and the horizontal direction is for the real spatial position of the electrons scattered from the sample. This mode usually gave maximum transmission through the lens to give the optimal signal of the spectra. As for my experiment, which focuses on the valence electron and surface states, this transmission mode is not useful since it lacks all the *k* wave vector information of the electrons. However, as the first step to optimize the signal of the spectra while adjusting the sample position, this transmission mode is very handy.

(2) Angular disperse mode: By allowing the lens element voltages to vary in a different way with kinetic energy, it is possible to image the emission angle distribution at the lens exit instead of a real image. The emission angle distribution represents the information of the *k* wave vector of the electrons. Therefore, the angular disperse mode is the best for my experiment, which requires high-resolution information of both energy and k moments of the electron state in the sample crystal.

3. Spectra mode:

(1) Single/EDC: This kind of spectra is the same as those from all the traditional energy analyzers. The spectra just show the single curve of intensity versus energy. All the $Be(10\bar{1}0)$ and $Mg(10\bar{1}0)$ data taken by the Scienta energy analyzer were in this mode. When using this spectra mode, the setup of the detector window is extremely important, as shown by the rectangular frame in Figure 3.10. This detector window, which normally determines active detector area in the energy dispersion (y direction) and either a spatial or angular dispersion (x direction), can work as a slit for a single/EDC mode. As mentioned before, the spanned angle of aperture is $\pm 7.5^{\circ}$, the only way we can increase the angular resolution for single EDC spectra is to shrink down the detector window in the x direction. Figure 3.10 b,c shows that the detector window size in the x direction indeed influences the energy resolution due to the change of angle resolution. The dimension of the detector window in the y direction does not matter much since the energy resolution is mainly decided by the passing energy and the width of front slit. Figure 3.11 shows examples of surface state dispersion spectra from Au(111) at the initial stage of testing the Scienta 200 energy analyzer in CAMD by using this spectra mode. From comparison between the surface state bands measured by the Scienta 200 and Jensen's group [11], respectively, Scienta 200 works quite properly.

(2) Angle(detector): This is the so-called imaging mode which records simultaneously data from different take-off (emission)angles. This is the most important feature of the Scienta energy analyzer, but it is pity that the Scienta 200 in CAMD still cannot perform this function well. The reasons will be discussed in the next subsection. Figure 3.12 is an example of the 2D image (K.E vs θ) for the surface state dispersing around $\bar{\Gamma}$ on Be(0001), measured by the Scienta 2002 at the Advanced Light Source (ALS). The

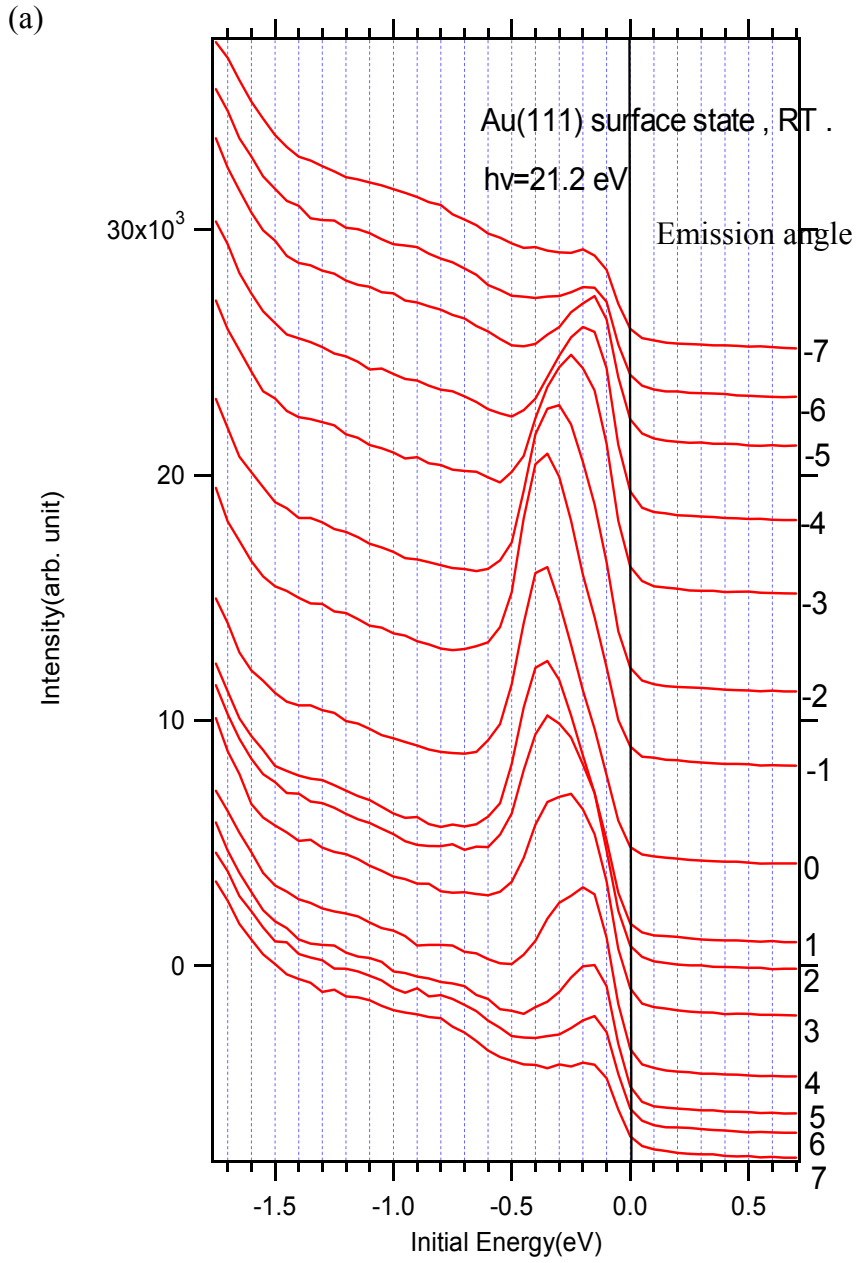

Figure 3.11 The test result of Scienta 200 energy analyzer on the surface state of Au(111) (a) Dispersion of the surface state on Au(111), measured by Scienta. (b) Comparison of the Au(111) surface state band between the Scienta result (square marks) and that from reference 11. The dashed line and dot-dashed line are the two surface state bands because of the spin orbital splitting.

(b)

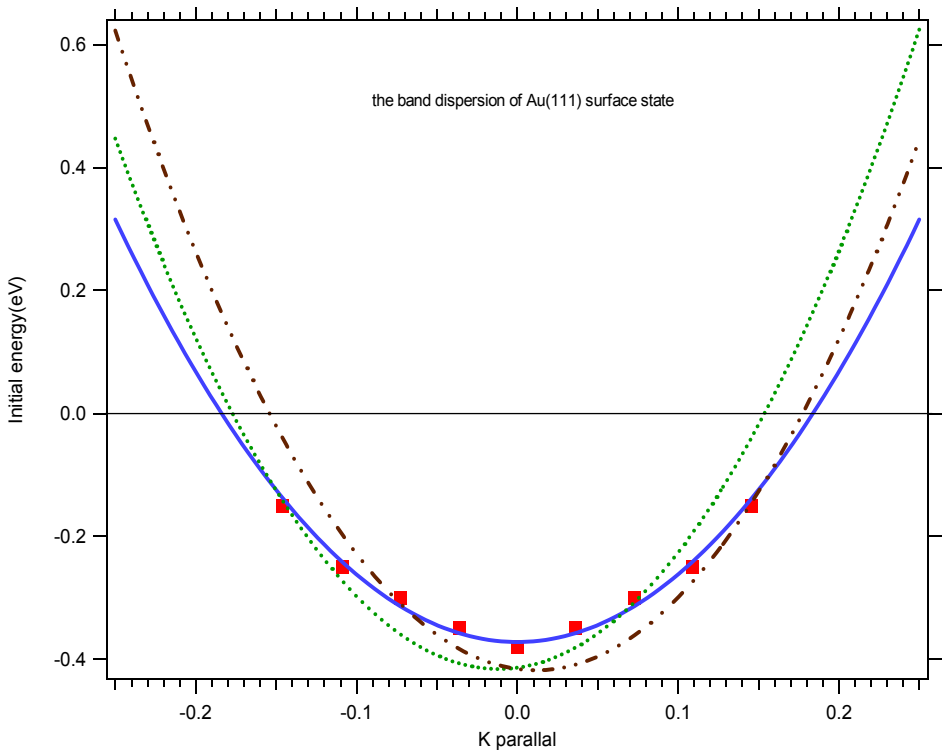

Figure 3.11 Continued

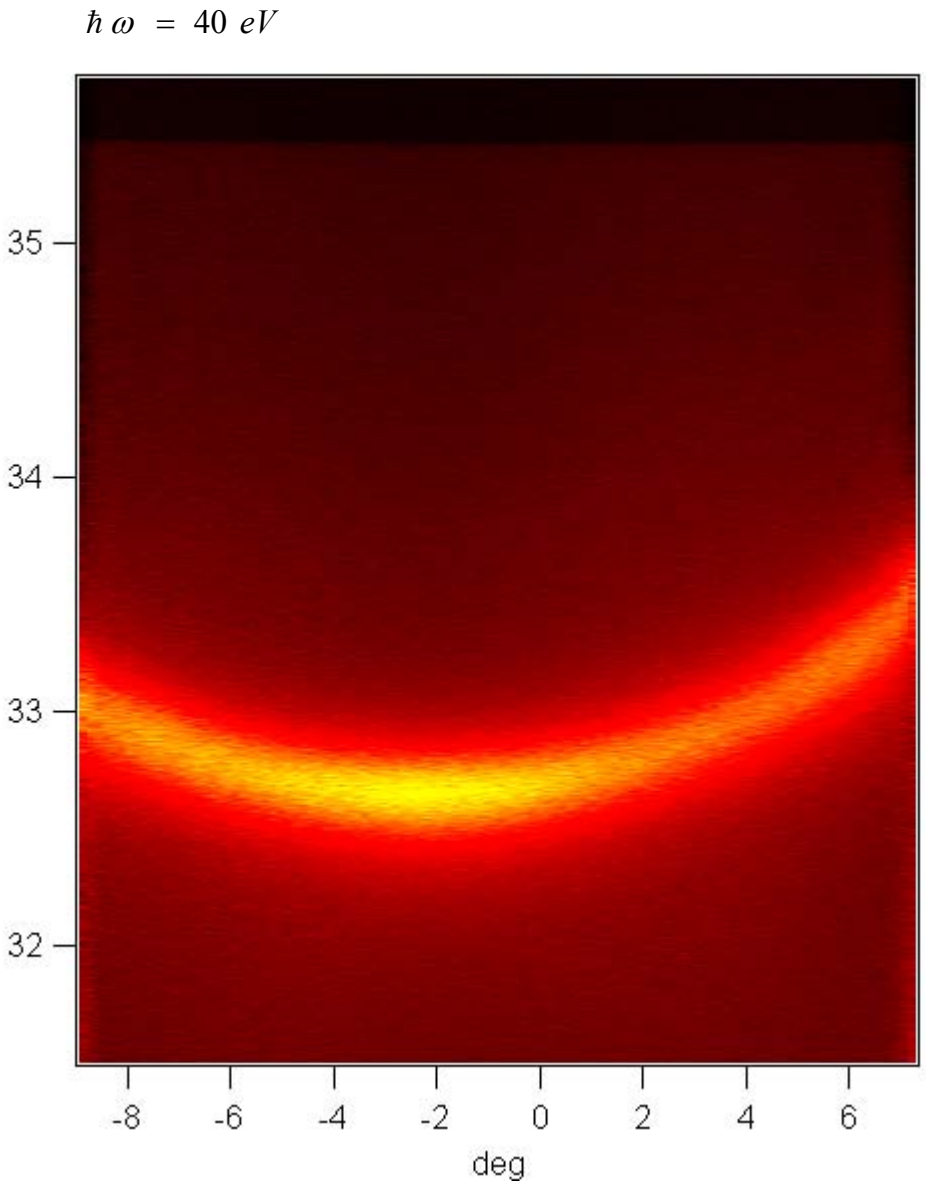

Figure 3.12 2D image of the surface state band dispersing around $\overline{\Gamma}$ on Be(0001). The y axis is the kinetic energy (eV), and the x axis is the emission angle θ

image is actually composed of 220 energy dispersion curves (EDC's) at different angles continuously from -8.5° to $+6.5^{\circ}$. In other words, the angular resolution is $\Delta\theta = 15^{\circ} / 220 = 0.07^{\circ}$.

3.2 The Problems of the Scienta Energy Analyzer System at CAMD and Some Suggestions

As the first person to do extensive testing of the Scienta energy 200 analyzer at CAMD and then get good and convincing data of the surface states in Be$(10\bar{1}0)$ and Mg$(10\bar{1}0)$, I organized the problems and made suggestion for this Scienta energy analyzer as follows.

(1) There is a quite large shift in energy of the spectra when switching the passing energy, which is illustrated in Figure 3.13. The cause for this can be due to incorrect slit voltage Vo applied to the entrance slit of the sphere in several passing energy modes. The lens voltage table at different passing energy modes for this analyzer had to be readjusted. As for me, the passing energy 5 eV was most reliable and often used to take the data.

(2) Angle mode does not work. This is mostly due to the large magnetic fields inside the experimental chamber. I used to hold a magnet and move it around the chamber. The image from the real time monitor was extremely distorted. This μ metal experimental chamber is too old and it has windows for magnetic fields at the welding parts. Mounting

muitiple layers of new μ metal shields to the inner walls of the chamber is very necessary.

(3) To get the Secienta energy analyzer fully functional, the intense and high-resolution light source is important. As mentioned before, a smaller entrance slit would make the resolution of energy analyzer higher at the expense of losing the intensity of spectra signal. Lately, this energy analyzer has finally connected to the NIM beam line [12], which is able to provide a highly intensive beam at the photon energies from 15 to 30 eV. The future experiments conducted with this Scienta energy analyzer at Nim beam line were very in perspective.

4) The Scienta energy analyzer is large and fixed. To change the emission angle, the only way is to rotate the sample even though the incident angle also changes at the same time. Lack of the rotation freedom of the energy analyzer makes the study of the spin-polarized dependence of electronic state impossible. The solution to improve this only has to do with how much money is to be invested.

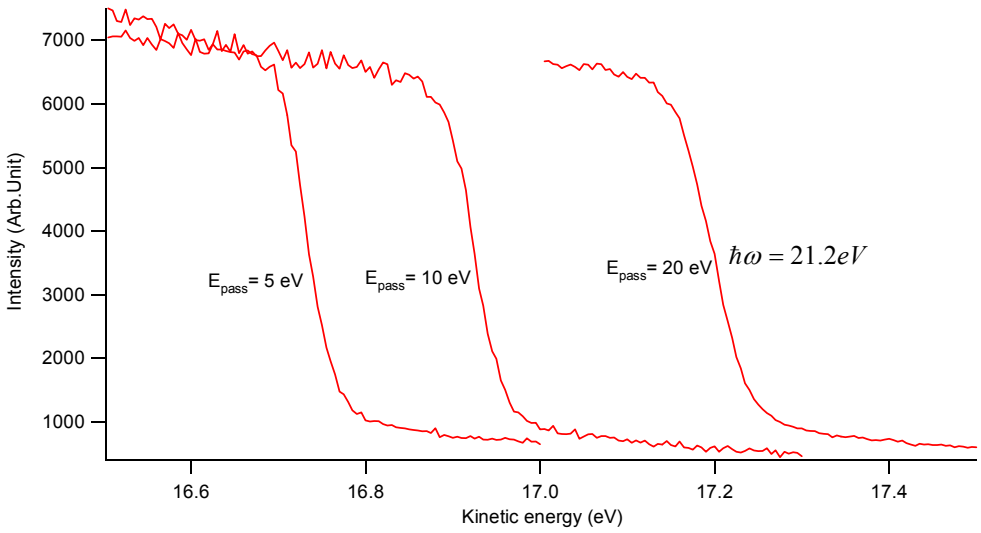

Figure 3.13 The abnormal shift of Fermi edge with passing energy from Scienta 200 energy analyzer

CHAPER 4: The Electronic Structure and Electron-Phonon Coupling on Be$(10\bar{1}0)$

4.1 Introduction:

Beryllium is an intriguing and exceptional metal. Its unique properties on the surface and in the bulk have always been the center of interest. Starting from the smallest unit, atoms, Be atoms have only two *s* electrons in the valence shell and the energy cost in promoting electrons from 2*s* to 2*p* is only 2.72 eV [1]. Were it not for this small promotion energy, Be would act as an inert gas. Be_2 is weakly bonded because each Be ion core has a positive charge of only 2, and that charge is partially screened by the valence electrons that remain nearby. However, when there is more coordination for bonding, the cohesive energies will increase and the bonding length will further decrease. This is against the usual bond-order-bond length correlation that the dimer bond is shorter than the nearest-neighbor distance in the solid. The Be crystal is a hcp structure, as shown in Figure 4.1. M.Y. Chou et al. [2] have calculated the structure and electronic properties of Beryllium by the self-consistent pseudopotential approach within the local-density-functional scheme. She found the smaller c/a ratio, 1.586 for Be, than the ideal number 1.633 has to do with a stronger covalent bonding in the c axis direction, and it is due to the absence of core p orbitals, which results in compactness of the valence *p* orbitals and the relative effectiveness of the *s-p* hybridization. Figure 4.2 shows her result of the plot of the charge density distribution in the $(11\bar{2}0)$ basal plane. It does

show the enhancement of bonding along the c-axis direction with extra charge accumulation right above and below each atom, as shown by the arrows. Figure 4.3 shows the density of states distribution with the individual contributions from different angular momentum of the wave function. Z direction is along the c axis, and the x direction is perpendicular to it. The characteristic feature of the total density of states is the dip from all components near the Fermi level, which indicate the semimetal property of Be bulk. The contribution from momentum P_z is obviously higher than others, and this is consistent with the larger covalent bonding in the z (c axis) direction inside the Be bulk.

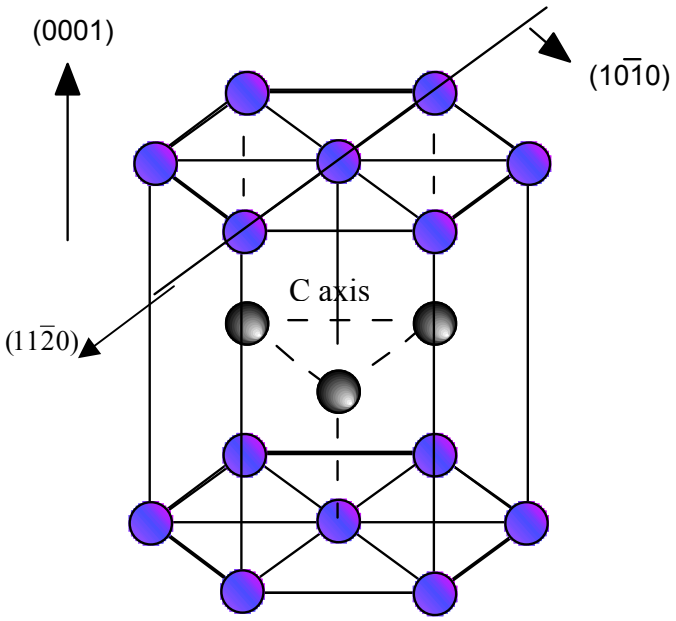

Figure 4.1 Lattice structure of a typical hcp crystal and three different directions of the surfaces

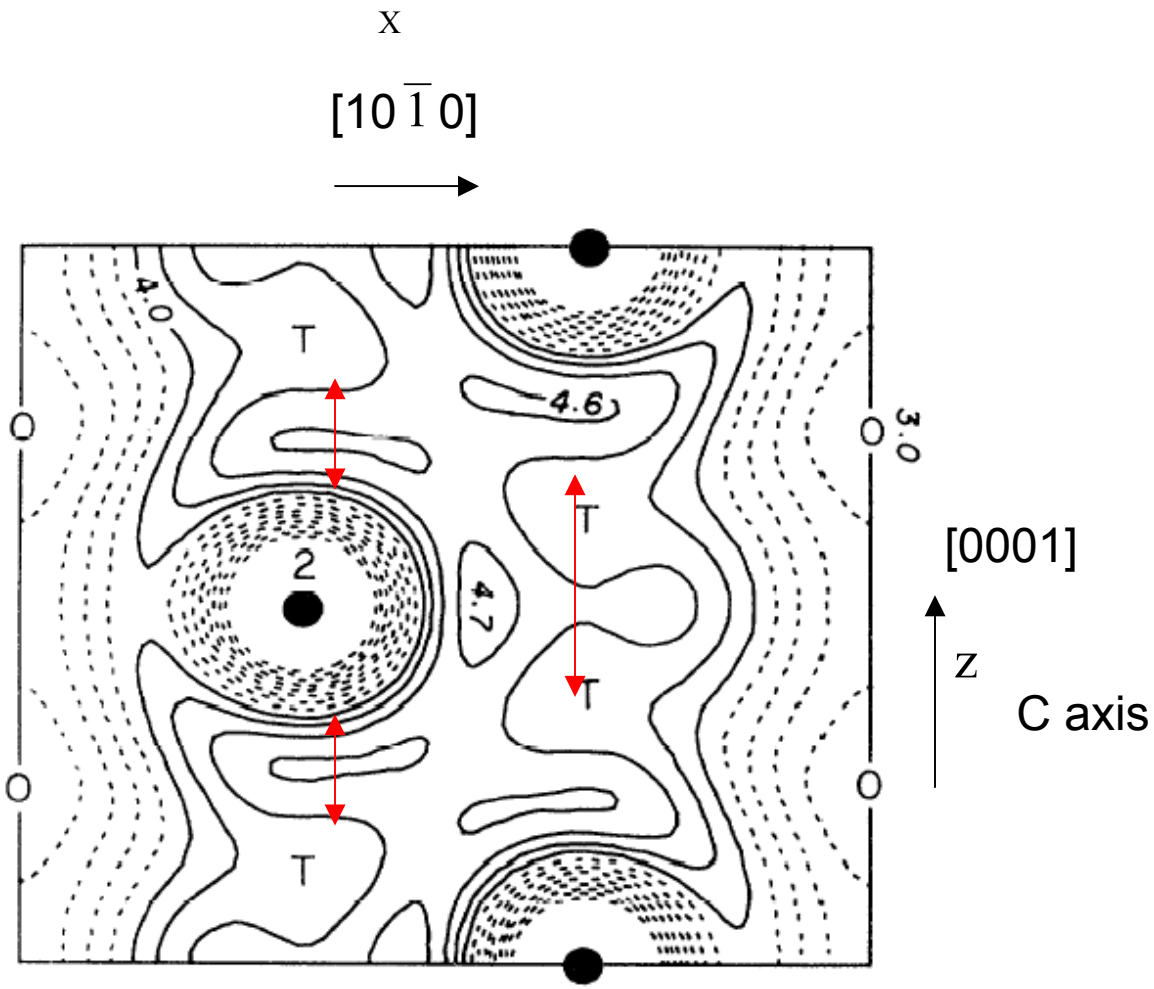

Figure 4.2 Contour plot of the calculated charge density distribution of the bulk beryllium on the $(11\bar{2}0)$ cut plane [2].

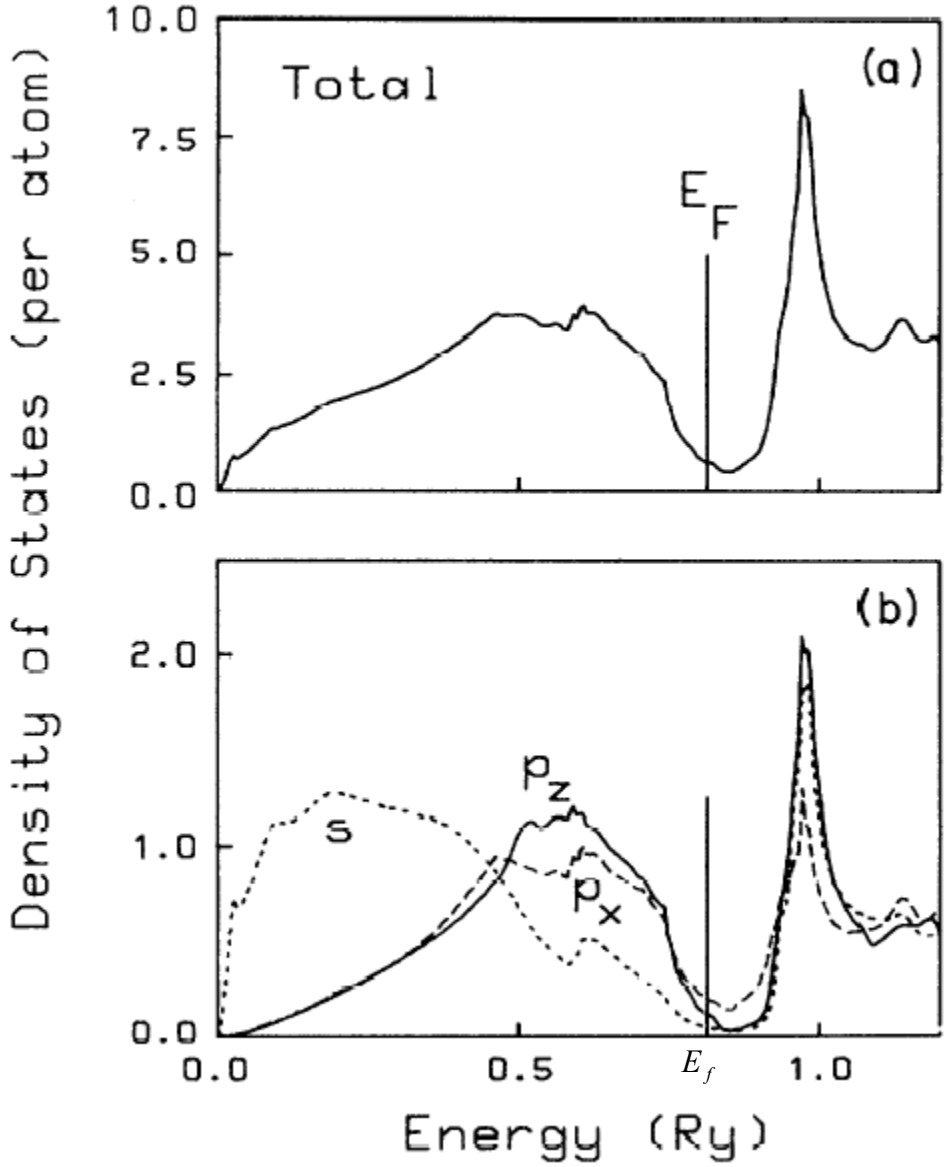

Figure 4.3 Total charge density distribution and different orbital contributions of bulk beryllium [2].

4.2 The Lattice Structure of the Be $(10\bar{1}0)$ Surface

The $(10\bar{1}0)$ surface as shown from Figure 4.1 is one of the six side planes for the hcp structures. This is an open surface in the sense that the in-plane spacing between two nearest neighbor atoms is larger than the interlayer spacing. There are two types of terminations for this surface, short termination with smaller d_{12} and long termination with longer d_{12}, respectively as shown by the side view of Figure 4.4. In the short termination plane, a surface atom has 8 nearest neighbors, and the plane distance between the surface and sub-surface is only half the distance compared to the long termination that only has 6 nearest neighbors.

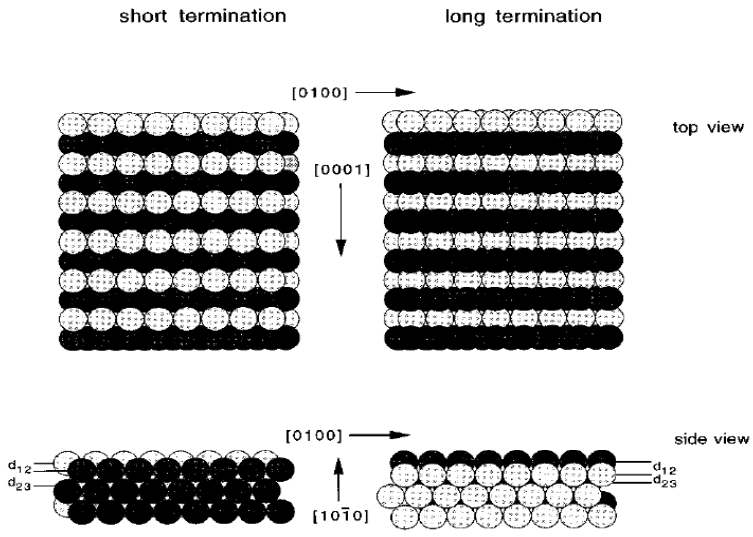

Figure 4.4 Lattice structure of $(10\bar{1}0)$ plane of hcp structure [3].

R. Stumpf et al [3] have used first-principle calculations to determine the surface lattice structure of $Be(10\bar{1}0)$. The result clearly shows the short termination is the more stable structure with a surface energy of 137 meV/Å^2, much smaller than that for long termination, 235 meV/Å^2. Furthermore, the calculation and LEED-IV measurement [3] both show that there is extraordinarily large contraction of the first layer, and subsequent layers have the oscillatory relaxation as shown in Table 4.1.

As mentioned before, Be has no *p*-core electrons, and the bonding between closed-shell beryllium atoms must be achieved by promoting 2*s* electrons into 2*p* states. The bonding energy, which compensates for this costly promotion, depends strongly on the coordination of the Be atoms. Hence, the physical property of Be surfaces is expected to differ strongly from the bulk, and the surface lattice behavior is certainly related to the electron structure on the surface.

Table 4.1 Experimental (LEED-IV) and theoretical result s(first-principle) of surface lattice relaxation in percent for the short termination on $Be(10\bar{1}0)$ [3].

	d_{12}	d_{23}	d_{34}	d_{45}
Experiment	−25 (−4/+3)	+5 (−3/+5)	−11 (−5/+8)	+2 (−2/+4)
Theory	−20	+4.4	−13	+3.8

4.3 The Electronic Structure of the Be$(10\bar{1}0)$ Surface

The electronic structure of the Be$(10\bar{1}0)$ surface has been found to be a lot different from that in the bulk. V. M. Silkin et al. [4], through a self-consistent pseudopotential calculation, found that the value of the density of states at the Fermi level for the Be$(10\bar{1}0)$ surface layer is almost five times higher than the bulk layers. Figure 4.5 shows the density of states from the first layer of the Be$(10\bar{1}0)$ surface. The hatched region shows the positive part of the difference between the density of states of the first layer on the surface and the center layer in the bulk. In comparison with Figure 4.3, the density of states from the first layer has much more contribution at the Fermi level than that from the bulk. It is therefore likely that the Be$(10\bar{1}0)$ surface is more free electron-like as opposed to the bulk which is a semimetal.

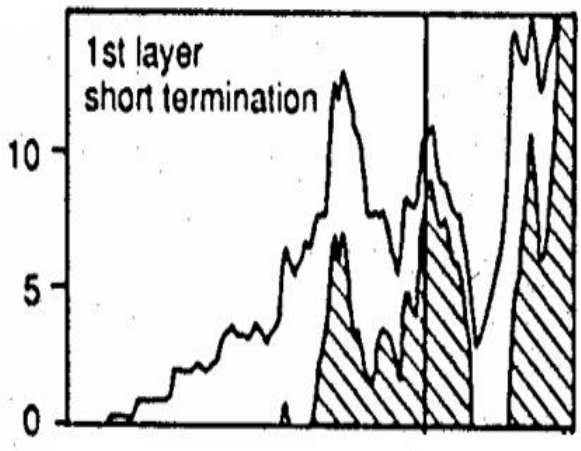

Figure 4.5 Charge density distribution contributed from first layer of Be$(10\bar{1}0)$ [4].

The reciprocal hcp structure and surface Brillouin zone of $(10\bar{1}0)$ surface is shown in Figure 4.6a,b. I measured dispersion of the surface states from $\bar{A}$ to $\bar{\Gamma}$. In Figure 4.6 b, the shaded area indicates the projection of the bulk Fermi surface, and the solid curves around $\bar{A}$ are the Fermi lines contributed from the surface state. It is obvious that from $\bar{A}$ to $\bar{\Gamma}$, there is a large bulk projected band gap across the Fermi level.

Figure 4.7 shows the energy distribution curves (EDC) as a function of emission angle along the $\overline{\Gamma A}$ direction. The bottom spectrum (0° emission angle) corresponds to normal emission ($\bar{\Gamma}$-point) and the increasing angle corresponds to increasing parallel momentum across the surface Brillouin zone, which has a large bulk projected band gap. 25.2° and 28° are the emission angles corresponding to $\bar{A}$ for the S1 and S2 surface states, respectively. The third peak, observed at higher binding energy, is a surface resonance (SR) that disperses in the bulk band continuum from $\bar{\Gamma}$ toward the bulk band edge at $\bar{A}$ [5]. Such a state, which degenerates with the bulk state, propagates deeply into the bulk, but nevertheless retains large amplitude close to the surface.

Figure 4.8 shows the corresponding surface state band dispersions of my measurement, and Figure 4.9 shows J-H Cho's calculations [6] of the surface state bands and bulk project bands on the Be$(10\bar{1}0)$ surface with my measured result superimposed. Measurements and calculations match each other very well. The size of the bulk projected inverted band gap at $\bar{A}$ is as large as 6 eV which accommodates two surface states, S1 at binding energy 0.37 eV and S2 at binding energy 2.62 eV. $\bar{A}$ at the $(10\bar{1}0)$

(a)

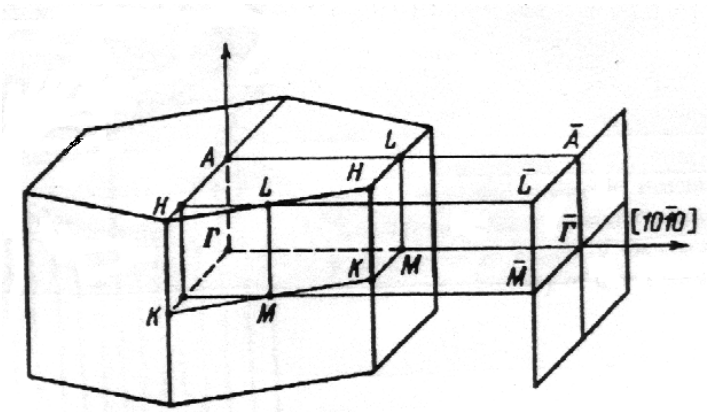

(b)

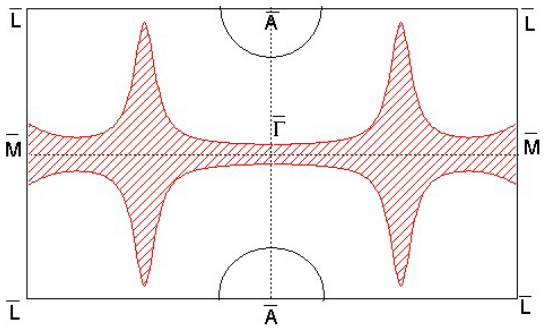

Figure 4.6 The reciprocal hcp structure and $(10\bar{1}0)$ surface Brillouin zone

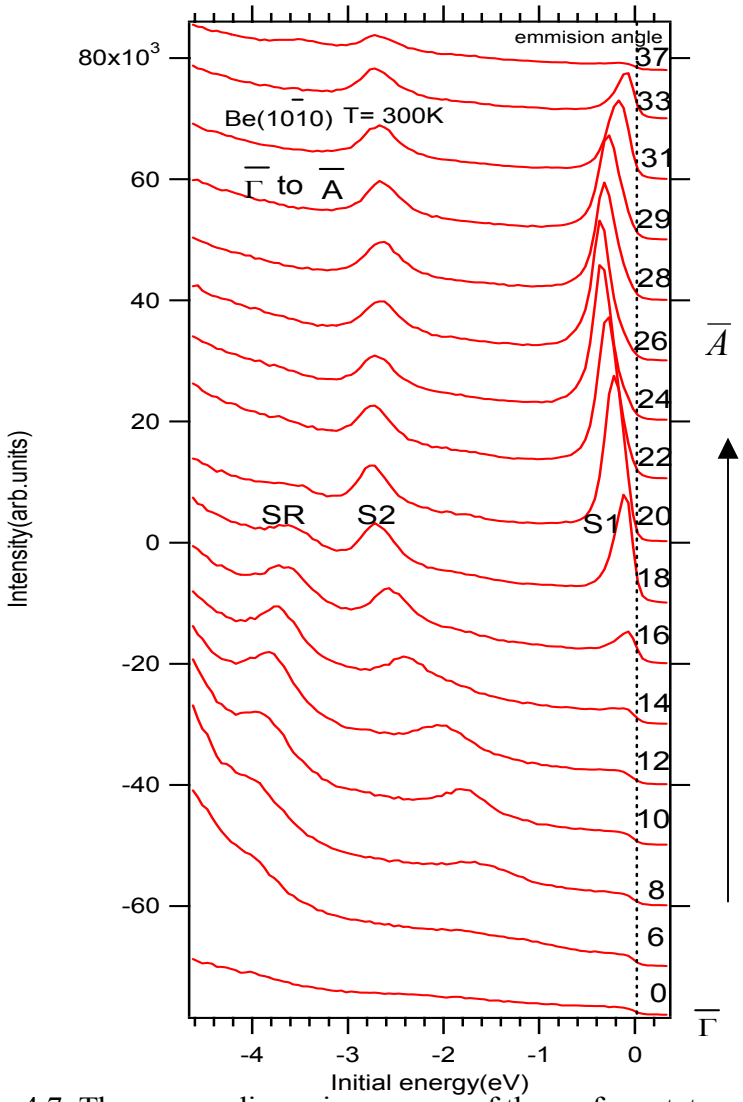

Figure 4.7 The energy dispersion curves of the surface states on Be$(10\bar{1}0)$ between $\bar{\Gamma}$ and $\bar{A}$. These curves were measured by the Scienta 200 energy analyzer with helium light of 21.2 eV

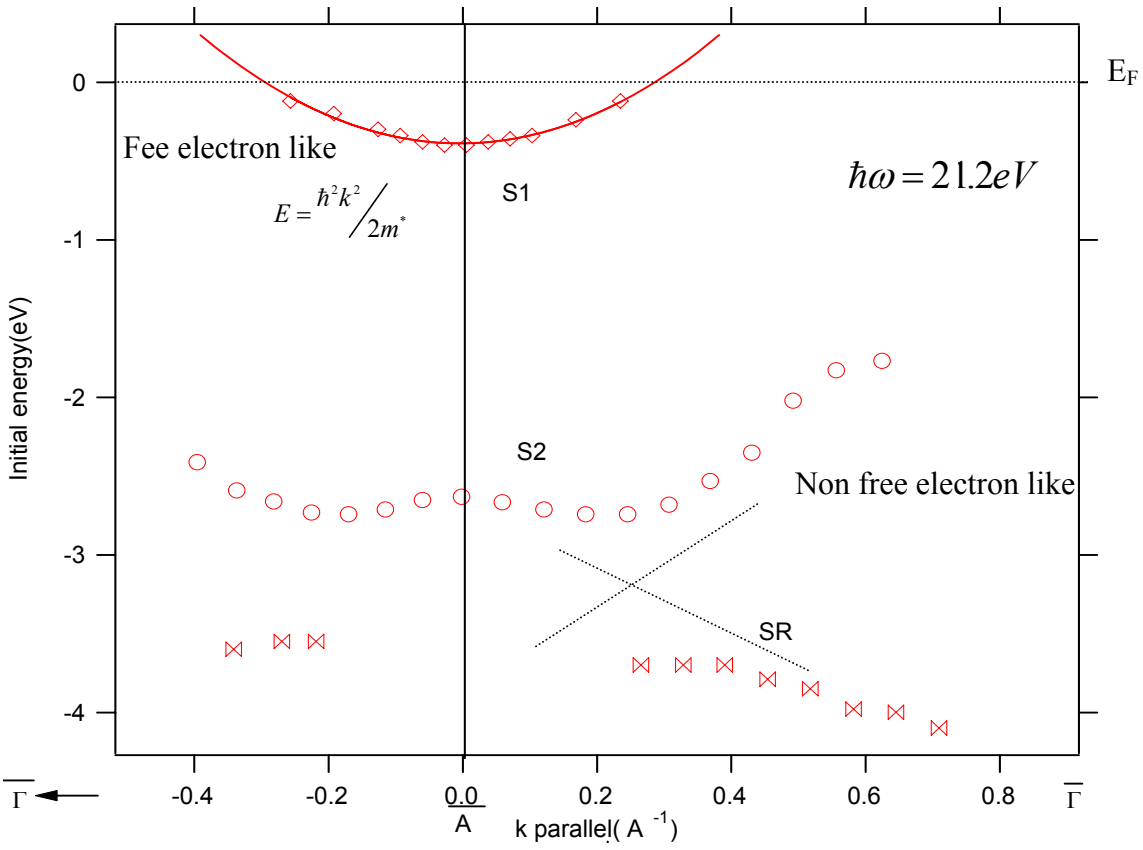

Figure 4.8 Measured surface state band dispersions (S1, S2 and SR) between $\overline{A}$ and $\overline{\Gamma}$

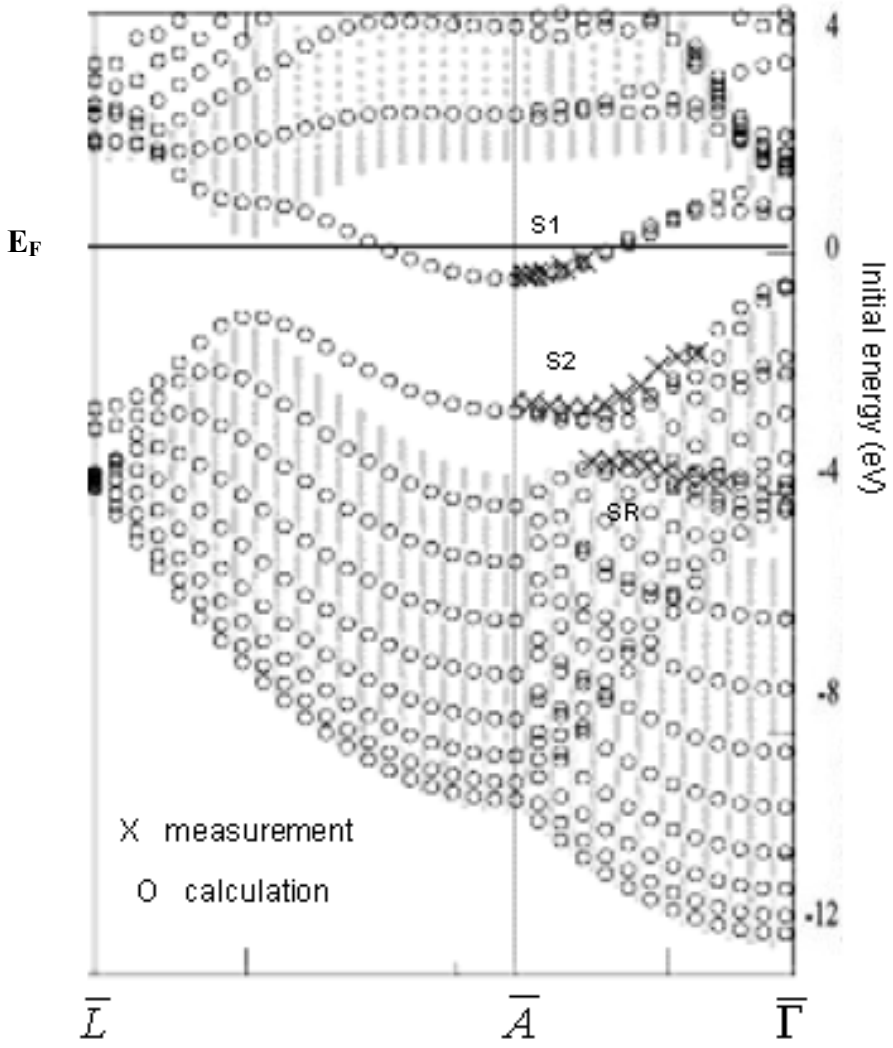

Figure 4.9 Calculated surface state band dispersions (circles) and bulk project bands (bars) on Be$(10\bar{1}0)$ [6] with measured data (crosses) imposed from Figure 4.8.

surface Brillouin zone is the projection of the bulk band from A to L, as shown in Figure 4.6a. The reason for the existence of two surface states is due to the double degeneracy at L point, which produces two gaps. Each of them has one surface state with different symmetry. The S1 surface state is much more localized on the surface than the S2 surface state in terms of the energy separations between the surface states and their corresponding bulk band edges. This has been illustrated in Figure 1.6a in Chapter 1. It is worth noting that the corresponding bulk band edge L is also the same edge for the bulk projected band gap of the size around 4 eV at $\overline{M}$ on Be(0001) [7]. As has been found by Bartynski et al. [8], there are also two surface states existing at binding energies 1.8 and 3.0 eV, respectively. The energy separation, 2.25 eV, between two surface states at $\overline{A}$ on Be$(10\overline{1}0)$ is a lot larger than that, 1.2 eV, at $\overline{M}$ on Be(0001). And, from Eq (1.27) in Section 1.3, the band gap size is proportional to the crystal potential U_1. By using the concept that the energy separation of the two different symmetry surface states at the same band gap is the indicator of crystal potential on the surface [9] (surface corrugation), the Be$(10\overline{1}0)$ surface seems to have more covalent-like property than Be(0001). When we further examine the dispersion of these two surface states S1and S2 from $\overline{A}$ to $\overline{\Gamma}$ in Figure 4.8, more interesting things show up. The S1 surface state band is simply parabolic shaped, as shown by the solid fitting curve, with free electron character of the effective mass $m^*/m_e = 0.53$ and $k_f = 0.30$ Å^{-1}. However, the S2 surface state band dispersion is non-free-electronic-like with its maximum binding energy at the k position around 0.2 Å^{-1} away from the zone boundary $\overline{A}$. And, it further disperses toward Fermi level when getting near $\overline{\Gamma}$. Figures 4.10 a,b are the 2D surface state band

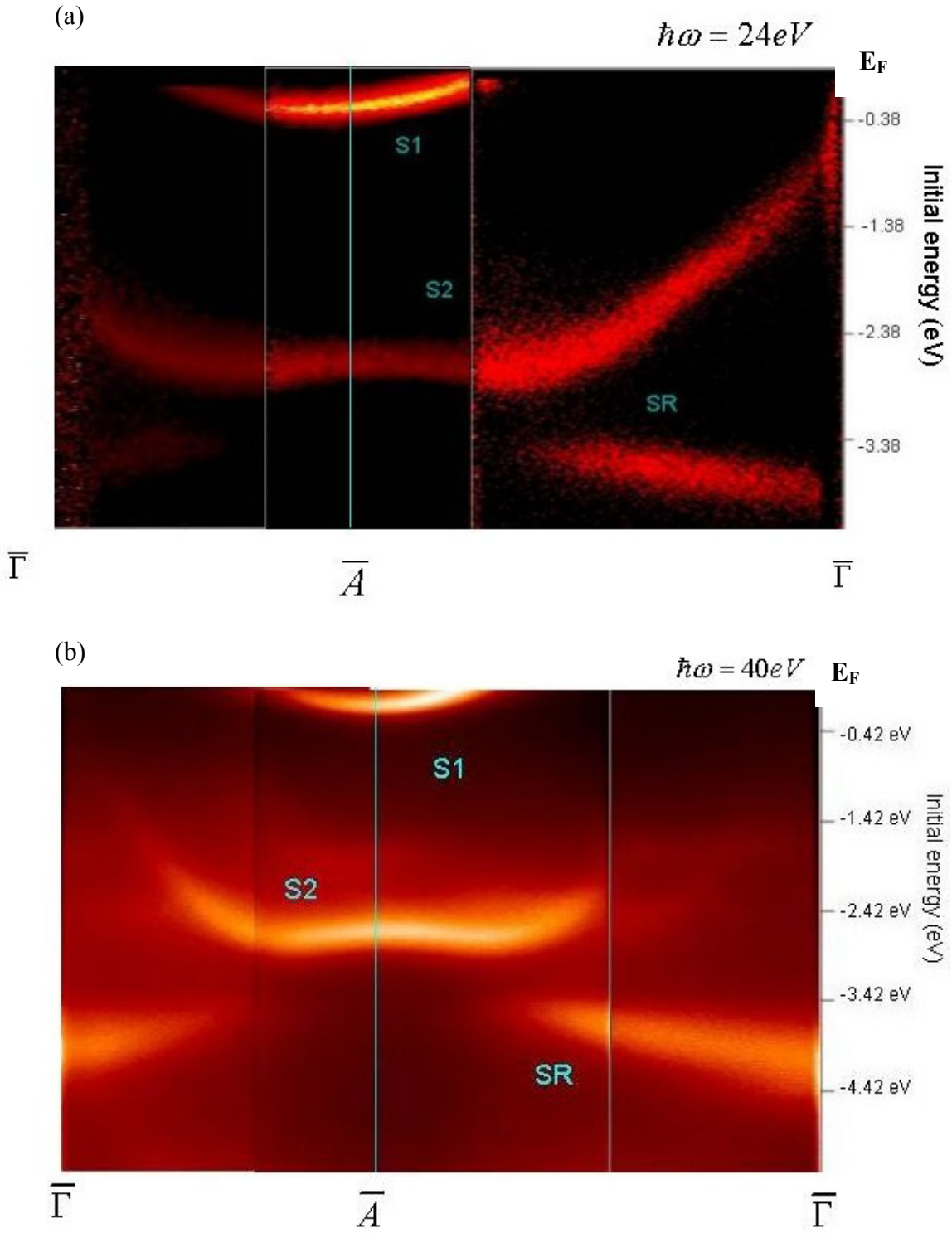

Figure 4.10 2D image of surface state band dispersions of $\mathrm{Be}(10\bar{1}0)$ taken at photon energy (a) $\hbar\omega = 24$ eV and (b) $\hbar\omega = 40$ eV

dispersions imaged directly from the high resolution Scienta 2002 energy analyzer at photon energies 24 and 40 eV, respectively. As has been explained in Chapter 3, the energy of the surface state is independent of $k_{\perp}$ and thus photon energy. Therefore, the consistency of the unique shape of S2 at different photon energies indicates an intrinsic surface property. There is a possibility that this shape is simply bent by the bulk band edge since the S2 surface state is so close to the bulk band edge. However, from J-H Cho's first-principle calculations, the dispersion of bulk band edges (the ends of the gray bars in Figure 4.9) from $\overline{A}$ to $\overline{\Gamma}$ is parabolic. Then, when we further examine the shape of the surface resonance (SR) band from $\overline{\Gamma}$ to $\overline{A}$, it actually turns non-free-electron-like when getting close to $\overline{A}$. When comparing both shapes of S2 and SR, the picture of hybridization between these two bands is clearly shown as indicated by the crossed dash lines in Figure 4.8.

4.4 The Temperature Dependence of the Surface States on Be $(10\bar{1}0)$

As I mentioned in the previous chapter, a part of the surface state hole lifetime is contributed to by the electron-phonon interaction, which has the most temperature dependence. Therefore, studying temperature dependence of the surface state is a direct way to extrapolate information from the electron-phonon interaction on the surface. In this study, I took the data of surface states (S1 and S2 at $\overline{A}$) within a large temperature regime from 45 to about 700 K. The reason why we wanted to take the data within such a large temperature regime is that Be has a very large Debye temperature (1400 K for the

bulk and 700 K for the surface). As shown in Chapter 2, the temperature dependence of the surface state peak width contributed to by the electron-phonon interaction can be represented by the general function (2.15) for the imaginary part of self-energy with an assumed model for the density of phonon states, Eliashberg coupling function $\alpha^2 F(\omega)$. As for the Debye model, Eq(2.20), when the temperature is much less than the Debye temperature, the relation between the peak width and temperature is nearly T^3, as shown by Eq (2.23). When the temperature is much larger than the Debye temperature, the relation between the two will turn to be linear, as shown by Eq (2.24). Due to the large Debye temperature, 700 K, of Be$(10\bar{1}0)$, the shape of the curve for the surface state peak width vs temperature in this large temperature regime (45 to 700 K) would neither be T^3 nor linear T shape. This fortunately brings us a good chance to try different models of phonon density of states for the Eliashberg coupling function $\alpha^2 F(\omega)$ in the general function, Eq (2.15), to fit the data. The model that gives the best fitting to the data would reveal the special character of the electron-phonon coupling for the corresponding surface state. In the general function fitting, Eq (2.15), the fitting parameters are ω_{MAX} representing the corresponding phonon energy for the assumed model in the system (i.e., ω_D for Debye energy, ω_E for Einstein energy), and ω representing the energy of the surface state hole. The resulting parameters are λ, which is included in $\alpha^2 F(\omega)$, representing electron-phonon coupling strength and a constant offset indicating the contribution from electron-electron interaction and surface defects.

The temperature dependence of the two surface states, S1 and S2, at $\bar{A}$ are shown in Figures 4.11a and 4.11b, respectively. After removing a Shirley background for each

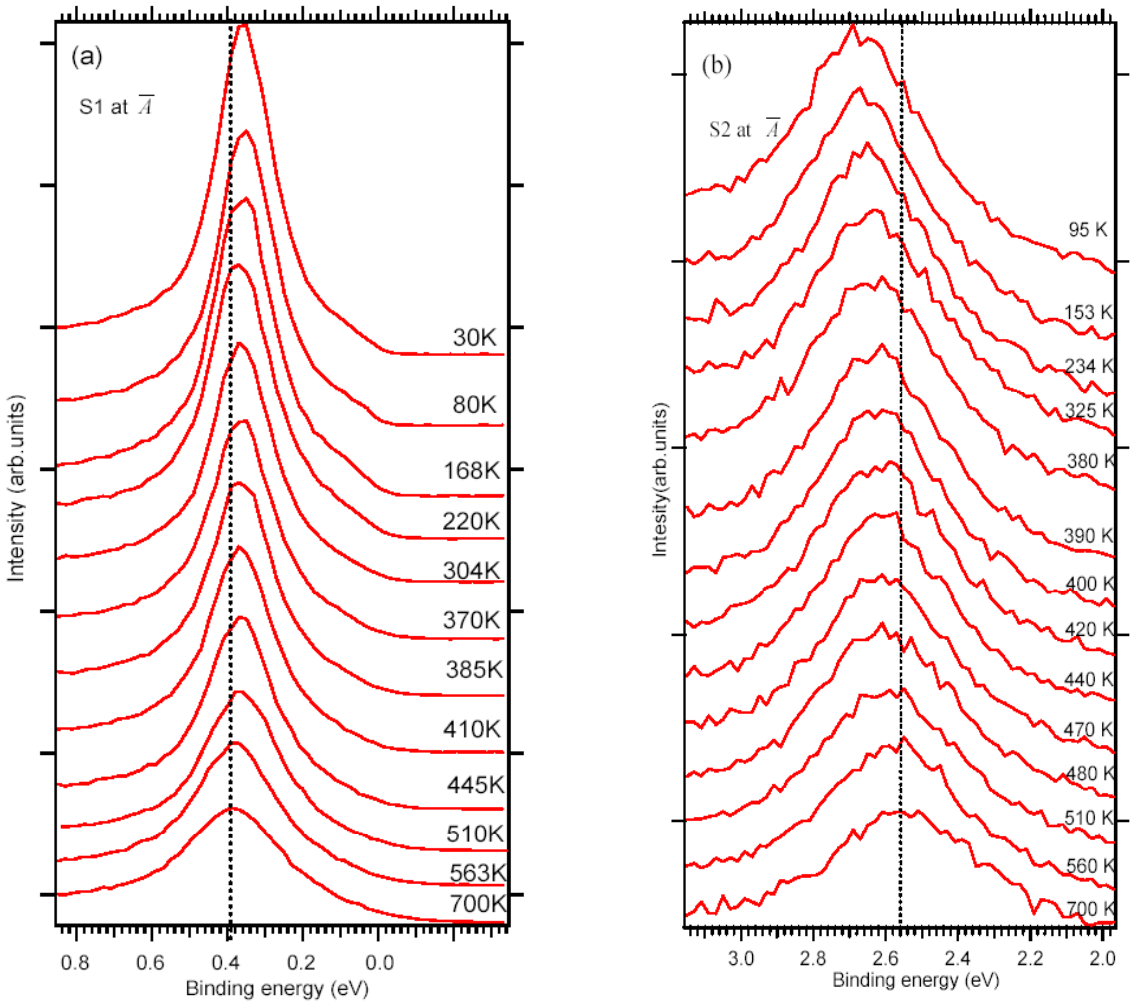

Figure 4.11 The temperature dependence of S1 and S2 surface states at $\overline{A}$. Dashed lines indicate the position at T = 700 K.

temperature EDC, the S1 peak was fitted with a Lorentzian line shape to extract both peak width and energies. Because S2 has an asymmetrical shape due to the bulk band edge at the higher binding energy (E_B) side and surface defect peak at the lower banding energy side, the peak was partially fit with a Lorentzian line shape (full low E_B side and partial high E_B side of the peak) after the Shirley background was removed. From this fitting procedure, one can immediately see that, as expected, the linewidth increases with temperature; however, quite surprisingly, the peak positions of S1 and S2 shift in opposite directions. I will discuss the temperature-dependent energy shifts of both surface states first before the exploring the temperature-dependent peak width for electron-phonon coupling.

4.4.1 Energy Shift

Figure 4.12 shows the initial energy (peak position) of both surface states as a function of temperature. As seen, the S1 and S2 states shift in opposite direction with the temperature at the rate of $(-0.61 \pm 0.3) \times 10^{-4}$ eV/K and $(1.71 \pm 0.8) \times 10^{-4}$ eV/K, respectively. Just for reference, due to thermal expansion, the bandwidth of typical bulk states decreases with temperature (i.e., $\Delta E_{bulk} / \Delta T > 0$), which is in agreement with what is observed for the S2 state only. As mentioned previously (Figure 4.9), this surface state lies energetically close to the bulk band edge at $\overline{A}$, and 40% of its charge distribution lies below the second atomic layer [4]. Similar to what has been observed with Schockley surface states on noble metals [10], the temperature-dependent initial state of S2 is dictated by bulk band properties. Table 4.2 lists the rate of temperature dependent initial

energy shift for the Shockley surface at zone center or zone boundary on different noble metal surfaces [10–12]. They all show that the surface state energies shift toward the Fermi level with increasing temperature. In contrast to S2, the S1 surface state is centered in a bulk-gap at $\overline{A}$, and its charge density is extremely localized in the first atomic layer. 70% of its charge is distributed on top of the surface [4]. Needless to say, the strange negative temperature dependence (i.e., $\Delta E_{S1}/\Delta T < 0$) of S1 is intimately tied to the unique static and dynamic properties of the Be(10$\overline{1}$0) surface. This phenomenon has been observed in other systems. For example, previous ARUPS studies on Cu(100)

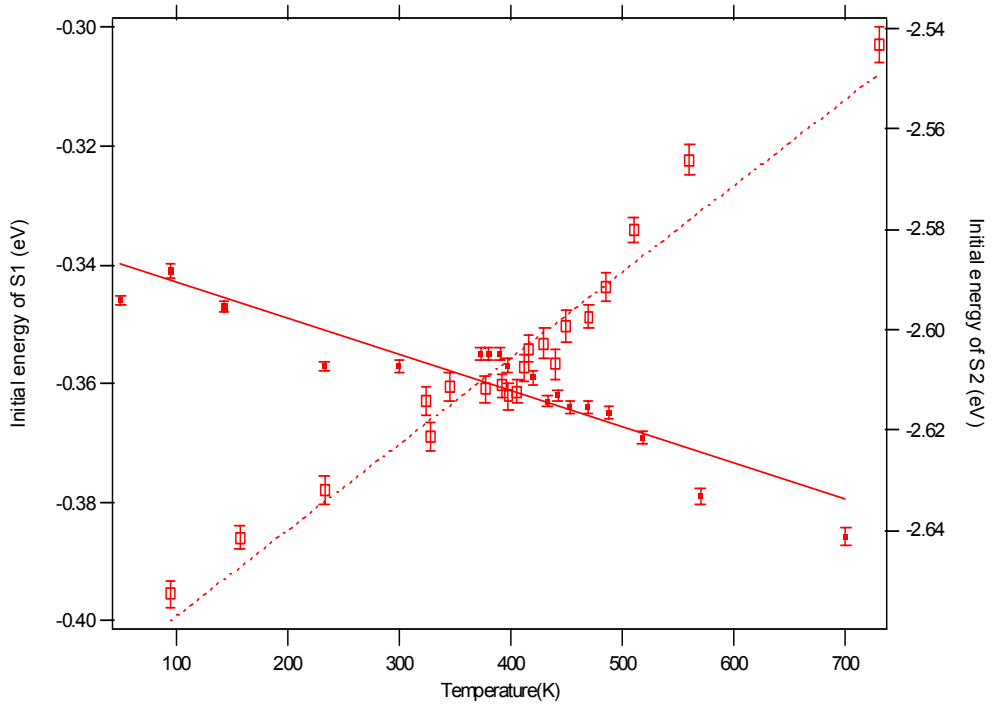

Figure 4.12 Temperature dependence of the initial state energy E_i of the surface state S1 (solid square, left axis) and S2 (open square, right axis) at $\overline{A}$. The solid and dashed lines are the linear fit; the resulting slopes are (-0.61 ± 0.3) × 10^{-4} for S1 and (1.71 ± 0.8) × 10^{-4} eV/K for S2, respectively. The error bar for each data point corresponds to statistical fitting uncertainties

Table 4.2 The temperature-dependent initial energy shift of the Shockley surface states on Cu(111) [10], Cu(110) [11], Ag(111) [10], and Ag(110) [12]

	The rate of surface state initial energy shift $\frac{\Delta E}{\Delta T}$ (eV/K)
Cu(111) $\overline{\Gamma}$	$(1.8\pm0.1)\times10^{-4}$
Cu(110) $\overline{Y}$	$(2.6\pm0.2)\times10^{-4}$
Ag(111) $\overline{\Gamma}$	$(1.7\pm0.1)\times10^{-4}$
Ag(110) $\overline{Y}$	$(1.7\pm0.1)\times10^{-4}$

have shown that a Tamm surface state centered at $\overline{M}$ shifts to lower binding energy when the temperature decreases ($\Delta E_{Cu(100)}/\Delta T$ = -0.6 × 10^{-4} eV /K) [13]. This Tamm state, with *d*-band symmetry, is known to be highly localized in the top surface layer. Although the S1 on Be(10$\overline{1}$0) and the Tamm surface state on Cu(100) are quite different overall, their 2D charge localization and corresponding temperature binding energy properties are similar.

The somewhat strange $\Delta E_{S1}/\Delta T$ observation on this surface must correlate with the corresponding static relaxation in the near surface atomic structure. Based on 10-layer slab calculations, O.Hjorstam et al. [14] compared the differences between the surface projected density of surface states of the relaxed and unrelaxed atomic configuration for Be(10$\overline{1}$0). Upon relaxation, they found that the large first-layer contraction affects the LDOS near E_F, specifically that states near E_F are pushed to higher binding energy (lower initial energy). Extending this argument, knowing the S1 surface state dominates the LDOS near E_F [4], the binding energy of S1 should correspondingly increase upon contraction. Based on a LEED-*IV* experimental study, Ismail et al. [15] showed that the first layer in Be(10$\overline{1}$0) indeed contracted with increasing temperature toward 500 K ($\Delta d_{12}/\Delta T < 0$). Our observations are in agreement with these prior theoretical and experimental results. The contraction, due to the *negative* thermal expansion and the negative thermal shift of S1 ($\Delta E_{S1}/\Delta T < 0$), is indeed correlated due to the large surface localization. In other words, the temperature-dependent shift of S1 is dictated by the localized nature of the surface charge and the observed thermal contraction of the surface. They certainly involve the dynamic interplay between the

anharmonic potential of the surface atomic lattice and corresponding surface energy dictated by the degree of 2D localization and corrugation of the surface. The detailed coupling between the surface state(s) charge density, the surface phonons, and the resulting thermal expansion is a challenging many-body problem and requires further theoretical input. I will do more discussions and propose some models in Chapter 6.

4.4.2 Peak Width

Figure 4.13a shows results for the S1 peak width versus temperature, along with a fitting curve of Eq.(2.15) employing a Debye phonon model. The solid line corresponds to a fit of the data between a temperature range of 303 and 700 K using a surface Debye energy 60 meV obtained from previous LEED-*IV* measurements.[3] The result of this fitting yields $\lambda_{S1} = 0.657 \pm 0.03$, which is equal, within the error, to the result $\lambda = 0.642 \pm 0.031$ obtained from a previous experimental study on $Be(10\bar{1}0)$ by T. Balasubramanian et al. [16] who just considered the data above room temperature. This agreement adds credibility to the results of both studies; an equivalent electron-phonon coupling parameter is determined upon fitting ARUPS data over equivalent temperature range and Debye energy. However, when the fitted line is extrapolated (dashed line) using Eqn. (2.15) to lower temperatures, specifically, 303 to 45 K, one can see that the overall fit to the extended data range is no longer adequate. Although previous studies have employed this methodology, in the present case, it is found that using a Debye phonon model is

insufficient to fit the data from this extended temperature range and indicates a breakdown in the approach.

This breakdown can be seen more clearly from the fit (dashed line) found in Figure 4.13b. As opposed to the limited temperature range fitting and subsequent extrapolation that were shown in Figure 4.13a, all the temperature range data were used this time in the fitting analysis. The dashed line corresponds to a fit, employing a Debye phonon model (ω_D = 60 meV) in Eqn. (2.15), yielding $\lambda_{S1} = 0.476 \pm 0.0243$. As seen by eye, the best-fitted line, as determined from a chi-squared analysis, does not adequately reproduce the high-temperature data. Figure 4.14 (open circles) shows the results of the goodness of fit (χ^2) using the Debye phonon model over the extended temperature range as a function of the Debye energy (ω_D). Here, we only consider the range of Debye energy between 60 and 100 meV where the resulting peak width offset, which represents the temperature-independent contribution from *e*-*e* interaction and *e*-defect scattering, are physically reasonable (30 to 100 meV)[17]. From this figure, it is evident that the overall fit to the ARUPS data is optimized when the Debye energy increases and approaches 100 meV. However, even when fitting parameters are optimized, this approach does not adequately, as judged by the χ^2 reliability factor, reproduce the temperature-dependent linewidth data. This leads to the conclusion that a Debye phonon model is not appropriate in determining the electron-phonon coupling parameter of the S1 surface state but , nevertheless, we still get a hint from this analysis that the electron-phonon coupling for S1 surface state could favor the higher phonon frequency more. Although this approach has been widely used for other systems, the failure of the Debye

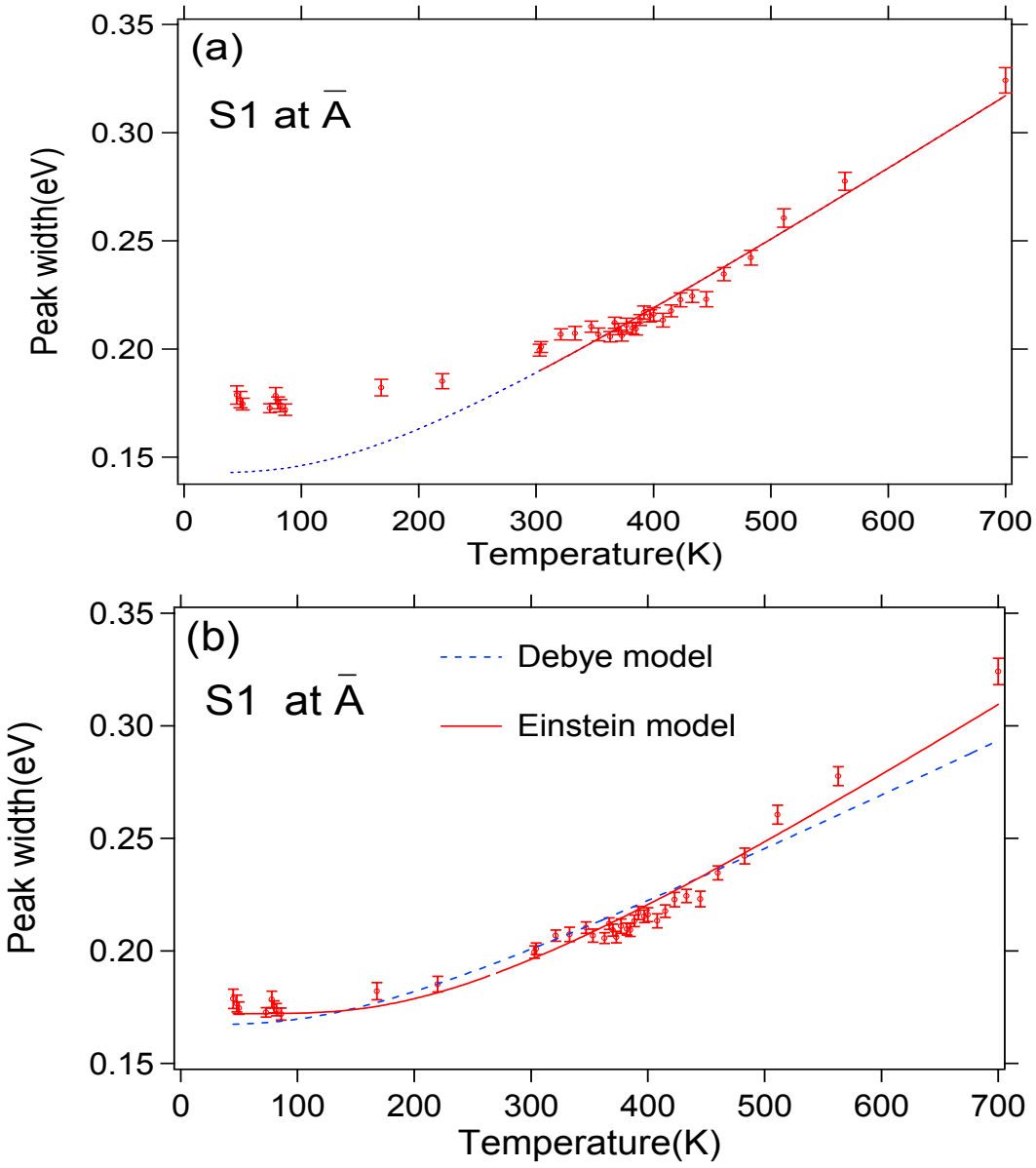

Fig 4.13 Data of surface state S1 peak width at $\bar{A}$ versus temperature. (a) The solid line is the fitting only for the higher temperature range, 303 to 700 K , through the general function with the Debye model at Debye energy 60meV. The dashed curve is the extension of this fitting to the lower temperature range. The resulting λ is 0.657 ± 0.03. (b).The dotted line represents the fitting of the data for the whole temperature range, 45 to 700 K, by Debye model at Debye energy 60 meV. The resulting λ is 0.476 ± 0.024. The solid curve represents the fitting of the data for the whole temperature range by the Einstein model at Einstein phonon energy 63.7 meV. The resulting λ is 0.646 ± 0.0209. The error bar for each data point is according to statistical fitting uncertainties

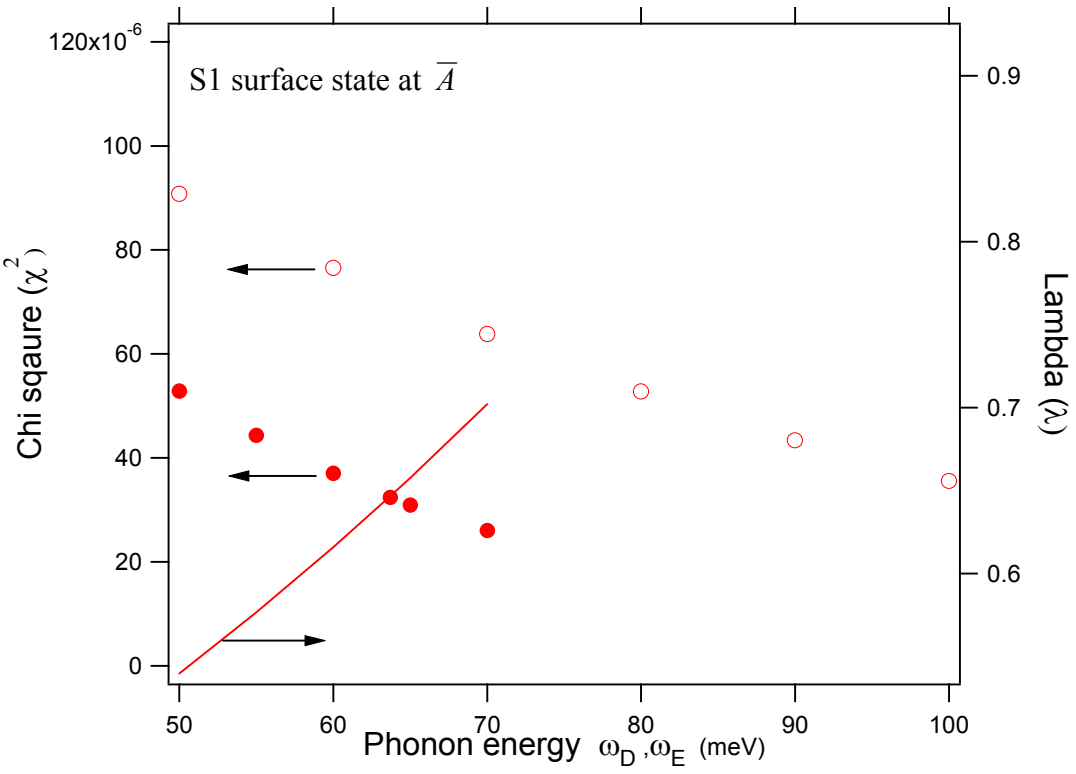

Figure 4.14 The detailed analysis of the fitting goodness with two different phonon models at different phonon energies. Left axis: Chi Square versus Debye energy(Einstein energy) for the fitting of the whole temperature range by the Debye model as indicated with open circles (Einstein model with filled circles). Right axis: λ versus Einstein energy for Einstein model as indicated with solid curve

model as applied to the S1 surface state is not unexpected, due to the strong 2D charge localization of this state in the top layer. In the Debye phonon model, the phonon density of states is taken to be a smooth, continuous function up to cutoff energy (ω_D). The model is independent of the detailed shape and dimensionality of the phonon spectrum; basically, the electron-phonon interaction is smoothed out in energy and, more importantly, momentum space. However in the present case, because of the high 2D localization of this surface state, there may be a limited number of phonon modes at the surface that dominate the electron-phonon coupling mechanism. In other words, a phonon density of states more akin to an Einstein phonon model, instead of a Debye phonon model, is perhaps a more appropriate approach for properly describing the electron-phonon interaction in the present case. If this type of approach is assumed, a different functional form of the Eliashberg coupling coupling function in Eqn.(2.15) must be used. In the case of an Einstein phonon model, the Eliashberg coupling function takes the form,

$$\alpha^2 F(\omega) = \frac{\lambda \omega_E}{2} \delta(\omega - \omega_E) \tag{4.1}$$

Assuming this model can be used, Figure 4.14 (solid circles) shows the results of the goodness of fit (χ^2) using the Einstein phonon model over the extended temperature range as a function of the frequency parameter, ω_E. As seen, throughout a wide range of ω_E (50 to 70 meV) [17], this model yields overall better fits to the extended temperature range data than the Debye phonon model described above (i.e., $\chi^2(\omega)$ is a factor of two lower than the corresponding fit from Debye model). This indicates that an Einstein phonon model methodology indeed better describes the S1 electron-phonon interaction.

Because there is not a distinct minimum in χ^2 (Figure 4.14), a proper choice of ω_E, which consequently yields a value of λ, must be made with additional input. From bulk properties and prior electron-phonon studies of Be, one would expect that if an Einstein phonon model, which models the density of states with a delta function at one frequency, were invoked, the physically reasonable range of ω_E should be between 50–80 meV [18]. The justification for using an Einstein model in the present case is that the known high 2D localization of this surface state and thus the electron-phonon coupling mechanism are limited to phonon modes localized to the surface. In accordance, Michele et al. [19] have calculated the theoretical surface phonons on Be($10\bar{1}0$) using a 104-layer slab model, as shown in Figure 4.15. Results of this study indicate that at the $\bar{A}$ point of the surface Brillouin zone, the density of states are dominated by two acoustic modes at 26.4 and 32.3 meV, polarized mainly perpendicular to the surface and, more importantly, one surface optical mode at 64 meV polarized along the surface. The latter mode has a shear-horizontal character and 50% of the total displacement localized in the first two layers [20], dispersing weakly through the surface Brillouin zone. If we assume that this surface localized optical phonon mode dominates the electron-phonon interaction, fitting the S1 data over the extended temperature range yields a value of $\lambda_{S1} = 0.646 \pm 0.021$. As seen in Figure 4.13b (solid line), this goodness of fit is much better than the Debye mode.

If the fitting methods applied to S1 are now applied to the S2 state, the results indicate a fundamental difference in the physics associated with the coupling of the surface states to different phonon modes. Specifically, the phonon model used to

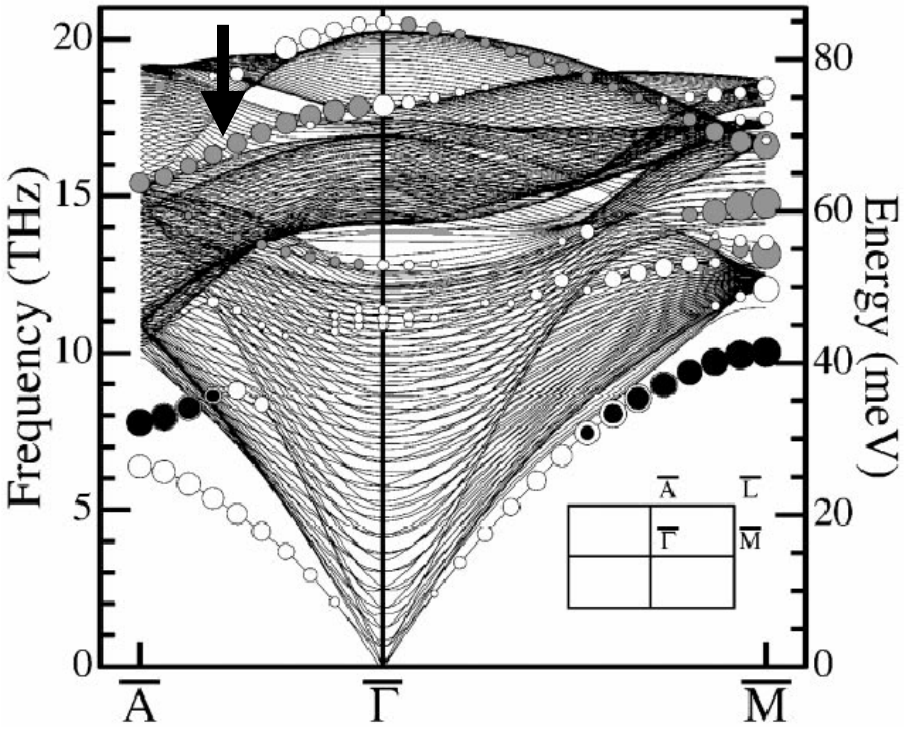

Figure 4.15 The calculated surface phonon band on the relaxed surface of $Be(10\bar{1}0)$. The arrow indicates the optical phonon dispersion around 64 meV [19].

characterize the interaction is different between S1 and S2. Figure 4.16a shows the analyzed temperature-dependent peak width data (Fig. 4.11b) of the S2 surface state. Compared to the S1 state, there is more scatter in the data, primarily due to the lower signal-to-noise and the intrinsic asymmetric line shape, alluded to above. Figure 4.16b shows, similar to Figure 4.14, the goodness-of-fit (χ^2) to the data (Figure. 4.19a) for a broad range of phonon energies (ω_E and ω_D) for both Einstein and Debye phonon models. In the case of S2, the Debye phonon model results in a better reliability factor for all phonon parameter frequencies. Moreover, in spite of the somewhat large scatter in the data, using a Debye model yields a broad minimum in χ^2 near ω_D = 60 meV, a value equivalent to that extracted from a LEED-*IV* study [3]. Using this parameter, the resulting electron-phonon coupling is determined to be $\lambda = 0.49112 \pm 0.04$ and is shown in Figure 4.16a (solid line). For comparison, the χ^2 value of the fit employing an Einstein model (ω_E = 64 meV), as used in the analysis of the S1 state, is larger and does not adequately fit the ARUPS temperature-dependent data. The offsets (*e*-*e* and *e*-defect contribution) from the fitting of the S2 peak width versus temperature via both Debye and Einstein model are, in general, large (~ 300 meV) compared to the S1 data. Because the S2 state is less localized at the surface and penetrates into the bulk states, its extra broadening is attributed to consequent scattering into bulk states [21].

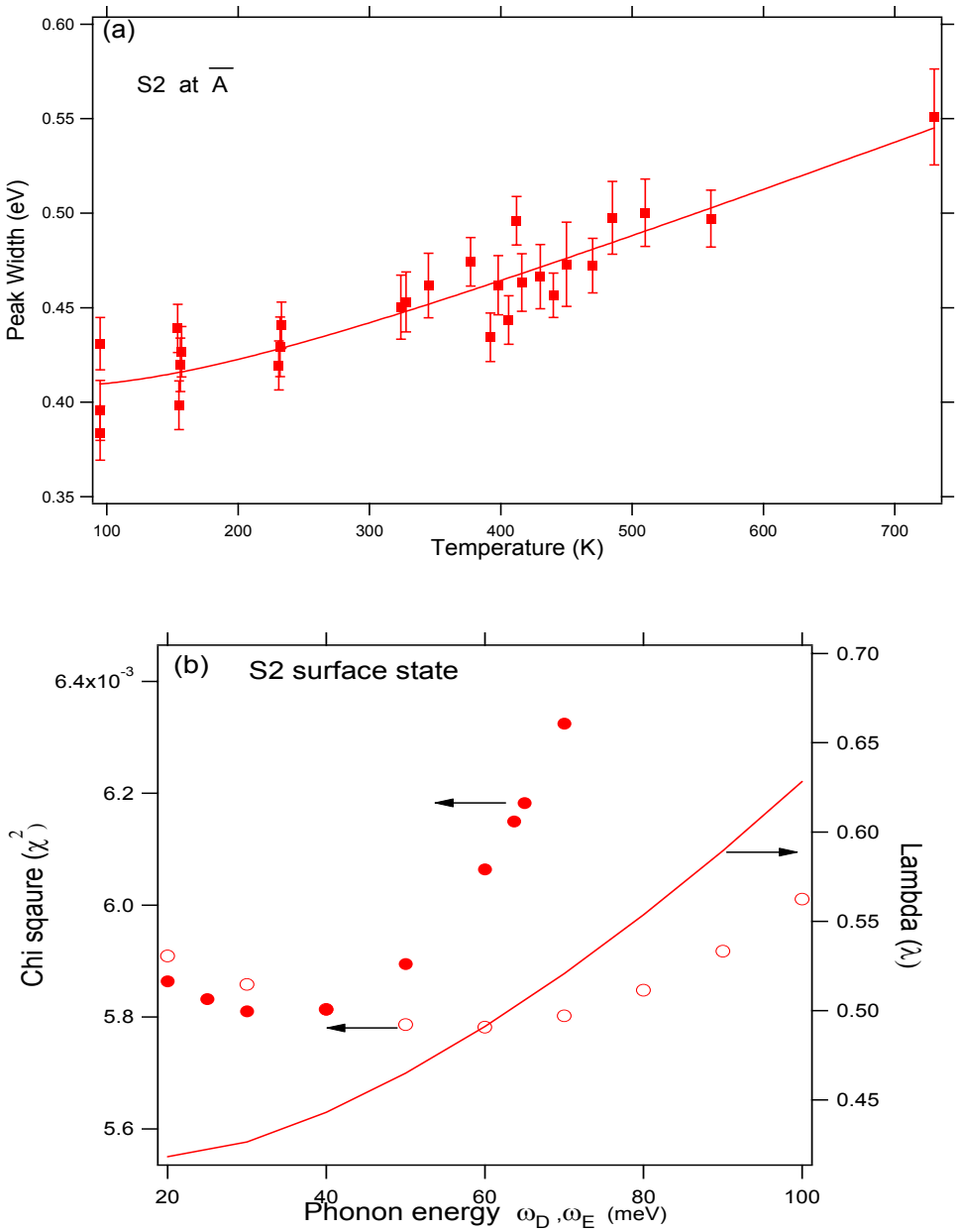

Fig 4.16 The data of surface state S2 peak width at $\overline{A}$ versus temperature . (a)The solid line is the fitting for the whole temperature range, 95 to 730K, through the general function with the Debye model at Debye energy 60 meV. The resulting λ is 0.491 ± 0.04. The error bar for each data point is according to statistical fitting uncertainties. (b)Left axis: Chi Square versus Debye energy (Einstein energy) for the fitting of the whole temperature range by the Debye model as indicated with open circles (Einstein model with filled circles). Right axis: λ versus Debye energy for Debye model as indicated with solid curve.

4.5 Surface State Band Distortion via Coupling with Optical Phonon Mode

In Section 4.4, I investigated in detail the temperature dependence of the imaginary part of self-energy due to electron phonon interaction. The conclusion is that the S1 surface state, due to its high localization on the surface, has the most dominant electron-phonon coupling with localized optical surface phonon dispersing around 64 meV. And, this localized surface state-localized surface phonon interaction is the cause of large electron-phonon coupling strength on $\mathrm{Be}(10\bar{1}0)$, three times larger than the bulk value. Before going further to explore the physics behind it, there is a question in my mind " Does the real part of self-energy say the same thing as the imaginary part?" They, by all means, have to be consistent. As I mentioned in Chapter 2, the real part of self-energy physically represents the ionic screening effect which causes an obvious change of the effect mass and velocity of the quasi particles with the energies close to the Fermi level. From the electron band structure, we would see an anomalous dispersion in the region around the Fermi level. In the photoemission spectra, the unique line shape of the surface state peak in that region would be correspondingly observed. Figure 4.17a [22] and Figure 4.17b [23] show the calculated relation of the real part and the imaginary part self-energy versus the qausiparticle energy for the Einstein model and Debye model, respectively. The maximum Debye phonon energy and Einstein phonon energy play the same role in both models as a boundary separating two parts. The region between the Debye (Einstein) energy and Fermi level is the place where the real part of self-energy has the maximum value, but the region above the Debye (Einstein) energy is where the

imaginary part of self-energy dominates. Therefore it is extremely interesting to see how the line shape of the surface state peak changes in the region between Debye (Einstein) phonon energy and Fermi level because of the large contribution from the real part of self-energy Eq (2.14) to the spectra function, Eq (2.2), in Chapter 2.

Figure 4.18 and 4.19 show the dispersions of the surface states near Fermi level on Be(0001) and Be$(10\bar{1}0)$ at T = 20 and 30K, respectively. It has been shown in Chapter 2 that the real part of electron-phonon self-energy is at maximum at 0 K. As is easily seen, the line shape of the surface state on Be(0001) is obliviously different from that of the S1 surface state on Be$(10\bar{1}0)$. Actually, the line shape of the surface state on Be(0001) can be approximated well by the spectra function with Debye model for the

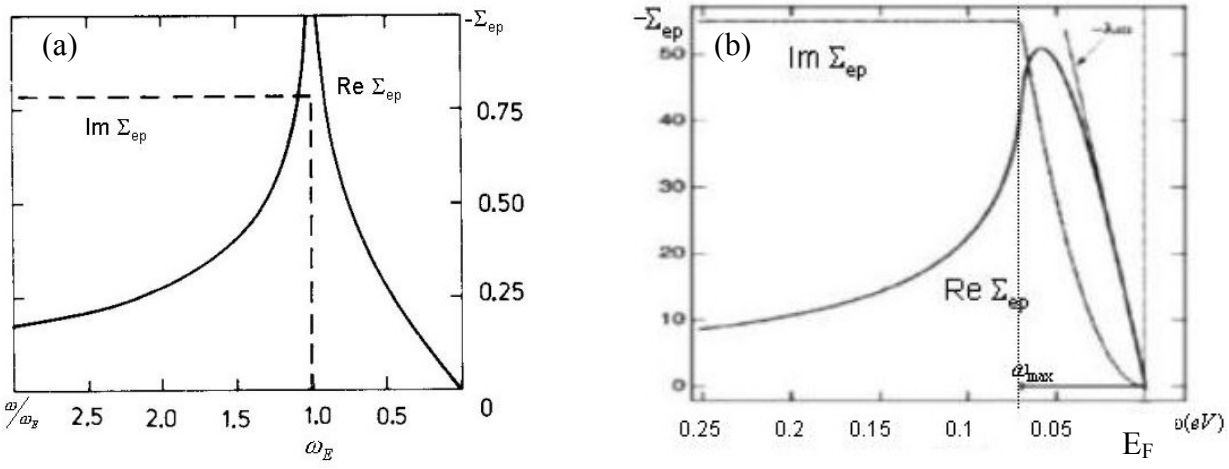

Figure 4.17 The calculated imaginary and real parts of electron phonon coupling self-energy at $T = 0$ for different phonon models (a) Einstein model [22] and (b) Debye model [23]

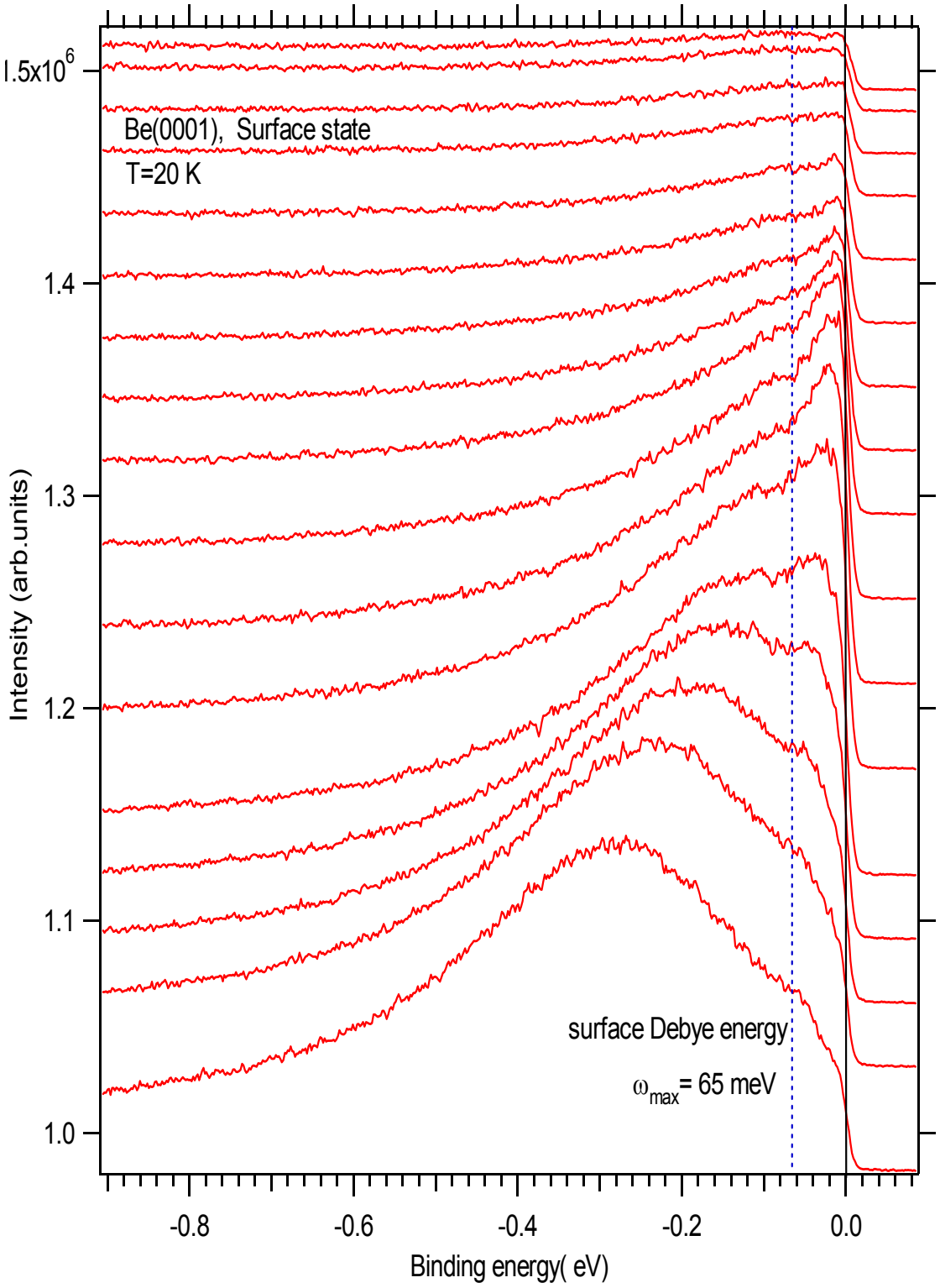

Figure 4.18 The surface state dispersion near Fermi level in the direction from $\overline{\Gamma}$ to $\overline{M}$ on Be(0001). The dashed line is the position of maximum surface phonon energy

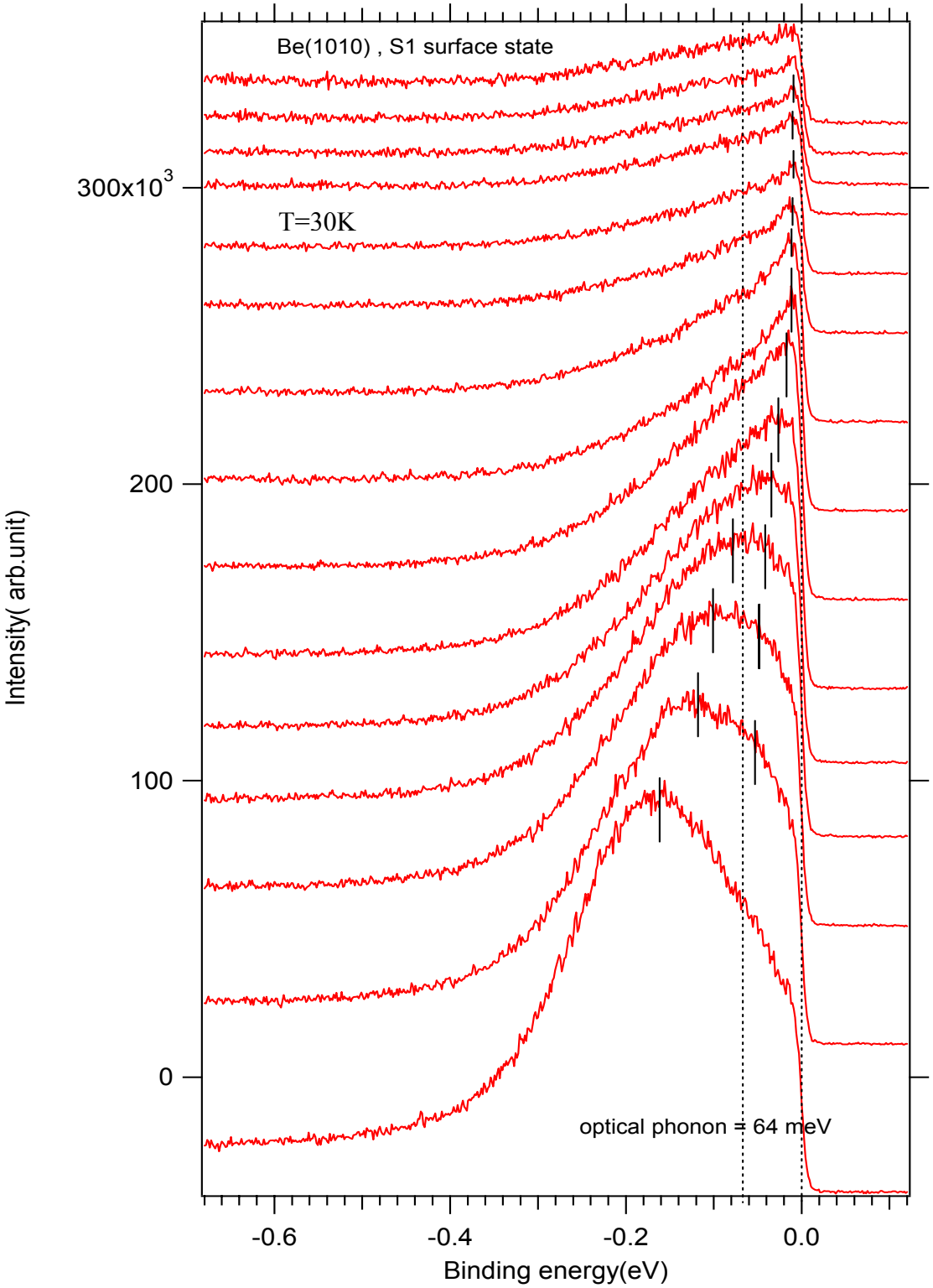

Figure 4.19 The surface state dispersion near Fermi level in the direction from $\overline{A}$ to $\overline{\Gamma}$ on Be$(10\overline{1}0)$. The dashed line is the position of the optical phonon energy

the self-energy by M. Hengsberger et al. [23] and S. Lashell et al. [24]. As for $\mathrm{Be}(10\bar{1}0)$, the line shape of the S1 surface state can be separated into two parts by the single dashed line at around 64 meV. This is similar to the H(D)/W(110) system where the single adsorbate optical phonon dominates the *e-p* coupling of the surface state [25]. Figures 4.20 a,b show that the dashed line separates surface state line shape at optical phonon energy 161 meV for H/W(110) and at 117 meV for D/W(110). The reason why the line shape of spectra can be divided into two branches at the dominant optical phonon energy is easily shown through the spectra function for the Einstein model [29].

When $|\omega| < \omega_E$

$$A(\omega,k) = \delta(\omega - \varepsilon^0(k) + \frac{\lambda\omega_E}{2}\ln\left|\frac{\omega+\omega_E}{\omega-\omega_E}\right|) \tag{4.2}$$

when $|\omega| > \omega_E$

$$A(\omega,k) = \frac{\lambda\omega_E}{2}\left\{\left[\omega - \varepsilon^0(k) + \frac{\lambda\omega_E}{2}\ln\left|\frac{\omega+\omega_E}{\omega-\omega_E}\right|\right]^2 + \left[\frac{\lambda\pi\omega_E}{2}\right]^2\right\}^{-1} \tag{4.3}$$

The Einstein phonon energy ω_E serves as the boundary between two different functions. Figure 4.21a shows ANexample of the spectra function with the free single particle energy at 0.75 ω_E [26]. Above the Einstein phonon energy, it is a broad shape function, which, at higher energy, is a broad Lorenzian quasiparticle peak mainly contributed by the scattering effect of electron-phonon coupling. However, below the Einstein energy, it is a delta function which is the quasiparticle peak mainly contributed by the strong ionic screening effect. Figure 4.21b shows that, below the Einstein energy, the delta function-

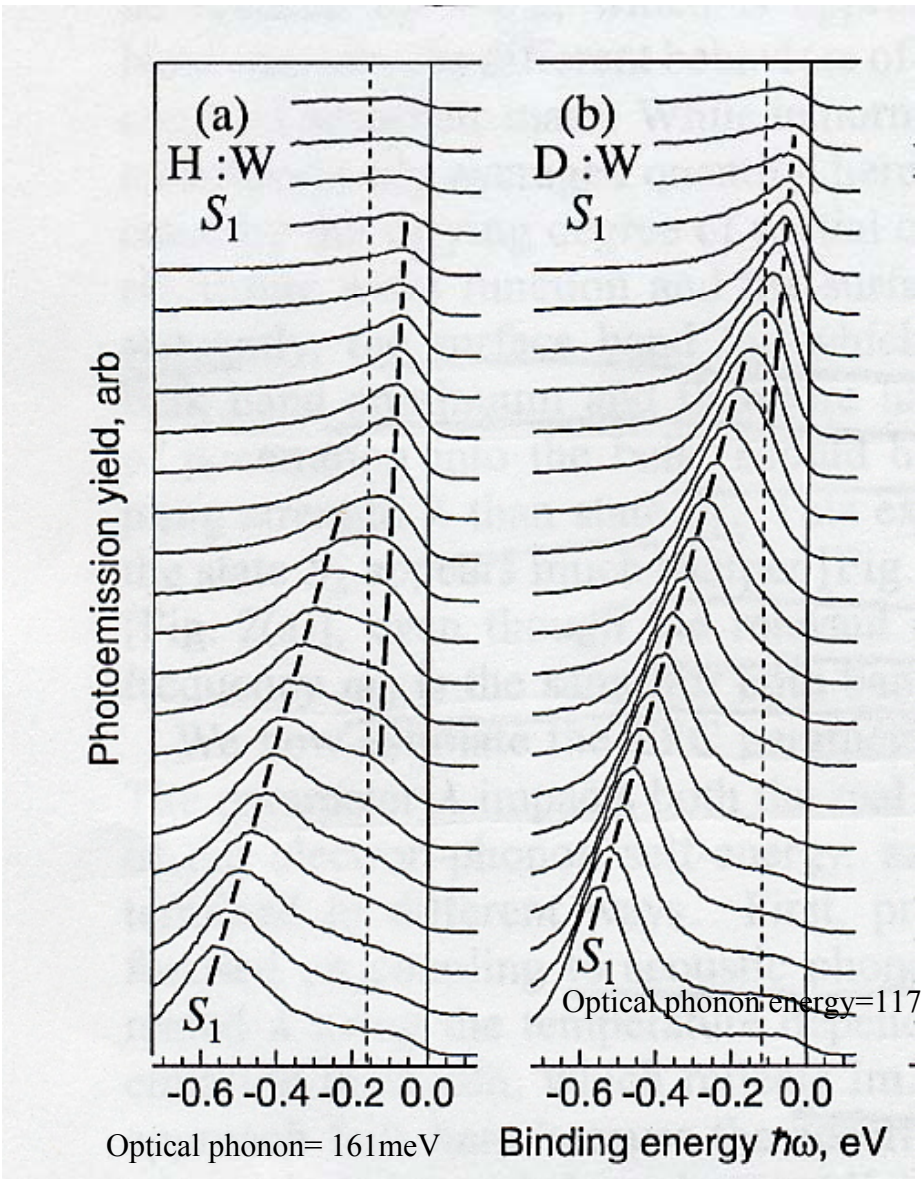

Figure 4.20 The surface state dispersions of (a) H/W(110) and (b) D/W(110). The dashed line position represents the optical phonon energies of the adsorbates, which clearly separates the splits of the band due to the strong e-p coupling [25].

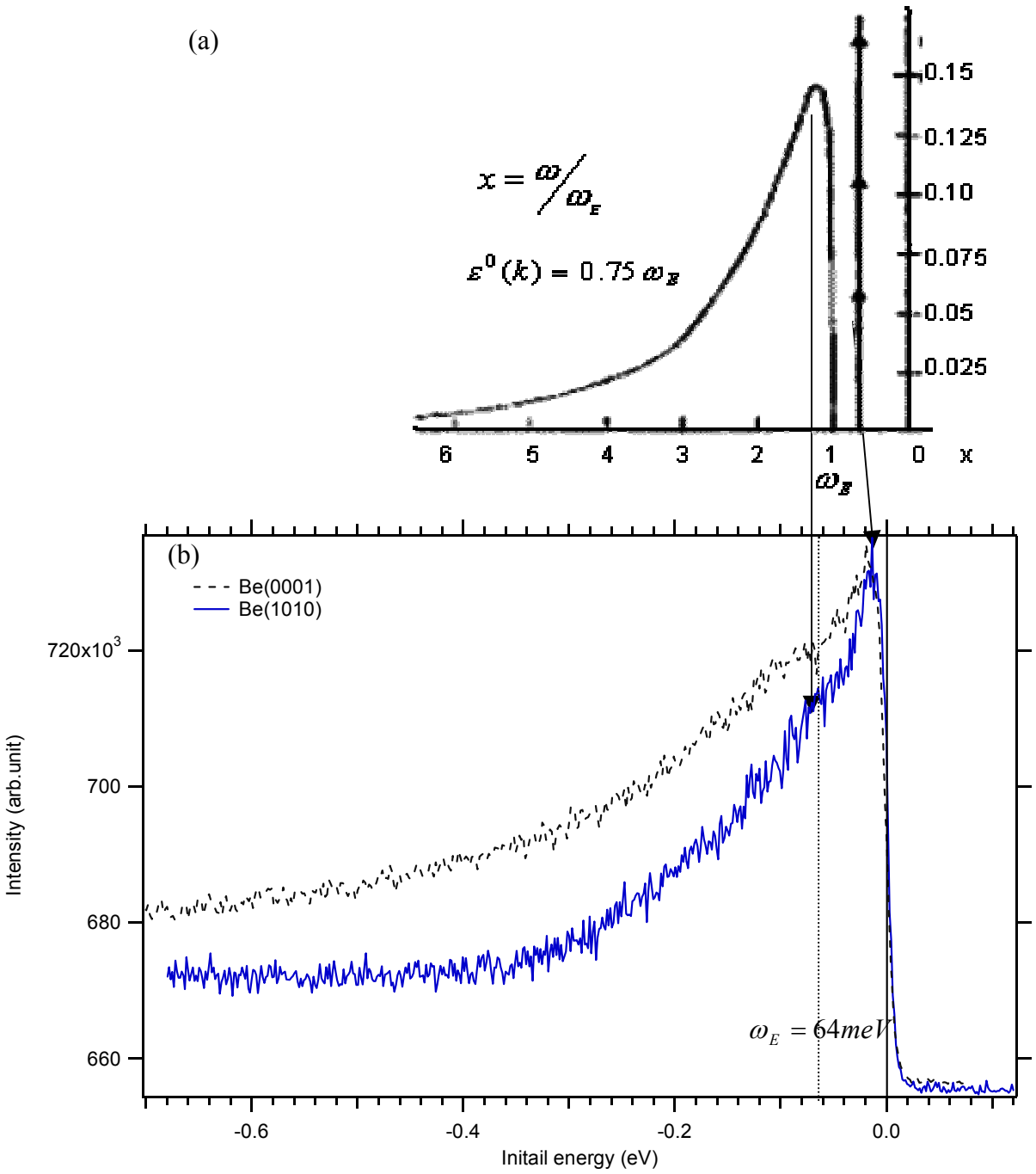

Figure 4.21 Illustration of resemblance of the line shapes between the spectra from ideal calculation results for the Einstein model and that from the Be$(10\bar{1}0)$ surface state. (a) The calculated spectra function of the Einstein model [26] (b) The comparison of the line shape of the surface states at the similar energy between Be$(10\bar{1}0)$ and Be(0001).

like quasiparticle peak of Be$(10\bar{1}0)$ is much narrower than the quasiparticle peak of Be(0001) below the Debye energy. This is consistent with the previous calculation results for the spectra function of the Einstein and Debye models, respectively [26]. One thing needed to note is that the Einstein model is an extremely limited approximation model as opposed to Debye model, which is general. It is difficult to fit the line shape of the surface state on Be$(10\bar{1}0)$ in Figure 4.19 by the spectra function (4.2) and (4.3) of the Einstein model because the optical phonon around 64 meV is dominant but not the only one participating in the *e-p* coupling, and there are also other factors such as defect scattering and the energy dependence of phonon coupling strength to consider [25]. But, at least, Figure 4.19 shows obviously the major character of the line shape for the Einstein model that all the spectra at different energies can be divided by the same single line at the optical phonon energy around 64 meV. This is obviously not the case for surface state spectra of Be(0001) in Figure 4.18. Instead of using the Einstein model spectra function to fit, I tried to use two Lorentzian peaks to fit the line shape of the surface state to determine the peak maximum positions. Figure 4.22a shows the band dispersion of the S1 surface state on Be$(10\bar{1}0)$ from the peak maximum positions in Figure 4.19. Due to the strong screening interaction between optical phonon and surface state hole, the slope of the dispersion below the optical phonon is different from that of the free particle energy dispersion above the optical phonon energy.

From this, we can easily extract the electron-phonon coupling constant from the relation

$$(\lambda + 1) = \frac{v_2(k)}{v_1(k)} = \frac{d\varepsilon_2 / dk_2}{d\varepsilon_1 / dk_1} = \frac{slope\ \ 2}{slope\ \ 1} = 1.901\ , \quad \lambda \approx 0.9 \tag{4.4}$$

v_1 and v_1 represents the velocity of the excitation as determined by the two band dispersion with different slope below and above the optical phonon energy. The resulting value $\lambda = 0.9$ is larger than the value, $\lambda = 0.648$, obtained from the temperature dependent width at the bottom of the band at $\bar{A}$. It is understandable because the surface state close to the Fermi level is certainly more localized on the surface, and localization is the key to the enhanced electron-phonon coupling. The 2D image of the S1 surface state band of $\mathrm{Be}(10\bar{1}0)$, Figure 4.22b, shows the band has a wider tail after crossing optical phonon energy toward the Fermi level as opposed to the typical " kink shape " for the distorted band dispersion which is usually observed from the electron-phonon coupling of the Debye model. Figure 4.23b shows the 2D image of kink shape of the surface state band dispersion near Fermi level on Be(0001). However, if we examine Figure 4.22b more closely, the side lines at the left clearly shows two different slopes separated right at the optical phonon energy. I put the data points, taken from the maximum peaks of the spectra, into the 2D band image to indicate that this band image is still essentially kink.

Actually the wide tail of the S1 band of $\mathrm{Be}(10\bar{1}0)$ around the optical phonon energy might have to do with the failure of the qusiparticle picture for electron-phonon coupling. According to the qausiparticle picture [26], the spectra function of the qausiparticle peak has to be Lorentzian and exhaust the sum rule,

$$\int_{-\infty}^{\infty} A(k,\omega)d\omega = 1 \tag{4.5}$$

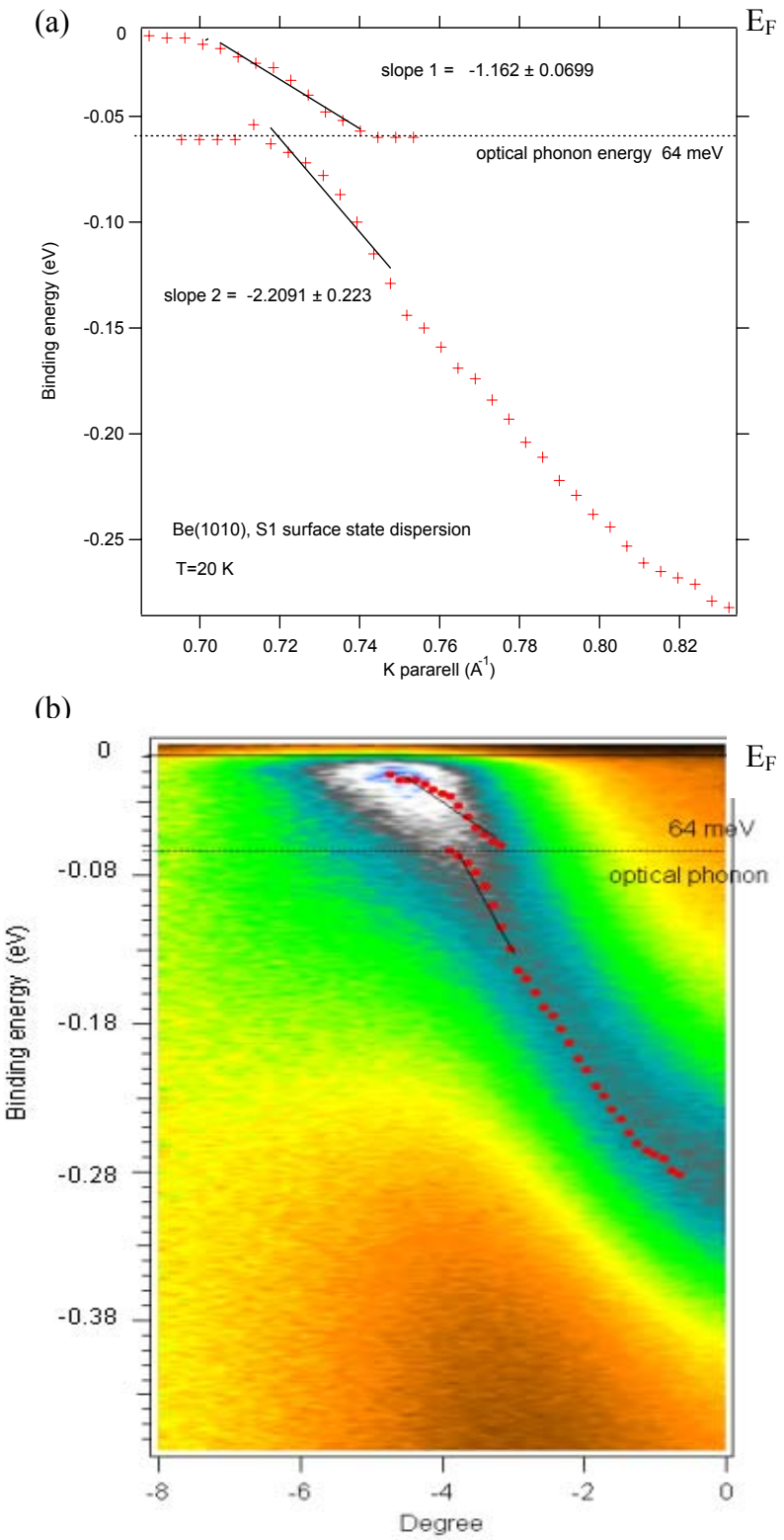

Figure 4.22 The surface state band dispersion of Be$(10\bar{1}0)$ near the Fermi level taken from (a) the maximums of the spectra and (b) direct 2D image

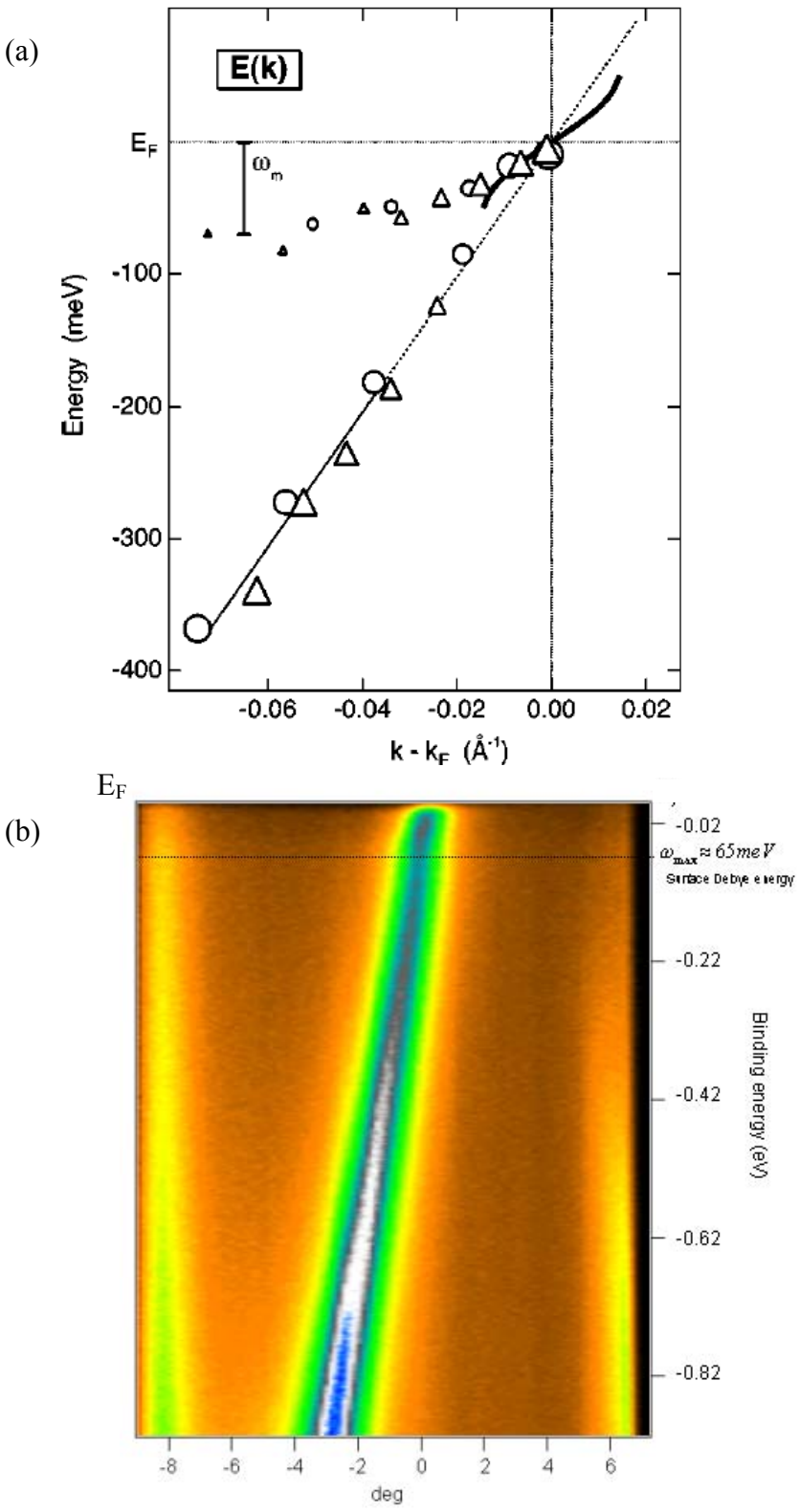

Figure 4.23 The surface state band dispersion of Be(0001) near Fermi level taken from (a) the maximums of the spectra [23] and (b) direct 2D image

When the free particle energy $\varepsilon^0(k) \to \infty$, the strength of the delta function peak decreases exponentially, but the peak above the Einstein energy will approach this free particle energy and exhaust the sum rule. In this case, the peak far above the Einstein energy is called the quasiparticle peak. On the contrary, when the free particle energy is very close to the Fermi level, $\varepsilon^0(k) \to 0$, the delta function peak is the dominant part of the spectra function and thus the quasiparticle peak. Therefore, in the region, $\varepsilon^0(k) \sim \omega_E$, where two peaks coexist, the quasiparticle picture breaks down. This region just corresponds to the region where the wider tail is observed in the 2 D image of Figure 4.22b. Possibly, the wide tail across the Einstein optical phonon energy is due to the broadening of the spectra function contributed by these two peaks. In this intermediate region, the two-peak structure reflects the interplay of different exciting channels, and the calculated spectra no longer account for elementary excitations [23]. The quasiparticle picture also breaks down in the region $\varepsilon^0(k) \sim \omega_{MAX}$ for the Debye model [23]. However, due to the fact that the peak below ω_{MAX} is broader than the corresponding one in the Einstein model, as shown in Figure 4.21b, and the ω_{MAX} does not serve as the extreme boundary between two peaks [27], the breakdown for the Debye model is not as serious as the Einstein model. The 2D image of the surface state band of Be (0001) still shows the kink shape (Figure 4.23b). Nevertheless, M. Hengsberger et al. [23] still illustrated the breakdown of the qausiparticle picture for the Debye model by comparing the positions of the peak maximum with the quasiparticle bands, as shown in Figure 4.23a. The thick solid line is the free particle band dispersion where the quasiparticle peak energy would approach when $\varepsilon^0(k) \to \infty$. The thick solid curve near

the Fermi level is the quasiparticle dispersion due to the screening by the ionic clouds. As is clearly seen, the experimental data points, (squares and triangles), only match the quasiparticle dispersions well either at the higher energy side or very near the Fermi level.

I have also tried to analyze the S1 surface state band dispersion of Be$(10\bar{1}0)$ through the momentum dispersion curve, MDC. The momentum dispersion curve shows the intensity as a function of parallel momentum at constant energy. If one assumes negligible momentum dependence of self-energy and $\varepsilon^0(k)$ and k are nearly proportional, the spectra function can also be applied to MDC [24]. Besides, MDC near or at the Fermi level is Lorenzian symmetry, free from the influence of Fermi function cut-off. Figure 4.24a shows the S1 surface state band dispersion from the bottom of the band to the Fermi level obtained through the MDC'S analyses. As seen, the interesting kink ranges from the binding energy 0.1 eV toward the Fermi level. The dip of the kink sits right about the optical phonon energy ~64 meV, as clearly shown in Figure 4.24b. The dashed parabolic curve approximates the free electron band. The subtraction of the free electron band from the data is equivalent to the real part of self-energy, Re $\sum$, as shown in Figure 4.25a. Compared with the calculated real part of self-energy in Figure 4.17a, the one I measured is a lot broader. However, the measuring temperature 30 K rather than 0 K and the surface defect are all big factors suppressing the real part of self-energy. Nevertheless, the top of the energy distribution of Re$\sum$ is about 61 meV which is close to the optical phonon energy. The electron-phonon coupling strength λ extrapolated from the slope close to the Fermi level, Eq (2.13), ranges between 0.76 and

0.99. The average is $\lambda \sim 0.875 \pm 0.1$. The imaginary part of self-energy, Figure 4.25b, was obtained by the relation [28],

$$\hbar v_k \Delta k = \frac{\hbar v_k}{l} \approx \left| 2 \operatorname{Im} \Sigma \right| \tag{4.6}$$

where l is the mean-free path, Δk is the extrapolated width of MDC, and v_k is the velocity of the surface state hole, which can be determined from the slope of the surface state band The steep step of $\operatorname{Im}\Sigma$ around the optical phonon energy is due to the abrupt change of the surface state hole velocity below and above the dip of the kink in the band dispersion.

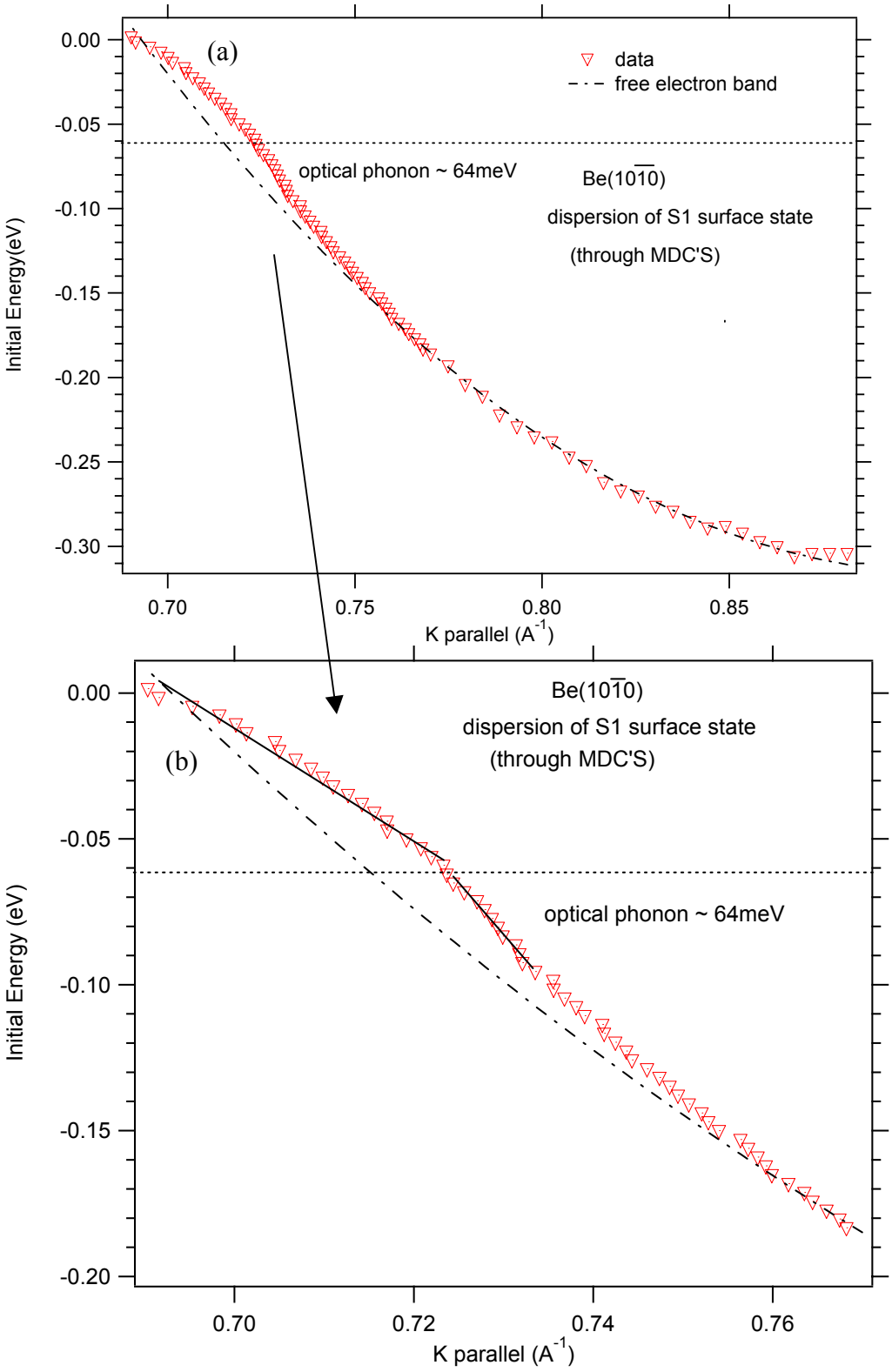

Figure 4.24 The S1 surface state dispersion obtained from MDC analysis (a) from the bottom of the band to the Fermi level (b) the kink part

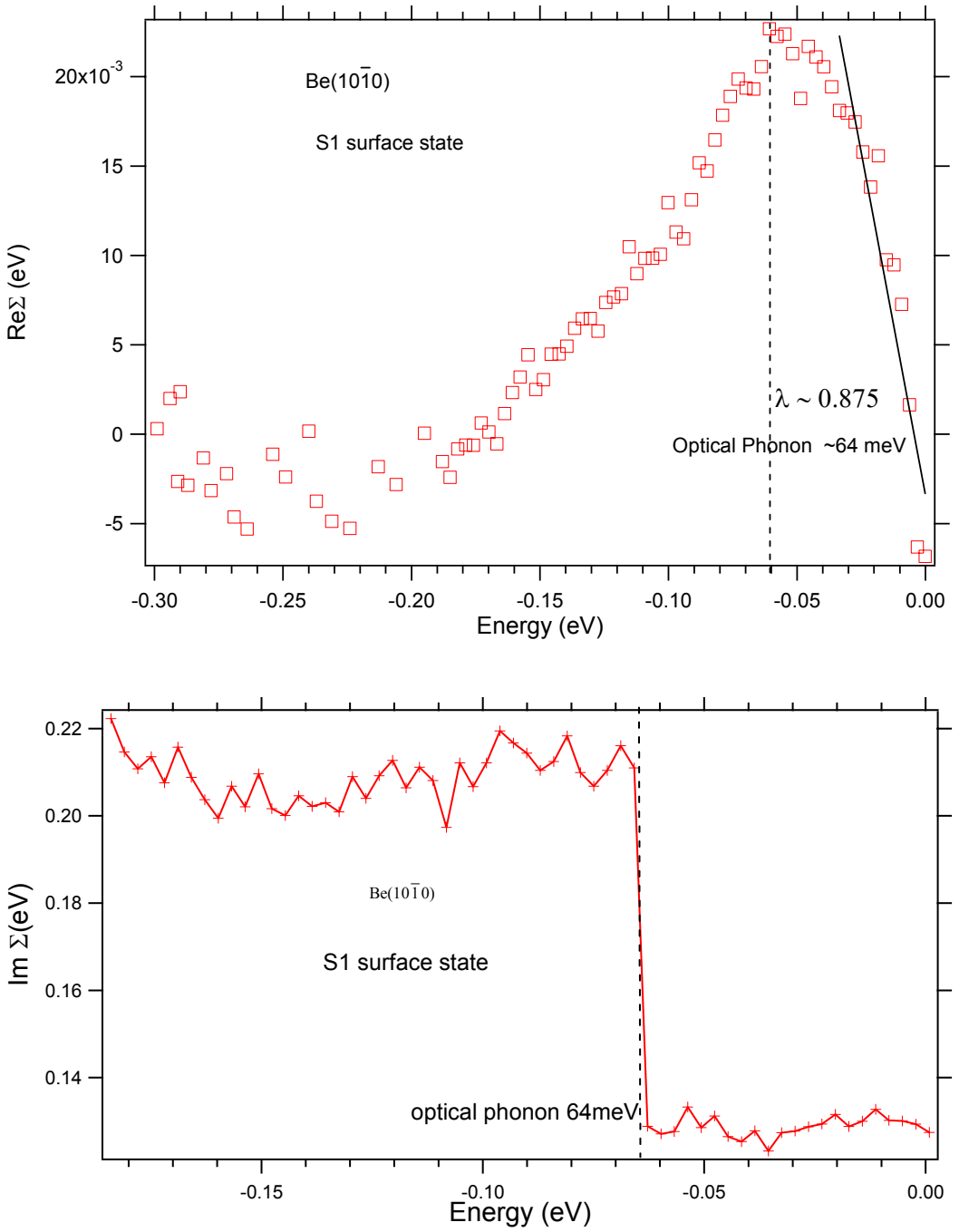

Figure 4.25. The energy distribution of the self-energy for electron-phonon coupling of the S1 surface state obtained through MDC analysis (a) Real part and (b) Imaginary part

CHAPER 5: The Electronic Structure and Electron-Phonon Coupling on Mg$(10\bar{1}0)$

5.1 Introduction

Magnesium is the second element after beryllium in the alkaline metal family. It also has hexagonal-close-packed (hcp) structure, but as opposed to Beryllium, its electronic structure is completely free electronic-like whether the bulk or on the surface [1,2]. The lattice c/a ratio of Mg is almost ideal with a value ~1.61 which is larger than that of beryllium ~1.56 [2]. This further indicates an isotropic electron system in Mg as opposed to Be which has more covalent bonding structure in one direction. Figure 5.1 shows the calculated density of states versus electron energies for a Mg(0001) surface slab and the bulk, respectively [3]. There is almost no difference between the surface and the bulk on the distributions of densities of states. Namely, they all approximately show the typical free electron gas behavior where $D(\varepsilon) \sim \sqrt{\varepsilon}$. It is interesting to investigate the many-body effects on the Mg surface; however, as opposed to Be whose bulk and surface properties are entirely different, the relation between the Mg bulk and surface is intimate. The many-body effects on the surface would thus be influenced a lot by the bulk properties, and the enhancement of many-body effects due to lower dimension should be less likely. This is one of the important points I want to confirm through my experimental results from the Mg$(10\bar{1}0)$ surface, and many-body effects on the electron-phonon interaction are still the properties I mainly investigated because of their dominant

temperature-dependent contribution to the surface state width. In addition, I also correlated surface electronic structures to the surface lattice structure and dynamic behavior on $Mg(10\bar{1}0)$. Since the $Mg(10\bar{1}0)$ surface is free electron-like, the model used to build the bridge might be different from that used for the covalent-like $Be(10\bar{1}0)$ surface. Nevertheless, the unique properties of the $Be(10\bar{1}0)$ surface were the most interesting and the center of my research. However, the study of electronic structure and electron-phonon coupling on $Mg(10\bar{1}0)$ was very helpful for comparison.

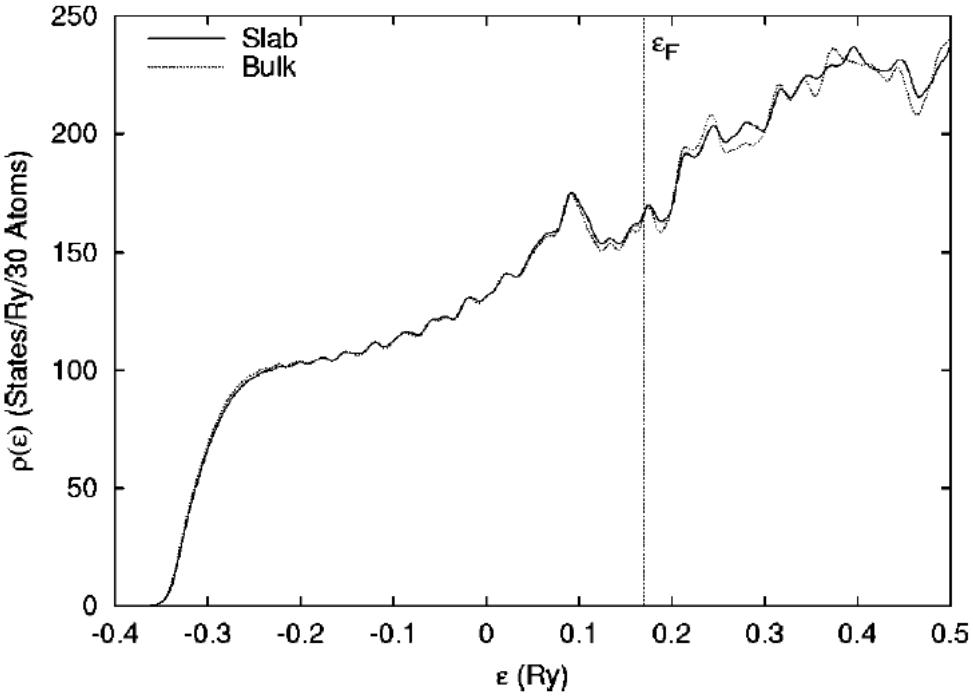

Figure 5.1 The charge density distribution of bulk Mg and Mg(0001) slab [3]

5.2 The Electronic Structure of the Mg $(10\bar{1}0)$ Surface

I also investigated the surface state band dispersion between $\bar{\Gamma}$ and $\bar{A}$ on the $(10\bar{1}0)$ surface Brilliuon zone. The main data were taken using an HA1250 large analyzer and TGM beam line. A few data were taken using an Scienta 200 with helium light at 21.2 eV. Figure 5.2 shows the energy distribution curves (EDC's) as a function of emission angle along the $\bar{\Gamma}\bar{A}\bar{\Gamma}$ direction taken with photon energies of 38 eV. The emission angle increases from the bottom spectrum to the top, corresponding to increasing parallel momentum across the surface Brillouin zone. The dispersions of two states about $\bar{A}$ are clearly seen. The emission angles corresponding to these two states at $\bar{A}$ are 11.75° and 11.84°, respectively. To ensure these two states originate from the surface, I took a series of the spectrum at $\bar{A}$ at different photon energies from 30 to 64 eV. As shown in Figure 5.3, it appears that these two features, in spite of the variations of their intensities, do not shift with the photon energies and stay at the binding energy of 0.6 and 1.12 eV, respectively. Their identities are thus certified as S1 and S2 surface states. Figure 5.4 shows the S1 and S2 band structures between $\bar{A}$ and $\bar{\Gamma}$ from my measurements at two different photon energies of 21.2 and 38 eV. As opposed to $\mathrm{Be}(10\bar{1}0)$, both surface bands on $\mathrm{Mg}(10\bar{1}0)$ show typical parabolic shape, which characterizes free electron-like properties. The effective mass of S1 band is m^*/m_e = 0.476, and the Fermi wave vector is k_F = 0.354 Å^{-1}. The S2 band has the effective mass m^*/m_e = 0.618, and it disperses into bulk band continuum at around k = 0.4 Å^{-1} from $\bar{A}$.

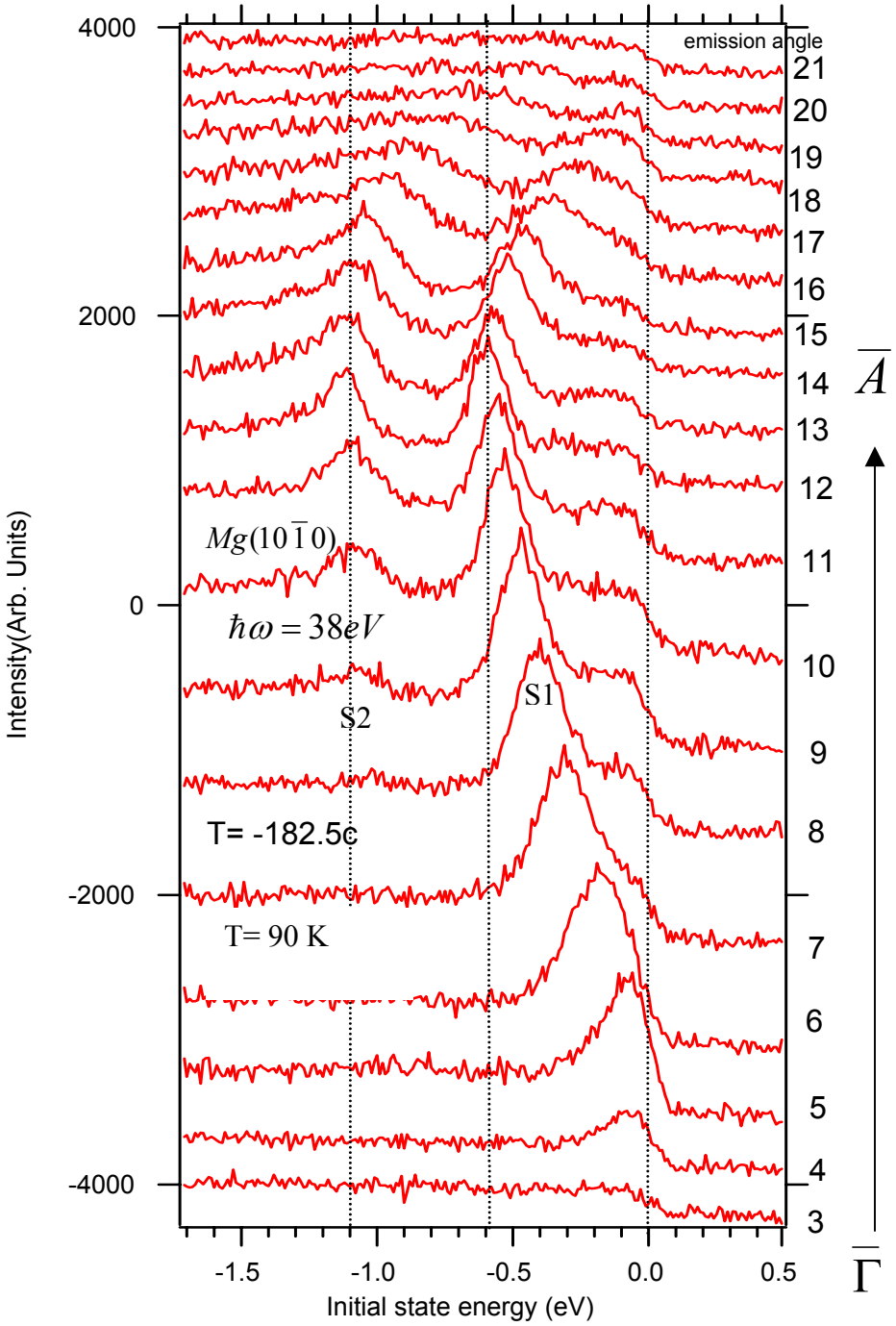

Figure 5.2 Energy dispersion curves of the surface states on $Mg(10\bar{1}0)$ between $\overline{\Gamma}$ and $\overline{A}$.

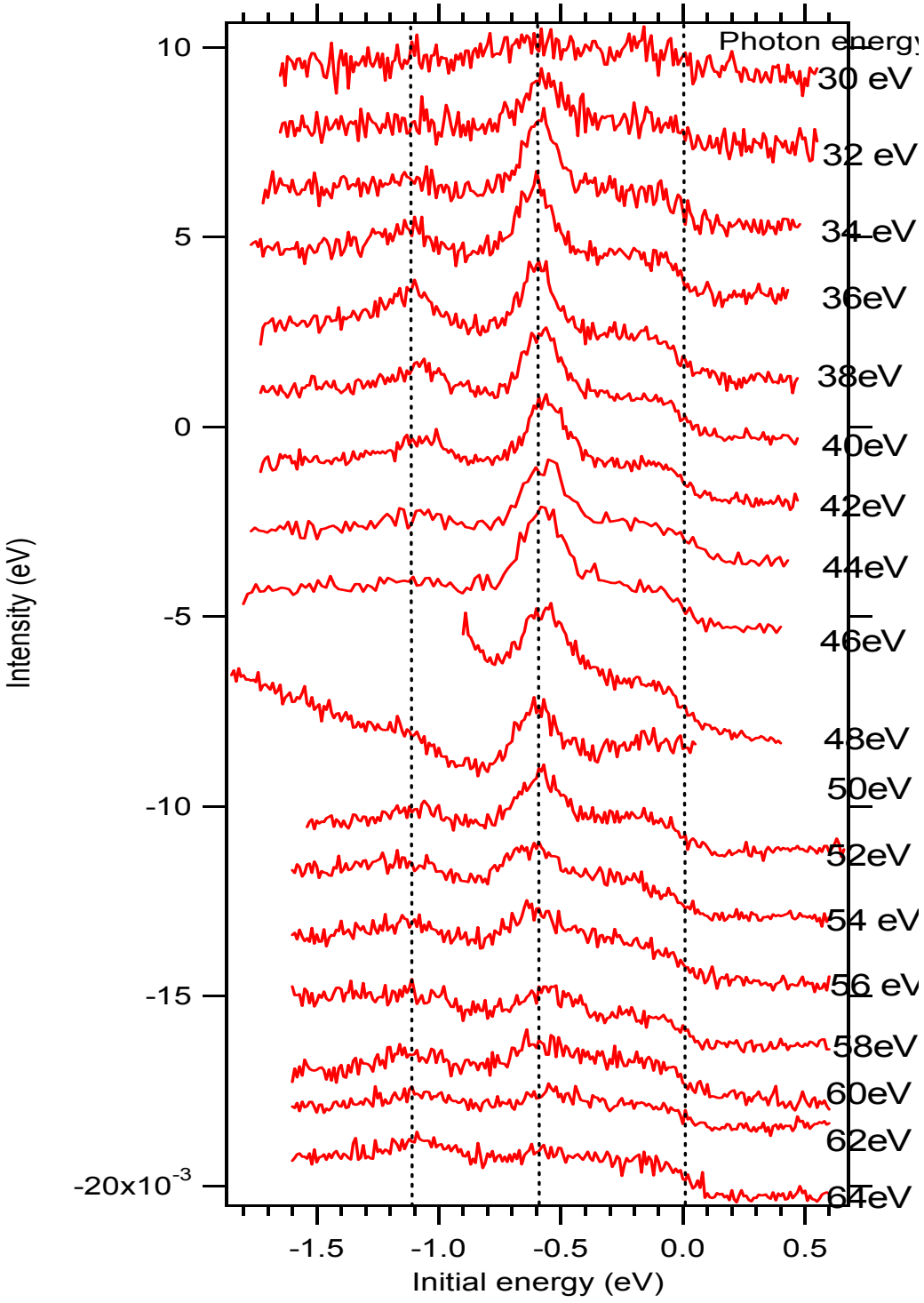

Figure 5.3 Photon energy dependence of the surface states at $\bar{A}$ on Mg$(10\bar{1}0)$

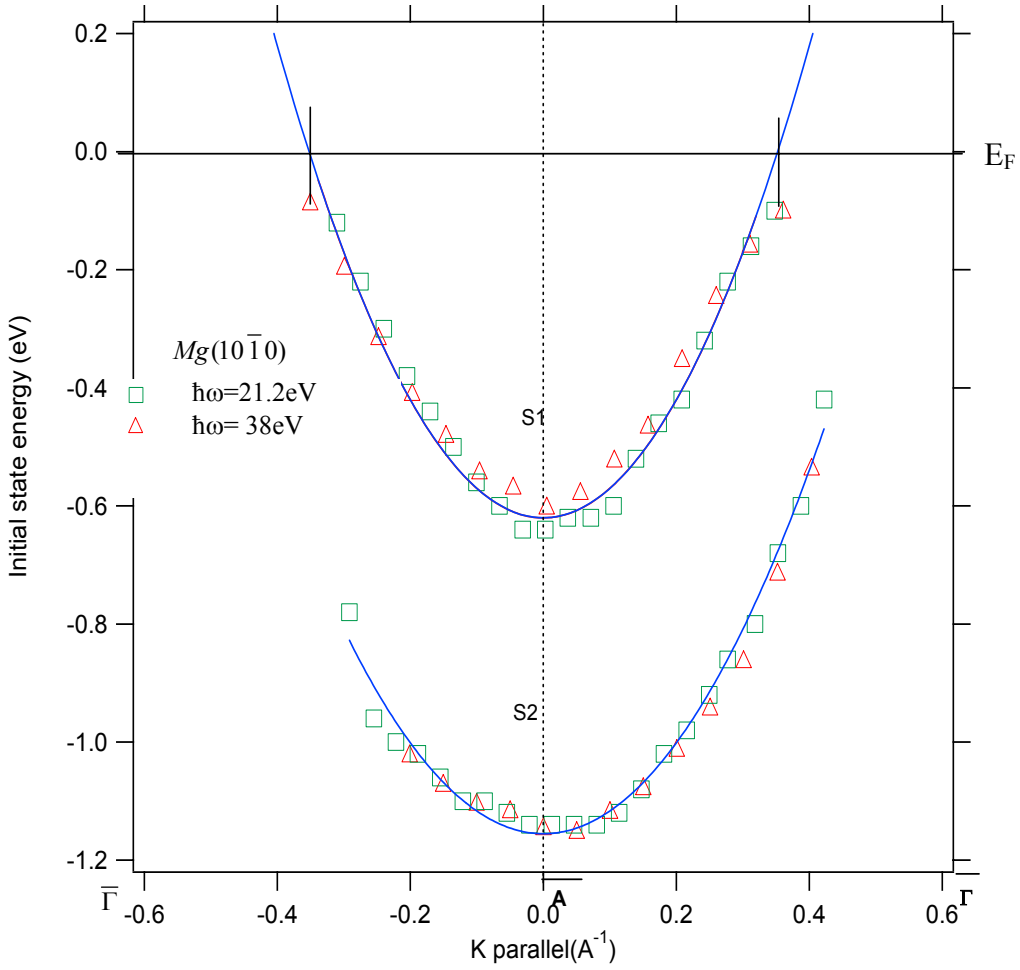

Figure 5.4 Measured surface state band dispersions (S1 and S2) from $\overline{A}$ to $\overline{\Gamma}$ on Mg $(10\,\overline{1}\,0)$ at two different photon energies.

Figure 5.5 shows the first-principle calculation results [4] of surface state band dispersions and bulk-projected bands on the Mg$(10\bar{1}0)$ surface Brillouin zone. The filled dark circles are the calculated dispersions of states derived from the surface. My measured dispersions were also superimposed for comparison. The measured (calculated) binding energies of S1 and S2 surface states at $\bar{A}$ are 0.6 eV (0.55 eV) and 1.12 eV (1.32 eV), respectively. The calculated bulk projected band on $(10\bar{1}0)$ shows the band gap at $\bar{A}$ is very small down to around 0.5 eV. As I mentioned before, the crystal potential component U_g is proportional to the size of the band gap. The free electron-like property on Mg$(10\bar{1}0)$ is reflected by its small energy band gap. This small band gap size even greatly affected the S1 and S2 line shapes, as shown in Figure 5.6. The top bulk band edge, at around 0.5 eV, raised up the right side of the S1 surface state peak and the bottom bulk band edge, at around 1.25 eV, raised up the left side of S2 surface state, causing the asymmetry shapes of both states. The calculated binding energy, 1.32 eV, of S2 is higher than the bottom bulk band edge, making it a resonance state. The bulk band edge positions at $\bar{A}$ in Figure 5.6 are according to the first-principle calculation results in Figure 5.5 [4]. It is necessary to actually measure their positions and compare them with the calculation results. The position of the top bulk band edge is difficult to obtain since the energy range, ~0.5 eV, between the S1 surface state and the Fermi level is too small. However, the bottom bulk band edge is measurable since the bulk band dispersion in the direction projected to $\bar{A}$ (from A to L, Figure 1.4) has a bandwidth up to 5 eV [3]. Figures 5.7a,b,c,d show the spectra of the bulk state

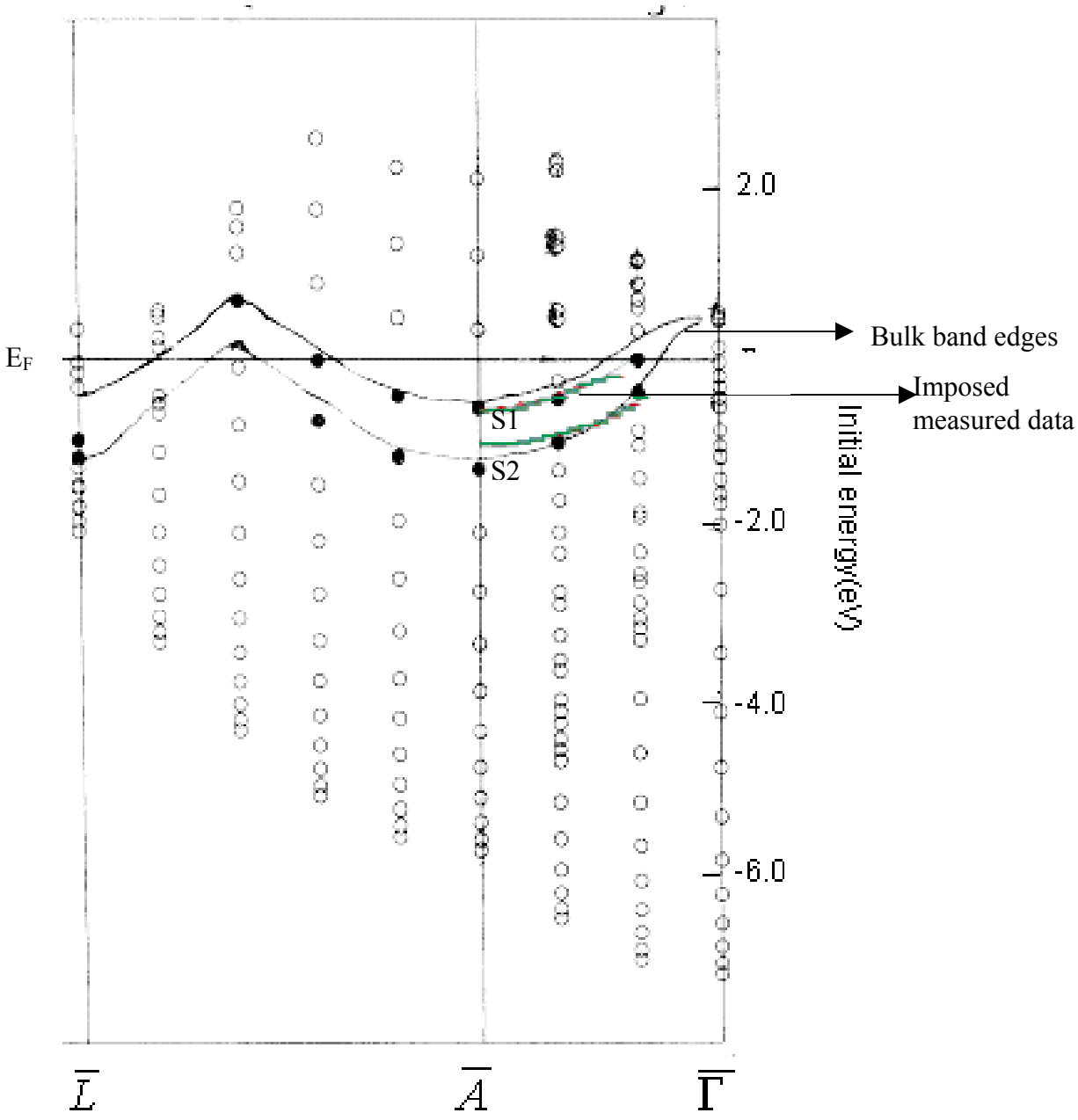

Figure 5.5 Calculated surface state band dispersions (dark filled circles), bulk projected band (empty circles), bulk band edges (thin solid lines) ,and superimposed measured data from Figure 5.4 (thick solid lines) for Mg $(10\bar{1}0)$.

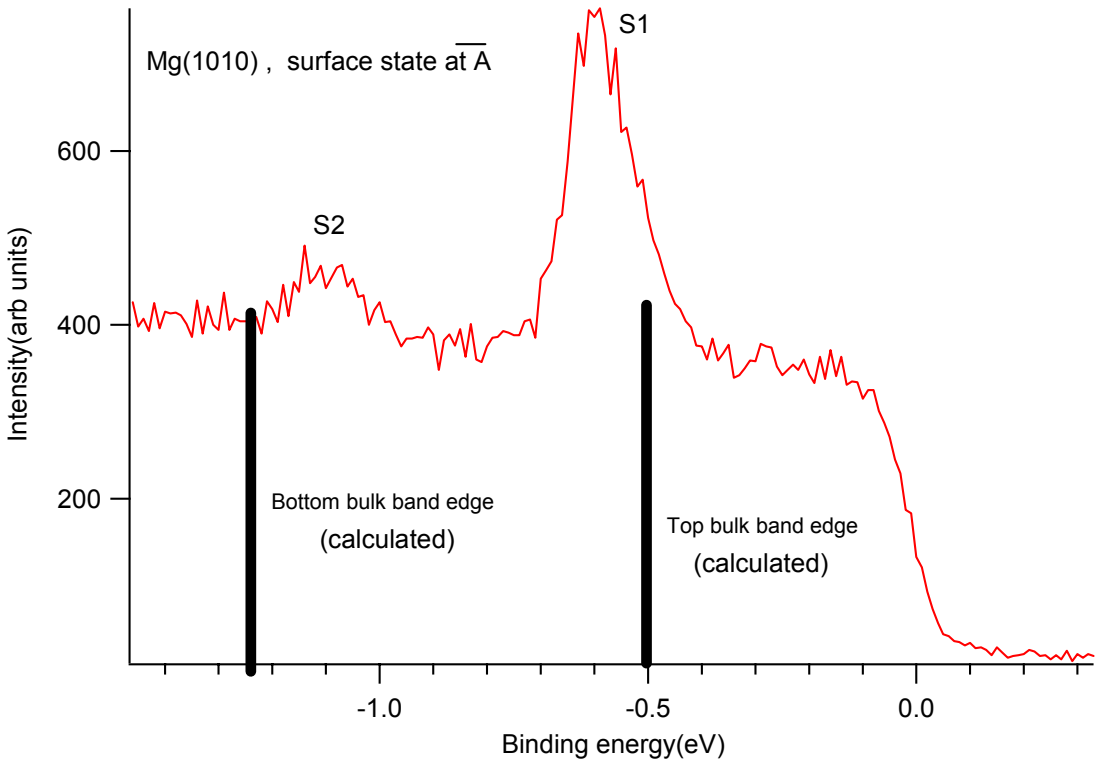

Figure 5.6 The asymmetry line shape of the surface states at $\overline{A}$ on $\mathrm{Mg}(10\overline{1}0)$

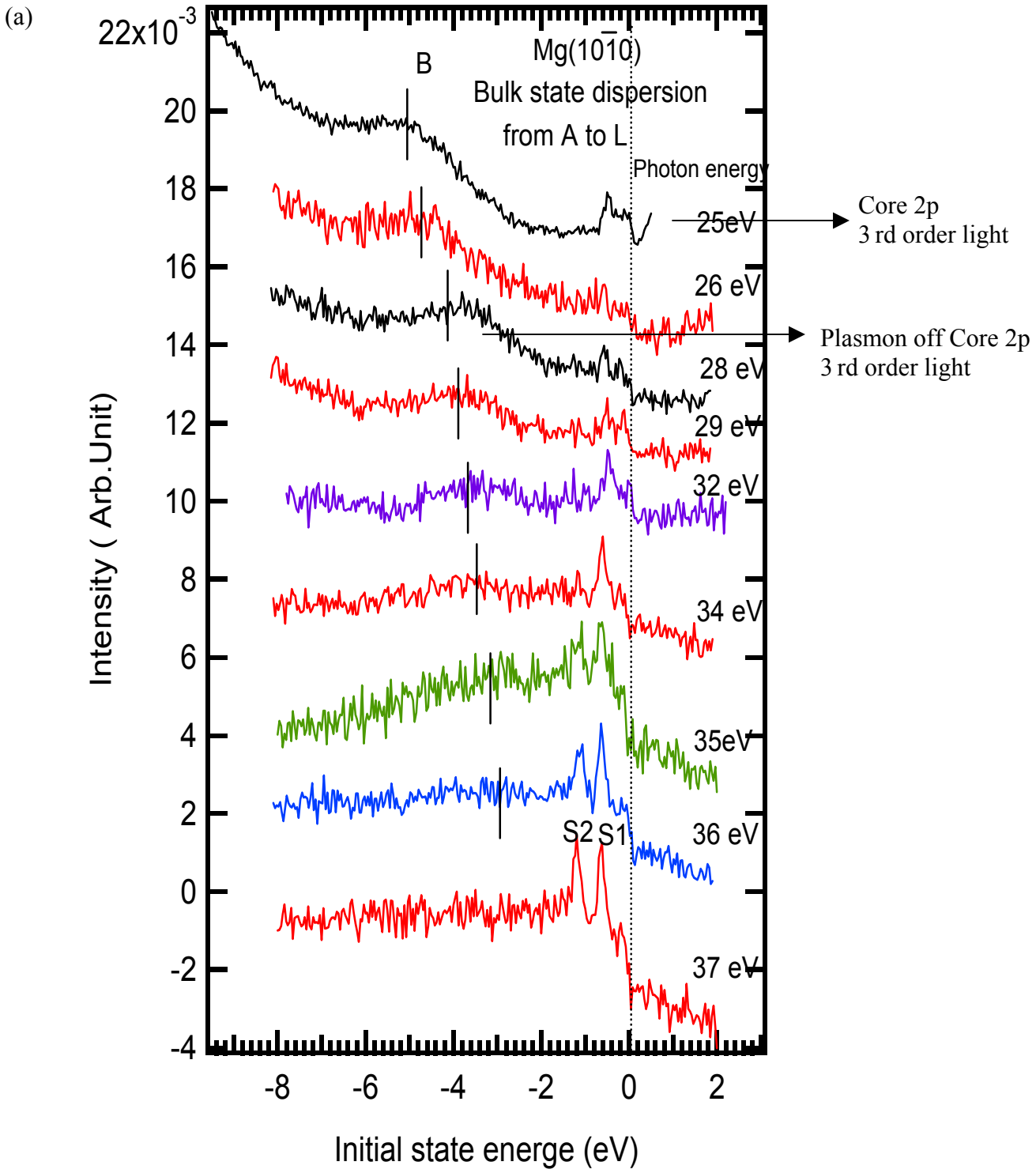

Figure 5.7 The bulk state dispersion from A to L (a) $\hbar\omega = 25 \sim 38$ eV (b) $\hbar\omega = 42 \sim 70$ eV (c) $\hbar\omega = 66 \sim 110$ eV (d) $\hbar\omega = 112 \sim 140$ eV

(b)

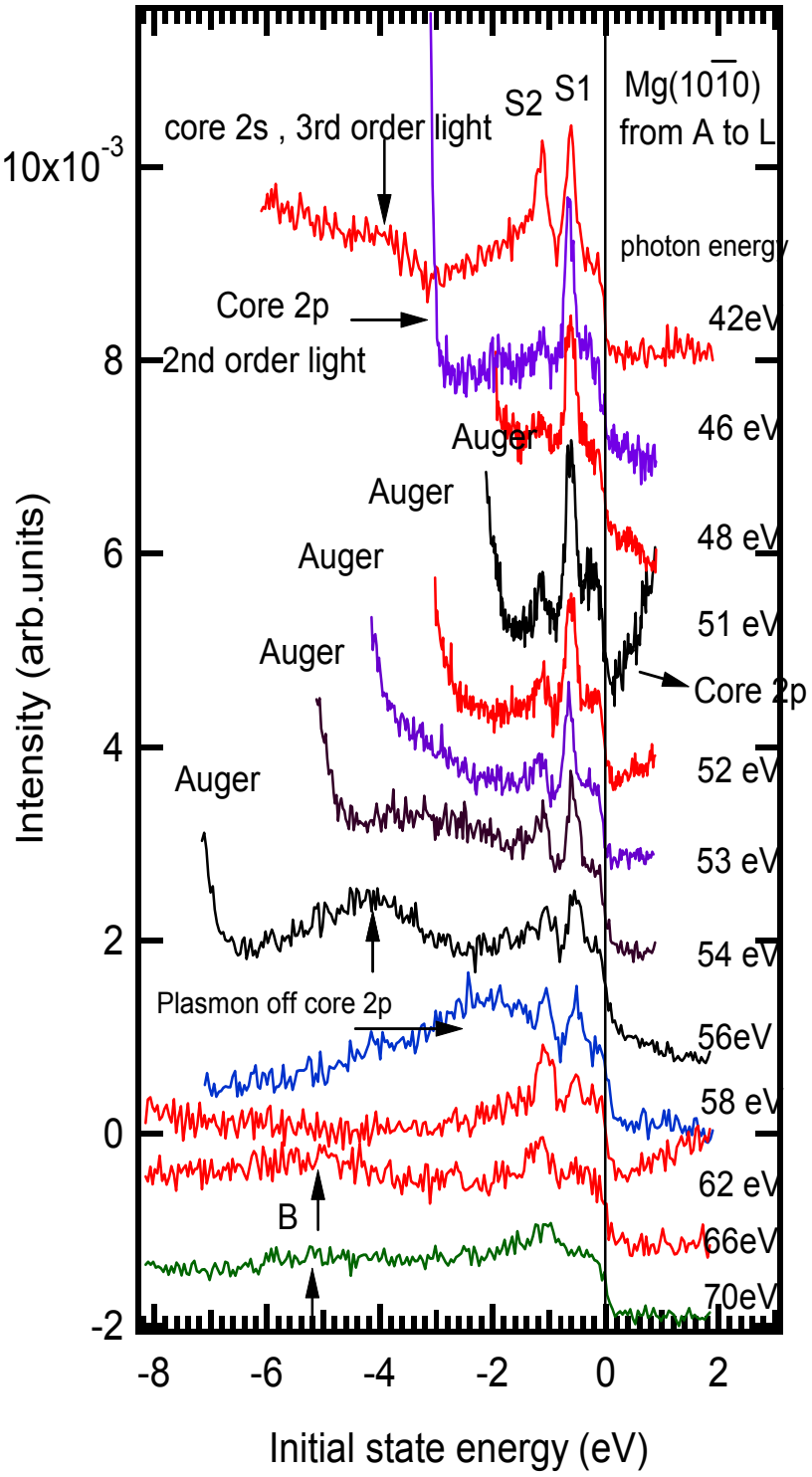

Figure 5.7 Continued

(c)

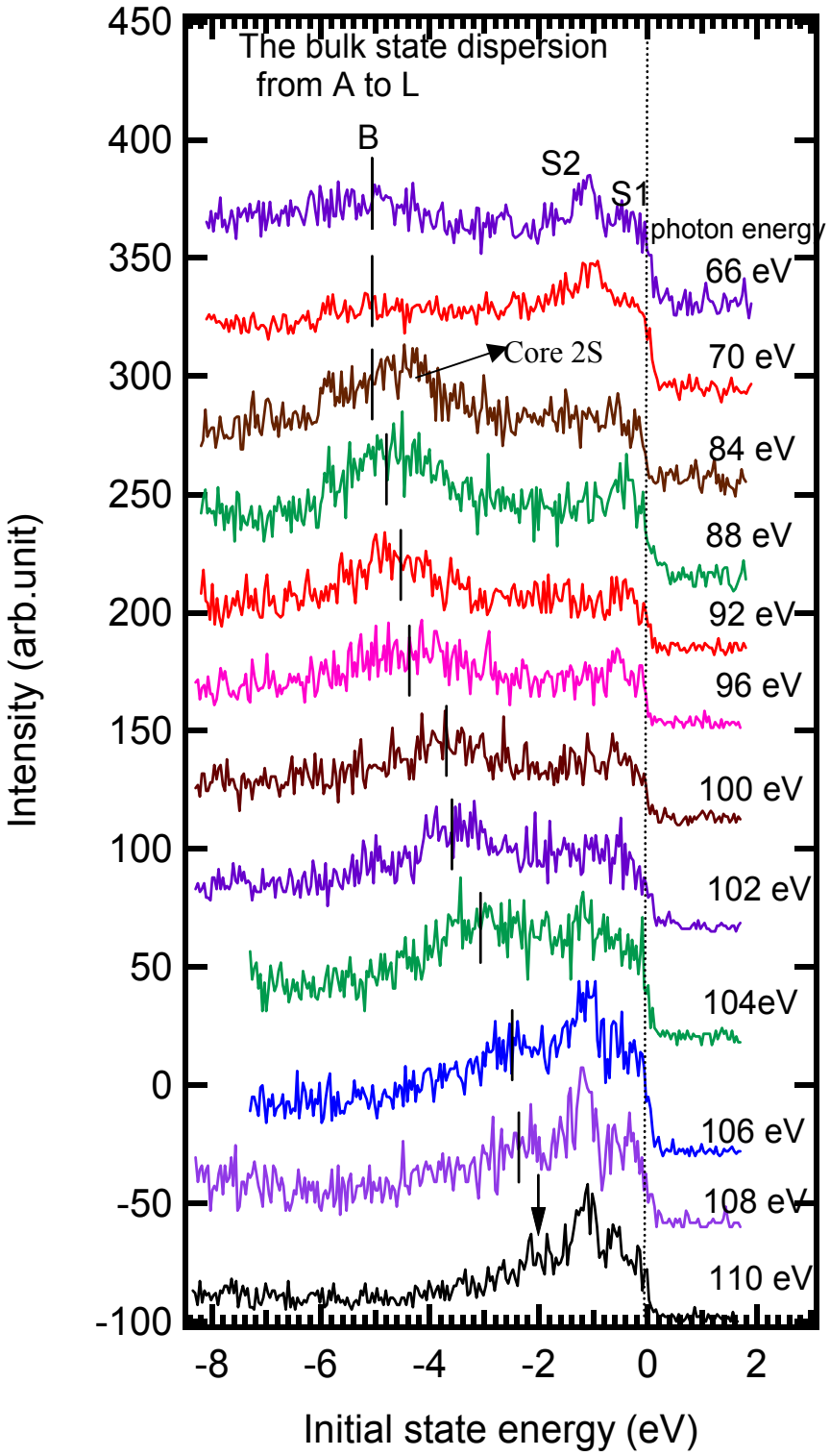

Figure 5.7 Continued

(d)

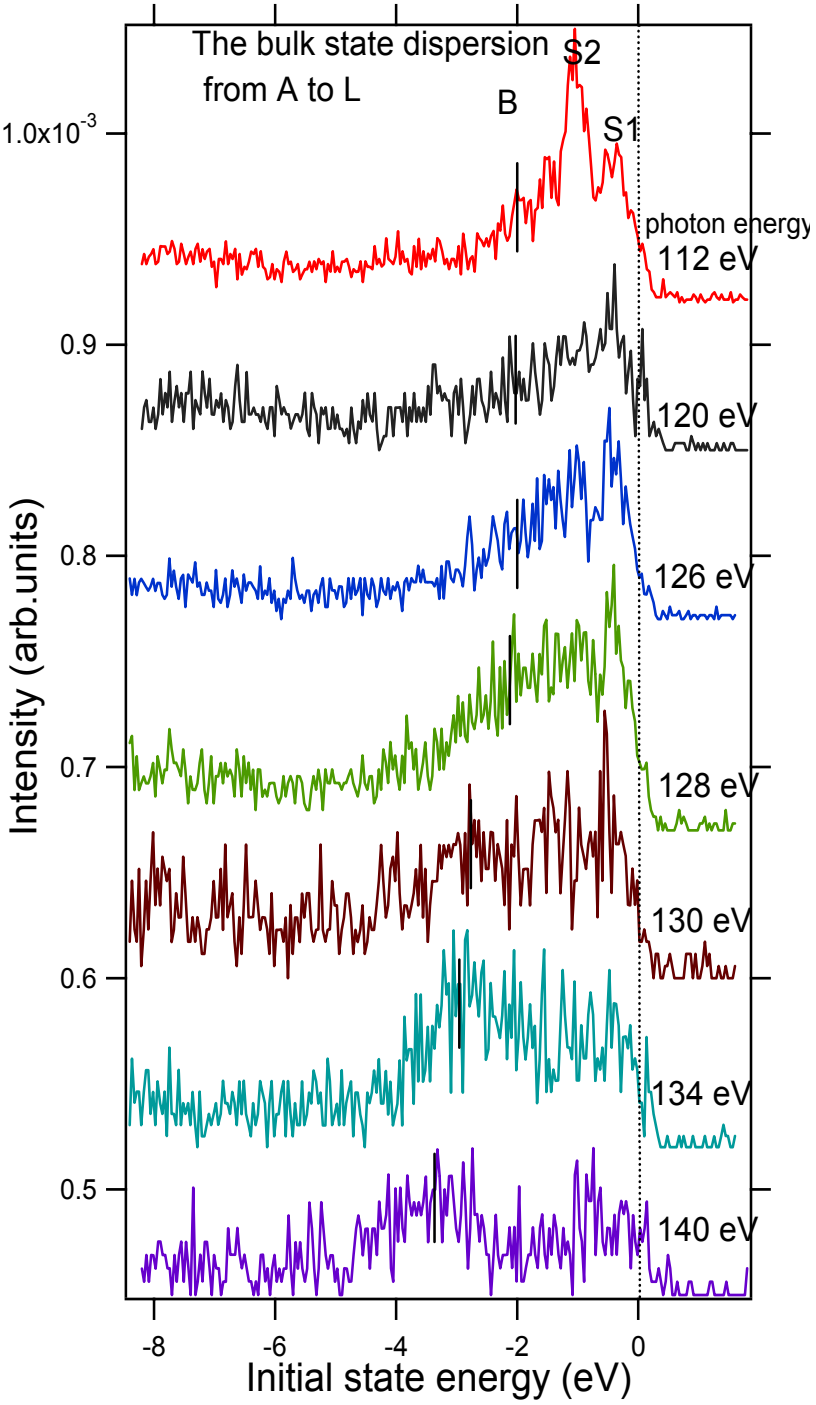

Figure 5.7 Continued

dispersion between A and L from a photon energy of 25 up to 140 eV. When taking these spectra, the emission angle was adjusted with photon energies to keep the k_{II} of the bulk state staying at $\overline{A}$. From this series of figures, one can see why it is such a big task to measure the band dispersion on $\mathrm{Mg}(10\bar{1}0)$. The *2p* core level peak and the features associated with it all show up in the valence electron energy range due to the second and third order light from the grating of the beam line. Figure 5.8 shows the photoemission spectra of core 2*p* and core 2*s* at a photon energy of 120 eV. The binding energies of core 2*p* and core 2*s* are 49.6 and 88.6 eV, respectively. The work function of Mg is 3.64 eV. Therefore, the corresponding kinetic energies of these two peaks are 27.76 and 66.76 eV, which are consistent with the positions of these two peaks in the spectra. The broad peak at around 42 eV is caused by the scattering Auger electrons, which are due to the strong decaying process of the core 2*p* hole. However, on the other hand, the valence electrons tend to screen the core hole, reducing the energy needed to remove the core electron. The interaction between the core hole and remaining electrons inevitably leads to the possibility of electronic excitations-plasmons, which give the satellite structures. The peak at around 56 eV comes right from the plasmon satellite off the core 2p peak [2]. These features confirm that there are indeed electron-electron many-body effects in the Mg bulk. In Figure 5.7a, a broad bulk state peak occurs at a binding energy of ~5 eV at $\hbar\omega$ = 25 eV. This bulk peak disperses toward E_F with increasing photon energies until $\hbar\omega$ reaches 36 eV where the intensity of the S2 surface state becomes so high that the bulk peak emission is largely suppressed. This also goes with the concept proposed by S. G. Louie et al. [5] that a intensity resonance of a surface state can result from strong

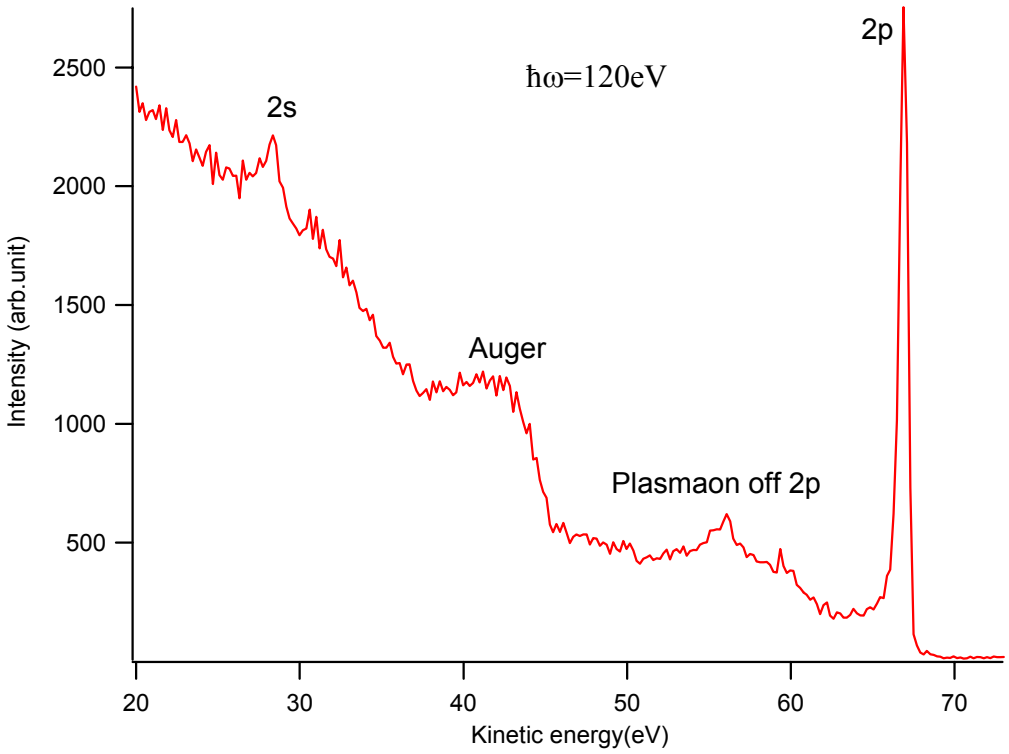

Figure 5.8 Core level electronic structures on Mg$(10\bar{1}0)$

coupling of the surface state wave function to that of the final state for the bulk band edge. From the spectrum at $\hbar\omega$ = 42 eV to that at $\hbar\omega$ = 70 eV, Figure 5.7b, the kinetic energy ranges are mostly coincident with that of the core level spectrum in Figure 5.8. In other words, the spectra of this part are mostly messed up by those core level features due to the second or third order light. The assignments of the peaks to the corresponding core level features are indicated by arrows in the figures. If it were not for the interference from the core level features, I could have made a good sketch of the bulk band dispersion easily. The only way left to do it is to keep increasing to the higher photon energies even though they are not favorable for the cross section of valence electrons. Figure 5.7c clearly shows that the bulk peak at the binding energy of about 5.15 eV at $\hbar\omega$ = 66 eV disperses toward E_F with subsequent higher photon energies. At $\hbar\omega$ =110 eV, one can still see the weak bulk emission at the binding energy around 2 eV (indicated by an arrow). When the photon energy further goes above 120 eV, this bulk peak starts dispersing back toward higher binding energy. In order to determine the exact binding energy of the top of the band at L, I used Eq (3.15) derived from the free final state band to do the bulk band mapping between A to L. The first thing is to get the inner potential, V_0. When inspecting Eq(3.6), Eq(3.7), Eq (3.13) and Eq(3.14), one can see that inner potential is actually the sum of the work function and Fermi energy. Using the free electron energy for the final state band has assumed the origin to be at the bottom of the bulk band. The binding energy of the bottom of the bulk band is about 5.15 eV, according to Figure 5.7c. The work function is 3.64 eV. Thus, I took 9 eV to be the approximate inner potential V_0. The kinetic energies E_k and the emission angle were determined from the spectra in Figures 5.7a,b,c,d. The result of the bulk band dispersion

between A and L is shown in Figure 5.9. The distance between A and L is 1.12 $\dot{A}^{-1}$. From the parabolic fitting of the band dispersion around the top of the band, the binding energy of the bottom bulk band edge at L is 1.79 eV. This is a lot larger than that of the first-principle calculations, 1.25 eV, and the common result, 1.38 eV, from the full–potential linear-augmented-plane-wave (FP-LAPW) method [6] and the liner muffin-tin orbital (LMTO) method [7]. The surface state status of S2 is certified according to the energy position of the bottom bulk band edge at L, as determined from the measurements. On the other hand, the measured binding energy of the bottom of the band at A is around 5.15 eV, which is also smaller than that of the common calculated result, 5.44 eV, from the FP-LAPW method [6] and the LMTO method [7]. The large deviation between the calculated and measured result is possibly attributed to the strong e-e interaction many-body effects in the bulk as is a similar case to Mg (0001) where the measured band gap size between Γ_3 and Γ_4 is twice as large as the calculated one, and the measured band width is 10% smaller than the calculated [2]. Therefore, it is also very likely that the top bulk band edge at L is at smaller binding energy than the calculated result, 0.5 eV. According to my investigations at different photon energies from 25 to 140 eV, I could not observe an obvious peak above the S1 surface state. I speculate that the top bulk band edge may sit at an energy merely above the Fermi level. To get the exact energy position, other techniques such as inverse photoemission should be used.

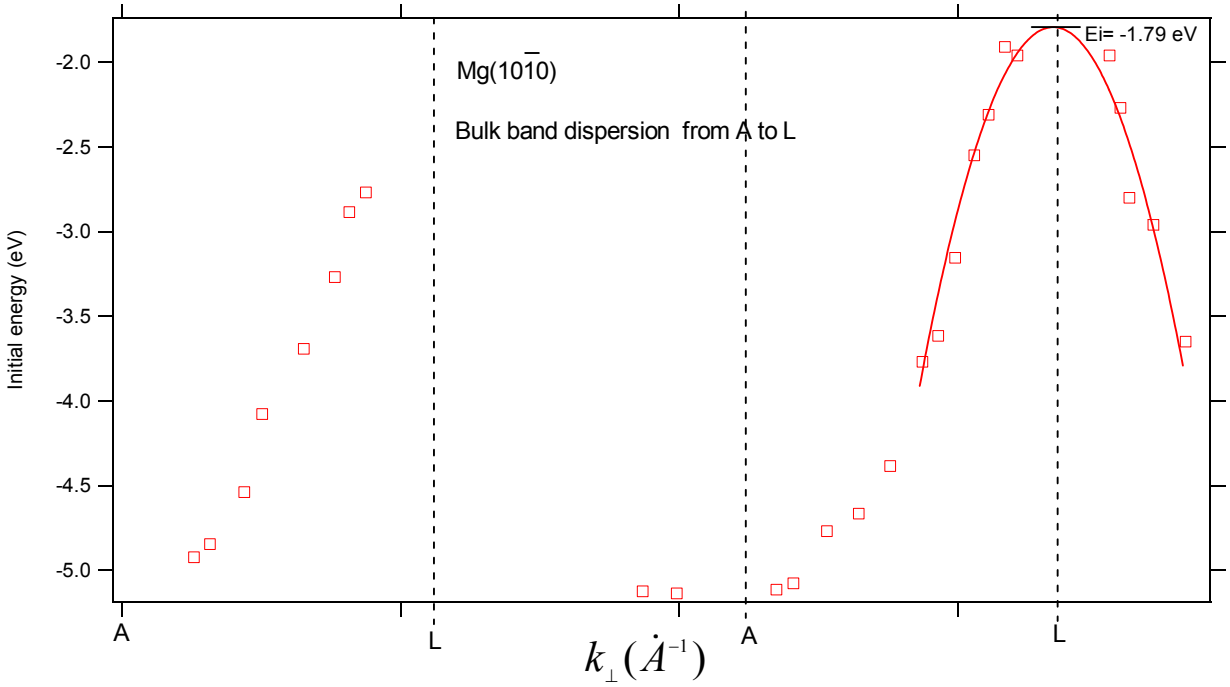

Figure 5.9 The bulk band structure in the direction A-L-A-L -A toward $\bar{A}$ on the Mg$(10\bar{1}0)$ surface Brillouin zone

5.3 The Temperature Dependence of Surface States on Mg$(10\bar{1}0)$

Similar to what has been done for Be$(10\bar{1}0)$, I also measured the temperature dependence of the two surface states at $\bar{A}$ on Mg$(10\bar{1}0)$. It is very interesting to see the temperature-dependent behavior of surface states on the free-electron-like surface of Mg $(10\bar{1}0)$ compared to those on the covalent-like surface of Be$(10\bar{1}0)$. Figure 5.10a shows a series of the EDCs taken at different temperatures from T = 295 K to T = 90 K at a photon energy 38 eV by using the HA1250 large analyzer. The change of peak widths and initial energies for both S1 and S2 surface states are not as relevant as those of Be$(10\bar{1}0)$. The smooth solid curves are the fitting of the spectra by a combination of two Lorenzian functions, Fermi functions and the linear background. The fitting is not very satisfying due to the asymmetry shape of the two surface state peaks. I have also tried to use the Shirley background instead of the linear background for the fitting, but the result was not any better. Figure 5.10b shows the fitting result after the Shirley background was taken out. I obtained information on the temperature-dependent width and initial energy shift of surface state S1 and S2 from the fitting of four different sets of temperature-dependent spectra like that in Figure 5.10a. The results will be presented in the following sections. Figure 5.10c shows the temperature-dependent EDCs taken at the photon energy 21.2 eV by the Scienta 200 energy analyzer. The temperature-dependent width and initial energy shift of the surface state extrapolated from this figure will also be presented for comparison.

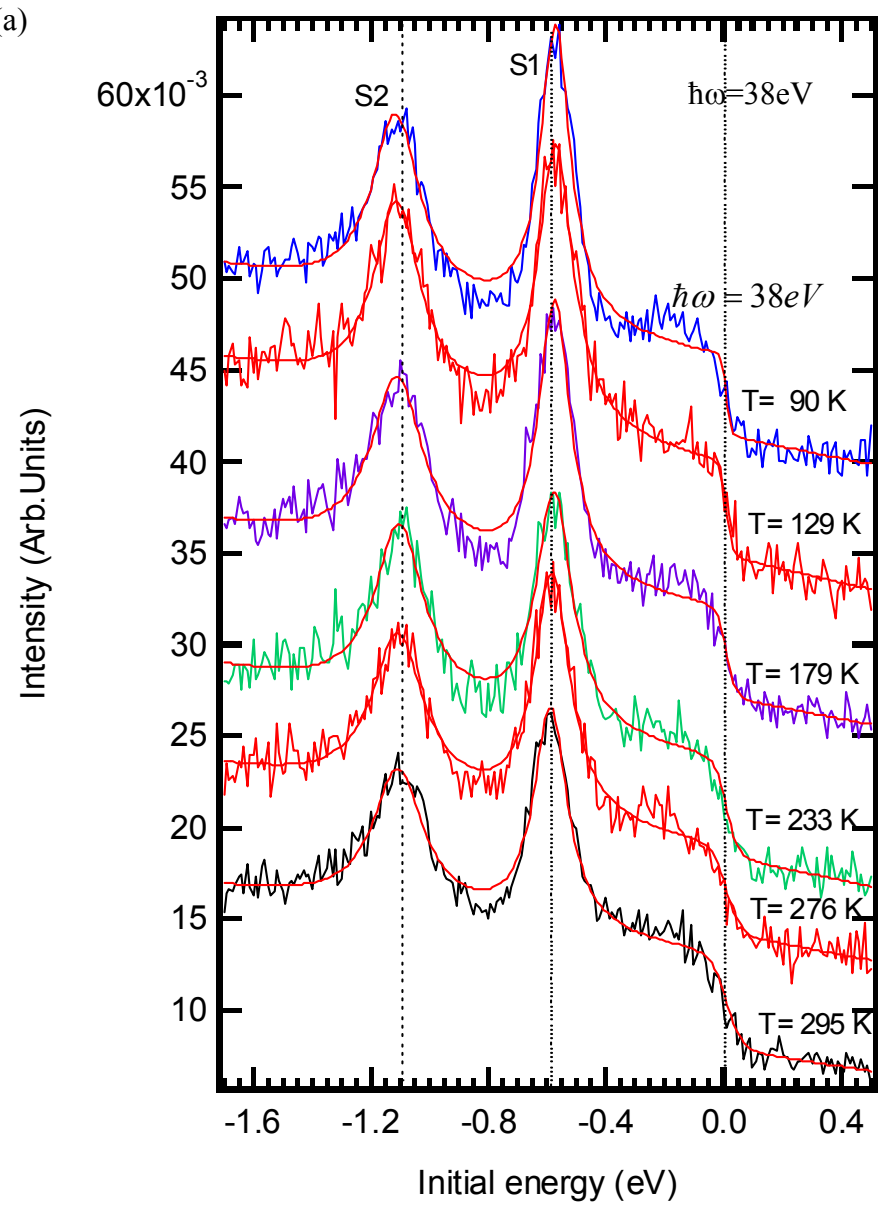

Figure 5.10 Temperature dependence of the surface states at $\bar{A}$ on Mg$(10\bar{1}0)$ (a) Results from the HA1250 large analyzer; (b) Shirley background is removed ; and (c) Results from the Scienta 200 analyzer

(b)

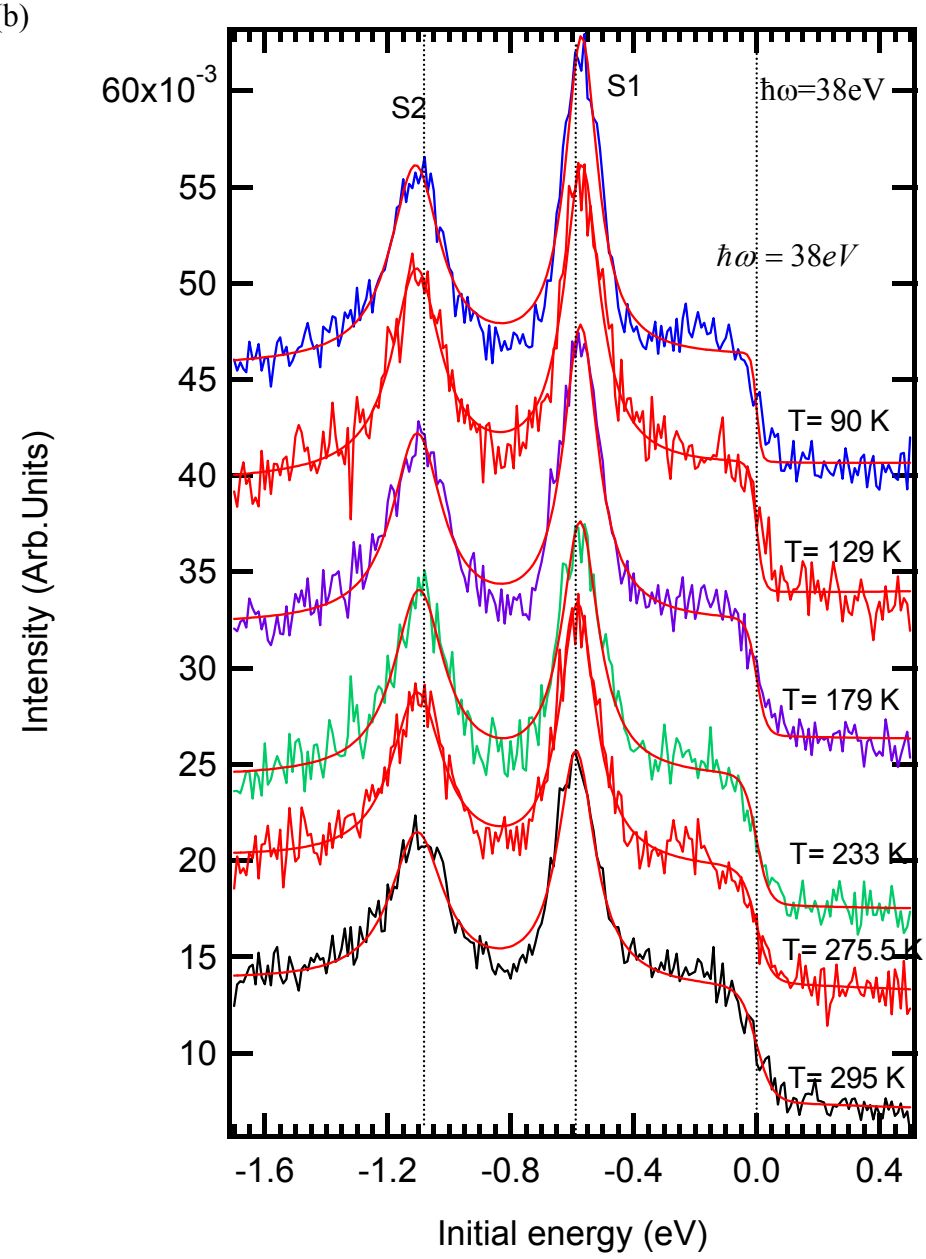

Figure 5.10 Continued

(C)

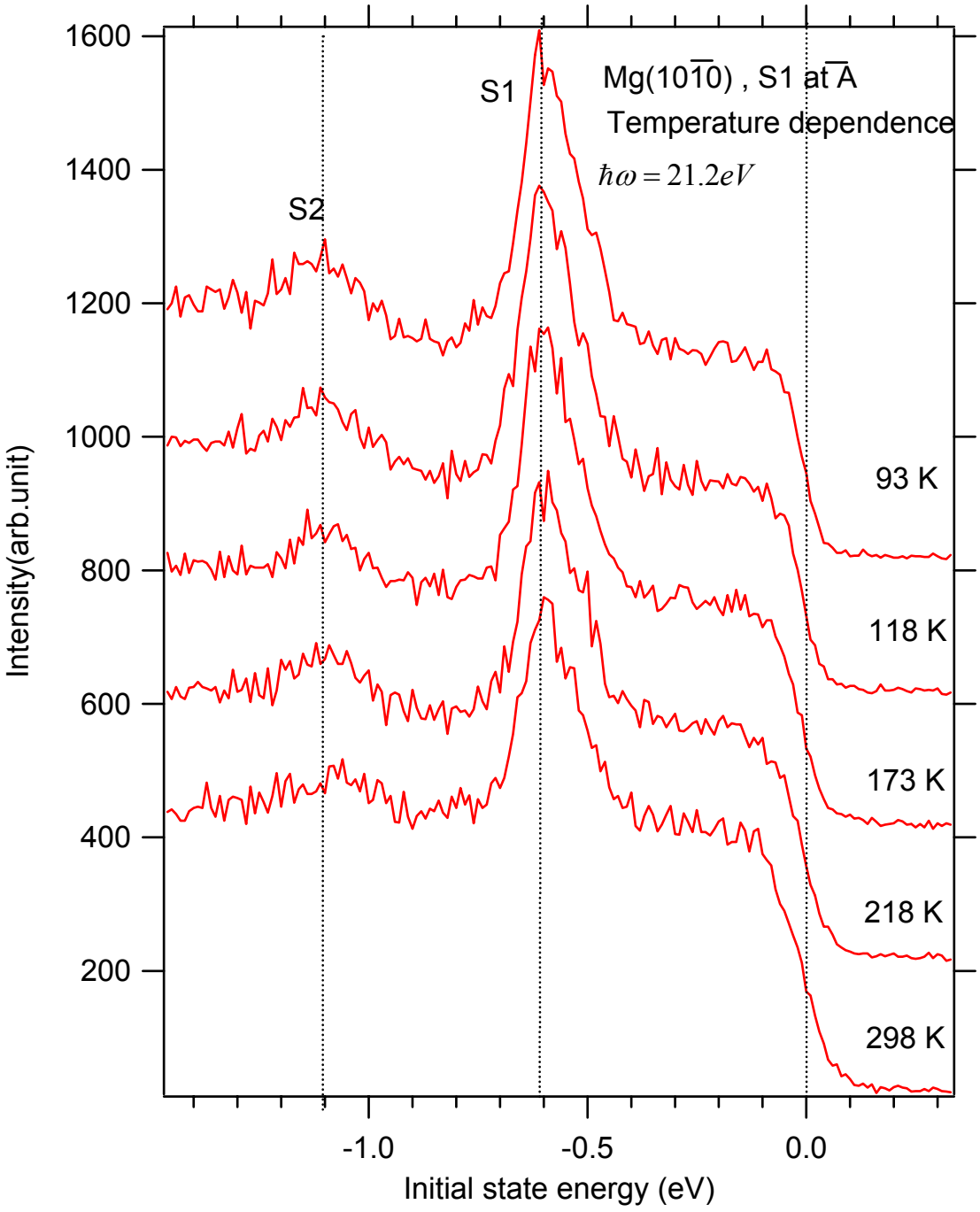

Figure5.10 Continued

5.3.1 Peak Widths

Figure 5.11a shows the temperature dependence of peak width for S1 and S2 surface states. It is obvious that the relation is close to being linear within the measured range between 90 and 300 K. This is consistent with the fact that Mg has a low Debye temperature around 318 K. Also , the T^3 curve relation only occurs when $T << T_{Debye,}$ as shown in Eq (2.23). Hence, there is not much relevance in comparing the fitting goodness through different phonon models because the Debye and Einstein models can both give good linear relations within this temperature range as is clearly shown from the solid and dashed fitting lines in Figure 5.11a. Therefore, the emphasis on studying the electron-phonon coupling of the surface states on $Mg(10\bar{1}0)$ is not only the phonon model any more. Instead, my focus is on the difference of the electron-phonon coupling strength, λ, between two surface states. The measured electron-phonon coupling strength of the S1 and S2 surface states by the Debye (Einstein) model are $\lambda_{S1} = 0.206 \pm 0.016$ (0.233 ± 0.02) and $\lambda_{S2} = 0.314 \pm 0.041$ (0.358 ± 0.046), respectively. These results were obtained using the HA1250 large analyzer and the TGM beam line. The total energy resolution of that system is about 100 meV. In order to confirm these results, I also measured electron-phonon coupling strength of the S1 surface state using a higher resolution system (50 meV), Scienta 200, and a helium lamp. The electron-phonon coupling strength of the S1 surface state is $\lambda_{S1} = 0.194 \pm 0.032$ (0.216 ± 0.049) by the Debye (Einstein) models, as shown in Figure 5.11b. The results from the two different systems are consistent. The offset in the fitting, which represents the contributions from

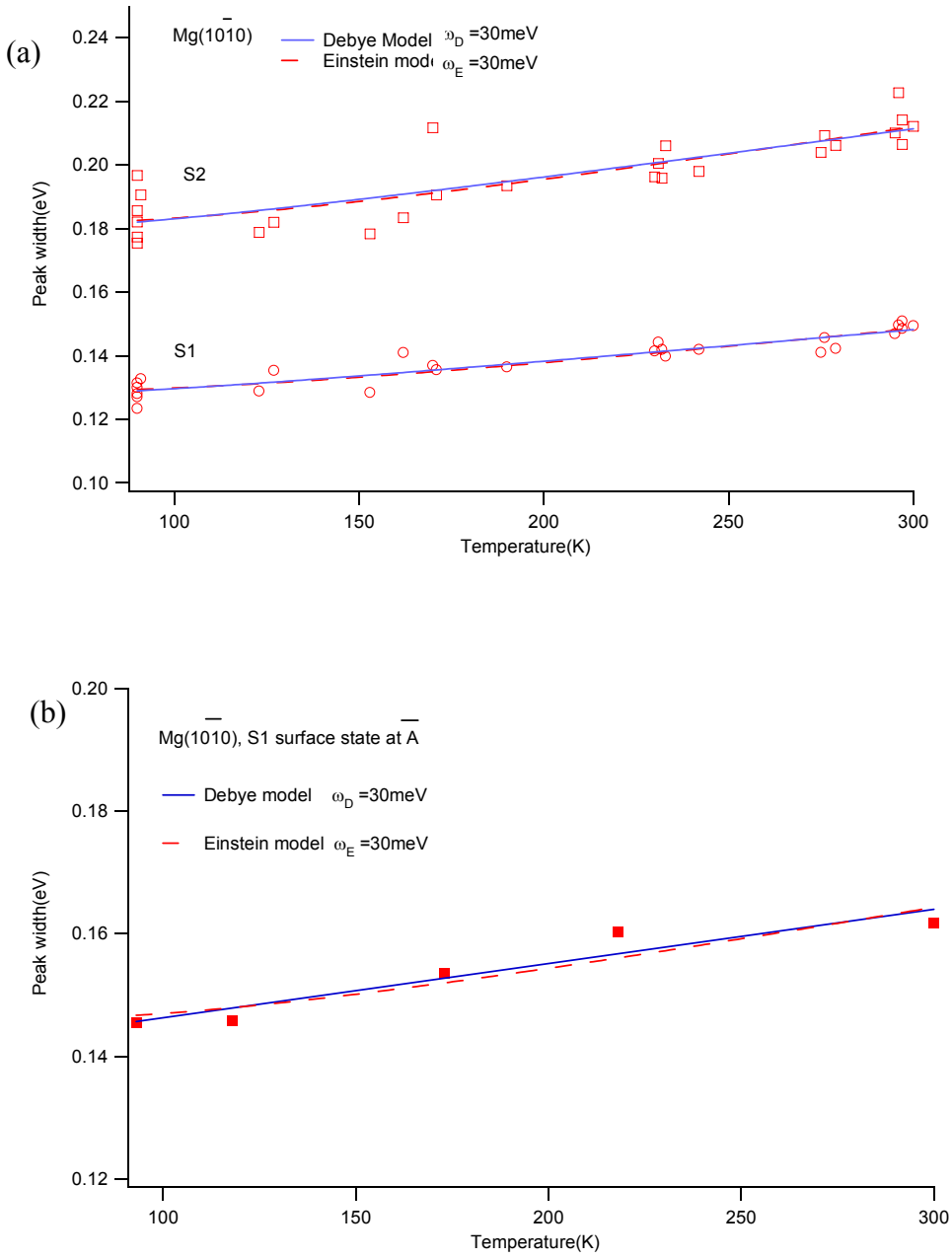

Figure 5.11 Temperature-dependent width of the surface states at $\bar{A}$ on Mg$(10\bar{1}0)$. (a) Results using the HA1250 large analyzer and (b) results using the Scienta 200 analyzer

electron-electron interaction and surface defects, is about 0.10 eV for S1 surface state and 0.15 eV for S2 surface state. The larger offset value for S2 surface state than S1 indicates more scattering channels for S2 surface state electrons in the electron-electron interactions.

The interesting thing from these results is that the electron-phonon coupling of S2 is higher than S1 and closer to the bulk value, $\lambda_{bulk} = 0.031 \pm 0.05$ [8]. This is completely reverse to the case for Be$(10\bar{1}0)$. For the typical free electron Mg$(10\bar{1}0)$ surface, the band gap size at $\bar{A}$ is so small (~0.5 eV) that the penetration length of two surface states at the surface zone boundary $\bar{A}$ must be long and deep through several layers. Therefore, the electron-phonon coupling of the surface state must involve high percentage of bulk phonons. This is actually very similar to the case of Cu(111) and Ag(111) where the bulk phonons contribute at least 50% of the electron-phonon coupling of the deep bound Shockley surface state at $\bar{\Gamma}$ [9]. In addition, the calculated results for most of the noble metal surfaces show that the electron-phonon coupling strength on the surface is less than that in the bulk [10]. R. Matzdorf has given similar conclusions through examining the electron-phonon coupling of the Tamn state at $\bar{M}$ and the Shockely state at $\bar{\Gamma}$ on Cu(111) [11]. The Tamn state at $\bar{M}$ with most distribution within the outmost layer has a much smaller λ value, 0.085, than the λ value, 0.14, of the Shockley surface state at $\bar{\Gamma}$ which has deep penetration into the bulk. It has been well known that the bulk projected band gap in the noble metal surface is very small, and the behavior of the Shockley surface state in the gap is dominated greatly by the bulk state at the bulk band edge [12]. The intimate relation between the surface and bulk

electronic structure makes it unlikely that the surface would have more electron-phonon coupling than the bulk. On the contrary, the surface state with more relation to the bulk would have a closer λ value to the bulk value. Thus, for these two surface states in the small bulk projected band gap in Mg$(10\bar{1}0)$, the larger λ value of the S2 surface state than the S1 indicates that the S2 surface state is more delocalized into the bulk.

5.3.2 Energy Shift

If the surface state is really dominated by the bulk, the temperature dependence of surface state initial energies should be consistent with that for the bulk state at the bulk band edge. Figure 5.12a shows the measured temperature dependence of initial energies of the S1 and S2 surface states at $\bar{A}$ using the HA1250 large analyzer and the TGM beam line as well as the calculated temperature dependence of the corresponding bulk band edge at L [13]. The calculation was done by E. V. Chulkov through first-principle calculations based on density-functional theory within the local-density approximation [13]. From figure 5.12a, the S1 surface state shifts at the rate of $(-0.668 \pm 0.12) \times 10^{-4}$ eV/K; however, the top bulk band edge shifts in the opposite direction at the rate $(0.07 \pm 0.11) \times 10^{-4}$ eV/K. The S2 surface state and bottom bulk band edge shifts in the same direction at the rate of $(0.17 \pm 0.14) \times 10^{-4}$ eV/K and $(0.46 \pm 0.014) \times 10^{-4}$ eV/K, respectively. Figure 5.12b shows the temperature-dependent results from the Scienta 200 energy analyzer and helium light. The S1 and S2 surface states all shift in the same direction as the bulk band edges at the rate of $(0.12 \pm 0.22) \times 10^{-4}$ eV/K and (2.6 ± 0.52)

$\times 10^{-4}$ eV/K, respectively. The direction and amounts of the energy shift rate for the S1 surface state in Figure 5.12a are similar to that for the S1 surface state on $Be(10\bar{1}0)$. However, there is no way to put them in the same case. The S1 surface state on $Be(10\bar{1}0)$ is extremely localized on the surface so its initial energy shift must result from the unique and large electron-phonon coupling on the surface. As for the S1 surface state on $Mg(10\bar{1}0)$, its energy position is so close to that of the top bulk band edge that the line shape is affected greatly, as shown in Figure 5.6. Therefore, the observed peak shift toward the Fermi level with decreasing temperatures must be due to the enhanced intensity of the top bulk band edge. The energy resolution of the spectroscopy system is also a big factor. The HA1250 large analyzer and TGM beam line have a total energy resolution of about 0.1 eV, as shown by the error bar in Figure 5.12a, which is worse than the resolution, 0.05 eV, as shown by the error bar in Figure 5.12b, using the Scienta 200 energy analyzer with helium light. In order to confirm this point, I also show the temperature-dependent energy dispersion curves which were taken by the small angle-resolved hemisphere analyzer and PGM beam line with a total energy resolution of 0.4 eV. As seen in Figure 5.13, the Fermi edge is not even resolved, and the shift of the peaks toward the Fermi level with decreasing temperatures is large and obvious. Therefore, the temperature dependence of initial energies for the S1 and S2 surface states on $Mg(10\bar{1}0)$ is as weak as the bulk band edges at the top and bottom. This again confirms the intimate relation between the surface and bulk electronic structure.

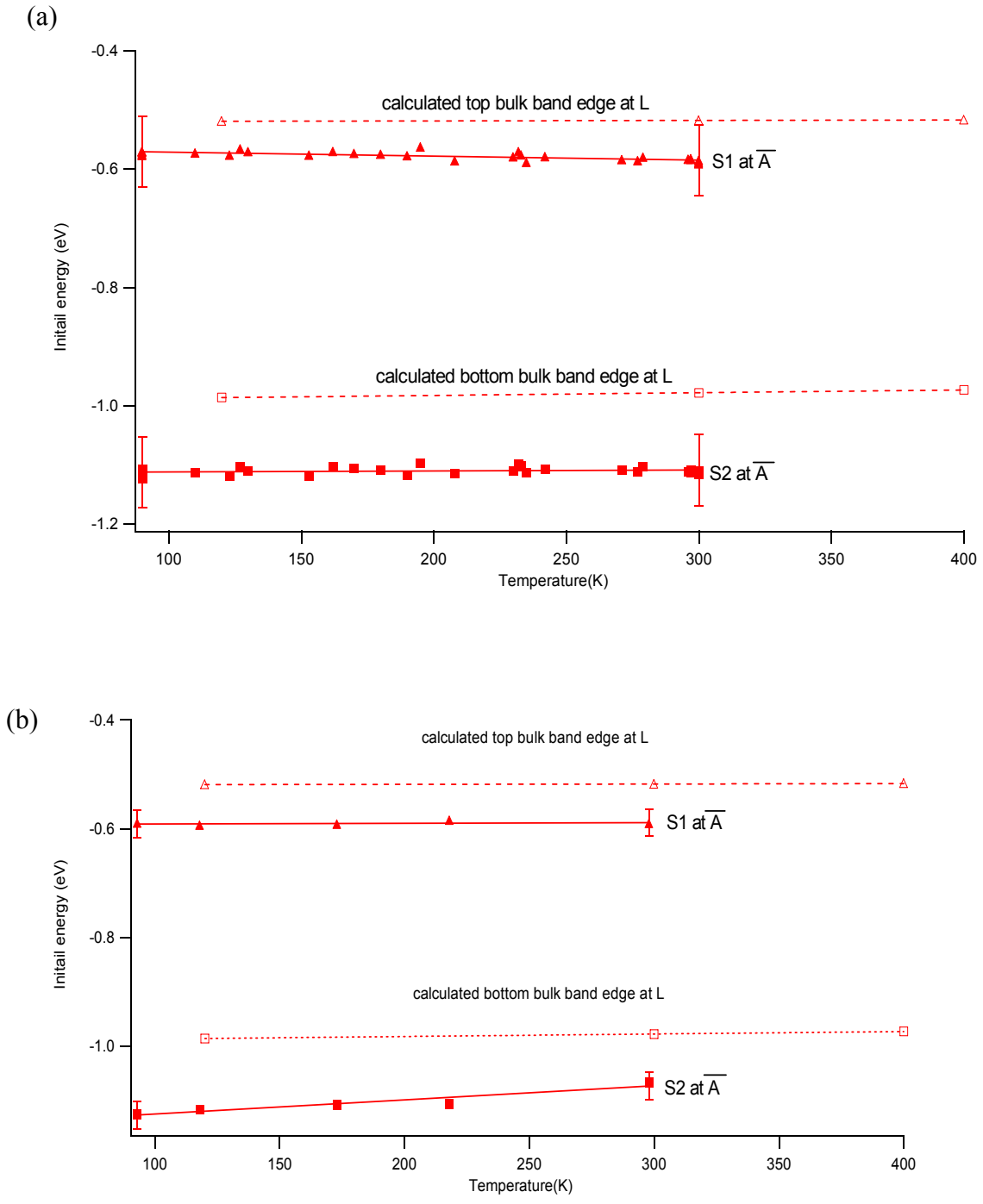

Figure 5.12 Temperature dependence of the surface state initial energy shift at $\overline{A}$ on Mg$(10\bar{1}0)$

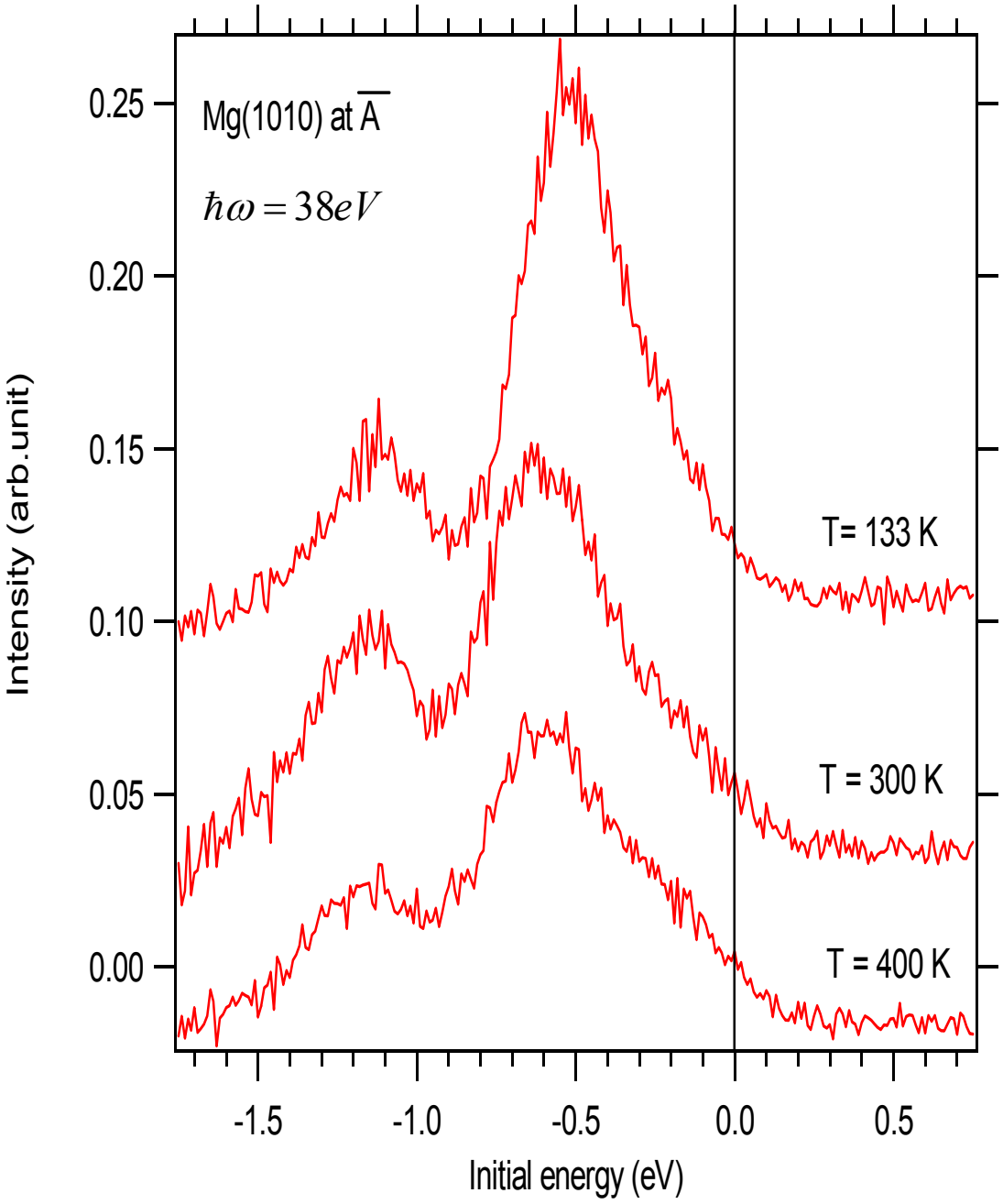

Figure 5.13 An illustration of bad resolution effects on measuring the temperature-dependent initial energy shift

Chapter 6 Discussion and Conclusion of Experimental Results

6.1 Surface State Electronic Structures on Be $(10\bar{1}0)$

6.1.1 Surface Relaxation

There have been discussions of several different models of the outer layer contraction of the metal surfaces in the past [1]. The first is an electrostatic result of the Smoluchowski effects [2]. When one cuts a crystal to form a surface, the electronic charge density relaxes so as to weaken its corrugation. The smoothing of the electron charge density is equivalent to taking charge from the regions directly above surface atoms and moving it to the hollow regions between them. Thus, this attracts the positive ion cores closer to the rest of the crystal. The second model comes from effective-medium theory (EMT) of the metallic bonding [3]. In the EMT picture, when a crystal is truncated to form a surface, the surface atoms find that the electron density provided by their neighbors is reduced and thus they would move in such a way as to return to the optimal electron density. Because they need to find positions where the electron density is higher, they move toward the rest of the crystal. The third explanation comes from the concept of bond-order-bond-length correlation. Every atom has a fixed number of valence electrons. As atoms coordination increases, those electrons must be distributed into a larger number of bonds. The number of valence electrons in each bond is therefore reduced, and the bond length therefore increases. Formation of the surface is the reversal of this argument in that the surface atoms lose several neighbors. The electrons that were involved in bonding to these neighbors therefore redistribute themselves nearer to the

atoms in the layer below (back bonding). This strengthens the bond between the first and second atomic layers, and, hence, reduces their separations. From the three models above, we can see that electronic structures on the surface take an extremely important role in the surface layer relaxation, and thus it is very likely that the real driving mechanism for the surface relaxation can be revealed through exploring the behavior of the surface state. As for the Be(0001) closed surface, a large outward relaxation was found [4]. This is against the argument for the three models above. However, as mentioned in Section 4.1, the bonding length of the Be_2 dimer is larger than that of the bulk Be crystal so it is actually not surprising that, on forming the surface, the reduced coordination of the atoms on the first layer makes the interlayer spacing between the first and second layer larger. In addition, Feibelman [1], by examining the charge density distribution for unrelaxed and relaxed Be(0001) surfaces, proposed that the loss of three neighbors for the atoms on the Be(0001)surface makes the energy cost of s to p_z electron promotion, which is necessary for the formation of strong bonds to the next layer down, less energy profitable than in the bulk. Therefore, the effect of the demotion from p_z to s is dominant on Be(0001) and favors the surface layer expansion (the z direction is perpendicular to the surface). However, as for $\mathrm{Be}(10\bar{1}0)$, Ph. Hofmann et al. [5] used the back bonding model to explain the large 25% inward relaxation of the first layer. The finding of hybridization between S2 and SR states from my experimental results may reflect the back bonding model between the first and deeper layers. In 1985, K. M. Ho et al. [6] have already proposed the idea of the "back bonding" model (due to rehybridization of broken surface bonds) to explain the first layer inward relaxation on Al(110), through the change of calculated density of states distributions before and after

the surface relaxes. As for Be$(10\bar{1}0)$, due to its unique surface electronic structure, this model can somehow be directly proved from the measured surface state band dispersion. To complete the picture for this model, we have to know more about the roles of the S2 and SR surface states on Be$(10\bar{1}0)$. As mentioned in the introduction to this chapter, the Be bulk has a larger covalent bonding in the direction along the C axis, which is just parallel to the $(10\bar{1}0)$ surface. Therefore the formation of the $(10\bar{1}0)$ surface will only partially break this covalent bonding and it would be more energy favorable for the partial broken bonds to back bond to the atoms in the sublayers. The S2 surface state at $\bar{A}$ is p_y-orbital-like [7] (the $(10\bar{1}0)$ surface normal is in the z direction); thus, this surface state might stem from the covalent bonding along the C axis in the bulk. It has 50% of the charge on the first layer and 40% below the second layer as shown in Figure 6.1b [8]. The SR state at $\bar{\Gamma}$, with its dangling bond character, has *s* and p_z symmetry [7] . 50% of its charge resides on the first layer, but the rest decreases into the sub layer deeply and slowly down to the 12th sub layer, as shown in Figure 6.1a [8]. Comparing Figure 6.1a with Figure 6.1b, one can see that the charge density distributions of both states are similar between the 2nd and 8th layer. This indicates that the symmetry of both states is similar because of hybridization. O. Hjortstam et al. [9] compared the difference between the surface projected density of states of the relaxed and unrelaxed atomic configuation for a 10-layer thick slab of Be$(10\bar{1}0)$. They found that the surface relaxation has the effect of pushing electrons away from energies around E_F, since the difference spectrum is mostly negative around E_F and positive at lower energies. Further, there is a quite sharp positive peak in the difference spectrum at around 3.4 eV below E_F,

which happens to be the energy range where the S2 and SR bands are closest to each other between $\overline{A}$ and $\overline{\Gamma}$, as shown in Figure 4.8. Feibelman [1], in order to explain the failure of the s-demoted to- p_z model for Be$(10\overline{1}0)$, proposed that as the outer Be$(10\overline{1}0)$ layer moves in, its bonds to the second atoms not only become shorter, but significantly closer to the surface plane. This makes it advantageous to move p_z electrons into p_x and p_y orbitals, instead of demoting them into S states. The small energy separation between the S2 (p_y) type and SR (p_z) in the middle of $\overline{A}\overline{\Gamma}$ would favor this electron scattering between them and, hence, cause hybridization. Without doubt, the combined picture of O. Hjortstam and Feibelman is reflected from the hybridization of S2 and SR bands between $\overline{A}$ and $\overline{\Gamma}$. Based on those explained above, the hybridization of S2 and SR bands revealed in the

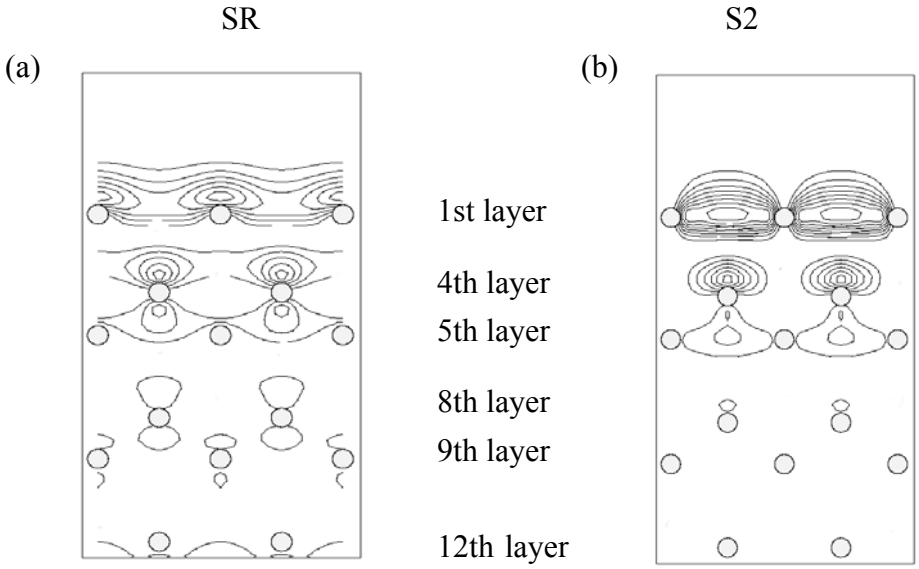

Figure 6.1 Contour plot of the charge distributions of S2 and SR surface states on a (0100) cut plane [8] where only 1st, 4th , 5th, 8th, 9th, and 12th layers … are in the cut plane

surface state band dispersions is a very important indicator for the back bonding in the surface region, which causes the large inward relaxation of the first layer on $Be(10\bar{1}0)$.

6.1.2 Surface Core Level Shift

Hybridization between S2 and SR states is also very relevant to the uniquely large surface core level shifts (LSCLS) on $Be(10\bar{1}0)$ [10]. J-H Cho et al. [11], through examining 1D charge density distribution profiles between relaxed and unrelaxed surfaces for $Mg(10\bar{1}0)$ and Be(1010), found that there is a large charge accumulation about the second layer after surface relaxation of $Be(10\bar{1}0)$. He attributed this phenomenon to the covalent-like property near the $Be(10\bar{1}0)$ surface. Therefore, the valence electrons close to the surface are stiff enough to screen the information of oscillatory multilayer relaxation, and thus, the LSCLS of $Be(10\bar{1}0)$ persist down to the fifth layer as opposed to the free-electron-like $Mg(10\bar{1}0)$ surface whose SCLS is only relevant from the first layer. The calculation of R. Stumpf et al. [12] through local density theory shows that the surface core level shift from the second layer is larger than that from the first layer. LSCLS can be divided into initial (electrostatic and exchange-correlation) and final state (screening) contributions. For the second layer, the electrostatic contribution is very large (-0.59 eV), while the exchange-correlation and screening contributions are small. At the first layer, LSCLS is almost entirely given by the screening (-0.34 eV), with only a small initial state contribution. The larger contribution to LSCLS from the second layer was also further confirmed by the

experimental results of forward photoelectron diffraction [13]. This LSCLS puzzle is now clearer with respect to my finding. The S1 surface state is free-electron-like with over 70% of its charge on the top layer [7]. It certainly mainly contributes to the screening effect on the first layer, which, in turn, contributes to the SCLS from the first layer. S2 and SR , as shown in Figures 6.1a,b, have about 50% of their charges below the first layer so the hybridization of these two states would indicate a special chemical environment of dense covalent bonding about the second layer. This completely explains why there is negligible screening, but a large electrostatic contribution, to make LSCLS from the second layer.

6.1.3 Non Free Electron Friedel Charge Density Oscillation

With more free electron-like property on the first layer and more covalent like property on the second layer, what kind of surface is $\mathrm{Be}(10\bar{1}0)$? I would say it is intermediate between a typical nearly free electron surface and a typical semiconductor surface. It does not have surface reconstruction as a typical semiconductor surface usually does, but it has a large 25% inward relaxation mainly caused by the back bonding. Furthermore, the free electrons (contributed by the S1 surface state) on the first layer is mainly subject to the ionic potential from the second layer. The best evidence is from the anisotropic behavior of charge density oscillations on $\mathrm{Be}(10\bar{1}0)$ [14]. It has been found that there is an intense wave-like pattern originating from the step edges along the $\bar{\Gamma}\ \bar{M}$ direction, but no waves or only very weak waves, however, are found at step edges in the $\bar{\Gamma}\ \bar{A}$ direction. The wave pattern originating from the point defects is

semi-elliptic [14] as opposed to the pure circular shape of the waves originating from the point defects on the Be(0001) surface[15]. As mentioned in Chapter 1, this behavior can only be approached if we use the Bloch function to represent S1 surface state electrons dispersing from the zone boundary $\overline{A}$, instead of purely plane wave function. At the surface zone boundary where the Brag reflection effect takes place, surface state electrons should experience more crystal potential. This is true for all the surface states originating from the surface zone boundary where the crystal potential has a component parallel to the surface [16]. However, unusual covalent bonding around the second layer on Be$(10\bar{1}0)$ would strengthen the crystal effect on the S1 surface state electrons on the first layer. This might explain why the Friedel charge density oscillation on Cu(110), as observed by L. Petersen et al. [17], is mush less aniotropic than that on Be$(10\bar{1}0)$.

Non-free-electron-like screening on the Be$(10\bar{1}0)$ surface would also give the possibility of observing defect states by photoemission. On taking the surface state band dispersions between $\overline{\Gamma}$ and $\overline{A}$ at ħω = 40 eV, we observed that there is a small broad peak showing up and dispersing weakly at the lower binding energy side of the S2 surface state around $\overline{A}$, as shown in Figure 6.2. By analyzing two energy dispersion curves at two different photon energies, 40 and 24 eV, as shown in Figures 6.3a,b, through the curve fitting, we see this unknown peak is very broad up to the width around ~1.2 eV and at a fixed binding energy around ~1.9 eV. If we see the S1 and S2 surface states as the edges of surface band gap caused by the surface crystal potential [16], then this unknown peak sits right inside the gap. It is obvious that this broad peak represents the surface defect states, which break the 2D symmetry of the surface.

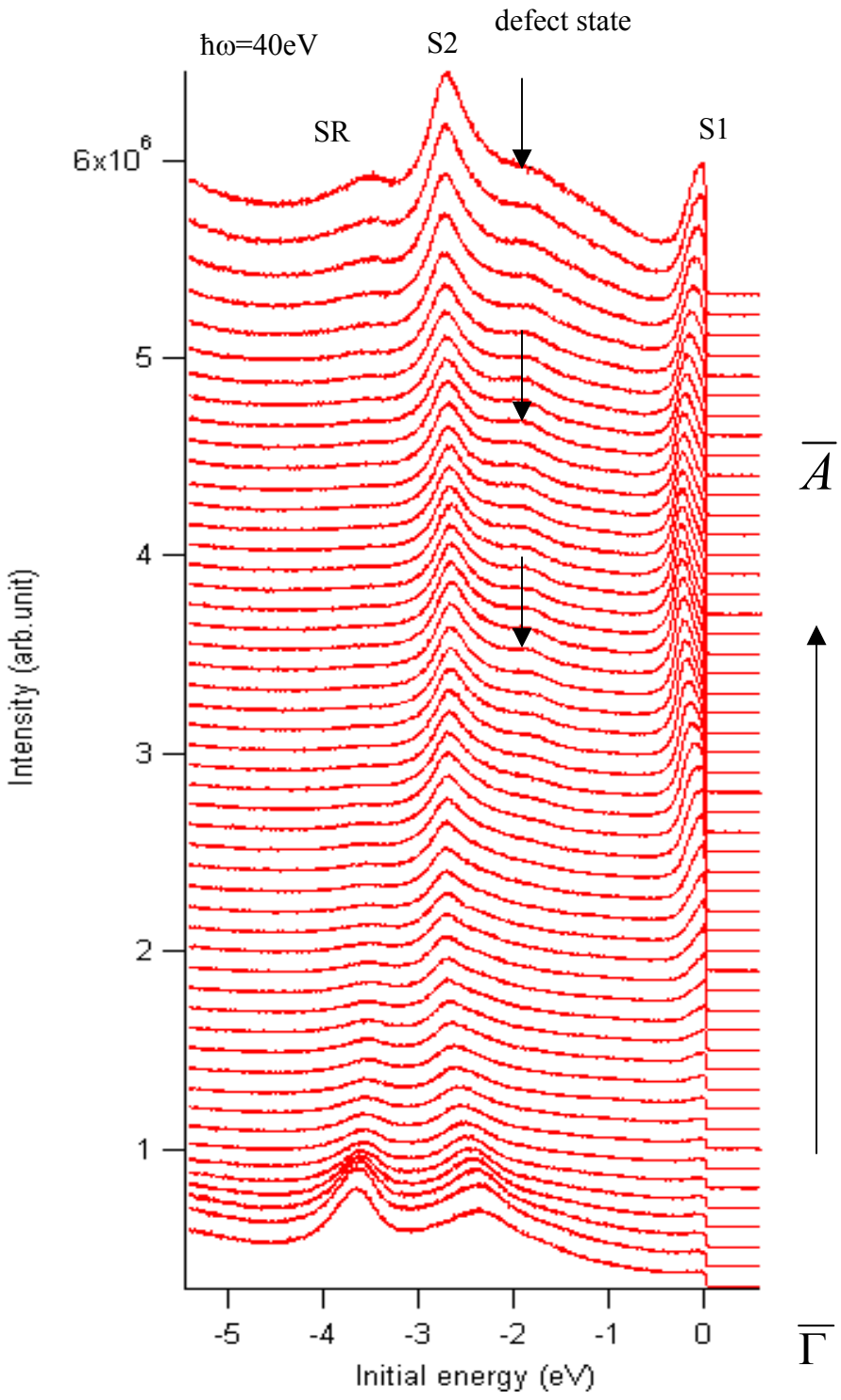

Figure 6.2 The flat dispersion of defect state around $\overline{A}$ on Be$(10\bar{1}0)$

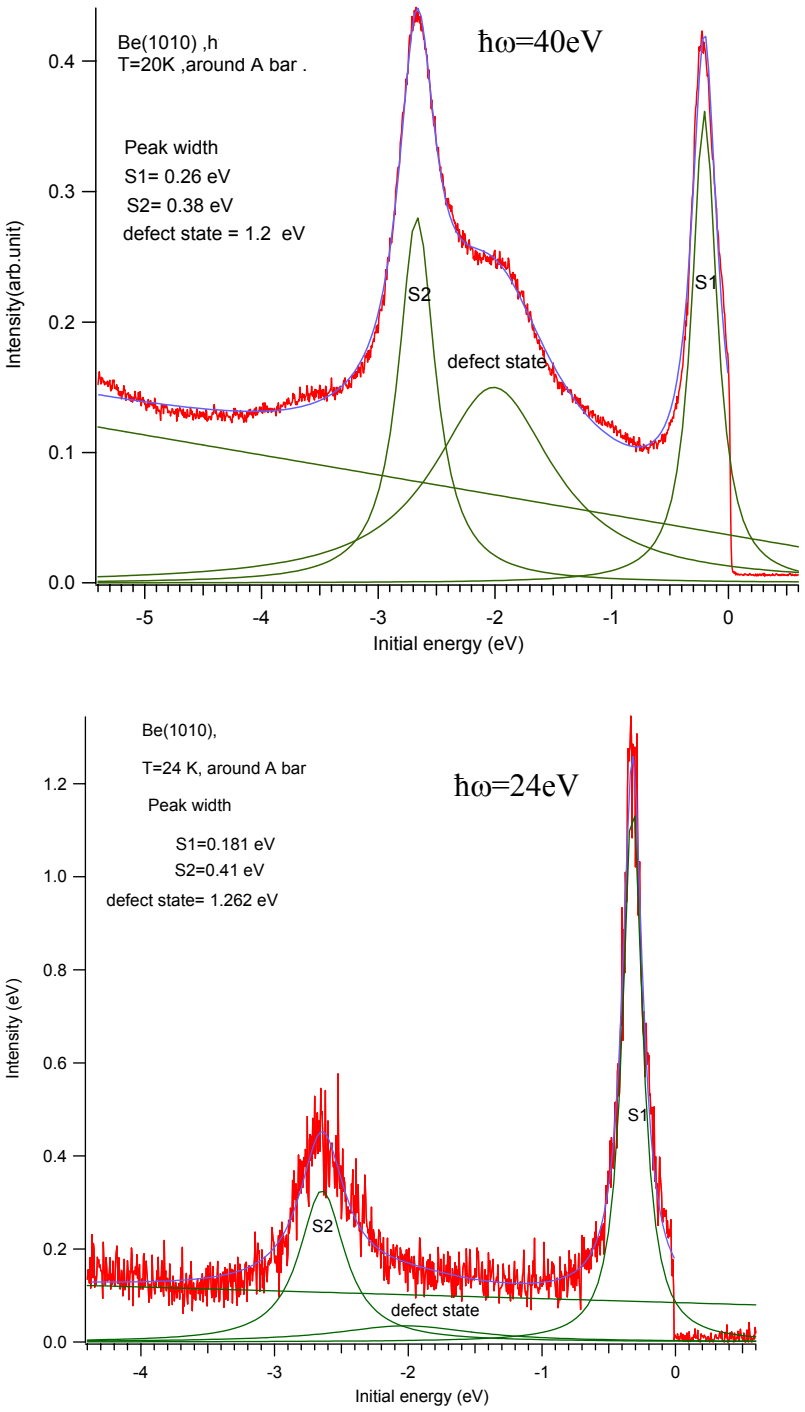

Figure 6.3 Curve fittings for defect states on Be $(10\bar{1}0)$ at two different photon energies. The spectrum is fitted with three Lorentzians and a linear background.

6.2 Electron-Phonon Interaction on Be$(10\bar{1}0)$

6.2.1 Surface Thermal Expansion on Be$(10\bar{1}0)$

From the discussion in Sections 4.5 and 4.6, imaginary and real part self-energies show consistent results that the S1 surface state has dominant electron-phonon coupling with the optical surface phonon around 64 meV. Now, the question arises "What is the physics behind this?" The first thing I would associate with this is the unique large negative thermal expansion of Be$(10\bar{1}0)$. The information implied from my results is that this optical phonon must dominate the density of the phonon states on the first layer and because of its shear horizontal character, the first layer of Be$(10\bar{1}0)$ might have dominant in-plane vibrations. Indeed, Narasimhan [18] has concluded that for most fcc open metal surfaces, atoms on the top layer have larger amplitudes of vibration in the surface plane than normal to it. Through *ab initio* density functional theory calculations combined with the frozen phonon approach, she attributed this behavior to a strong coupling between the first and third layers. Also, this strong first-to third layer force constant can be explained in terms of the bond length and bond order. Figure 6.4a shows the geometry layout of the atoms on the first three layers on a fcc open surface. It is obvious that the bond between the atoms on the first and third layers is normal to the surface. Thus, when the first layer contracts from the bulk-truncated surface, the bond length between the atoms on the first and third layers stretches more than the bond length between the atoms on the first and second layers. The force constant is therefore more

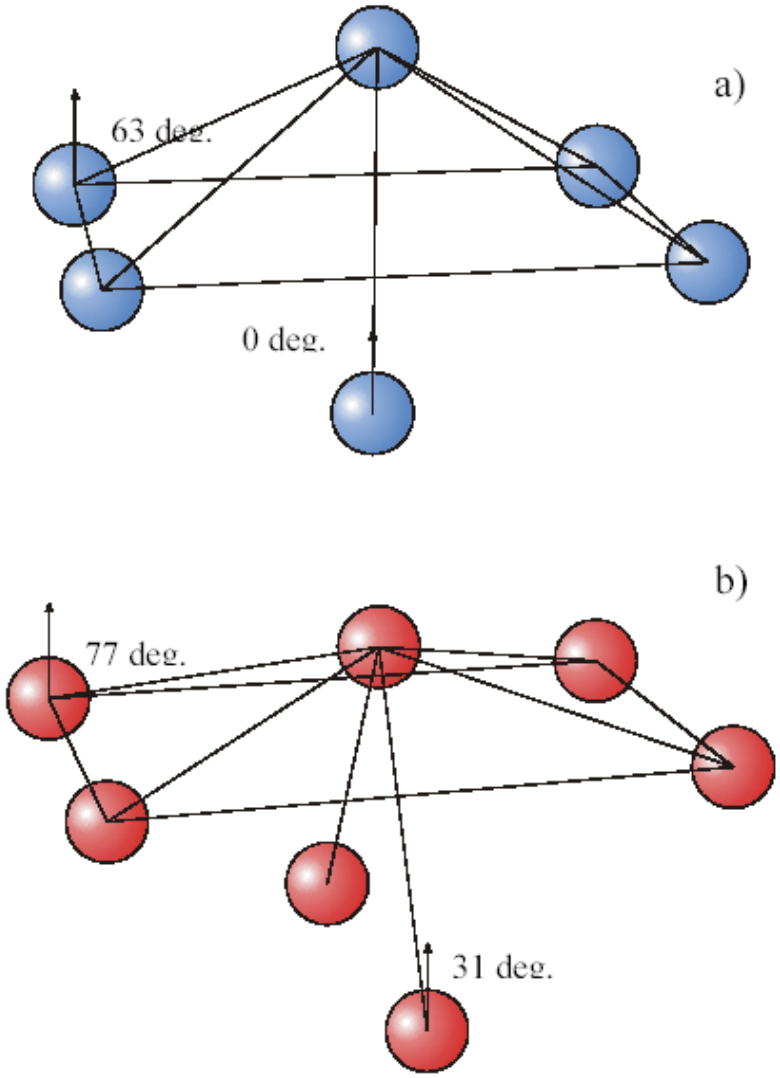

Figure 6.4 Marble model of nearest neighbor configurations for different surfaces: (a) fcc(110) and (b) hcp($10\bar{1}0$) [19]

enhanced between the first and third layers after the surface relaxes. This can also be applied to the open surface of the hcp structure, as shown in Figure 6.4b. The direction of the bond between the atoms on the first and third layers is not normal to the surface but just 31 degrees off which is much smaller than the off-normal angle, 77 degrees, for the direction of the bond between the first and second layers. The hybridization of S2 and SR in $Be(10\bar{1}0)$ indicates the back bonding either for first-second layer or first-third layer. According to the geometry model above, the latter should have much stronger effects to reduce the out-plane vibrations of the first layer on $Be(10\bar{1}0)$. Therefore, the larger in-plane vibrations (anharmonicity) of the first layer of $Be(10\bar{1}0)$ are expected and on the other hand this is also predicted from my electron-phonon coupling results that the S1 surface state, with over 70% charge on the first layer, has the most coupling with the surface optical phonon with shear horizontal character. Ismail et al have measured the thermal expansion of $Be(10\bar{1}0)$ with LEED-IV [19]. He found that there is a large thermal contraction of the first layer, as shown in Table 6.1. Michele et al. [20] used the quasiharmonic approximation to calculate the thermal expansion of $Be(10\bar{1}0)$ by minimizing the Helmholz free energy *F*. The calculated result simulates the experimental results of Ismail well [20], and furthermore, he found the anharmonicity of the out-of-plane vibrations on the second layer are much larger than that on the first layer. He considers it as the major reason for the thermal contraction of the first layer d_{12}. However, I think of it in a completely opposite way that the "less anharmonicity" of the out- of-plane vibration on the first layer should be much more relevant and interesting because it is against the common sense approach that less coordination and symmetry of

Table 6.1**:** Geometric parameters with respect to the bulk extracted from the best-fit spectra to the LEED *I-V* data for Be($10\bar{1}0$) as a function of temperature, where $\Delta d_{ij}(T)=[d_{ij}(T) - d^{bulk}(T)]/d^{bulk}(T)$ [19].

	T=0 K β_{ij}(Å/K) Extrapolated	T=110 K	T=300 K	T=500K	
Δd_{12}(%)	-27	-23.5(±3.0)	-26.7(±3.4)	-30.8(±3.8)	-12.3×10^{-5}
Δd_{23}(%)	+5.4	+6.6(±1.5)	+7.1(±1.7)	+9.6(±1.9)	$+11.8\times10^{-5}$
Δd_{34}(%)	-13.6	-13.4(±3.4)	-15.1(±3.8)	-14.2(±4.5)	-0.7×10^{-5}
Δd_{45}(%)	+1.5	+3.0(±1.8)	+3.3(±1.9)	+6.5(±2.2)	$+13.5\times10^{-5}$
d_{12}^{bulk}(Å)	0.6579	0.6589	0.6598	0.6618	0.789×10^{-5}
d_{23}^{bulk}(Å)	1.3358	1.3178	1.3196	1.3262	1.60×10^{-5}

the atoms should have more vibrational anharmonicity. It has been found that there is 4.1–4.8 times larger anharmonicity for out-of-plane vibrations on the surface layer of Cu(110) than in the bulk [21]. The enhanced outward thermal expansion of the open surface layers of Cu(110), Ni(100), and Pb(110) was all considered as the result of greatly enhanced anharmonicity of vibrations perpendicular to the surface [22]. Therefore the large inward thermal expansions of the $Be(10\bar{1}0)$ surface should be directly related to the less anharmonicity of the out-of-lane vibration on the first layer. My immediate intuition tells me this abnormal behavior has to do with the large electron-phonon coupling between the S1 surface state and high-energy optical phonon on the first layer and also the covalent-like electronic structure on the surface. Narasimhan's idea of the first-third layer coupling due to geometry consideration was used only to explain the smaller out-of-plane vibration amplitudes than the in-plane vibration on the first layer for all the fcc open surfaces, but was not able to determine the cause of negative surface thermal expansion of Al(110) [23] and outward surface thermal expansion of Cu(110) [24]. I believe the electronic back bonding structure, which further strengthens the coupling between the first and third layers, plays a crucial role, and the case is certainly most extreme for $Be(10\bar{1}0)$. Figure 6.5a and Figure 6.5b [25] show the calculated surface phonon bands on $Be(10\bar{1}0)$ for the relaxed and bulk-truncated surfaces, respectively. The biggest change of the phonon structure is that the optical phonon band is abnormally enhanced for about 20 meV after the surface relaxes. Actually, similar behavior has been observed from the surface phonon band of Al(110), where two highly localized shear mode surface phonons at $\bar{X}$ and $\bar{Y}$ are enhanced by 6.6 and 4.6 meV,

(a)

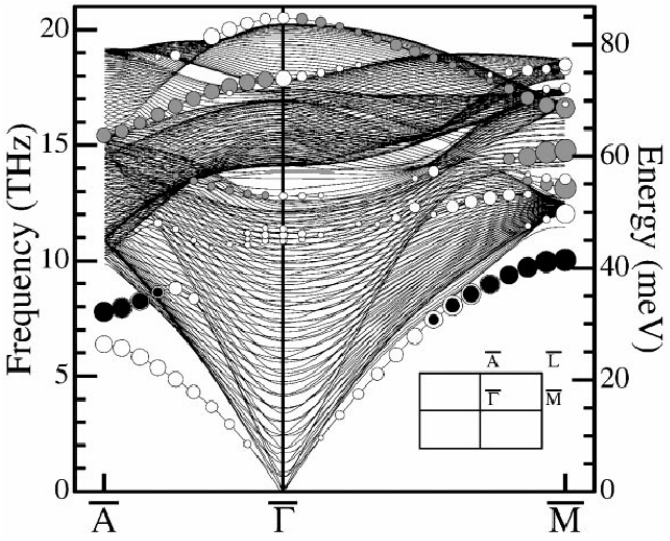

(b)

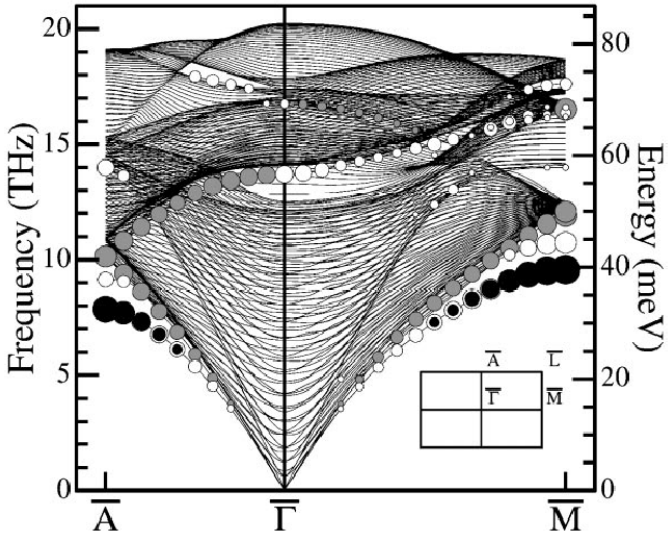

Figure 6.5 Calculated surface phonon bands for the (a) relaxed and (b) bulk-truncated Be$(10\bar{1}0)$ surfaces. The dark filled circles represent the Rayleigh wave localized on the first layer [25].

respectively, from an unrelaxed to a relaxed surface [26]. K. M. Ho attributes this only to the charge accumulation between the atoms on the first and deeper layers because of the back bonding when the surface relaxes [27]. Be atoms are much lighter than Al atoms so with much stronger back bonding strength in $\mathrm{Be}(10\bar{1}0)$, the large 20-meV enhancement of the shear mode phonon on the first layer is reasonable. In other words, the high-energy shear horizontal optical phonon ~64 meV localized on the first layer is the reflection of strong covalent-like bonding between the first and second or third layer, which in turn causes huge corrugation of the interlayer potential parallel to the surface. Narasimhan has shown that most of the fcc open surfaces have dominant in-plane vibrations on the first layer. In fact the anharmornicity of the in-plane vibrations on the first layer is dramatically enhanced with increasing temperature as was found from Al(110) [23,28], Cu(110) [29] and Ag(110) [30]. The enhancement of the in-plane vibrations anharmornicity was also found on closed surfaces and considered as the cause of the thermal expansions on those surfaces such as Ag(111) [31], Rh(111) [32], and Be(0001) [33]. My point emphasizes that whether interlayer spacing between the first and second layer, d_{12}, thermally expands or contracts, the anhormonacity of in-plane vibration on the first layer plays a same and very important role; that is, to reduce the vibrational free energy through the softening of shear-mode phonons. The thermal dynamic state of the surface can be determined by the minimum of Helmholtz free energy [31]. That is,

$$F(d_{12},T) = E_{stat}(d_{12}) + \sum_i F_{vib}^i(d_{12},T) \tag{6.1}$$

The first term is the static interlayer potential between the first and second layer. The second term is the vibrational free energy corresponding to vibrations in the i-th direction, which, in the quasiharmonic approximation, is given by

$$F_{vib}^{i}(d_{12},T) = k_B T \ln\left\{2\sinh\left(\frac{\hbar\omega_i(d_{12})}{2k_B T}\right)\right\} \tag{6.2}$$

As for the thermal expansion, both terms (static and vibrational) are equally important in the sense that when the temperature increases, surface electrons would rearrange and the vibrations of atoms would turn more anharmonic to reduce both static and vibrational contributions to the surface free energy. However, this can be a difficult case for $\mathrm{Be}(10\bar{1}0)$ where there is a strong covalent like back bonding structure near the surface, causing large inward 25% relaxation at $T = 0$. Therefore, when the temperature increases, it is energetically unfavorable to break this strong back bonding to make the first layer expand. On the contrary, the surface electron charge would move in such a way to strengthen the attraction between the first and second layer and thus lower the static interlayer potential to a new minimum. This behavior may cause less anharmornicity of the out-of-plane vibration on the first layer than on the second layer with increasing temperature. It is worth noting that between $\bar{A}$ and $\bar{\Gamma}$, the Rayleigh wave, whose amplitude is perpendicular to the surface, localized on the first layer (indicated by the dark full circle in Figure 6.5a) has larger energy than the Rayleigh wave localized on the second layer (indicated by the empty circles) on the $\mathrm{Be}(10\bar{1}0)$ relaxed surface [25]. It would be necessary to measure or calculate the temperature dependence of both Rayleigh waves localized on the first and second layers, respectively.

Therefore, it is possible that the thermal contraction behavior on the first layer is the result of combat between surface electron charges and normal lattice thermal expansion, and the electron-phonon coupling is somehow a mediator. Under this picture, I propose two models for the thermal contraction of the $Be(10\bar{1}0)$ surface.

I. Dynamic Charge Smoothing Model

$Be(10\bar{1}0)$ has very large charge corrugation on top of the surface, and this charge corrugation is mostly contributed by the S1 surface state, as shown by the charge density distribution contours in Figure 6.6. Hybridization of the S2 and SR states set up a very firm coupling between the first and third layer. At T = 0, charge smoothing allows a reduction of the kinetic energy of electron charges corrugated on the surface. When the temperature increases, the S1 surface state electrons would tend more to move into the hallow region between atoms on the surface to make the first layer further contract and also to smoothen the potential corrugation parallel to the surface. According to Narasimhan's calculation from Ag(111) [31], when the interlayer potential corrugation parallel to the surface decreases, the anharmonicity of the in-plane vibration of the surface layer will increase. Therefore, if the S1 surface electron charges do the job of screening ion cores on the surface, then the dynamic charge smoothing effect would enhance the in-plane vibration of the $Be(10\bar{1}0)$ surface and decrease the energy of the shear horizontal optical phonon. I consider this enhanced screening between S1 electrons and ions as an indicator of enhanced electron-phonon coupling between the S1 surface state and optical phonon on the surface.

My results of the temperature dependence of a surface initial energy shift support this idea. As shown in Figure 4.20, the initial energies of the S1 and S2 surface states shift in opposite directions so that the energy separation between two surface states gets smaller with increasing temperatures. As mentioned previously, the energy separation between two different symmetry surface states at the surface zone boundary is the measure of surface potential corrugation. Thus, it is obvious that surface potential corrugation on Be$(10\bar{1}0)$ is reduced with increasing temperatures. The S1 surface state is so localized on the surface that its initial energy shift with temperature is completely independent of the bulk lattice expansion. It is reasonable to attribute the abnormal shift of the S1 surface state to the many-body effects — electron-phonon coupling. The slight shift of the S1 surface state to lower initial energy with increasing temperatures might be connected to the increasing imaginary part of self-energy through the Kramers-Kronig relation with the real part of self-energy. Anyhow, the biggest problem for dynamic charging smoothing effects is that no convincing driving force can be identified for the temperature dependence of surface charge smoothing.

II. Nonadiabatic Electron-Phonon Coupling Model

The elementary meaning of electron-phonon coupling is the excitation of the electron–hole pair though absorbing or creating a phonon. Thus electron-phonon coupling can be viewed as a direct manifestation of the breakdown of the adiabatic approximation in the solid. In the Born-Oppenheimer adiabatic approximation, the

motion of atoms and electrons in a solid are considered to be completely independent. This is often a valid approximation because electron velocities are far larger than atom velocities in most solids. However, the adiabatic approximation will break down if the velocity of electrons is reduced. In an one-electron band picture, the requirement of slow electrons translates as a need for nearly flat bands. Additionally, because phonon vibrational energies are typically much smaller than electron binding energies, a strong breakdown of adiabaticity will only occur if flat electron bands reside close to E_f. This nonadiabatic electron-phonon coupling concept has been used to explain the softening of certain surface phonons at certain directions between the zone center and zone boundary, the Kohn anomaly, in the systems such as W(001), Mo(001), H/W(001) and H/Mo(001) [34-36]. All these systems have very localized surface states dispersing flatly and dominating the density of states close to the Fermi level. Further more, the unique surface reconstruction of W(001) and Mo(001) at low temperatures has been attributed to the instability of the surface caused by the strong nonadiabatic electron-phonon coupling [37]. The temperature-driven phase transitions on these two surfaces accompany the quasi one-dimensional Fermi surface nesting [37] and damping of certain surface phonons through electron-hole excitation on the Fermi surface.

Turning back to our object, $\mathrm{Be}(10\bar{1}0)$, there is also a very localized S1 surface state dispersing flatly and dominating the density of states close to the Fermi level. In addition, I found that there is dominant electron –phonon coupling between the S1 surface state and the surface optical phonon. Even though there is no surface reconstruction observed on $\mathrm{Be}(10\bar{1}0)$, the nonadiabatic electron-phonon coupling picture can still be plugged into the physics of large thermal contraction of this surface.

Furthermore, the high energy of the surface optical phonon, 64meV, indicates the faster speed of ions and thus facilitates the nonadiabatic interaction with electrons.

To build the nonadiabatic model for the thermal contraction of the Be$(10\bar{1}0)$ surface, we have to start from the inward relaxation at $T = 0$. When forming the surface, surface electrons with p_z orbital character would either scatter to p_x and p_y obitals or demote itself to *s* obitals. The former can be represented by the hybridization between S2 and SR states, which caused the back bonding of the surface layers and the latter occurs to the S1 surface state, causing most of its charge localized on top of the atom on the surface. The S1 surface state is *s* and p_z type. As shown in Figure 6.6, the 70% of charge density distribution of the S1 surface state on top of the surface is *s* type and the 30% of its charge between the first and third layers is p_z type. Therefore, the S1 surface state is actually a very localized dangling bond state, which "borrows" some electrons from the bulk states through demotion from p_z to *s* when the surface relaxes. However, when the temperature increases, the promotion of the electrons from the *s* orbital to the *p* orbital will be more and more favored through the spilling of electrons from the S1 surface state back to the bulk. This process is equivalent to the excitation of the S1 surface state electrons close to the Fermi level to the unoccupied bulk states. More S1 surface electrons moving to the bulk *p* states indicates there would be more bonding between the surface layers and deeper layers and, thus causing thermal contraction. In addition, more "bonding" and less "dangling" for the S1 surface state with increasing temperature can explain why its initial energy goes lower as shown in Figure 4.20. Needless to say, the role of phonons in this model is helping to assist the

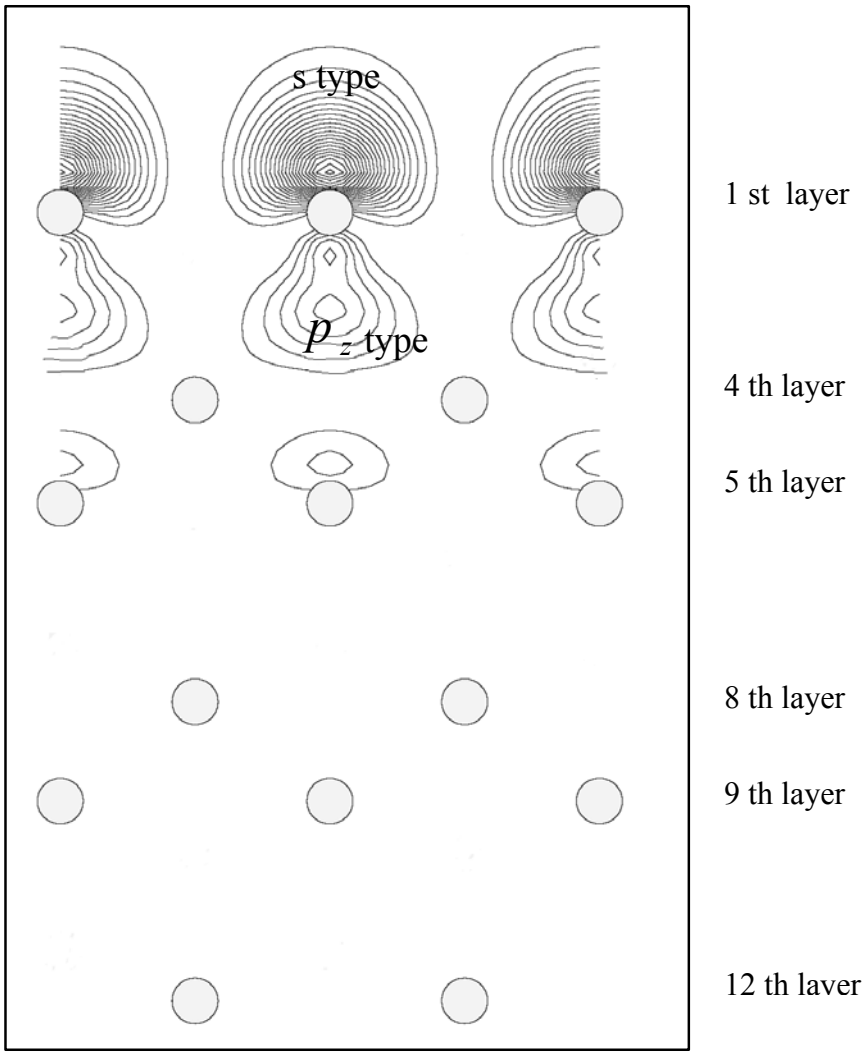

Figure 6.6 Contour plot of the charge distributions of the S1 surface state on (0100) cut plane where only 1st, 4th , 5th, 8th, 9th,and 12th layers … are in the cut plane. 70% of it charge is *s* type above the top layer, and 30 % of its charge is p_z type below the surface [8].

excitation of the S1 surface state electrons to the unoccupied bulk state band in addition to thermal excitation. The benefits of dominant coupling with optical phonons for the S1 surface state are (1) The momentum conservation for the excitation of the electron-hole pair by the phonon can be neglected due to the weak dispersion of optical phonon over momentum k space. In other words, S1 surface state electrons can be excited to an arbitrary unoccupied bulk state band in all directions and positions in k space to compensate for the fact that there is only a small bulk Fermi surface on the $(10\bar{1}0)$ surface Brillouin zone, as shown in Figure 4.7b. (2). From Figure 4.3b for the bulk density of states distribution in Be, there is a dip about the Fermi level. In order for there to be optimum excitation from the S1 surface state to the unoccupied bulk state, higher energy optical phonon is definitely favored. The softening of this optical phonon dispersion around 64 meV with increasing temperature is expected. The Kohn anomaly has been observed to happen to adsorbate optical phonons on the H/Mo(110) and H/W(110) systems [38].

This model works best for the system where there is a very localized surface state and small Fermi surface contributed by the bulk state. For a typical semiconductor surface, there are hardly any bulk state bands near the Fermi level, the surface state electrons would only be spilled to other surface state bands and cause the in-plane surface reconstruction. For a typical free-electron-like metal surface, the Fermi surface is mostly contributed by the bulk state, and the surface state itself is already very delocalized into the bulk. It is worth noting that Cu(110) and Ag(110) also have two different symmetry surface states at the zone boundary $\bar{Y}$ [39,40]. Their S1 surface state with *s* and p_z symmetry is unoccupied and above the Fermi level. This nonadiabatic model for

Be$(10\bar{1}0)$, hence, has no way to work for these two metal surfaces. As mentioned previously, Cu(110) and Ag(110) have very large thermal expansion. This model seems more reasonable than the dynamic charge smoothing model, but the only incomplete part is that the role of in-plane vibration of the optical phonon in this model has not be identified.

6.2.2 Surface Superconductivity on Be$(10\bar{1}0)$

I. From the Conventional BCS Picture

Another interesting surface property which my results of electron-phonon coupling on Be$(10\bar{1}0)$ can lead to is surface superconductivity. The properties of the conventional weak-coupling superconductors were already developed in the 1950s and attributed to the electron-phonon interaction, based on the work of Bardeen, Cooper, and Schrieffer (BCS) [41] . The key concept of this theory is the electron phonon interaction that, below the transition temperature T_C, correlates two electrons to a Cooper pair. The result of this pairing is a lowering of the total energy of the system and the opening of a narrow superconducting gap of the order of a few meV in the electronic density of states (DOS) around the Fermi level. The ratio of the energy gap Δ at T= 0 K to the transition temperature T_C is predicted to be the same for all the conventional superconductors and can be given (in the weak coupling limit) by

$$2\Delta / k_B T_c = 3.5 \tag{6.3}$$

The temperature dependence of the gap at finite temperature below T_C is given by a universal function of T/T_C, namely,

$$\Delta(T) = 3.2k_B T_C \sqrt{1-\frac{T}{T_C}} \tag{6.4}$$

W. L. McMillan [42] further formulated important relations between the superconductivity property and electron-phonon coupling as follows

$$\lambda = N(0)\langle I^2 \rangle \,/ M\langle \omega^2 \rangle \tag{6.5}$$

$$k_B T_C = (\hbar\omega_D / 1.45)\exp\left[-\frac{1.04(1+\lambda)}{\lambda - \mu^*(1+0.62\lambda)}\right] \tag{6.6}$$

where $N(0)$ is the DOS at the Fermi level per spin per atom, $\langle I^2 \rangle$ is the properly averaged electron-ion matrix element squared, M is the atomic mass, $\langle \omega^2 \rangle$ is the averaged phonon frequency, and μ^* represents the effective Coulomb interaction and is typically 0.1. From relations (6.5),(6.6), it is easy to see why the Be bulk has such a low electron-phonon coupling value $\lambda = 0.24$ and that is because Be bulk has very few electron DOS at the Fermi level and a large average phonon frequency. However, for either the Be(0001) or Be$(10\bar{1}0)$ surface, the large contributions to DOS at the Fermi level and smaller averaged phonon frequency certainly cause much larger electron-phonon coupling of the surface states, as we observed. If we plug surface Debye energy $\hbar\omega_D = 60meV$ and $\lambda = 0.64$ for Be$(10\bar{1}0)$ to the relation (6.6), the high transition temperature is obtained, $T_C \approx 17\,\mathrm{K}$, which is 600 times larger than the bulk value

$T_C \approx 0.024\,\mathrm{K}$[43]. The same thing applies to the Be(0001) surface [44]. However, we have to be careful with the fact that the Cooper pairs formed in the surface region where the interaction is high can leak into the bulk and break apart [45]. Thus a thin Be film grown on the insulator should exhibit high T_C. It is well know that amorphous thin films of Be have T_C near 10 K. Another concern is that impurities/defects will likely play a more important role in destabilizing the system than they can do in homogeneous superconductors. The problem is that the impurities scatter surface states into bulk states, the one-electron eigenstates become linear combinations of surface and bulk states, and the pairing interaction is averaged over the surface and the bulk. This averaging certainly destroys superconductivity at the surface. The zero temperature coherence length of a superconductor can be written as

$$\xi = \hbar v_F /(2\pi k_B T_C) \tag{6.7}$$

where v_F is the Fermi velocity. The surface defect and impurities reduced the mean free path of the surface state electrons. If the mean free path of the surface state electrons is smaller than the coherence length of the superconductor, then superconductivity is less likely. From the two concerns above, Be$(10\bar{1}0)$ has far more chances to have high-T_C superconductivity than Be(0001). S1 surface state on Be$(10\bar{1}0)$ is more localized on the top layer than the surface state on Be(0001) [7,46]. And under the first layer, the electronic structure is more covalent-like because of the back bonding. The chance the cooper pairs formed by the surface state would leak into the bulk is correspondingly less. Furthermore, the S1 surface state on Be$(10\bar{1}0)$ has less Fermi velocity v_F than the surface state on Be(0001), and this would cause less coherent length. A smaller coherent

length would allow more surface state electrons to form the Cooper pairs. In addition to the surface defect scattering, the electron-electron scattering must be mainly surface-to-surface since the S1 surface state is so localized in the center of the band gap. As for electron-phonon scattering, needless to say, the dominant e-p coupling between the S1 surface state and localized optical phonon further ensures the surface-to-surface scattering channel.

II. From the Unconventional HTSC Picture

The high-temperature superconductotor (HTSC) is unconventional in the sense that the transition temperature T_C measured from this material is much higher than those predicted from the BCS theory. The transition temperature of $\mathrm{Be}(10\bar{1}0)$ predicted by the BCS theory is about 17 K which is still low compared to that of HTSC. However, since nobody has measured the superconductivity of the $\mathrm{Be}(10\bar{1}0)$ surface so far, the possibility of a higher T_C value cannot be ruled out. Futhermore, the relation (6.5) from the BCS theory shows that the electron-phonon coupling strength λ is inversed to the phonon frequencies. Therefore, our conclusion that the dominant coupling of the localized S1 surface state and localized higher energy optical phonon causes enhanced electron-phonon coupling on the surface seems controversial to the conventional BCS theory. It ss instructive to look at some of the arguments developed for HTSC and compare them with the unique properties I observed from $\mathrm{Be}(10\bar{1}0)$ surface.

The group led by Z.X. Shen [47] has proposed that the electron-phonon interaction is still the most important mechanism for the high-temperature

superconductivity. They found a common "kink" in the dispersion of the band around 50-80 meV from the Fermi level in the high resolution photoemission spectra over three different families of copper oxide superconductors at different dopings and with different sizes of superconducting gaps. This phonon interpretation receives strong support from the neutron scattering data that show the energy of the zone boundary in-plane oxygen-stretching longitudinal optical (LO) phonon, identified by neutrons as being strongly coupled to charge, coincides with the kink energy between 50 and 80 meV. This mode is identified as the highest energy phonon that contributes strongly to the "kink," which still persists above the transition temperature as expected for electron phonon interaction except that a thermal broadening is present. This common phenomenon in several different HTSC systems happens to coincide with my findings on Be$(10\bar{1}0)$ that the S1 surface state has dominant coupling with the high-frequency optical phonon, and in the S1 surface state band, it also has a kink shape centered at this optical phonon energy at around 64 meV.

The discovery of superconductivity with $T_C \approx 39\,\mathrm{K}$ in magnesium diboride (MgB_2) in January, 2001 has caused excitement in the solid state physics community because it introduced a new, simple (three atoms per unit cell) binary intermetallic superconductor with a record high (by nearly a factor of 2) superconducting transition temperature for a nonoxide and non-C60-based compound [48]. The reported value of $T_C \approx 39\,\mathrm{K}$ is either above or at the limit suggested by the conventional BCS theory, phonon-mediated superconductivity. According to the previous studies on MgB_2, I find there are actually several similarities of the properties between the MgB_2 and Be$(10\bar{1}0)$.

First, the structures are both simple, and the atoms of both are light. Light atoms are beneficial for superconductivity from BCS theory. Second, the calculated band structure shows that MgB_2 is a typical *sp* metal with a typical DOS around the Fermi level. However, this particular sp metal is held together by strong covalent B-B bonding and ionic B-Mg bonding. Strong bonding induces strong electron-ion scattering and, hence, strong electron-phonon coupling [49]. Third, the superconductivity of MgB_2 is mainly induced by the electron-phonon coupling of the boron σ band state and in-plane B-B E_{2g} vibration phonon at high energy, 64 meV [50]. Especially, the σ band state is almost two-dimensional and contributes strongly to the DOS around the Fermi level [50]. Attempts have been made to calculate the transition temperature only from the electron-phonon coupling between the boron σ band state and in-plane E_{2g} vibration phonon through the relations (6.5),(6.6) form the BCS theory. The resulting T_C is 32–46 K, consistent with the experimental result. It is possible that the covalent-like bonding between the first and deeper layers in $Be(10\bar{1}0)$ and the resulting high frequency optical phonon around 64 meV, which dominates the coupling with localized S1 surface state, make $Be(10\bar{1}0)$ have a similar superconducting property to MgB_2.

Therefore, it seems that if the electron-phonon coupling is still the cause for high-T_C superconductivity, then the BCS theory needs to be modified and generalized. One of the key things for the modification should be the consideration of the dominant coupling of the high frequency phonon and electron states. Nevertheless, according to the analysis above in terms of either conventional BCS theory or HTSC arguments, I definitely believe that the $Be(10\bar{1}0)$ surface has high-T_C superconductivity. Be has a very simple

sp structure so a finding of the high-T_C superconductivity on the Be$(10\bar{1}0)$ must have a big influence on the solid state physics because it will definitely give the most original and exact picture of how electron-phonon coupling mediates the high-T_C superconductivity.

6.3 The Relation between the Electronic Structure and Lattice Structure on Mg$(10\bar{1}0)$

From the study of temperature dependence of surface states on Mg$(10\bar{1}0)$, the electronic structure on the surface is closely related to the bulk. Therefore, the special lattice behavior on the Mg$(10\bar{1}0)$ surface is more difficult to associate with the surface states. However, as measured by Ismail through LEED-IV [52], the first layer of Mg$(10\bar{1}0)$ also has the property of inward relaxation. Table 6.2 shows his measurement results with first-principle calculations results.

Table 6.2 Measured and calculated results for the surface relaxation on Mg$(10\bar{1}0)$ in percentages [52]

Data source	Δd_{12}	Δd_{23}	Δd_{34}	Δd_{45}	Δd_{56}
theory	-14.9%	6.9%	-7.5%	1.7%	-4.7%
experiment	-14.5%	6.5%	-7.5%	3.0%	-5.0%

The free electronic-like property of the $Mg(10\bar{1}0)$ surface indicates a strong electron screening effect on the surface. Based on the realization that the biggest defect at a surface is the very presence of the surface itself and the screening of this defect by the itinerant electrons establishes electron density oscillations propagating into the bulk, J-H. Cho et al. [53] have used the Freidel oscillation model as a driving force for multilayer oscillatory relaxation on the $Mg(10\bar{1}0)$ surface. When comparing the charge density profile for the bulk-truncated surface and bulk Mg, he found that the change in the charge density on the bulk-truncated surface relative to the bulk shows the damped density oscillations away from the surface. These oscillations do not follow the periodicity of the lattice but instead, the period of oscillations is close to the wavelength of the Freidel oscillations obtained by assuming a spherical Fermi surface in the bulk. The electronic static force between layers accompanied by the damped density oscillations causes multilayer relaxation on the surface. The picture of $Mg(10\bar{1}0)$ will be clearer in comparison with $Be(10\bar{1}0)$. Figures 6.7a,b show the one-dimensional charge density profiles for the bulk-truncated and relaxed $Be(10\bar{1}0)$ and $Mg(10\bar{1}0)$ surfaces. Figures 6.7c,d show the change of charge density, relative to the bulk crystal, at the bulk-truncated and relaxed $Be(10\bar{1}0)$ and $Mg(10\bar{1}0)$ surfaces [15]. The electron density variations from the bulk to the bulk-truncated surface is significant on $Mg(10\bar{1}0)$ but faint on $Be(10\bar{1}0)$. It confirms the existence of 3D Freidel oscillation from the $Mg(10\bar{1}0)$ surface into the bulk but as for $Be(10\bar{1}0)$, the covalent chemical bonding under the first layer limits the Freidel oscillation completely to the 2D surface [14].

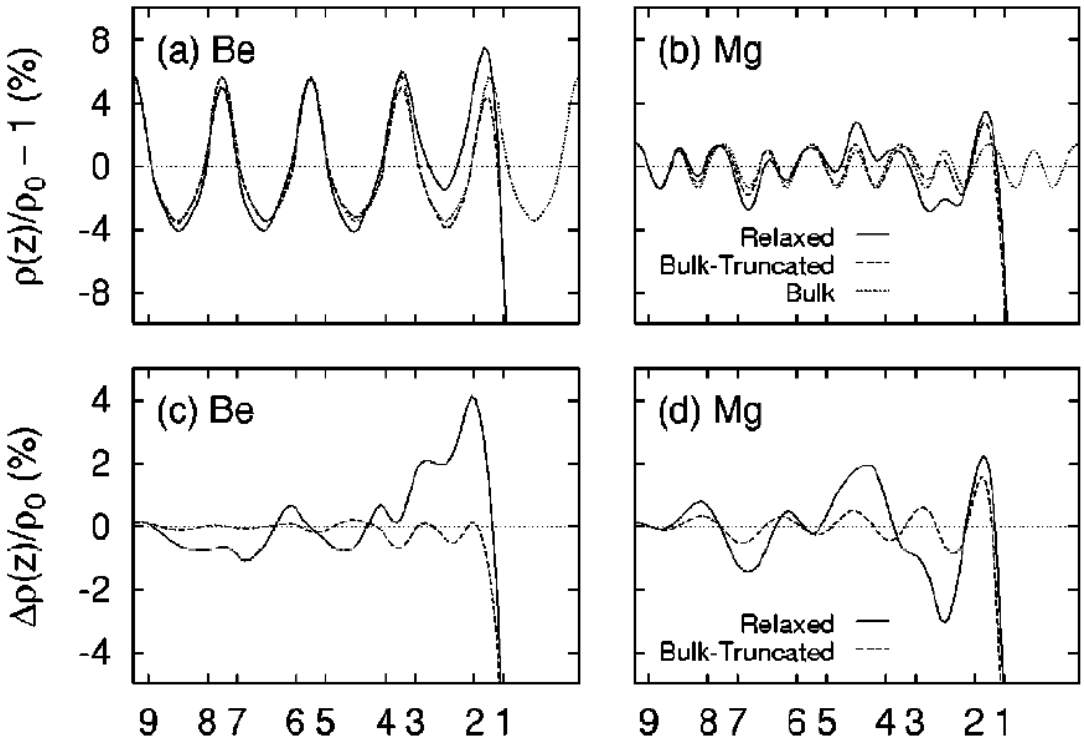

Figure 6.7 One-dimensional charge density profiles for the bulk-truncated and relaxed surfaces, (a) Be$(10\bar{1}0)$, and (b) Mg$(10\bar{1}0)$. Change of charge density related to the bulk crystal at bulk-truncated and relaxed surfaces, (c) Be$(10\bar{1}0)$, and (d) Mg$(10\bar{1}0)$ [53]

From the bulk-truncated surface to the relaxed surface, the charge density change is negligible on $Mg(10\bar{1}0)$ but incredibly strong on $Be(10\bar{1}0)$. It indicates such a strong electron screening mechanism from the $Mg(10\bar{1}0)$ surface to the bulk that the change of the lattice layer positions is completely "blocked out." However, as for $Be(10\bar{1}0)$, the big change of charge density profile for the relaxed surface just corresponds to the intense formation of the back bonding between the first and deep layers from the surface broken bonds. This behavior of the charge density profile is reflected from the surface core level shifts (SCLS). The SCLS at $Be(10\bar{1}0)$ persist down to the fifth layer, and the second layer gives the most contribution. However, according to J-H. Cho's calculations [53], only one SCLS comes from the first layer atoms on $Mg(10\bar{1}0)$. Actually, my measurements of core *2p* spectra on $Mg(10\bar{1}0)$ also show the same thing. Figure 6.8 shows the measured core *2p* peak and fitting curves with Doniach-Sunjic background. The core *2p* peak is split due to a spin-orbital effect. Through the fitting, only one surface component can be extracted, and the shift amount is about 0.25 eV, which is very close to J-H Cho's result [53], 0.23 eV, for first-layer contribution.

Another electronic model, which has been proposed for explaining the oscillatory relaxation of the $Mg(10\bar{1}0)$ surface, is to focus on the S1 surface state at $\bar{A}$ [54]. If one uses the wave vector perpendicular to the surface at the bulk band edge at L, the charge density profile derived from the S1 surface state wave function at a suitable phase can be similar to that derived from Friedel oscillations. It would be interesting to see the initial energy shift of the S1 surface state from bulk truncated to relaxed surface through calculations.

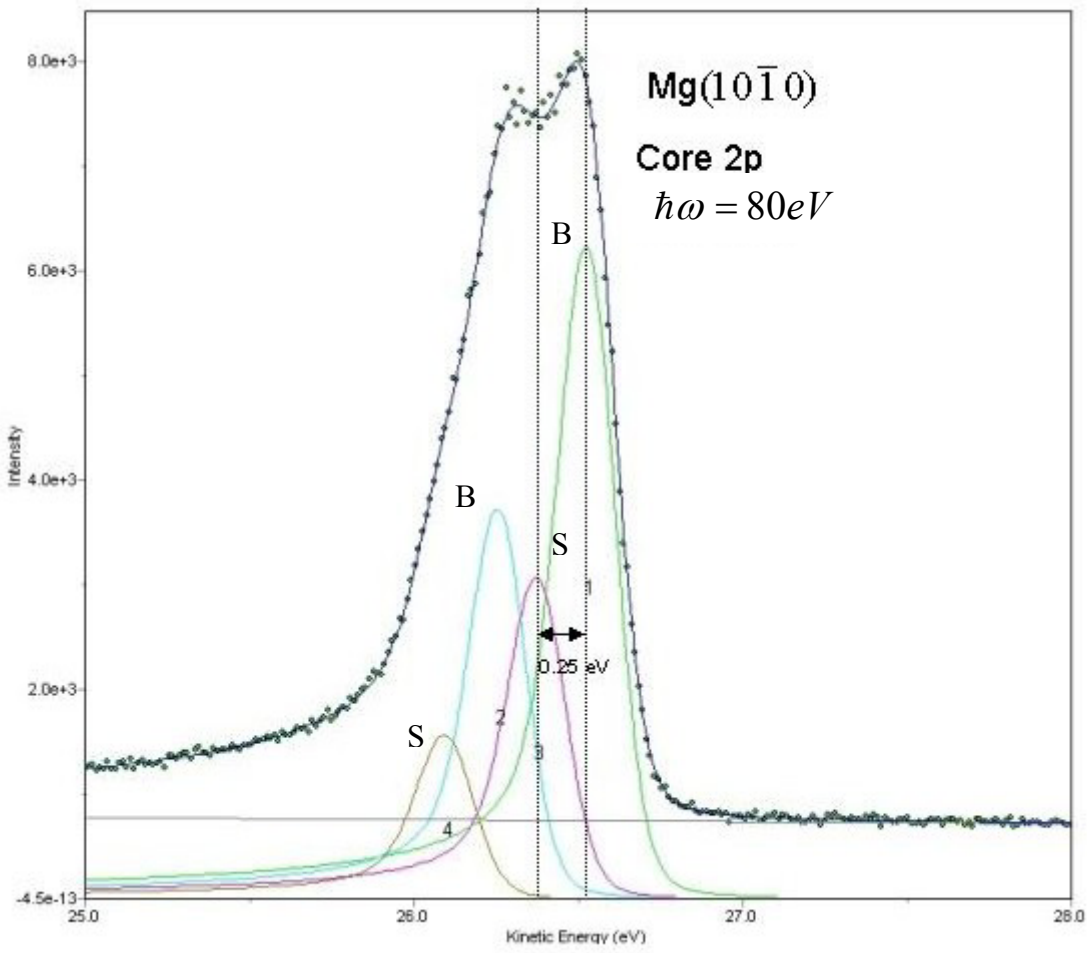

Figure 6.8 Analyzed core 2*p* spectra on $Mg(10\bar{1}0)$. The peak labeled by B (S) is contributed to by the bulk (surface). Each contribution is split due to the spin-orbital interaction

The biggest problem of the Friedel oscillations model and the S1 surface state model is the lacking of experimental support and a difficulty to relate to the thermal dynamic behavior. I have tried to see the 2D Friedel oscillations on $Mg(10\bar{1}0)$ by Sanning tunneling microscopy, STM, but could not observe it because of the surface roughness. And, as mentioned before, my temperature-dependent data show the surface states at $\bar{A}$ on $Mg(10\bar{1}0)$ have an intimate relationship between the surface and bulk. This makes it difficult to extrapolate the importance of the surface state for special surface lattice behavior.

As for the surface thermal expansion, Ismail's temperature-dependent LEED-IV results in Table 6.3 [55] show the oscillatory thermal expansion with increasing temperature on $Mg(10\bar{1}0)$. Mechele [20] has used the quasiharmonic approximation (QHA) by minimizing the Helmholtz free energy F at different temperatures and achieved good agreement with the experimental results. According to his calculations, the anharmonicity for the out-of-plane vibrations on the first layer is still larger than that on the second layer as opposed to the case for $Be(10\bar{1}0)$. However, he found the in-plane lattice expansion plays an important role for the contraction between the first and second layers. Even though Mechele attributed it to the static contribution, I myself believe it indicates that the anharmonicity for the in-plane vibration on the first layer is very important for the first layer thermal contraction, as is the case for $Be(10\bar{1}0)$. Figure 6.9 shows Mechele's calculated surface and bulk projected phonon bands on $Mg(10\bar{1}0)$ for the relaxed surface [56]. There is also optical phonon band dispersing between 20 and 30 meV from $\bar{A}$ to $\bar{\Gamma}$. Compared to the calculated surface phonon bands on

Table 6.3 The measured surface oscillatory thermal expansion on $Mg(10\bar{1}0)$ by LEED-IV

Temperature	120 K	300 K	400 K
Δd_{12} (%)	-16.4 ± 2.0	-21.1 ± 2.0	-20.6 ± 2.7
Δd_{23} (%)	$+7.8\pm1.0$	$+9.4\pm1.4$	$+10.6\pm1.6$
Δd_{34} (%)	-10.5 ± 3.0	-15.3 ± 3.0	-17.5 ± 4.0
Δd_{45} (%)	$+3.8\pm1.6$	$+4.9\pm2.0$	$+4.3\pm2.0$
Δd_{56} (%)	-5.5 ± 3.0	-12.1 ± 4.0	-6.9 ± 5.0
Δd_{67} (%)	$+0.6\pm2.0$	$+2.9\pm2.5$	$+2.0\pm3.5$
d_{12}^{bulk} (Å)	0.923	0.927	0.929
d_{23}^{bulk} (Å)	1.846	1.854	1.858

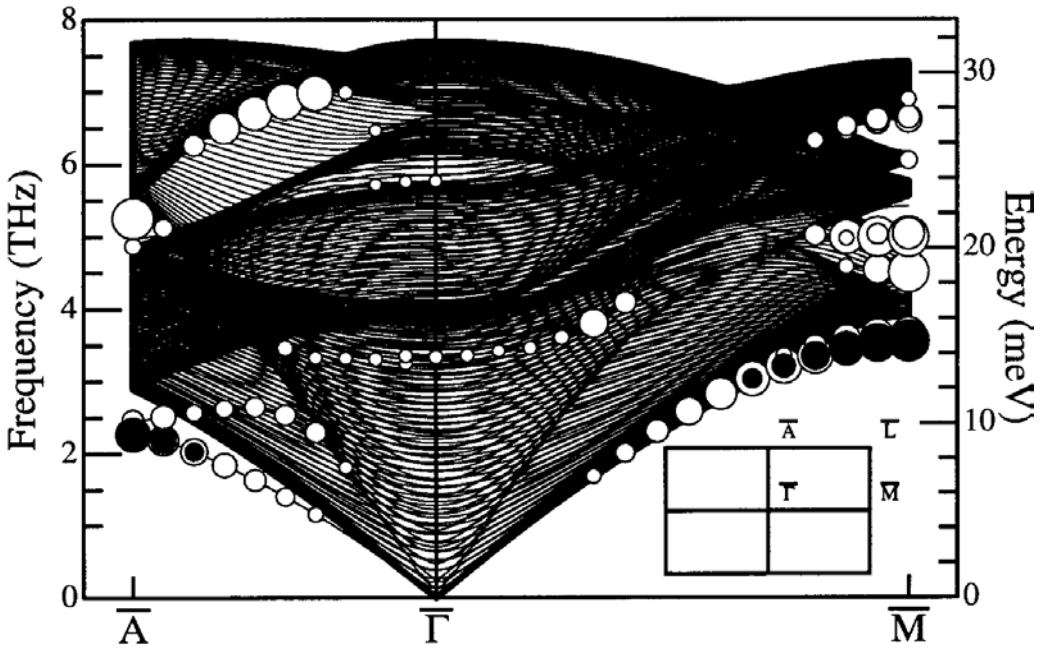

Figure 6.9 The calculated surface phonon band on the relaxed surface of $Mg(10\bar{1}0)$. The dark filled circles represent the Rayleigh wave localized on the first layer [56].

$Be(10\bar{1}0)$, the dispersions of two Raleigh wave phonons from $\bar{A}$ to $\bar{\Gamma}$ on $Mg(10\bar{1}0)$ are normal in the sense that the phonons with lower energy are more localized in the first layer, as shown by full dark dots at around 10 meV. In the previous section, I emphasized that the higher phonon energies of the optical phonons and Raleigh wave phonons localized on the first layer of $Be(10\bar{1}0)$ are due to the strong electrostatic back-bonding force between the first and the deeper layers. Therefore, it is clear that back bonding is not as relevant on $Mg(10\bar{1}0)$. The energy separation between the S1 and S2 surface states on $Mg(10\bar{1}0)$ is around 0.5 eV much smaller than that of 2.3 eV on $Be(10\bar{1}0)$. The charge corrugation smoothing effect, which further strengthens the attraction between the first and second layer, on $Mg(10\bar{1}0)$ is thus not as much as on $Be(10\bar{1}0)$. With most of theFermi surface contributed by the bulk states on the surface Brillouin zone and much deeper penetration of the surface states into the bulk, the nonadiabatic model for charge spilling from the surface state to the bulk state is less likely to apply to $Mg(10\bar{1}0)$. Possibly, these are the reasons why $Mg(10\bar{1}0)$ has less first-layer inward relaxation and thermal contraction than $Be(10\bar{1}0)$[Table 4.1,6.1,6.2,6.3]. Nevertheless, surface relaxation is the process of redistribution of the electronic charge due to the reduced dimensionality to achieve lower surface free energy and the resulting charge distribution would cause the position change of the surface layers. As for surface thermal expansion, the temperature dependence of both electronic charge and phonon distributions has to be considered. There is no as unique a surface electron structure on $Mg(10\bar{1}0)$ as there is on the $Be(10\bar{1}0)$ surface. Therefore, the lattice and atomic property would be relatively a more important factor in the case for

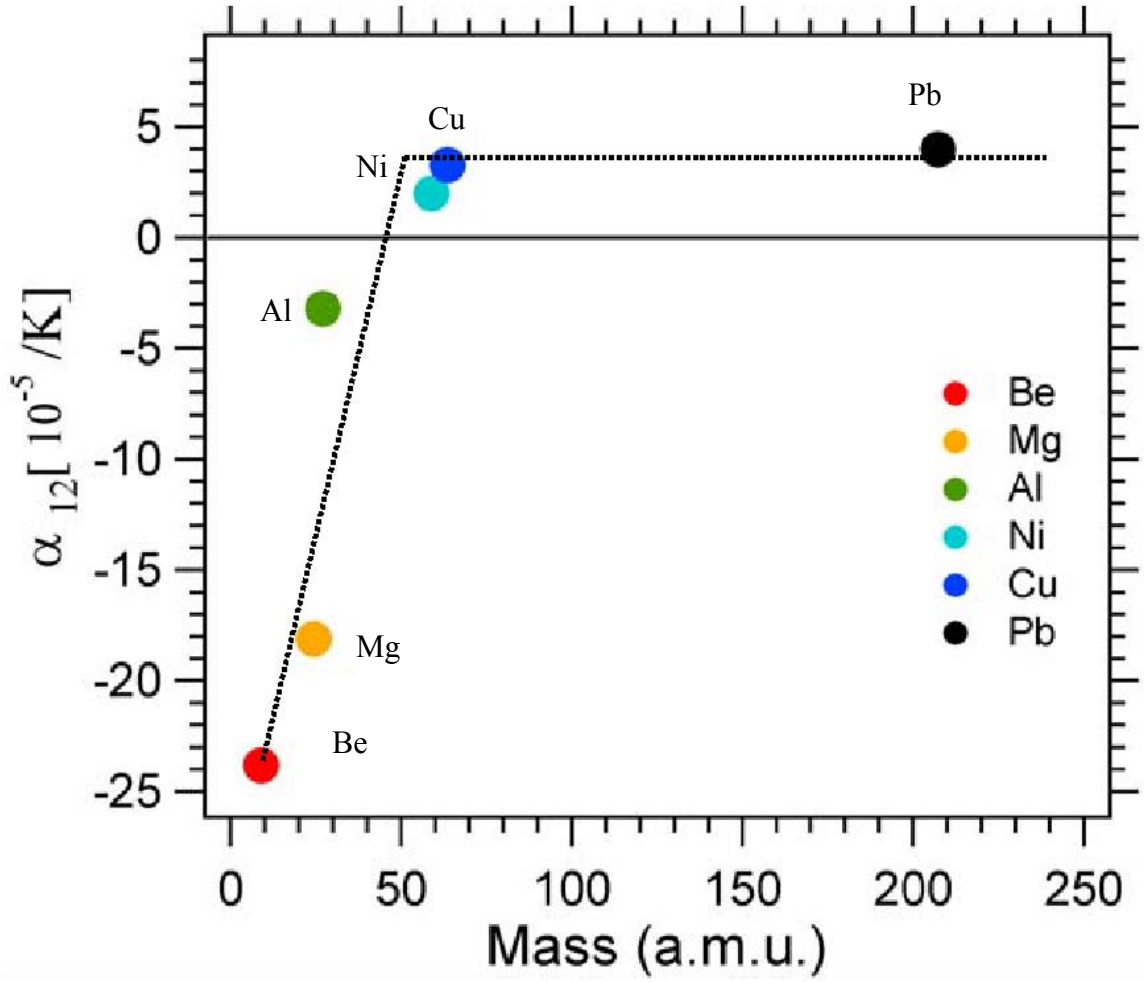

Figure 6.10 Surface thermal expansion coefficient in the first interlayer α_{12} as a function of the mass of the atom in the crystal for the open surfaces [19]

$Mg(10\bar{1}0)$. As concluded by Ismail, thermal contraction in the first interlayer spacing occurs experimentally only for light mass materials where the mass is less than 50 a.m.u [19]. For masses greater than 50, the thermal expansion is always positive. Figure 6.10 shows Ismail's analyzed result of the thermal expansion coefficient, $\alpha_{12} = \frac{1}{d_{12}} \frac{\partial d_{12}}{\partial T}$, versus atomic mass. Apparently, the lighter masses of the Be and Mg atoms favor their first layer thermal contraction of open surfaces.

6.4 Construction of the Universal Rule for Thermal Expansion on the Open Surface

Up to now, most study on the thermal expansion of the open surface focused on the geometry structure, atomic, and vibrational properties. My work here is to pinpoint the importance of the surface electronic structure to the surface thermal expansion. When a metal is separated into two halves exposing two pristine surfaces, due to the reduced symmetry and missing coordination, the electronic charge near surfaces have to redistribute themselves to lower the surface free energy and screen the presence of the surface from the bulk. In the case for the open surface, surface charge smoothing and back bonding of the surface broken bonds are more likely to happen [1], and thus the first layer contraction is universal [5]. However, when temperature increases, things may change. Inside the 3D bulk, the lattice always expands with increasing temperature so that more lower energy phonons are populated. The electronic structure in the bulk does not take an effective role for bulk lattice expansion. However, as for the surface, the special charge distribution due to the formation of the surface, which hence leads to

surface layer contraction on the open surface, would surprisingly go against the normal lattice thremal expansion when temperature increases. The unique 2D surface circumstance gives the possibility of this strange and interesting phenomenon. I illustrated this phenomenon in detail through the surface states and large negative thermal expansion on $\mathrm{Be}(10\bar{1}0)$. This competition between the surface electronic charge and lattice vibration can be seen from the contributions to the surface free energy, the static free energy term for the electrostatic first-second layer inner potential and vibrational free energy term for the lattice vibration. In the common sense, both terms will minimize themselves for the stable surface condition. However, in the case for $\mathrm{Be}(10\bar{1}0)$, the first-and-third layer coupling strengthened by the back bonding favors further contraction of the first layer with increasing temperature. The vibrational free energy contributed to by out-of-plane vibrations on the first layer will hence be less likely to minimize. The beauty of the nature is that through the dominant electron-phonon coupling of S1 surface state and shear horizontal optical phonon, the in–plane vibrations are getting softer with increasing temperature to compensate for the less anharmonicity of out-of-plane vibrations. Therefore, for a more precise description, an extra term representing self-energy of electron-phonon coupling should be included in the surface free energy. According to Finnis and Heine's model [56], surface charge smoothing can be regarded as the result of minimizing large self-energy on the surface where the screening electrons are no longer distributed symmetrically about their ion core. In accordance, electron-phonon coupling on the surface should continue decreasing the self-energy when the temperature increases. $\mathrm{Be}(10\bar{1}0)$ is the extreme case illustrating the competition between surface electron structure and lattice vibration. To generalize this idea to all

other open surfaces of other metals, other factors such as atomic mass should also be considered. Anyway, the first-and third-layer coupling from the geometry consideration is an universal property for the entire open relaxed surfaces. Starting from this, the next consideration should be the important factors for strengthening this coupling. The back bonding from surface electronic charge distribution is one, and the lighter atomic mass is another. $Be(10\bar{1}0)$ has the strongest back bonding force and lightest atomic mass to cause the largest negative thermal expansion. To examine other open surfaces of other metals, one should precisely calculate the enhanced percentage of force constant between the first and third layers after relaxation, contributed to by both factors. I believe there should be a criterion for the enhanced force constant percentage, above which the surface charge wins, causing thermal contraction of the surface layer, such as $Be(10\bar{1}0)$, $Mg(10\bar{1}0)$, and Al(110), and below which the lattice vibration wins, causing the thermal expansion of the surface layer, such as Cu(110), Ag(110), and Pb(110) [22]. In the latter case where the large anharmoniciy of out-of plane vibrations happens, I believe the breakdown of the first-and third-layer coupling with increasing temperature indicates that the surface electronic charge distribution would change in a different way to assist the out-of-plane vibration to reduce the surface-free energy. The interplay between the surface states and the surface lattice behavior for this scenario is another interesting subject to investigate. Figure 6.11 illustrates my picture between the surface electron structure and lattice structure for the open surfaces of metals.

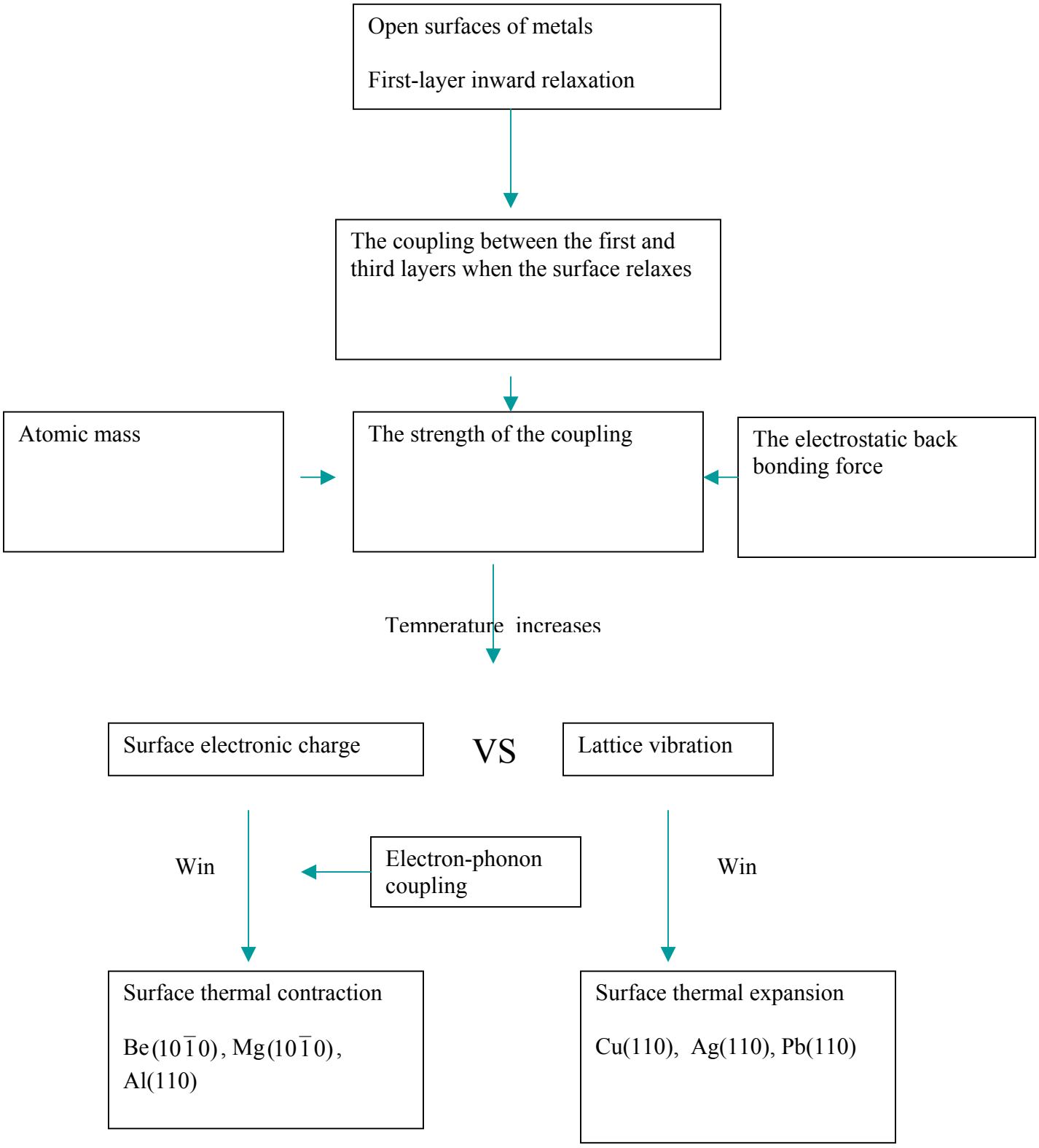

Figure 6.11 Picture for the relationship between THE electronic structure and THE lattice structure for thermal expansion (contraction) on open surfaces of metals

6.5 Future Experiments to Do

My research is to examine one of the most important many-body effects — electron-phonon interaction — on the surface. The distinct difference between the bulk and surface for Be makes its surface a very interesting object for investigating th electron-phonon interaction. Through surface state band structure study, I found the hybridization of S2 and SR states, which makes the $\mathrm{Be}(10\bar{1}0)$ surface nearly covalent-like even though there is still the S1 surface state contributing to the density of states about the Fermi level. Then, when examining the temperature dependence of the surface state, I found the localized S1 surface state has the most dominant coupling with localized shear horizontal high-energy optical phonons. After a big effort of study, I found these two results could lead to the whole picture of the unique large inward relaxation and thermal contraction on this surface. In other words, the intimate relation between electronic structure and lattice behavior is proved and first illustrated through my study on the $\mathrm{Be}(10\bar{1}0)$ surface. Based on my results, I can think of several future experiments to conduct.

1. Investigating the electronic structures and electron-phonon coupling on Al(110). The Al(110) surface has a similar relaxation and thermal expansion behavior [6,23] as Be(1010). The first layer out-of-plane vibration also has less anharmonicity than that of the second layer. It would be interesting to see if the surface state behavior on Al(110) would be similar to that on $\mathrm{Be}(10\bar{1}0)$.

2. Investigating the electronic structures and electron-phonon coupling on $\mathrm{Be}(11\bar{2}0)$. As from previous study, the $\mathrm{Be}(11\bar{2}0)$ surface is more open than $\mathrm{Be}(10\bar{1}0)$ and further has surface reconstruction (1×3)[58]. It would be interesting to study the relation between the electron phonon coupling and surface reconstruction on this surface.
3. Measuring the temperature dependence of the surface phonon bands on $\mathrm{Be}(10\bar{1}0)$. According to my picture, I predict the optical phonon dispersion between $\bar{A}$ and $\bar{\Gamma}$ would show a temperature-dependent Kohn effect due to dominant coupling with the S1 surface state.
4. Measuring superconductivity on $\mathrm{Be}(10\bar{1}0)$ by investigating the shift of the Fermi edges in the low temperature regime using high-resolution photoemission. According to the high electron-phonon coupling constant λ value, 0.64, on $\mathrm{Be}(10\bar{1}0)$ and its similar property to other high-T_c superconductivity materials, high-T_c superconductivity on $\mathrm{Be}(10\bar{1}0)$ is predicted.

References

References for Chapter 1

1. N.W. Ashcroft and N.D Mermin, *Solid State Physics* (Saunders College, Philadelphia, 1976).
2. Sydney G. Davison and Maria Steslicka, Basic Theory of surface states (Oxford University Press, New York, 1992).
3. N. V. Smith, Phys. Rev. B **32**, 3549 (1085).
4. P. M. Echenique and J. B. Pendry, J. Phys. C **11**, 2065 (1978)
5 D. Straub and F. J. Himpsel, Phys. Rev. Lett. **52**, 1922 (1984) .
6 B. Reihl, K. H. Frank and R. R. Schlittler, Phys. Rev. B **30**, 7328 (1984).
7. D. P. Woodruff, W. A. Royer and N. V. Smith, Phys. Rev. B **34**, 764 (1986).
8. A.W. Maue, Z. Physik **94**, 717 (1935).
9. E. T. Goodwin , Proc. Camb. Phil. Soc. **35**, 205 (1939)
10. F. Forstmann, F, Z. Physik 235, **69** (1970)
11. J. B. Pendry and S. J. Gurman, Surf. Sci. **49**, 87 (1975)
12. E. T. Goodwin, Proc. Camb. Phil. Soc **35**, 221 (1939b)
13. W. Shockley, Phys. Rev. **56**, 317 (1939).
14. P. Heimann, J. Hermanson, H. Miosga, and H. Neddermeyer, Phys. Rev. Lett. **42**, 1782 (1979) ; Phys. Rev. B **20**, 3059 (1979)
15. E.W. Plummer, Physica Scripta **T17**, 186 (1987)
16. F. Forstmann, J. B. Pendry, Z. Physik **235**, 75 (1970)
17. E.W. Plummer and J.W. Gadzuk, Phys. Rev. Lett. **25**, 1493 (1970).
18. F.G Allen, G.W. Gobeli, Phys. Rev. **127**, 150 (1962)

19. G. Chiarotti, S. Nannarone, R. Pastore, and P. Chiaradia, Phys. Rev. B **4**, 3398 (1971)

20. H. Lüth, Appl. Phys. **8**, 1 (1975)

21. D. E. Eastman, J. Vac. Sci. Tech. **17**, 492 (1980)

22. E.W. Plummer and A. E. Bell, J. Vac. Sci. Tech. **9**, 583 (1972)

23. J. W. Gadzuk and E. W. Plummer, Phys. Rev. Lett. **25**, 1439 (1970)

24. P. O. Gartland, S. Berge, and B. J. Slagsvold, Phys. Rev. Lett. **30**, 916 (1973); P. O. Gartland and B. J. Slagsvold, Phys. Rev. B **12**, 4047 (1975)

25. S. G. Louie, P. Thiry, R. Pinchaux, Y. Petroff, D. Chandesris, and J. Lecante, Phys. Rev. Lett. **44**, 549 (1980).

26. S. D. Kevan and R. H. Gaylord, Phys. Rev. Lett. **57**, 2975 (1986).

27. T. C. Hsieh, P. John, T. Miller and T.-C. Chaing, Phys. Rev. B **35**, 3728 (1987).

28. S. D. Kevan and R.H. Gaylord, Phys. Rev. B **36**, 5809 (1987).

29. C. T. Chen and N. V. Smith, Phys. Rev. B **35**, 5407 (1987).

30. L. Petersen, P. T. Sprunger, Ph. Hofmann, E. Lægsgaard, B. G. Briner, M. Doering, H.-P. Rust, A. M. Bradshaw, F. Besenbacher, and E. W. Plummer, Phys. Rev. B **57**, R6858 (1998).

31. P. T. Sprunger, L. Petersen, E. W. Plummer, E. Lægsgaard, and F. Besenbacher, Science **275,** 1764 (1997).

32. B. G. Briner, Ph. Hofmann, M. Doering, H.-P. Rust, E. W. Plummer, and A. M. Bradshaw, Europhys. Lett. **39**, 67 (1997); Phys. Rev. B 58, 13 931 (1998).

33. L. Peterson, B. Shaefer, E. Laesgaard, I. Stensgaard, and F. Besenbacher, Surf. Sci. **457**, 319 (2000)

34. R. A. Bartynski, T. Gustafsson and Paul Soven, Phys. Rev. B **31**, 4745 (1985).

35. R. A. Bartynski, E. Jensen, T. Gustafsson and E. W. Plummer, Phys. Rev. B **32**, 1921 (1985).

36. R. A. Bartynski, R. H. Gaylord, T. Gustafsson, and E. W. Plummer, Phys. Rev. B **33**, 3644 (1986).

37. Ph. Hofmann, R. Stumpf, V.M. Silkin, E.V. Chulkov, E.W. Plummer, Surf. Sci. **355**, L278 (1996).

38. V.M. Silkin and E.V. Chulkov, Phys. Solid State **37**, 1540 (1995).

39. S.-J. Tang, Ismail, P. T. Sprunger, and E. W. Plummer, Phys. Rev. B **65**, 235428 (2002)

40. See chapter 4 and 5 in this Thesis.

References for chapter 2

1. L.D.Landau, Sov. Phys. JETP **3**,920 (1957); **5**,101 (1957); and **8**,70 (1959)
2. J. E. Inglesfield and E. W. Plummer, in *Angle Resolved Photoemission, Theory and Applications*, edited by S. D. Kevan (Elsevier, Amsterdam, 1992).
3. E.W Plummer, Phys. Scr. **T17**, 186, (1987)
4. P. Hohenberg and W. Kohn, Phys. Rev. **136**, B864 (1964)
5. W. Kohn and L. J. Sham, Phys. Rev. **140**, A1133 (1965)
6. L. Hedin and S. Lundqvist, in Solid State Physics, edited by F. Seitz, D. Turnbull, and H. Ehrenreich (Holt, Reinhardt and Winston, New York, 1969), Vol. 23, p. 1. ; L. Hedin, Phys. Rev. **A139**, 796(1965).
7. Zhu. X and Overhauser, A.W., Phys. Rev. B**33**, 925 (1986).
8. M. Y. Chou, P. K. Lam and M. L. Cohen, Phys. Rev. B **28**, 4179 (1983).
9. E. Jensen, R. A. Bartynski, T. Gustafsson, E. W. Plummer, M. Y. Chou, M. L. Cohen, and G. B. Hoflund, Phys. Rev. B **30**, 5500 (1984); E. Jensen, R. A. Bartynski, T. Gustafsson and E. W. Plummer, Phys. Rev. Lett. **52**, 2172 (1984)
10. L. Hedin and B. I. Lundqvist, J. Phys. **C 4**, 2064 (1971)
11. B. J. Slagsvold, J. K. Grepstad, and P. O. Gartland, Phys. Scr. **T4**, 65 (1983)
12. R. A. Bartynski, R. H. Gaylord, T. Gustafsson, and E. W. Plummer, Phys. Rev. B **33**, 3644 (1986) .
13. B. I. Lundqvist, Phys. Status Solidi **32**, 273 (1969)
14. E. V. Chulkov, V. M. Silkin, and E. N. Shirykalov, Surf. Sci. **188**, 287 (1987)
15. V.M. Silkin and E.V. Chulkov, Phys. Solid State **37**, 1540 (1995).

16. P. T. Sprunger, L. Petersen, E. W. Plummer, E. Lægsgaard, and F. Besenbacher, Science **275**, 1764 (1997).

17. B. G. Briner, Ph. Hofmann, M. Doering, H.-P. Rust, E. W. Plummer, and A. M. Bradshaw, Europhys. Lett. **39**, 67 (1997); Phys. Rev. B 58, 13 931 (1998).

18. L.I. Johansson, H.I.P. Johansson, J.N. Andersen, E. Lundgren, and R. Nyholm, Phys. Rev. Lett. **71**, 2453 (1993).

19. H. I. P. Johansson, L. I. Johansson, E. Lundgren, J. N. Andersen, and R. Nyholm Phys. Rev. B **49**, 17460 (1994).

20. H. L. Davis, J. B. Hannon, K. B. Ray, and E. W. Plummer, Phys. Rev. Lett. **68**, 2632 (1992).

21. K. Pohl, J.-H. Cho, K. Terakura, M. Scheffler, and E. W. Plummer, Phys. Rev. Lett. **80**, 2853 (1998).

22. Ph. Hofmann, K. Pohl, R. Stumpf, E.W. Plummer, Phys. Rev. B **53**, 13715 (1996).

23. Ismail, Ph. Hofmann, A. P. Baddorf, and E.W. Plummer, to be published in PRB.

24. T. Balasubramanian, L. I. Johansson, P. -A. Glans, C. Virojanadara, V. M. Silkin, E.V. Chulkov, and P. M. Echenique Phys. Rev. B **64**, 205401 (2001).

25. Ph. Hofmann, R. Stumpf, V.M. Silkin, E.V. Chulkov, E.W. Plummer, Surf. Sci. **355**, L278 (1996).

26. R. A. Bartynski, E. Jensen, T. Gustafsson, and E. W. Plummer Phys. Rev. B **32**, 1921 (1985)

27. V. M. Silkin, T. Balasubramanian, E. V. Chulkov, A. Rubio, and P. M. Echenique, Phys. Rev. B **64**, 085334 (2001).

28. J- H. Cho, private communication.

29. J. C. Boettger and S.B. Trickey, Phys. Rev. B**32**, 1356 (1985).

30. B.A. McDougall, T. Balasubramanian, E. Jensen, Phys Rev. B **51**, 13891(1995).

31. T. Balasubramanian, E. Jensen, X.L. Wu and S.L. Hulbert, Phys. Rev. B **57**, 6866 (1998).

32. M. Hengsberger et al., Phys. Rev. Lett. 83, 592(1999); M. Hengsberger, R. Fresard, D. Purdie, P. Segovia, and Y. Baer, Phys. Rev. B **60**, 10796 (1999).

33. S. Lashell, E. Jensen, and T. Balasubramanian, Phys. Rev. B **61**, 2371(2000).

34. S. D. Kevan, Phys. Rev. Lett. **50**, 526 (1983).

35. J. Tersoff and S. D. Kevan, Phys. Rev. B **28**, 4267 (1983).

36. S.D. Kevan, Phys. Rev. B **33**, 4364 (1986)

37. F. Theilmann, R. Matzdorf, G. Meister, and A. Goldmann, Phys. Rev. B **56**, 3632 (1997).

38. J. Quinn, Phys. Rev. **126**, 1453 (1962).

39. G. F. Giuliani and J. J. Quinn, Phys. Rev. B **26**, 4421 (1982).

40. P. R. Matzdorf, G. Meister, and A. Goldmann, Phys. Rev. B **54**, 14 807 (1996)

41. Straube, F. Pforte, T. Michalke, K. Berge, A. Gerlach, and A. Goldmann, Phys. Rev. B **61**, 14 072 (2000)

42. J. J. Paggel, T. Miller, and T.-C. Chiang, Phys. Rev. Lett. **83**, 1415 (1999).

43. A. Eiguren, B. Hellsing, F. Reinert, G. Nicolay, E. V. Chulkov, V. M. Silkin, S. Hüfner, and P. M. Echenique, Phys. Rev. Lett. **88**, 066805 (2002)

44. B. A. Sanborn, P. B. Allen, and D. A. Papaconstantopoulos, Phys. Rev. B **40**, 6037 (1989)

45. This thesis, chapter 5

46. T. Valla, A. V. Fedorov, P. D. Johnson, and S. L. Hulber, Phys. Rev. Lett. **83**, 2085 (1999).

47. S.-J. Tang, Ismail, P. T. Sprunger, and E. W. Plummer, Phys. Rev. B **65**, 235428 (2002)

48. Ph. Hofmann, Y. Q. Cai, Ch. Grütter, and J. H. Bilgram Phys. Rev. Lett. **81**, 1670 (1998).

49. J.-H. Cho, Ismail, Z.Y. Zhang, and E.W. Plummer, Phys. Rev. B **59**, 1677 (1999).

50. Ismail, E.W. Plummer, M. Lazzeri, and S. de Gironcoli, Phys. Rev. B **63**, 233401 (2001).

51. P. Goy and B. Castaing, Phys. Rev. B **7**, 4409 (1973).

52. Sung Ho Choh, W. R. Datars Phys. Rev. B **9**, 1160 (1974).

53. G. Grimvall, The Electron-Phonon interaction in Metals (North-Holland, New York, 1981).

54. G. Grimvall, J. Phys. Chem. Solids **29**, 1221 (1968)

References for chapter 3

1. G. Borstel, Appl. Phys.**A38**, 193 (1985).

2. Hans Lüth, *Surfaces and Interfaces of Solid Materials* (Springer, New York, 1995).

3. Andrew Zangwill, Physics at surfaces (Cambridge University Press, Cambridge,1988).

4. C.L. Allyn, T. Gustafsson, and E.W. Plummer, Rev. Sci. Instrum. **49**, 1197 (1978)

5. K.D. Koch, Dissertation.

6. E.Morikawa, J.D. Scott, E. D. Poliakoff, R. L. Stockbauer, and V. Sailie, Rev. Instrum. **63**, 1300 (1992)

7. K. D. Koch, Ch. V. Mohan, J. L. Erskine, P. T. Sprunger, and J. D. Scott, Nucl. Instr. And Meth. **222**, 103 (1984)

8. B. C. Craft, V. Saile, J. D. Scott, and E. Morikawa, Nucl. Instrum. Methods Phys. Res. B **56/57**, 379 (1991).

9. B. C. Craft, M. Feldman, E. Morikawa, E. D. Poliakoff, V. Saile, J. D. Scott, and R. L. Stockbauer, Rev. Sci. Instrum. **63**, 1561 (1992)

10. J. D. Scott, H. Bluem, B. C. Craft, L. Marceau-Day, A. Mihill, E. Morikawa, V. Saile, Y. Vladimirsky, and O. Vladimirsky, Proc. SPIE **1736**, 117 (1992).

11. S. LaShell, B.A. McDougall, and E. Jensen, Phys. Rev. Lett. **77**, 3419 (1996).

12. E. Morikawa, C. M. Evans, and J. D. Scott, AIP Conf. Proc. **576**, 730 (2001).

References for Chapter4

1. L. Pauling, *The Nature of the Chemical Bond, 3rd ed.* (Cornell University Press, Ithaca, NY, 1960).
2. M.Y. Chou, P.K. Lam, and M.L. Cohen, Phys. Rev. B **28**, 4179 (1983); M.Y. Chou and M.L. Cohen, Solid State Commun. **57**, 785 (1986).
3. Ph. Hofmann, K. Pohl, R. Stumpf, and E.W. Plummer, Phys. Rev. B **53**, 13 715 (1996).
4. V.M. Silkin and E.V. Chulkov, Phys. Solid State **37**, 1540 (1995).
5. Ph. Hofmann, R. Stumpf, V.M. Silkin, E.V. Chulkov, E.W. Plummer, Surf. Sci. **355**, L278 (1996).
6. Private communication with J-H. Cho
7. E. V. Chulkov, V. M. Silkin, and E. N. Shirykalov, Surf. Sci. **188**, 287 (1987)
8. R. A. Bartynski, E. Jensen, T. Gustafsson and E. W. Plummer, Phys. Rev. B **32**, 1921 (1985)
9. N. V. Smith, Phys. Rev. B **32**, 3549 (1085).
10. R. Paniago, R. Matzdorf, G. Meistter, A. Goldmann, Surf. Sci. **336**, L113 (1995).
11. A. Gerlach, G. Meister, R. Matzdorf, A. Goldmann, Surf. Sci. **443**, L221 (1999).
12. P. Straube, F. Pforte, T. Michalke, K. Berge, A. Gerlach, and A. Goldmann, Phys. Rev. B **61**, 14 072 (2000).
13. R. Paniago, R. Matzdorf, A. Goldmann and R. Courths, J. Phys: Condens. Matter **7**, 2095 (1995).

14. O. Hjortsam, J. Trygg, J.M. Wills, B. Johansson, O. Eriksson, Surf. Sci. **355**, L214 (1996).

15. Ismail, Ph. Hofmann, A. P. Baddorf, and E.W. Plummer, to be published in PRB.

16. T. Balasubramanian, P-A. Glans and L.I Johansson, Phys. Rev B **61**, 12709 (2000). T. Balasubramanian, L. I. Johansson, P. -A. Glans, C. Virojanadara, V. M. Silkin, E. V. Chulkov, and P. M. EcheniquePhys. Rev. B **64**, 205401 (2001)

17. The range of phonon frequencies were selected based on reasonable physical properties which were both input and output from the fitting. For example, bulk Be has a Debye energy of 86 meV and thus the range of phonon energies input to the fit must be nearly equivalent (< 90 meV). Moreover, an additional variable in the fit is the offset, specifically the contribution of e-e and e-defect interactions, which cannot be unphysically negative. In reference 19, the contribution of both these effects to the localized surface state in Be$(10\bar{1}0)$ is about 50meV. In accordance, we believe an offset range between 30 meV and 100 meV is physically reasonable for their contribution to S1 peak width.

18. R. Stedman, Z. Amilius, R. Pauli, and O. Sundin, J. Phys. F **6**, 157 (1976).

19. M. Lazzeri, S. De Gironcoli, Surf. Sci. **454**, L442 (2000).

20. Ph. Hofmann, E.W. Plummer, Surf. Sci. **377**, L330 (1997).

21. S.D. Kevan, Phys. Rev. Lett. **50**, 526 (1983).

22. G. Grimvall, The Electron-Phonon interaction in Metals (North-Holland, New York, 1981).

23. M. Hengsberger, R. Fresard, D. Purdie, P. Segovia, and Y. Baer, Phys. Rev. B **60**, 10796 (1999).

24. S. Lashell, E. Jensen, and T. Balasubramanian, Phys. Rev. B **61**, 2371(2000).

25. E. Rotenberg, J. Schaefer, and S. D. Kevan, Phys. Rev. Lett. **84**, 2925 (2000).

26. S. Engelsberg and J.R. Schrieffer, Phys. Rev. **131**, 993 (1963).

27. Please compare the figure2 with figure 14, figure3 with figure 15,figue 4 with figure 16, and figure 5 with figure 17 in Reference 34.

28. Valla, T.et al. Science **285**,2110-2113 (1999)

References for chapter 5

1. M.Y. Chou and M.L. Cohen, Solid State Commun. **57**, 785 (1986).
2. R. A. Bartynski, R. H. Gaylord, T. Gustafsson, and E. W. Plummer, Phys. Rev. B **33**, 3644 (1986).
3. H. J. Gotsis, D. A. Papaconstantopoulos, and M. J. Mehl Phys. Rev. B **65**, 134101 (2002)
4. Private communication with J.-H. Cho.
5. S. G. Louie, P. Thiry, R. Pinchaux, Y. Petroff, D. Chandesris, and J. Lecante, Phys. Rev. Lett. **44**, 549 (1980).
6. P. Blaha, K. Schwarz, and P. H. Dederichs, Phys. Rev. B **38**, 9368 (1988).
7. S. Daniuk, T. Jarlborg, G. Kontrym-Sznajd, J. Majsnerowski, and H. Stachowiak, J. Phys.: Condens. Matter **1**, 8397 (1989).
8. P. B. Allen and M. L. Cohen, Phys. Rev. 187, 525 (1969); B. A. Sanborn, P. B. Allen, and D. A. Papaconstantopoulos, Phys. Rev. B **40**, 6037 (1989)
9. A. Eiguren, B. Hellsing, F. Reinert, G. Nicolay, E. V. Chulkov, V. M. Silkin, S. Hüfner, and P. M. Echenique, Phys. Rev. Lett. **88**, 066805 (2002).
10. D.-A. Luh, T. Miller, J. J. Paggel, and T.-C. Chiang Phys. Rev. Lett. **88**, 256802 (2002)
11. R. Matzdorf, G. Meister, and A. Goldmann, Phys. Rev. B **54**, 14 807 (1996).
12. R. Paniago, R. Matzdorf, G. Meistter, A. Goldmann, Surf. Sci. **336**, L113 (1995).
13. Private communication with E.V. Chulkov.

References for chapter 6

1. P.J. Feibelman, Phys. Rev. B 46, 2532 (1992); P. J. Feibelman, Phys. Rev. B **53**, 13740 (1996)
2. R. Smoluchowski, Phys. Rev. **60**, 661 (1941).
3. J. K. Nørskov and N. D. Lang, Phys. Rev. B **21**, 2131 (1980); (b) M. J. Stott and E. Zaremba, Solid State Commun. **32**, 1297 (1979); and, Phys. Rev. B **22**, 1564 (1980); (c) M. S. Daw and M. I. Baskes, **29**, 6443 (1984).
4. H. L. Davis, J. B. Hannon, K. B. Ray and E. W. Plummer, Phys. Rev. Lett. **68**, 2632 (1992).
5. Ph. Hofmann, K. Pohl, R. Stumpf, and E.W. Plummer, Phys. Rev. B 53, **13** 715 (1996).
6. K. M. Ho and K.-P. Bohnen, Phys. Rev. B **32**, 3446 (1985).
7. V.M. Silkin and E.V. Chulkov, Phys. Solid State **37**, 1540 (1995).
8. Private communication with J-H. Cho
9. O. Hjortsam, J. Trygg, J.M. Wills, B. Johansson, O. Eriksson, Surf. Sci. **355**, L214 (1996).
10. H.I.P. Johansson and L.I. Johansson, Phys. Rev. B **49**, 17460 (1994).
11. J.-H. Cho, K. S. Kim, S.-H. Lee, M.-H. Kang, and Z. Zhang, Phys. Rev. B **61**, 9975 (2000).
12. Ph. Hofmann, R. Stumpf, V.M. Silkin, E.V. Chulkov, E.W. Plummer, Surf. Sci. **355**, L278 (1996).

13. S. Lizzit, K. Pohl, A. Baraldi, G. Comelli, V. Fritzsche, E. W. Plummer, R. Stumpf, and Ph. Hofmann, Phys. Rev. Lett. **81**, 3271 (1998)

14. B. G. Briner, Ph. Hofmann, M. Doering, H.-P. Rust, E. W. Plummer, and A. M. Bradshaw, Phys. Rev. B **58**, 13931 (1998)

15. P. T. Sprunger, L. Petersen, E. W. Plummer, E. Lægsgaard, and F. Besenbacher, Science **275**, 1764 (1997).

16. N. V. Smith, Phys. Rev. B **32**, 3549 (1085).

17. L. Peterson, B. Shaefer, E. Laesgaard, I. Stensgaard, and F. Besenbacher, Surf. Sci. **457**, 319 (2000).

18. S. Narasimhan, Phys. Rev. B **64**, 125409 (2001)

19. Ismail, Ph. Hofmann, A. P. Baddorf, and E.W. Plummer, to be published in PRB.

20. M. Lazzeri, and S. de Gironcoli, Phys. Rev. B **65**, 245402 (2002).

21. A.P. Baddorf and E.W. Plummer, Phys. Rev. Lett. **66**, 2770 (1991)

22. Y. Cao and E. Conrad, Phys. Rev. Lett. **65**, 2808 (1990); P. Statiris, H. C. Lu, and T. Gustafsson, Phys. Rev. Lett. **72**, 3574 (1994); G. Helgesen, D. Gibbs, A. P. Baddorf, D. M. Zehner, and S. G. J. Mochrie, Phys. Rev. B **48**, 15 320 (1993).

23. N. Marzari, D. Vanderbilt, A. De Vita, and M.C. Payne, Phys. Rev. Lett. **82**, 3296 (1999).

24. G. Helgesen, D. Gibbs, A.P. Baddorf, D.M. Zehner, and S.G.J. Mochrie, Phys. Rev. **48**, 15320 (1993).

25. M. Lazzeri, S. De Gironcoli, Surf. Sci. **454**, L442 (2000).

26. K.M. Ho and K.P. Bohnen, Phys. Rev. B **38**, 12 897 (1988).

27. K.M. Ho and K.P. Bohnen, , Phys. Rev. Lett. **56**, 934 (1986).

28. B. W. Busch, and T. Gustafsson, Phys. Rev. B **61**, 16 097 (2000).

29. L. Yang and T. S. Rahman, Phys. Rev. Lett. **67**, 2327 (1991).

30. Talat S. Rahman, Z.-J. Tian, J.E.Black, Surf. Sci. **374**, L9 (1997).

31. S. Narasimhan and M. Scheffler, Z. Phys. Chem. (Munich) **202**, 253 (1997)

32. J.-H. Cho and M. Scheffler, Phys. Rev. Lett. **78**, 1299 (1997).

33. K. Pohl, J.-H. Cho, K. Terakura, M. Scheffler, and E. W. Plummer, Phys. Rev. Lett. **80**, 2853 (1998).

34. H.-J. Ernst, E. Hulpke and J. P. Toennies, Phys. Rev. Lett. **58**, 1941 (1987).

35. E. Hulpke and D.–M. Smilgies, Phys. Rev. B **40**, 1338 (1989).

36. J. E. Reutt, Y. J. Chabal, and S. B. Christman, Phys. Rev. B **38**, 3112 (1988).

37. K. E. Smith and S. D. Kevan, Phys. Rev. B **43**, 3986 (1991).

38. Jörg Kröger et al., Phys. Rev. B **66**, 073414 (2002).

39. J. I. Pascual, Z. Song, J. J. Jackiw, K. Horn, and H.-P. Rust, Phys. Rev. B **63**, 241103 (2001)

40. R. A. Bartynski, T. Gustafsson and Paul Soven, Phys. Rev. B **31**, 4745 (1985).

41. J. Bardeen, L. N. Cooper, and J. R. Schrieffer, Phys. Rev. **106**, 162 (1957); **108**, 1175 (1957)

42. W. L. McMillan, Phys. Rev. **167**, 331 (1968).

43. T. Balasubramanian, P-A. Glans and L.I Johansson, Phys. Rev B **61**, 12709 (2000).

44. T. Balasubramanian, E. Jensen, X. L. Wu, and S. L. Hulbert, Phys. Rev. B **57**, 6866 (1998).

45. P. G. De Gennes, Rev. Mod. Phys. **36**, 225 (1964).

46. E. V. Chulkov, V. M. Silkin, and E. N. Shirykalov, Surf. Sci. **188**, 287 (1987)

47. A. Lanzara et al., Nature (London) **412**, 510 (2001).

48. S. L. Bud'ko et al., Phys. Rev. Lett. **86**, 1877 (2001).

49. J. Kortus , I. I. Mazin, K. D. Belashchenko , V. P. Antropov, and L. L. Boyer, Phys. Rev. Lett. **86**, 4656 (2001).

50. C. Joas, I. Eremin, D. Manske, and K. H. Bennemann, Phys. Rev. B **65**, 132518 (2002).

51. J. M. An and W.E. Pickett, Phys. Rev. Lett. **86**, 4366, (2001).

52. J.-H. Cho, Ismail, Z. Zhang, and E. W. Plummer, Phys. Rev. B **59**, 1677 (1999).

53. J.-H. Cho, K.S. Kim, S.-H. Lee, M.-H. Kang and Z. Zhang, Phys. Rev. B **61**, 9975 (2000).

54. Ismail, S.-J. Tang, P. T. Sprunger, E. V. Chulkov, V. M. Silkin, and E. W. Plummer (unpublished).

55. Ismail, E.W. Plummer, M. Lazzeri, and S. de Gironcoli, Phys. Rev. B **63**, 233401 (2001).

56. M. Lazzeri, Ph. D. thesis, SISSA-ISAS, (1999).

57. M. W. Finnis and V. Heine, J. Phys. **F 4**, L37 (1974)

Vita

Shu-Jung Tang was born in Taipei, Taiwan (R.O.C) on May 16 in1970. He graduated from Chang-Gou high school in 1988. He entered Tamkang University in Taipei in 1989 and received a bachelor degree of science in Physics in 1993. After two years of tough life as a soldier in military service, he went to University of Tennessee, Knoxville to study Physics for Master degree in 1995. He turned to PH.D program and joined the surface science group under the conduct of professor Ward Plummer after he passed PH.D qualified exam in 1997. In the same year, he moved to Baton Rouge, Louisiana to do experiments by the Photoemission technique in a synchrotron center called CAMD. In 2002, he received a Doctor of Philosophy degree in solid state Physics. Areas of his study have included the investigation of the electronic structures in the simple metals thin films on the semiconductors (Be/Si(111), Mg/Si(111)) and electron phonon coupling on the simple metal surfaces (Be$(10\bar{1}0)$, Mg$(10\bar{1}0)$).